Universität Siegen

Naturwissenschaftlich-Technische Fakultät

UNIVERSITÄT SIEGEN

DISSERTATION

First observation of $t\bar{t}\gamma\gamma$ production and measurement of the $t\bar{t}\gamma\gamma/t\bar{t}\gamma$ cross section ratio at $\sqrt{s} = 13$ TeV using the ATLAS detector

Dissertation
zur Erlangung des Grades eines Doktors
der Naturwissenschaften
(Dr. rer. nat.)

vorgelegt der

Naturwissenschaftlich-Technischen Fakultät
der Universität Siegen

vorgelegt von

Arpan Ghosal

aus *Delhi, India*

Siegen 2025

Betreuerin und erste Gutachterin:
PD Dr. Carmen Diez Pardos, Universität Siegen

Zweiter Gutachter:
Prof. Dr. Ivor Fleck, Universität Siegen

Mitglieder der Promotionskommission:
Prof. Dr. Guido Bell, Universität Siegen
Prof. Dr. Carsten Busse, Universität Siegen

Tag der mündlichen Prüfung:
10.10.2025

.

Abstract

This thesis presents the first observation of top-quark pair production process in association with two photons ($t\bar{t}\gamma\gamma$), which is not only rare in the Standard Model but also constitutes an irreducible background to the $t\bar{t}H$ ($H \to \gamma\gamma$) process. The related $t\bar{t}\gamma$ process, in which a top-quark pair is produced in association with a single photon, has been well studied, and its inclusive cross section was recently measured by the ATLAS experiment at the Large Hadron Collider (LHC).

The work presented in this thesis focuses on the measurement of the $t\bar{t}\gamma\gamma$ process with the ATLAS experiment. The measurement is performed in the single-lepton decay channel. The data correspond to an integrated luminosity of $140\,\text{fb}^{-1}$ in proton–proton collisions collected during Run 2 at a centre-of-mass energy of 13 TeV. The measurement is carried out within a fiducial phase space volume defined at particle level using kinematic requirements for the lepton, photons, and jets.

The $t\bar{t}\gamma\gamma$ production cross section is measured using the profile likelihood method and a Boosted Decision Tree (BDT). The BDT was trained to separate the $t\bar{t}\gamma\gamma$ signal process from the background processes. Additionally, the ratio of the cross sections of the $t\bar{t}\gamma\gamma$ and $t\bar{t}\gamma$ processes is extracted from a simultaneous fit.

The $t\bar{t}\gamma\gamma$ production cross section is found to be $2.42^{+0.58}_{-0.53}$ fb and corresponds to an observed significance of 5.2 standard deviations, which constitutes the first observation of this process. Furthermore, the measured ratio of the cross sections of $t\bar{t}\gamma\gamma$ to $t\bar{t}\gamma$ yields a value of $(3.30^{+0.70}_{-0.65}) \times 10^{-3}$. However, in the absence of corresponding theoretical predictions, no direct comparison with the experimentally measured values can be performed at present.

Zusammenfassung

Diese Dissertation präsentiert die erste Beobachtung der Paarproduktion von Top-Quarks in Verbindung mit zwei Photonen ($t\bar{t}\gamma\gamma$). Dieser Prozess ist nicht nur im Standardmodell selten, sondern stellt auch einen irreduziblen Untergrund für den $t\bar{t}H$ ($H \to \gamma\gamma$) Prozess dar. Der damit verbundene $t\bar{t}\gamma$ Prozess, bei dem ein Top-Quark Paar in Verbindung mit einem einzelnen Photon erzeugt wird, ist gut untersucht, und sein inklusiver Wirkungsquerschnitt wurde kürzlich vom ATLAS-Experiment am Large Hadron Collider (LHC) gemessen.

Die in dieser Dissertation vorgestellte Arbeit konzentriert sich auf die Messung des $t\bar{t}\gamma\gamma$ Prozesses mit dem ATLAS-Experiment. Die Messung wird im Zerfallskanal mit einem Lepton durchgeführt. Die Daten entsprechen einer integrierten Luminosität von $140\,\text{fb}^{-1}$ an Proton-Proton-Kollisionen, die während Run 2 bei einer Schwerpunktenergie von 13 TeV aufgezeichnet wurden. Die Messung wird innerhalb eines eingeschränkten Phasenraumvolumens durchgeführt, das auf Teilchenebene unter Verwendung kinematischer Kriterien für Leptonen, Photonen und Jets definiert ist.

Der Wirkungsquerschnitt der $t\bar{t}\gamma\gamma$ Produktion wird mit der Profile-Likelihood-Methode und einem Boosted Decision Tree (BDT) gemessen. Der BDT wurde trainiert, den $t\bar{t}\gamma\gamma$ Signalprozess von den Untergrundprozessen zu trennen. Zusätzlich wird das Verhältnis der Wirkungsquerschnitte der $t\bar{t}\gamma\gamma$ und $t\bar{t}\gamma$ Prozesse aus einer simultanen Messung extrahiert.

Der Wirkungsquerschnitt für die Produktion von $t\bar{t}\gamma\gamma$ beträgt $2{,}42^{+0{,}58}_{-0{,}53}$ fb und entspricht einer beobachteten Signifikanz von 5,2 Standardabweichungen, was die erste Beobachtung dieses Prozesses darstellt. Darüber hinaus ergibt die Messung des Verhältnisses der Wirkungsquerschnitte von $t\bar{t}\gamma\gamma$ zu $t\bar{t}\gamma$ einen Wert von $(3{,}30^{+0{,}70}_{-0{,}65}) \times 10^{-3}$. Da jedoch keine entsprechenden theoretischen Vorhersagen vorliegen, kann derzeit kein direkter Vergleich mit den experimentell gemessenen Werten durchgeführt werden.

Contents

1 Introduction 1

2 The Standard Model and the top quark 3
- 2.1 Introduction to the SM . . . 3
- 2.2 Basics of QFT . . . 4
- 2.3 The SM Lagrangian . . . 7
- 2.4 Top quark . . . 9
  - 2.4.1 Top quark production . . . 9
  - 2.4.2 Top quark production with photons . . . 10
  - 2.4.3 Theoretical calculations and experimental status . . . 12

3 The LHC and the ATLAS detector 15
- 3.1 The LHC . . . 15
- 3.2 The ATLAS detector . . . 18
  - 3.2.1 ATLAS Coordinate System . . . 18
  - 3.2.2 Inner Detector . . . 19
  - 3.2.3 Calorimeter Systems . . . 20
  - 3.2.4 Muon Spectrometer . . . 20
  - 3.2.5 Forward Detectors . . . 21
  - 3.2.6 Trigger System . . . 22
- 3.3 Reconstruction of physics objects . . . 22
  - 3.3.1 Primary Vertices . . . 23
  - 3.3.2 Reconstruction of Electrons . . . 23
  - 3.3.3 Reconstruction of Photons . . . 24
  - 3.3.4 Reconstruction of Muons . . . 24
  - 3.3.5 Reconstruction of Jets . . . 24
  - 3.3.6 Reconstruction of missing transverse momentum (E_T^{miss}) . . . 25
  - 3.3.7 Overlap removal between objects . . . 25

4 Simulation of signal and background processes 27
- 4.1 Hard scattering . . . 28
- 4.2 Parton showering . . . 30
- 4.3 Hadronization . . . 30
- 4.4 Underlying events . . . 31
- 4.5 Matching and merging . . . 31

4.6 Simulation of signal and background processes . . . 31
4.6.1 Samples with at least one photon at ME . . . 32
4.6.2 Inclusive samples (photons from parton shower) . . . 34
4.6.3 Sample-overlap removal procedure . . . 35
4.7 Categorisation of photons . . . 36

5 Event selection **39**
5.1 Data set . . . 39
5.2 MC normalisation . . . 39
5.3 Data-driven estimates of fake-photon background processes . . . 40
5.3.1 Electron-fake background (e-fake) . . . 40
5.3.2 Hadron-fake background (h-fake) . . . 41
5.4 Event selection in $t\bar{t}$ single lepton channel . . . 41

6 Signal and background discrimination **49**
6.1 Decision Tree . . . 49
6.1.1 Decision tree algorithm . . . 50
6.2 Ensemble Learning . . . 51
6.3 Boosted Decision Trees . . . 52
6.3.1 Introduction . . . 52
6.3.2 Key BDT Algorithms . . . 53
6.3.3 Hyperparameters of BDTs . . . 53
6.4 BDT framework used for signal-background discrimination . . . 54
6.4.1 Training dataset . . . 57
6.4.2 Variable selection for BDT training . . . 57
6.4.3 Training and optimization of the BDT . . . 58
6.4.4 Performance metrics of the BDT . . . 60
6.4.5 Correlation matrices . . . 67

7 Systematic uncertainties **75**
7.1 Overview of uncertainties . . . 75
7.2 Modelling uncertainties . . . 76
7.2.1 Renormalisation, factorisation and FSR scale uncertainties (μ_R, μ_F, and α_s) 76
7.2.2 Parton shower and hadronization model uncertainties . . . 76
7.2.3 ISR uncertainties . . . 76
7.2.4 Parton Distribution Function uncertainties . . . 77
7.2.5 Hard gluon emission uncertainties . . . 77
7.3 Experimental uncertainties . . . 77
7.4 Background uncertainties . . . 79
7.5 Data-driven fake estimate uncertainties . . . 80

8 Measurement of the $t\bar{t}\gamma\gamma$ cross section **81**
8.1 Fiducial phase space at particle level . . . 81
8.2 Likelihood Function . . . 82
8.2.1 The Likelihood function . . . 82

8.2.2 Profile Likelihood Function . . . 83
8.3 Cross section definition and profile likelihood fit . . . 83
8.3.1 Treatment of systematic uncertainties in the fit . . . 85
8.3.2 Treatment for modelling uncertainties . . . 86
8.4 Test of fit setup with Asimov data . . . 88
8.5 Measurement of the $t\bar{t}\gamma\gamma$ cross section . . . 92
8.5.1 Results for the $t\bar{t}\gamma\gamma$ cross section . . . 92
8.5.2 BDT input distributions after fit to data . . . 107

9 Measurement results for $t\bar{t}\gamma\gamma/t\bar{t}\gamma$ ratio **113**
9.1 Definition and extraction of ratio . . . 113
9.2 Test of fit setup with Asimov data . . . 116
9.3 Results for the ratio of $t\bar{t}\gamma\gamma$ to total $t\bar{t}\gamma$ processes . . . 120
9.4 Relative uncertainties in the measurements . . . 126

10 Summary and Conclusion **127**

A Preliminary studies with other variables **129**

B Treatment of negative weights in BDT training **131**

C BDT study with 3-class classification **137**
C.1 Training and optimization . . . 138
C.2 Measurement of $t\bar{t}\gamma\gamma$ cross-section . . . 140

D Pseudo-Experiments for Significance Estimation **143**

Bibliography **145**

List of Figures **155**

List of Tables **161**

CHAPTER 1

Introduction

The Standard Model (SM) of particle physics is a quantum field theory that describes the fundamental particles and three of the four known forces. It has demonstrated remarkable agreement with experimental observations over several decades. Despite its success, the SM does not answer some open questions. These shortcomings motivate precision studies of SM processes, which may reveal subtle deviations induced by physics beyond the Standard Model (BSM). The top quark occupies a unique position within the SM. Given the current era of high-energy colliders, top quarks and their properties are becoming more and more accessible for further studies. Of specific interest are associated production of top quarks with additional bosons such as photons. These measurements allow to access the electric charge and the electroweak dipole moments of the top quark and, more generally, to constrain modifications of the structure of these couplings.

The production of top-antitop quark pair ($t\bar{t}$) with a single photon has been studied in great detail and the inclusive and differential cross sections have been studied well by collaborations such as ATLAS and CMS. However, the considerably rarer $t\bar{t}\gamma\gamma$ process, which involves the production of a top quark and an anti-top quark pair in association with two photons, had remained unobserved so far. The main focus of the analysis presented in this thesis is to perform the first measurement of this process. Another aspect of the analysis is to measure the ratio of cross sections of the $t\bar{t}\gamma\gamma$ to the top-antitop quark pair with a single photon ($t\bar{t}\gamma$) process, which is facilitated by closely following the recent $t\bar{t}\gamma$ measurement done by ATLAS [1].

The thesis is structured as such. First, the SM and the underlying physics of the top-quark pair production in association with photons are discussed in Chapter 2. Chapter 3 discussed the experimental setup of the Large Hadron Collider and the ATLAS experiment, the data from which is used to perform the measurement. Chapter 4 discusses the simulation of signal and background processes used as theoretical predictions for the analysis. The selection of events from the data and simulations for the final measurement are discussed in Chapter 5. The signal-background discrimination to enhance the possibility to observe the $t\bar{t}\gamma\gamma$ process is done using a Boosted Decision Tree, discussed in Chapter 6. Chapter 7 discusses the uncertainties of the measuement. Finally, the measurement and the results are presented in Chapters 8 and 9.

CHAPTER 2

The Standard Model and the top quark

"It is more important to have beauty in one's equations than to have them fit experiment."

— Paul Dirac, *Scientific American, "The Evolution of the Physicist's Picture of Nature"* (1963)

Throughout the ages, humanity has tried to understand the nature of reality and contextualize these realizations in robust, mathematical forms. The Standard Model (SM) of particle physics, as of today, is a testament to this endeavour. It stands as one of the most rigorously tested and successful theories in the history of modern science [2].
This chapter, first, introduces the SM, in brief. Then, the underlying Quantum Field Theory (QFT) framework is described in Section 2.2, which discusses the theoretical underpinnings of various aspects of the SM. The organisation of SM is then described in Section 2.3, followed by the shortcomings it faces. The top quark and its production modes are described in Section 2.4. Finally, the production of top quark pair in association with photons is described in Section 2.4.2, along with the motivation for the $t\bar{t}\gamma\gamma$ measurements presented in this thesis.

2.1 Introduction to the SM

At its core, the SM provides a unified and self-consistent quantum field-theoretic description of the fundamental constituents of matter and the interactions that govern their dynamics, albeit with the notable exception of gravity. Within the SM, all known elementary particles are categorized as either fermions, which constitute matter, or bosons, which mediate the fundamental forces between them, as shown in Figure 2.1.
Fermions are further divided into quarks and leptons, each occurring in three generations that differ only in mass. Quarks are subject to all three of the fundamental interactions incorporated in the SM - the strong, weak and electromagnetic interactions. They combine to form hadrons such as protons and neutrons. Leptons include the charged fermions like electron (e), muon (μ), and tau (τ), along with their associated neutrally charged counterparts, the neutrinos (ν_e, ν_μ, ν_τ). In the SM, the charged leptons interact via the electromagnetic and the weak forces, while the neutrinos interact only via the weak force.
The gauge structure of the SM, i.e. the underlying symmetry group that dictates the interactions via force carriers (gauge bosons), is based on the product group $SU(3) \times SU(2) \times U(1)$, corresponding to

the strong, weak, and electromagnetic interactions, respectively. The dynamics of the corresponding gauge fields, associated with certain symmetries, give rise to the force-carrying bosons: the photon (γ), W^+, W^-, and Z bosons, and the eight gluons.
A central feature of the SM is the Higgs mechanism, which explains the spontaneous breaking of the electroweak symmetry and gives the W and Z bosons and the fermions their masses through their interaction with the scalar Higgs field. The discovery of the Higgs boson, the linchpin of the SM, at the Large Hadron Collider (LHC) in 2012 provided the final missing piece of the SM [3][4].

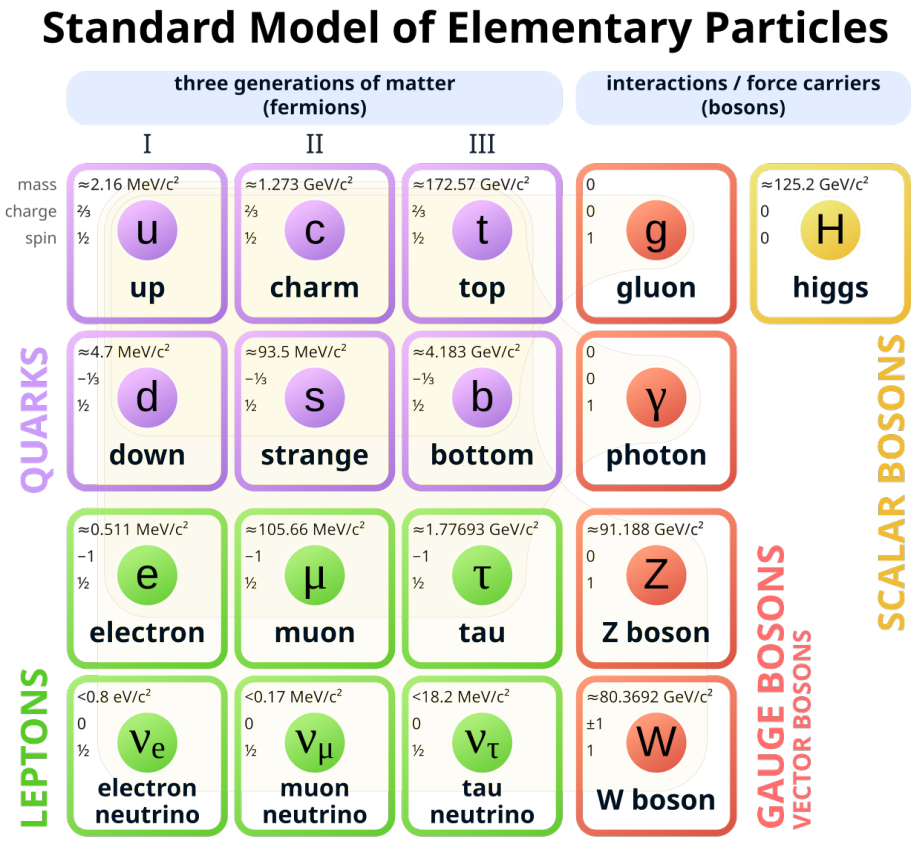

Figure 2.1: The Standard Model of particle physics, including all the known elementary fermions and bosons [5]

.

2.2 Basics of QFT

To understand the formulation and working of the SM, it is essential to first introduce the theoretical framework upon which it is built. QFT is the theoretical framework that underpins the SM and forms the foundation for our modern understanding of particle physics. It combines the principles of quantum mechanics and special relativity, and treats particles not as isolated points but as excitations of underlying quantum fields that permeate all of spacetime. In QFT, each type of particle is associated

with a corresponding field: for example, the electron is an excitation of the electron field, while photons arise from the quantized electromagnetic field. Interactions between particles are described in terms of interactions between these fields, and are typically formulated through a Lagrangian density ($\mathcal{L}$) that encodes the dynamics and symmetries of the system.

A central feature of QFT is the use of local gauge symmetry, which leads naturally to the introduction of force-carrying particles - the gauge bosons. These include the photon for electromagnetism, gluons for the strong interaction, and the W and Z bosons for the weak force.

The interaction between charged fermions and the electromagnetic field is described by the QFT called Quantum Electrodynamics (QED). It is the simplest example of a gauge field theory, based on a local $U(1)$ symmetry. In QED, the field content includes the Dirac spinor ψ, representing charged fermions such as the electron, and the vector gauge field A_μ, representing the photon. The QED Lagrangian is given as:

$$\mathcal{L}_{\text{QED}} = \bar{\psi}(i\gamma^\mu D_\mu - m)\psi - \frac{1}{4}F_{\mu\nu}F^{\mu\nu}. \tag{2.1}$$

In the above equation, the covariant derivative is defined as:

$$D_\mu = \partial_\mu + ieA_\mu \tag{2.2}$$

and the electromagnetic field strength tensor is given by:

$$F_{\mu\nu} = \partial_\mu A_\nu - \partial_\nu A_\mu. \tag{2.3}$$

The QED Lagrangian is invariant under the local $U(1)$ gauge transformation:

$$\psi(x) \to e^{i\alpha(x)}\psi(x), \quad A_\mu(x) \to A_\mu(x) - \frac{1}{e}\partial_\mu\alpha(x). \tag{2.4}$$

No spontaneous symmetry breaking occurs in QED i.e. the $U(1)$ gauge symmetry remains exact, and the photon remains massless.

Quantum Chromodynamics (QCD) is the theory of the strong interaction, describing how quarks interact via the exchange of gluons. It is a non-Abelian gauge theory based on the local $SU(3)_C$ symmetry, where C denotes the colour charge, an analog of the electric charge in QED. The field content includes six flavors of quarks, each carrying a colour charge, and eight massless gluon fields, G^a_μ, corresponding to the eight generators of $SU(3)$. The QCD Lagrangian is given by:

$$\mathcal{L}_{\text{QCD}} = \sum_f \bar{q}_f \left(i\gamma^\mu D_\mu - m_f\right) q_f - \frac{1}{4}G^a_{\mu\nu}G^{a\mu\nu}. \tag{2.5}$$

The covariant derivative in QCD is defined as:

$$D_\mu = \partial_\mu + ig_s T^a G^a_\mu, \tag{2.6}$$

where g_s is the strong coupling constant and T^a are the generators of the $SU(3)$ Lie algebra. The gluon field strength tensor is defined by:

$$G^a_{\mu\nu} = \partial_\mu G^a_\nu - \partial_\nu G^a_\mu + g_s f^{abc} G^b_\mu G^c_\nu, \tag{2.7}$$

where f^{abc} are the structure constants of $SU(3)$.

The QCD Lagrangian is invariant under local $SU(3)_C$ transformations, and this symmetry remains unbroken However, due to the non-Abelian nature of QCD, the theory exhibits the properties of confinement and asymptotic freedom - quarks and gluons inside hadrons are bound due to the increasing strength of the strong force at large distances, and they behave as free particles inside hadrons at shorter distances (or higher energies), respectively.

Higgs Mechanism and spontaneous symmetry breaking

To explain the masses of the weak gauge bosons and the fermions, the SM introduces the Higgs field, which is a complex scalar doublet field, Φ. The dynamics of this field are governed by the Lagrangian:

$$\mathcal{L}_{\text{Higgs}} = (D^{\mu}\Phi)^{\dagger}(D_{\mu}\Phi) - V(\Phi). \tag{2.8}$$

The scalar potential $V(\Phi)$ is given by:

$$V(\Phi) = \mu^2\Phi^{\dagger}\Phi + \lambda(\Phi^{\dagger}\Phi)^2. \tag{2.9}$$

The parameters satisfy $\lambda > 0$ (stability) and the sign of μ^2 controls symmetry breaking. For $\mu^2 < 0$, the potential has a non-zero minimum, and the field acquires a vacuum expectation value (VEV):

$$\langle\Phi\rangle = \frac{1}{\sqrt{2}}\begin{pmatrix}0\\ v\end{pmatrix}, \quad v = \sqrt{-\mu^2/\lambda}. \tag{2.10}$$

This spontaneous symmetry breaking reduces the electroweak symmetry $SU(2)_L \times U(1)_Y$ down to the electromagnetic $U(1)_{\text{em}}$, giving mass to the $W^{\pm}$ and Z bosons while leaving the photon massless.

Yukawa interactions and fermion masses

The fermions acquire mass through their interactions with the Higgs field via Yukawa couplings. A generic Yukawa interaction for a charged lepton is written as:

$$\mathcal{L}_{\text{Yukawa}} = -y_e\bar{L}\Phi e_R + \text{h.c.} \tag{2.11}$$

Here, L is the left-handed lepton doublet, e_R is the right-handed lepton singlet, and y_e is the Yukawa coupling. When the Higgs field acquires a VEV, $\langle\Phi\rangle = \frac{1}{\sqrt{2}}\begin{pmatrix}0\\ v\end{pmatrix}$ as in Equation 2.10, the Yukawa term becomes a mass term:

$$m_e = \frac{y_e v}{\sqrt{2}}. \tag{2.12}$$

Similar Yukawa terms exist for the quarks. For down-type quarks (e.g., d, s, b), the coupling takes a form analogous to that of the charged leptons:

$$\mathcal{L}^{d}_{\text{Yukawa}} = -y_d\bar{Q}\Phi d_R + \text{h.c.} \tag{2.13}$$

For up-type quarks (e.g., u, c, t), the Higgs doublet needs to be conjugated to preserve $SU(2)_L$ invariance, yielding:

$$\mathcal{L}^{u}_{\text{Yukawa}} = -y_u\bar{Q}\tilde{\Phi}u_R + \text{h.c.}, \quad \text{with} \quad \tilde{\Phi} = i\sigma_2\Phi^{*}. \tag{2.14}$$

In the above expressions, Q denotes the left-handed quark doublet, u_R and d_R are the right-handed up-type and down-type quark singlets, and y_u, y_d are the respective Yukawa couplings. After electroweak symmetry breaking, these terms generate fermion mass terms, with the masses proportional to their corresponding Yukawa couplings.

2.3 The SM Lagrangian

Once we have laid out the pieces of the puzzle, the complete Lagrangian of the SM emerges as the sum of the component terms:

$$\mathcal{L}_{\text{SM}} = \mathcal{L}_{\text{gauge}} + \mathcal{L}_{\text{fermion}} + \mathcal{L}_{\text{Higgs}} + \mathcal{L}_{\text{Yukawa}}, \tag{2.15}$$

where the components are:

1. $\mathcal{L}_{\text{gauge}}$: kinetic terms for the photon, gluons, W and Z bosons.
2. $\mathcal{L}_{\text{fermion}}$: kinetic terms and gauge interactions for quarks and leptons.
3. $\mathcal{L}_{\text{Higgs}}$: Higgs kinetic and potential terms.
4. $\mathcal{L}_{\text{Yukawa}}$: Yukawa couplings of the Higgs field to fermions.

As mentioned before, each part has then the following structure Lagrangian density structure:

1. **Gauge term**:
$$\mathcal{L}_{\text{gauge}} = -\frac{1}{4} G^a_{\mu\nu} G^{a\,\mu\nu} - \frac{1}{4} W^i_{\mu\nu} W^{i\,\mu\nu} - \frac{1}{4} B_{\mu\nu} B^{\mu\nu}, \tag{2.16}$$
where $G^a_{\mu\nu}$, $W^i_{\mu\nu}$, and $B_{\mu\nu}$ are the field strength tensors for the $SU(3)_C$, $SU(2)_L$, and $U(1)_Y$ gauge groups, respectively.

2. **Fermion term**:
$$\mathcal{L}_{\text{fermion}} = \sum_{\psi} \bar{\psi} i \gamma^\mu D_\mu \psi, \tag{2.17}$$
where the sum runs over all left- and right-handed quarks and leptons, and D_μ is the gauge-covariant derivative encoding their interactions with the gauge bosons.

3. **Higgs term**:
$$\mathcal{L}_{\text{Higgs}} = (D^\mu \Phi)^\dagger (D_\mu \Phi) - V(\Phi), \tag{2.18}$$
with the Higgs potential given by
$$V(\Phi) = \mu^2 \Phi^\dagger \Phi + \lambda (\Phi^\dagger \Phi)^2, \tag{2.19}$$
where Φ is the complex scalar Higgs doublet.

4. **Yukawa term**:
$$\mathcal{L}_{\text{Yukawa}} = -y_e \bar{L} \Phi e_R - y_d \bar{Q} \Phi d_R - y_u \bar{Q} \tilde{\Phi} u_R + \text{h.c.}, \tag{2.20}$$
where L and Q are the left-handed lepton and quark doublets, e_R, d_R, u_R are the corresponding right-handed singlets, and $\tilde{\Phi} = i\sigma_2 \Phi^*$.

Each component in the $\mathcal{L}_{\text{SM}}$ is constructed to respect the gauge symmetry $SU(3)_C \times SU(2)_L \times U(1)_Y$. The independent terms are essential to capture the dynamics of an observed particle in the SM.

What began in the nineteenth century with the formulation of Maxwell's equations of classical electrodynamics, evolved through the revolutions of relativity and quantum mechanics, was then formulated as QED, gradually integrated into the gauge theories of symmetry, and completed with the description of electroweak symmetry breaking in terms of the Englert-Brout-Higgs mechanism, finally culminated in the discovery of the Higgs boson. However, despite its immense experimental success, the SM still has several well-known limitations:

- **No gravity:** The SM describes three of the four known fundamental forces of nature but does not incorporate gravity, which is currently described by Einstein's General Theory of Relativity (GTR). The unification of the underlying quantum nature of SM with gravity still remains open to intense investigation.

- **No dark matter:** Astronomical observations provide evidence for the existence of dark matter which constitutes about 27% of the universe's total mass-energy density. The SM offers no fundamental particle candidate that could explain dark matter, though there are potential candidate hypotheses currently being tested in this regard.

- **Neutrino masses:** In the minimal formulation of the SM, neutrinos are predicted to be massless particles. However, experiments observing neutrino oscillations have demonstrated that neutrinos must possess a tiny but non-zero mass. This observation is a direct contradiction of the minimal SM predictions and necessitates extending the model.

- **Matter-antimatter asymmetry:** The universe is overwhelmingly dominated by matter over antimatter. The SM, while providing some mechanisms for charge-parity (CP) violation (a necessary condition for creating an asymmetry), cannot generate nearly enough of it to explain the much larger, observed imbalance of matter and antimatter.

- **Strong CP problem:** The strong nuclear force, as described by QCD within the SM, allows for a CP-violating term. If this term were present with any significant magnitude, it would manifest as an electric dipole moment for the neutron, which has been searched for with great precision but never observed. The experimental upper limits are so stringent that the value of this term must be incredibly close to zero, effectively leading to the "strong CP problem": why is this term absent or so small? The SM offers no natural explanation for this fine-tuning, but there already are proposals of new particles (axions) which might yield an answer in future.

- **No force unification:** While the SM successfully unifies the electromagnetic and weak forces into a single electroweak force at high energies, it does not extend this unification to include the strong nuclear force, nor does it include gravity as already mentioned. Many theoretical frameworks, such as Grand Unified Theories (GUTs), propose that at extremely high energies (much higher than those currently accessible by particle colliders), all three fundamental forces (electromagnetic, weak, and strong) might merge into a single unified force. The SM does not provide the mechanism for this unification, suggesting it is an effective theory valid up to a certain energy scale, beyond which new physics is required.

2.4 Top quark

Since its discovery in 1995 by the CDF and DØ experiments at the Tevatron collider [6][7], the top quark has remained an object of significant interest in the high-energy physics community. Among the six quark flavours, it is distinguished by a number of unique properties. Most notably, it is the heaviest known elementary particle, with a mass of approximately $m_t \approx 172.5\,\text{GeV}$, lying close to the electroweak symmetry-breaking scale. This large mass originates from its Yukawa coupling to the Higgs field, which is approximately unity ($y_t \approx 1$). This makes the top quark's interaction with the Higgs boson the strongest among all SM fermions. The top quark is a spin-$\frac{1}{2}$ particle with electric charge $+\frac{2}{3}e$, and it transforms as a fundamental triplet under the QCD gauge group $SU(3)_C$. As such, it participates in all three of the SM gauge interactions: the strong, the weak, and the electromagnetic forces. Its dominant decay mode is via the weak interaction: $t \to W^+b$, with a branching ratio close to 100%. A defining feature of the top quark is its extraordinarily short lifetime, estimated to be $\tau_t \sim 5 \times 10^{-25}$ s. This is significantly shorter than the typical hadronisation timescale $\tau_{\text{had}} \sim 1\,\text{fm}/c \approx 3 \times 10^{-24}$ s, the time over which coloured partons (quarks and gluons) form colour-neutral hadrons. As a result, the top quark decays before it has time to hadronise. This is in stark contrast to all other quarks, which form bound states prior to decaying. Consequently, the top quark offers a unique opportunity to study the properties of a 'bare' quark, free from the effects of non-perturbative QCD dynamics such as hadronisation. This feature enables direct access to intrinsic quantum properties of the top quark, such as its spin, polarization, and couplings, through the measurements of its decay products. Also, due to its large Yukawa coupling, the top quark plays a central role in electroweak symmetry breaking and phenomenology of the Higgs-sector.

2.4.1 Top quark production

Top quarks are produced in high-energy particle collisions primarily through strong and electroweak interactions. Since top quarks are heavy mass particles, they need extreme amount of energies to be produced, only available in cosmic rays or in particle accelerators such as the LHC. Their production depends on the $\sqrt{s}$ energy of the colliding particles, the type of colliding particles, and the available phase space where they can be reliably studied.

The first observation of the top quark occurred in $p\bar{p}$ collisions at the Tevatron collider at Fermilab, operating at $\sqrt{s} = 1.8$ and later at 1.96 TeV [7]. At these energies, the dominant production mechanism is top-quark pair production ($t\bar{t}$) via strong interactions, predominantly through quark-antiquark annihilation:

$$q\bar{q} \to t\bar{t}$$

Single top production via electroweak processes was also predicted and later observed at the Tevatron, though with lower cross sections [8][9].
At the LHC, operating with proton-proton collisions and higher centre-of-mass energies ($\sqrt{s} = 7$ to 13.6 TeV), the production mechanisms differ significantly from those at the Tevatron. Top-antitop pairs are predominantly produced via strong interactions at the LHC. The main subprocesses, as shown in Figure 2.2, are:

- **Gluon fusion:** $gg \to t\bar{t}$ (dominant production mode at the LHC due to high gluon luminosity)
- **Quark and antiquark annihilation:** $q\bar{q} \to t\bar{t}$

- ***t*-channel:** top quark pairs can also be produced via the t-channel process in which two gluons interact, resulting in the exchange of a virtual top quark and the production of a top quark and a top antiquark.

Single top quarks can also be produced via electroweak interactions. The main production channels, as shown in Figure 2.3, are:

- ***s*-channel:** $q\bar{q}' \to t\bar{b}$
- ***t*-channel:** $qb \to q't$ or $qg \to q't\bar{b}$ (dominant single top process at the LHC)
- **Associated *tW* production:** $gb \to tW^-$

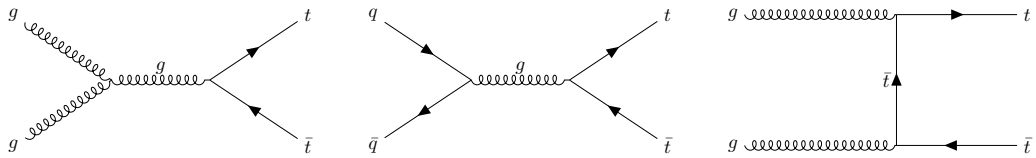

Figure 2.2: Examples of LO Feynman diagrams for top quark pair production via gluon-gluon fusion, quark-antiquark annihilation, and t-channel production.

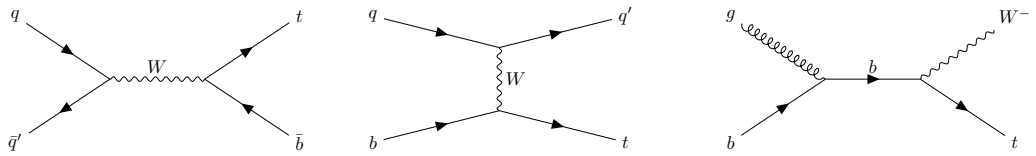

Figure 2.3: Examples of LO Feynman diagrams for single top quark production via s-channel, t-channel, and tW-channel, respectively.

Each production mode provides sensitivity to different aspects of the top quark's properties and its interactions, particularly with the W boson and the bottom quark. For instance, top-quark pair production is primarily driven by gluon fusion, making it sensitive to the top-gluon coupling. In contrast, single top-quark production is an electroweak interaction mediated by a virtual W boson, which allows for a direct probe of the top $- W - b$ vertex.

2.4.2 Top quark production with photons

In the SM, the interaction between the top quark and the photon arises from the electromagnetic coupling of the top quark to the photon field. This coupling is described at leading order by the following interaction Lagrangian:

$$\mathcal{L}_{t\gamma} = -\alpha_{\text{em}} Q_t \, \bar{\psi}_t \gamma^\mu \psi_t \, A_\mu, \tag{2.21}$$

where α_{em} is the fine-structure constant, $Q_t = +2e/3$ is the electric charge of the top quark, ψ_t is the Dirac spinor field of the top quark, and A_μ is the photon field. This vertex structure reflects the standard vector-like electromagnetic interaction of charged fermions.

For light quarks, the fermion–photon vertex can be probed directly in electron–positron collisions, such as $e^+e^- \rightarrow q\bar{q}$, where the $\sqrt{s}$ is sufficient to produce the quark–antiquark pairs. However, due to the large mass of the top quark ($m_t \approx 172.5\,\text{GeV}$), past and existing e^+e^- colliders have not achieved sufficient energy to produce top quarks in pairs. As a result, direct measurements of the top quark–photon interaction must be carried out at hadron colliders such as the LHC, where top quark production is abundant.

At the LHC, the $t\bar{t}\gamma$ process—top quark pair production in association with photon provides a direct probe of the top–photon vertex. Another relevant process is the associated production of a single top quark with a W boson and a photon. These processes allow precision measurements of the top–photon interaction and serve as sensitive probes for physics beyond the SM.

Many new physics scenarios predict modifications to the top–photon vertex. For instance, some models predict the presence of anomalous electromagnetic moments of the top quark—namely, a magnetic dipole moment and an electric dipole moment—which would alter the structure of the vertex.

These effects can be captured in an effective Lagrangian framework that extends the SM interaction with additional higher-dimensional operators:

$$\mathcal{L}_{t\gamma}^{\text{eff}} = -eQ_t\,\bar{\psi}_t\gamma^\mu\psi_t\,A_\mu - \frac{e}{2m_t}\bar{\psi}_t\,\sigma^{\mu\nu}\left(C_{2,V}^{\gamma} + iC_{2,A}^{\gamma}\gamma^5\right)\psi_t\,F_{\mu\nu}, \tag{2.22}$$

where e is the electromagnetic coupling, m_t is the top quark mass, $\sigma^{\mu\nu} = \frac{i}{2}[\gamma^\mu, \gamma^\nu]$ in terms of Dirac matrices, and $F_{\mu\nu}$ is the electromagnetic field strength tensor. The dimensionless coefficients $C_{2,V}^{\gamma}$ and $C_{2,A}^{\gamma}$ correspond to the anomalous magnetic and electric dipole moments of the top quark, respectively [10]. In the SM, these dipole coefficients vanish at tree level, i.e., $C_{2,V}^{\gamma} = C_{2,A}^{\gamma} = 0$, but they receive tiny contributions from higher-order quantum corrections [11] [12].

An important distinction needs to be made regarding the origin of the radiated photons in association with the $t\bar{t}$ pair. A photon can radiate during the production of the top quark pair either from an off-shell top quark or from one of the initial quarks. These are referred to as the radiative production process. If a photon is radiated either from an on-shell top quark, or any of the decay product of the top quark, the process is referred to as radiative decay. The production process is more sensitive to the top-photon coupling vertex because the photon is produced directly at the hard scattering vertex rather than being a byproduct of a subsequent decay.

Another process, which is the interest of this analysis, is the production of the top-quark pair in association with two photons ($t\bar{t}\gamma\gamma$), the cross section measurement of which is the main goal of the analysis presented in this thesis. It is a rare process in the SM, with an expected cross section $O(10^3)$ times smaller than the $t\bar{t}\gamma$ process ($t\bar{t}$ in association with a single photon), which itself has a cross section $O(10^3)$ smaller than the $t\bar{t}$ process. Of all the ttVV processes (V=γ,W,Z), $pp \rightarrow t\bar{t}\gamma\gamma$ has the second largest contribution [13]. It is also an irreducible background for the measurements of the production of the Higgs boson in association with $t\bar{t}$ ($t\bar{t}H$), with Higgs decaying to two photons. Moreover, the anomalous chromoelectric and chromomagnetic dipole moments in extensions of the SM, as mentioned earlier, are of particular interest because they are very small in the SM, arising only from higher-order loop corrections [14][15]. Therefore, any observed deviation from these tiny SM values of the dipole moments would be a hint for new physics beyond the SM. The $t\bar{t}\gamma\gamma$ has been proposed as a process that can act as a handle to constrain these anomalous moments [16]. In that regard, the ratio of the cross section between the $t\bar{t}\gamma\gamma$ and $t\bar{t}\gamma$ processes ($R_{2\gamma=\gamma} = \frac{\sigma_{t\bar{t}\gamma\gamma}}{\sigma_{t\bar{t}\gamma}}$) can act as an observable.

The above points lay out the motivation to search for the $t\bar{t}\gamma\gamma$ process and initiate further theoretical studies. The current theoretical and experimental state of the process are presented in the next section.

2.4.3 Theoretical calculations and experimental status

The production of $t\bar{t}\gamma$ process has been studied in great detail by the ATLAS and CMS Collaborations using proton-proton collision data at $\sqrt{s}$ = 8 and 13 TeV [1, 17–22]. Its inclusive and differential production cross-sections have been measured at $\sqrt{s}$ energies ranging from 7 to 13 TeV, in both the dilepton and single-lepton $t\bar{t}\gamma$ decay channels. Recent measurements by ATLAS focus specifically on the production of $t\bar{t}\gamma$ events, where the photon arises from initial-state radiation or an off-shell top quark, and measurements have been performed for inclusive and differential cross sections and the $t\bar{t}$ charge asymmetry in $t\bar{t}\gamma$ events [1] [23]. In the recent $t\bar{t}\gamma$ measurement [1], the inclusive cross section was measured using the dilepton and single lepton decay channels of the $t\bar{t}$ pair. The separation of $t\bar{t}\gamma$ from production and $t\bar{t}\gamma$ from decay is done with the help of neural networks, where a multiclass classification process was implemented for the single-lepton channel. The cross section was extracted with a profile likelihood fit at particle level.

The $t\bar{t}\gamma\gamma$ process, however, has not yet been studied throughly or had been observed so far by any particle collider experiment. The $t\bar{t}\gamma\gamma$ process has been discussed in several recent theoretical calculations, though with narrow width approximations of stable (non-decaying) top quarks, considering production stage only, and including the decays at parton level.

NLO QCD predictions for the $t\bar{t}\gamma\gamma$ process with stable top quarks have been known for quite some time and have been further matched to parton shower programs [24] [25]. In addition to higher-order QCD effects, NLO EW corrections for process have recently been reported [26], again, only for stable tops. In all these studies NLO QCD corrections were calculated for the $pp \rightarrow t\bar{t}\gamma\gamma$ production stage only, without including the decay. First full NLO QCD treatment of $t\bar{t}\gamma\gamma$ production including top decays in both dilepton and single-lepton channels, with investigations on mixed photon bremsstrahlung effects was done in Ref. [27] and the integrated cross section for $t\bar{t}\gamma\gamma$ was calculated. In Ref. [28] the complete NLO predictions for both $pp \rightarrow t\bar{t}\gamma$ and $pp \rightarrow t\bar{t}\gamma\gamma$ were calculated. However the calculation was done for $t\bar{t}$ dilepton channel, which has a smaller branching fraction and therefore, not very feasible for a search analysis.

Given the status of the current theoretical studies, the results provided in this thesis, which includes the first observation of this rare process and the measurement of the $R_{2\gamma=\gamma}$, are therefore, intended to serve as a stepping ground for theorists to study this process in more detail. The $t\bar{t}\gamma$ measurement [1] in single-lepton channel forms the basis of the ratio measurement in this analysis. To study the impact of the cancelation of systematic uncertainties, as one would expect in the ratio, the physics object definition and treatment of the uncertainties in the analysis presented in this thesis are kept similar to the ones in the $t\bar{t}\gamma$ measuement. Figure 2.4 illustrate two ways of $t\bar{t}\gamma\gamma$ production.

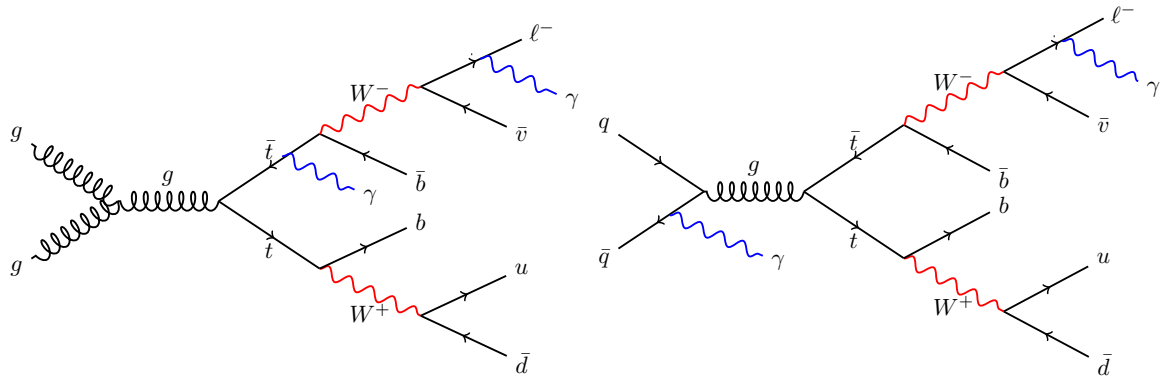

(a) (b)

Figure 2.4: Feynman diagrams for leading-order $t\bar{t}\gamma\gamma$ production in the single-lepton $t\bar{t}$ final state, with photons radiated by (a) an off-shell top quark and the charged lepton and (b) an initial-state quark and the charged lepton, respectively. [Diagrams taken from [29]]

CHAPTER 3

The LHC and the ATLAS detector

"Measure what can be measured, and make measurable what cannot."

— Galileo Galilei, *The Assayer* (1623)

This chapter details the experimental setup used for the measurement of the cross section of the $t\bar{t}\gamma\gamma$ process and the ratio of cross sections of the $t\bar{t}\gamma\gamma$ to $t\bar{t}\gamma$ processes. This includes the LHC, the accelerator where the proton-proton collision take place. The LHC has four interaction points where the collisions take place - ATLAS, CMS, ALICE and LHCb. The collisions take place in the heart of these experiments and are recorded for further analyses of various physics processes, such as the one presented in this thesis. The ATLAS is the largest of these experiments. It is a general-purpose detector designed to investigate a wide range of physics sectors - from SM processes to existence of beyond SM particles. The chapter provides an overview of the functioning of the LHC first, then describes the ATLAS detector along with its sub-detectors in Section 3.2, and finally outlines the methods by which different physics objects such as electrons, muons, and photons etc. are reconstructed from the recorded collision data in Section 3.3.

3.1 The LHC

The LHC is the world's largest and most powerful particle accelerator, located at the European Organization for Nuclear Research (CERN) near the French-Swiss border. Housed in a 27-kilometre circular underground tunnel at a depth of about 100 meters, the LHC reuses the infrastructure originally built for its predecessor, the Large Electron–Positron (LEP) collider. Operational since 2008, the LHC was constructed to explore some of the most fundamental questions in particle physics, including the origin of mass, the nature of dark matter, and the possible existence of new particles and symmetries beyond the SM. The LHC is designed to accelerate and collide two counter-circulating beams of protons (or heavy ions) at very high energies. It comprises two superconducting beam pipes, each guiding one beam in opposite directions. Proton bunches, each containing around 10^{11} protons, are accelerated by radio-frequency cavities and steered by an array of superconducting dipole and quadrupole magnets. These magnets operate at an ultra-cold temperature of 1.9 K, maintained using liquid helium. The beam pipes are maintained under ultra-high vacuum to prevent unwanted interactions with residual gas, and beam stability is ensured by a system of beam collimators. Upon completion of each run cycle, any remaining beams are extracted safely into a beam dump.

Before injection into the LHC, the proton beams undergo a sequence of acceleration stages through CERN's injector chain. The process begins with ionised hydrogen gas, from which protons are extracted and accelerated to 50 MeV in a linear accelerator (LINAC2). The bunches are then passed through a series of circular accelerators: first the Proton Synchrotron Booster (PSB), which raises the energy of each beam to 1.4 GeV; then the Proton Synchrotron (PS) to about 25 GeV; and finally the Super Proton Synchrotron (SPS), which boosts them to 450 GeV before finally injecting them into the two LHC rings. The proton bunches in the two beams circulate the LHC rings in opposite directions in the beam pipes until they attain a speed of about 0.99,999,999c (c is the speed of light). The beams are brought into collision at four, different interaction points around the LHC ring which are the four large particle detectors: ATLAS, CMS, ALICE, and LHCb. These experiments record and analyse the resulting events, enabling a wide array of precision measurements and discoveries.

The LHC operates over multiple years in periods, when particles are collided and the adjoining LHC experiments collect the output of the collisions as data. After a few years of data-taking, the LHC is closed during long shutdowns, when various upgrades and maintenance of its components are undertaken. The design luminosity of the LHC, which is a measure of the performance of a collider representing the number of particles that pass through a given area per second, is 10^{34} cm^{-2}s^{-1} for proton-proton collisions [30] per proton in each beam. For heavy ion (Pb) collisions, the design energy is 2.8 TeV per nucleon, with a peak luminosity of 10^{27} cm^{-2}s^{-1} [30]. The LHC operated at a $\sqrt{s}$ energy of 7 TeV in 2010 and 2011, and at 8 TeV in 2012 for proton-proton collisions. After a two-year shutdown, the LHC ran again from 2015-2018 at a centre-of-mass energy of 13 TeV. Another long shutdown took place from 2019 to 2021 for further upgrades and maintenance, and the LHC resumed operations in 2022 at a centre-of-mass energy of 13.6 TeV. For the second LHC data collecting period between years 2015-2018, called Run 2, the protons in each beam had energy equivalent of 6.5 TeV, thereby making the total $\sqrt{s}$ collision energy of 13 TeV. The analysis uses the data from this data-taking period.

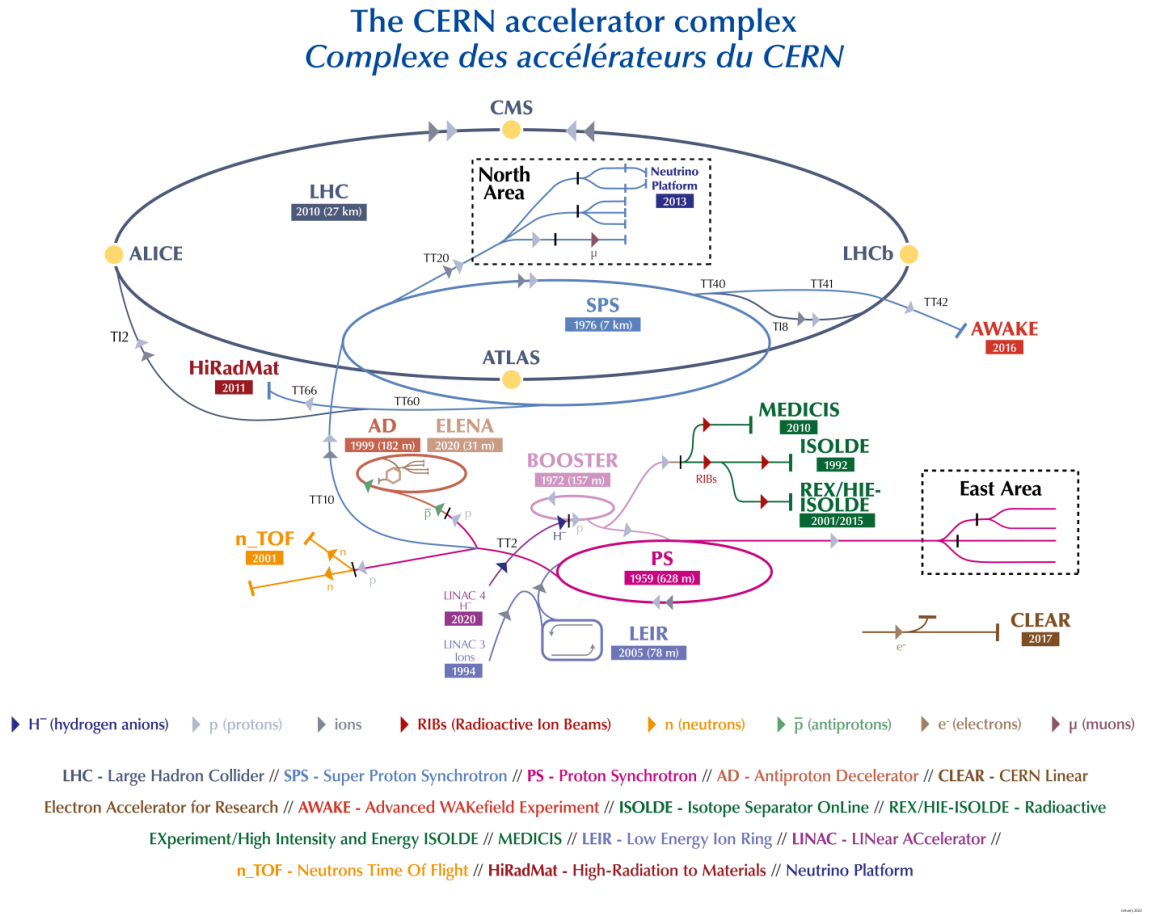

Figure 3.1: The CERN accelerator complex including the preaccelerators to the LHC, the Proton Synchrotron (PS) and the Super Proton Synchrotron (SPS). [31]

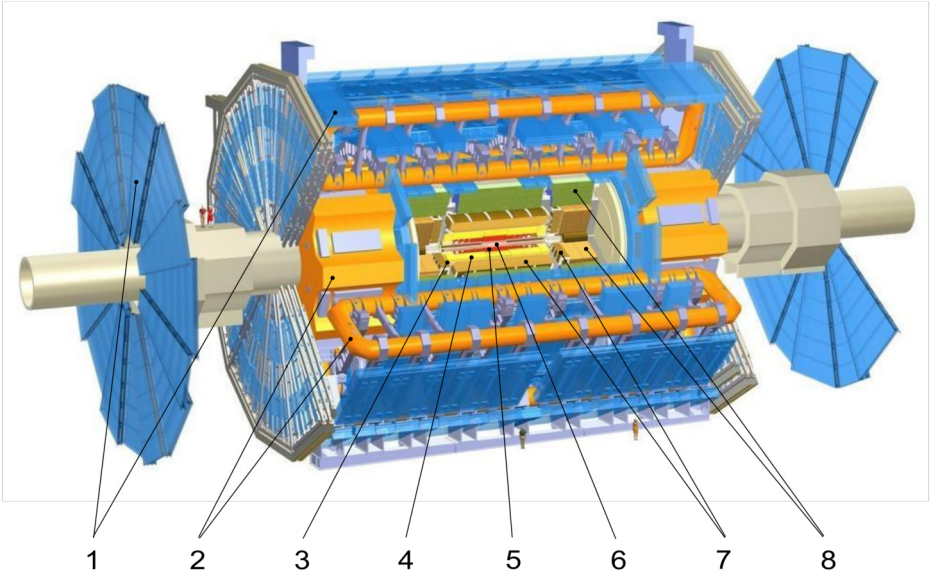

Figure 3.2: The ATLAS detector with all its sub-detector systems showing (1) Muon spectrometer in forward and barrel region (2) Toroid magnet in froward and barrel region (3) Solenoid magnet (4) Transition radion tracker (5) Semi-conductor tracker (6) Pixel detector (7) Liquid Argon calorimeter (8) Tile calorimeter.

3.2 The ATLAS detector

The ATLAS [32, 33] detector is a hermitic, multipurpose detector with a forward-backward symmetric cylindrical geometry with respect to the LHC beam axis. The innermost layers consist of tracking detectors in the pseudorapidity range $|\eta| < 2.5$. This inner detector (ID) is surrounded by a thin superconducting solenoid that provides a 2 T axial magnetic field. It is enclosed by the electromagnetic and hadronic calorimeters, which cover $|\eta| < 4.9$. The outermost layers of ATLAS consist of an external muon spectrometer within $|\eta| < 2.7$, incorporating three large toroidal magnetic assemblies with eight coils each. The field integral of the toroids ranges between 2.0 and 6.0 Tm for most of the acceptance. The muon spectrometer includes precision tracking chambers and fast detectors for triggering. Figure 3.2 shows a cut-away view of the detector, with all its sub-systems.

3.2.1 ATLAS Coordinate System

The ATLAS detector employs a right-handed coordinate system to describe the positions and trajectories of particles and detector components. The origin is defined at the nominal interaction point (IP), the centre of the detector where proton–proton collisions occur. The z-axis is aligned with the beam line, pointing along the direction of the counterclockwise circulating beam. The x-axis points from the IP towards the centre of the LHC ring, while the y-axis points vertically upward.

Angular coordinates are defined as follows: the azimuthal angle, ϕ, is measured in the transverse plane (perpendicular to the beam axis) from the x-axis, and the polar angle, θ, is measured from the z-axis. Since high-energy collisions often involve particles emitted close to the beam pipe, the

pseudorapidity variable η is used instead of θ, defined by

$$\eta = -\ln \tan\left(\frac{\theta}{2}\right).$$

This variable is particularly useful due to its invariance under Lorentz boosts along the beam axis. The transverse momentum, $p_T = p \sin\theta$, and transverse energy, $E_T = E \sin\theta$, are also commonly used since they are conserved in the plane transverse to the beam.

The following sections describe the sub-detector systems of ATLAS in more detail. They are complimentary to each other in capturing the essential data from the collisions [34].

3.2.2 Inner Detector

The Inner Detector (ID) is the central tracking system of the ATLAS experiment. It starts a few cms away from the beam pipe and is designed to reconstruct the trajectories of charged particles, determine their momenta with high precision, and identify both primary and secondary interaction vertices. Located at the heart of the detector, it plays a critical role in event reconstruction, flavour tagging, and vertex identification. The ID operates in the pseudorapidity range $|\eta| < 2.5$ and is immersed in a uniform axial magnetic field of 2T, provided by a superconducting solenoid surrounding the entire inner tracking volume. This magnetic field enables the measurement of the transverse momentum of charged particles via the curvature of their tracks.

The ID is composed of three nested sub-systems, each based on different detector technologies that complement each other in terms of spatial resolution, granularity, and coverage:

- **Pixel Detector:** The Pixel Detector is the innermost component of the ATLAS detector. It is made up of about 92 millions pixel sensors which provides high-precision tracking and hit measurements for charged particles. It comprises four concentric barrel layers (IBL, B-layer, L0, L1) and three disks per endcap. The IBL, the innermost layer, utilizes $50 \times 250\ \mu\text{m}^2$ silicon pixel sensors, while the external layers use $50 \times 400\ \mu\text{m}^2$ sensors. The detector reads out signals from the collisions every 25 ns. Its high granularity and good resolution, particularly enhanced by the IBL, are crucial for reconstructing secondary decay vertices from b- and c-quark hadrons, as well as improving impact parameter resolution.

- **Semiconductor Tracker (SCT):** Located around the pixel detector is the SCT. It consists of silicon microstrip sensors arranged in four double barrel layers and nine endcap disks on each side. It contributes significantly to pattern recognition and provides additional precision measurements of track positions in the r–ϕ plane, thereby improving momentum resolution when combined with pixel information.

- **Transition Radiation Tracker (TRT):** As the outermost component of the Inner Detector, the TRT serves as a combined straw tracker and transition radiation detector. It consists of approximately 298,000 drift tubes (straws), each 4 mm in diameter, providing track position measurements with a resolution of about 200 μm. These straws are filled with a gas mixture, primarily Xenon, that ionizes when charged particles pass through, generating signals. Another crucial aspect of this sub-system are the spaces between the straws which contain materials that

induce X-ray photon emission (transition radiation) from highly relativistic charged particles. This enables the TRT to identify light, high-speed particles, primarily electrons and positrons, by detecting these significantly stronger signals in the straws.

These three subsystems together enable efficient and accurate tracking of charged particles across a wide momentum range and pseudorapidity coverage, forming the foundation for high-level reconstruction tasks such as jet vertex tagging, lepton identification, and particle flow algorithms.

3.2.3 Calorimeter Systems

Beyond the solenoidal magent surrounding the ID is the calorimeter system which is designed to measure the energy and direction of particles through their electromagnetic and hadronic interactions. The calorimeters help in the reconstruction and identification of electrons, photons, hadronic jets, and in the determination of missing transverse energy ($E_{\mathrm{T}}^{\mathrm{miss}}$) by essentially absorbing the traversing particle. The ATLAS calorimeter system consists of distinct electromagnetic and hadronic components, which together provide hermetic coverage up to $|\eta| < 4.9$. These are segmented in both depth and azimuth to allow precise spatial and energy measurements.

- **Electromagnetic (EM) Calorimeter:** The EM calorimeter is a high-resolution sampling calorimeter that uses lead absorbers and liquid argon (LAr) as the active absorption medium. It is segmented into a barrel region ($|\eta| < 1.475$) and two endcaps ($1.375 < |\eta| < 3.2$), overlapping to ensure a seamless coverage. The fine granularity of the EMCal enables good separation of electrons and photons from hadronic backgrounds.

- **Hadronic Calorimeter (HCal):** The hadronic calorimeter is responsible for measuring the energy of strongly interacting particles such as pions, kaons, and protons. In the barrel region ($|\eta| < 1.7$), the Tile Calorimeter employs iron as the absorber and plastic scintillator tiles as the active medium. It is arranged in barrel and extended barrel modules to ensure full central coverage. For the endcap and forward regions (i.e. $1.5 < |\eta| < 4.9$), the calorimetry uses liquid Argon technology with copper or tungsten absorbers, providing radiation hardness and fine segmentation to cope with high particle fluxes.

Together, the electromagnetic and hadronic calorimeter systems provide energy measurements, angular resolution, and good particle identification, enabling reconstruction of jets, tau leptons, and photons.

3.2.4 Muon Spectrometer

The Muon Spectrometer (MS) forms the outermost layer of the ATLAS detector and is specifically designed to identify muons and measure their momenta independently of the ID with the help of magnetic field from the toroid magnets. Because muons interact only weakly with the calorimeters, they pass through them with minimal energy loss, making the implementation of the MS important for their identification. The spectrometer covers the range $|\eta| < 2.7$ and is embedded within a large system of air-core toroidal magnets—one barrel toroid and two endcap toroids—that generate a magnetic field from 2 to 6 Tm. The field bends the muon trajectories in the plane orthogonal to the magnetic field lines, allowing their momenta to be measured by the curvature of their tracks.

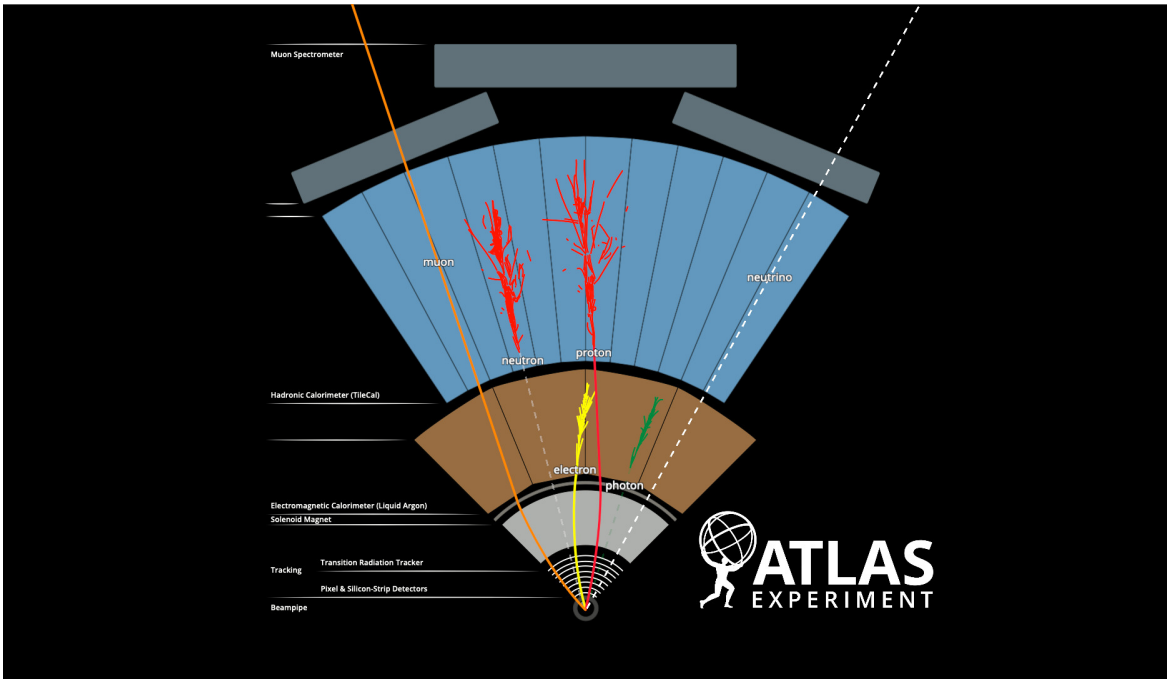

Figure 3.3: A cross sectional slice of the ATLAS detector including visualisations of how different particles interact with its different sub-detectors. [35]

The MS utilizes 4 different sub-detectors to precisely track muons and contribute to the trigger system: Monitored Drift Tubes (MDTs), forming the bulk of the system, provide highly accurate position measurements for reconstructing muon trajectories, especially for high transverse momentum muons. In the high-flux innermost forward regions, Cathode Strip Chambers (CSCs) offer high-resolution tracking with good timing and high occupancy resilience. For fast triggering, Resistive Plate Chambers (RPCs) are primarily used in the barrel, delivering quick responses and coarse spatial information for the Level-1 muon trigger, while Thin Gap Chambers (TGCs) serve a similar rapid triggering and coordinate measurement role in the endcap regions.

The MS operates independently from the ID but is carefully aligned to allow combined tracking for optimal performance.

3.2.5 Forward Detectors

As a brief mention, apart from the central ATLAS detector itself, several forward detectors are also installed along the beam line to detect particles produced at very small angles relative to the beam axis, thus complementing the central detector. These include LUCID-2, used for luminosity measurement; ALFA (Absolute Luminosity For ATLAS), used to measure elastic proton scattering at small angles; AFP (ATLAS Forward Proton), which detects protons scattered diffractively; and Zero Degree Calorimeter (ZDC), used to measure neutral particles at zero degrees.

3.2.6 Trigger System

At the LHC, proton-proton collisions take place at a frequency of up to 40 MHz, corresponding to one bunch crossing (an event) every 25 ns. However, recording data from every collision at this rate is practically unfeasible due to limitations in data storage, processing bandwidth, and offline analysis capabilities. Furthermore, most collisions correspond to low-energy, well-understood processes, while only a small fraction contain signatures of interest for new or rare physic processes such as $t\bar{t}\gamma\gamma$. To address this challenge, the ATLAS experiment employs a highly sophisticated trigger system, which filters events in real time and reduces the data rate to a manageable level, while retaining events most likely to contain relevant physics.

The ATLAS trigger system is structured in two sequential levels: L1 and HLT. Each level applies increasingly refined selection criteria to reject uninteresting events. Their roles are described in brief, below:

- **Level-1 Trigger (L1):** The L1 trigger is implemented in custom-designed hardware and is responsible for the initial and fastest event selection. Using coarse-grained information from the calorimeters and muon spectrometers, it makes a trigger decision within a latency of a few microseconds. The event rate is reduced from the initial 40 MHz to approximately 100 kHz. The decision logic is managed by the Central Trigger Processor (CTP), which consolidates inputs from subdetector trigger systems and applies predefined trigger conditions. The CTP also handles technical features such as dead-time enforcement between L1 accepts and rate throttling to avoid readout buffer overflows in the front-end electronics. Events accepted at this stage are passed to the HLT for further processing.

- **High-Level Trigger (HLT):** The HLT is a software-based system that operates on full event information, including fine-granularity detector data. It runs on a large computing farm and applies advanced reconstruction algorithms to further reduce the event rate from 100 kHz to about 1 kHz. To optimize resource usage, the HLT can use *Regions of Interest* (RoIs) identified by the L1 trigger to restrict processing to detector regions most likely to contain high-value signals. Only events passing the HLT selection are recorded to disk and stored for offline analysis.

Overall, this two-tiered trigger system ensures that ATLAS can cope with the high collision rate of the LHC while maintaining high efficiency for capturing the interesting physics events for further analyses.

3.3 Reconstruction of physics objects

The proton-proton collisions occur at a rate of 40 MHz in the ATLAS detector. The primary objective is to probe the hard interaction physics at the core of these collisions. The particles directly produced in these high-energy interactions are not observed; instead, they undergo a rapid series of decays into lighter particles before reaching the detector components.

The process of reconstructing the original physics objects from these decay products is essential for any experimental analysis. Particles like electrons and muons have sufficiently long lifetimes and high

momentum to traverse the ID, where they leave measurable tracks. Electrons then deposit their energy in the EMCal, while muons, being minimally interactive, penetrate further to the MS. These distinct signatures enable their precise reconstruction.

In contrast is the τ lepton, which has an extremely short lifetime and decays into other particles before reaching the detector's active layers. Similarly, quarks undergo hadronization, forming composite particles called hadrons. These hadrons can subsequently decay further until they become stable enough to travel through the detector, with their energy ultimately being measured by the HCal.

Given these complex decay chains and particle interactions, reconstructing the initial hard scattering event requires various dedicated algorithms. The following sections will detail the methods used by ATLAS to identify and characterize these physics objects from the raw detector signals, thereby allowing for the study of the fundamental processes themselves.

3.3.1 Primary Vertices

A primary vertex (PV) represent the locations where proton-proton interactions occur within the detector. Their precise reconstruction is essential to distinguish particles originating from the hard-scattering event from those produced in other simultaneous interactions (pile-up). PVs are formed by grouping reconstructed tracks that are spatially consistent with originating from a common point within the interaction region. A PV is chosen as the vertex with at least two associated tracks and the highest scalar sum of the squared transverse momenta ($\sum p_T^2$) of all tracks matched to that vertex, where only tracks with $p_T > 0.5$ GeV are considered in this sum.

3.3.2 Reconstruction of Electrons

High-energy electrons interact significantly with detector material. As the charged electrons traverse the ID, they ionize the detector medium, leaving a measurable track. Subsequently, electrons enter the EMCal, where they lose nearly all their energy by initiating cascades of electromagnetic showers. These showers involve repeated processes of bremsstrahlung radiation and electron-positron pair production. The reconstruction of electrons in ATLAS begins with the identification of these characteristic energy deposits within the central region of the electromagnetic calorimeters. These calorimeter energy clusters are then associated with reconstructed tracks originating from the ID sub-system. For a candidate to be identified as an electron, it must satisfy specific identification criteria, such as the *MediumLH* working point [36], which exploits various shower shape and track-cluster matching variables to distinguish electrons from other particles, particularly jets. Furthermore, electrons are typically required to satisfy stringent isolation criteria, such as the *PLVLoose* working point, which ensures that their energy deposit is not contaminated by other nearby particle activity. The reconstructed electron energies are precisely calibrated using methods detailed in Ref. [37], and scale factors derived from comparisons between data and Monte Carlo simulations are applied to correct for any remaining discrepancies. Only electrons with a calibrated transverse energy $E_T > 7\,\text{GeV}$ and an absolute pseudorapidity $|\eta| < 2.47$, excluding the problematic calorimeter crack region ($1.37 < |\eta| < 1.52$), are considered in the analysis. Additional requirements are imposed on the impact parameters of the associated track: the transverse impact parameter significance, $|d_0|/\sigma(d_0)$, must be less than 5, and the longitudinal impact parameter difference from the primary vertex, $|\Delta z_0 \sin(\theta)|$, must be below 0.5 mm. These criteria help to ensure that the reconstructed electron originated from the primary interaction point.

3.3.3 Reconstruction of Photons

Photons, being neutrally charged, do not leave direct tracks in the inner detector. They are primarily identified through their interaction with the EMCal, where they deposit their energy by initiating electromagnetic showers, similar to electrons. Photon reconstruction begins with the identification of energy deposits (clusters) in the central region of the electromagnetic calorimeters. Photon candidates can be classified into two main types: **unconverted** photons, where the calorimeter cluster is not associated with any reconstructed track in the ID system, indicating the photon directly interacted with the calorimeter; and **converted** photons, where the cluster is matched with reconstructed tracks that are consistent with originating from a photon conversion (i.e., the photon transformed into an electron-positron pair before reaching the calorimeter), and a conversion vertex is also successfully reconstructed. Both types of photons are considered in the analysis presented in this thesis. Identified photons are required to satisfy the stringent identification criteria of *Tight* working point [38], which distinguishes them from background, particularly neutral hadrons. Furthermore, stringent isolation requirements are applied using the *FixedCutTight* working point [38]. The energies of the reconstructed photons are further calibrated using the method outlined in Ref. [37], and scale factors are applied to the simulation to ensure consistency with data. For the analysis, only photons with a calibrated transverse momentum $p_T > 20\,\text{GeV}$ and an absolute pseudorapidity $|\eta| < 2.37$, excluding the calorimeter crack region ($1.37 < |\eta| < 1.52$), are considered.

3.3.4 Reconstruction of Muons

Muons, being ~200 heavier than electrons, interact differently with the detector. They produce minimal bremsstrahlung radiation and typically traverse the calorimeters with relatively little energy loss, leaving minimal electromagnetic showers. Their primary means of detection is through their distinct tracks in the ID and their passage through the dedicated MS. The strong toroidal magnetic field within the MS causes muons to bend, allowing their momentum to be measured with high precision.

Muon reconstruction in ATLAS employs a sophisticated combined algorithm that makes use of information from both the MS and the ID subsystems. This approach integrates track segments reconstructed in the various layers of the MS with precision tracks found in the ID. Candidate objects must follow the *Medium* identification quality criteria, and also satisfy isolation criteria, incorporated via the *PLVLoose* working point, to minimize contamination from hadronic activity. Similar to electrons, scale factors derived from data-to-MC comparisons are applied to correct the simulation. Only muons with a calibrated transverse momentum $p_T > 7\,\text{GeV}$ and an absolute pseudorapidity $|\eta| < 2.5$ are selected for the analysis. Stringent requirements are also applied to the impact parameters of the reconstructed muon track to ensure its origin from the primary vertex: the transverse impact parameter significance $|d_0|/\sigma(d_0)$ must be less than 3, and the longitudinal impact parameter difference $|\Delta z_0 \sin(\theta)|$ must be below 0.5 mm. The comprehensive methodologies for muon reconstruction, identification, calibration, and the extraction of scale factors are documented in more detail in Ref.[39].

3.3.5 Reconstruction of Jets

Jets are collimated sprays of hadrons that arise from the hadronization of quarks and gluons produced in the collisions. In ATLAS, jets are primarily reconstructed using the anti-k_t algorithm [40] with a radius parameter $R = 0.4$, implemented using the FastJet software package [41]. The input to this clustering algorithm consists of particle flow objects (PFlow) [42]. The PFlow algorithm

is a sophisticated technique that combines measurements from both the ID (charged tracks) and the calorimeters (energy deposits) to form particle-like inputs for jet reconstruction. This method significantly enhances the energy and angular resolution, reconstruction efficiency, and stability against additional soft interactions (pile-up). The energy and direction of these reconstructed jets undergo a multi-step calibration process, which involves simulation-based corrections combined with in situ data-driven adjustments [43]. For analysis, jets are required to have a transverse momentum $p_T > 25\,\text{GeV}$ and an absolute pseudorapidity $|\eta| < 2.5$. To mitigate contamination from pile-up, a Jet Vertex Tagger (JVT) discriminant [44] is applied to jets with $p_T < 60\,\text{GeV}$ and $|\eta| < 2.4$, with a requirement for the discriminant to be greater than 0.59. The JVT efficiency is corrected via scale factors derived from data-simulation comparisons.

b-tagging

An important aspect of jet identification is b-tagging, which aims to identify jets originating from the hadronization of bottom (b) quarks. This analysis employs the DL1r tagger [45], a deep neural network-based algorithm that utilizes a combination of input discriminants derived from the properties of tracks and secondary vertices within the jet. The DL1r tagger is trained to output a multi-class probability distribution indicating the likelihood of a jet being a b-jet, a charm ($c-$) jet, or a light-flavor jet at various working points. The jets satisfying the 70% efficiency working point of this tagger are called and utilised as b-tagged jets for the purposes of this analysis.

3.3.6 Reconstruction of missing transverse momentum (E_T^{miss})

The missing transverse momentum (E_T^{miss}) observable provides an estimate of the transverse momentum carried away by undetected, weakly interacting particles, such as neutrinos. It is not directly measured but is inferred from the imbalance of momentum in the plane transverse to the beam axis. The E_T^{miss} [46, 47] is computed as the magnitude of the negative vector sum of the transverse momenta of all reconstructed and precisely calibrated physics objects within the event, including electrons, photons, hadronically decaying τ-leptons, jets, and muons. In addition to these explicitly reconstructed objects, a component known as the soft-term (often denoted as $E_{T,\text{soft}}^{x(y)}$) is incorporated, which accounts for unclustered energy deposits in the calorimeter and tracks associated with the primary vertex that are not already assigned to any of the reconstructed high-p_T physics objects. This approach ensures that the E_T^{miss} calculation is as accurate as possible and takes into account all detectable energy and momentum in the event.

3.3.7 Overlap removal between objects

As discussed in Section 3.3, different physics objects are reconstructed independently from the detector signatures. This can lead to the same energy deposit in the calorimeters being reconstructed as different objects. For instance, a single energy deposit might be reconstructed as both a photon and an electron, or a jet might be misidentified as a photon. An overlap procedure is essential to ensure unique assigments of detector signatures to the physics objects and to avoid double counting the energy deposits or same track being reconstructed as two different objects. This removal procedure is performed as below:

- A muon candidate that uses calorimeter information during reconstruction and also shares a track with electron candidate is removed.
- Jets reconstructed within a cone of $\Delta R = 0.2$ of an electron are removed.
- Electrons reconstructed within a cone of $\Delta R = 0.4$ around the remaining jets are removed.
- If there is a muon and a jet close to each other, the jet is removed if it has no more than two associated tracks and is within $\Delta R < 0.2$ of the muon. If, otherwise, the muon is within $\Delta R < 0.4$ of the jet and the jet has more than two associated tracks, the muon is removed.
- Photons reconstructed within a cone of $\Delta R = 0.4$ of any remaining electron or muon are removed.
- Jets reconstructed within a cone of $\Delta R = 0.4$ around any remaining photon are removed.

CHAPTER 4

Simulation of signal and background processes

"The test of science is its ability to predict."

— Richard P. Feynman

The data collected by the detectors needs to be compared with the predictions from theoretical models. The data is what is observed by the detectors, and experimentalists need to ensure what they designate as signal is not just an artefact of some under-the-hood background process that can mimic the signal, or some underlying new physics effect. To achieve this, simulated events are generated, which should describe, as closely as possible, the real events in the detector. Event generators are used for this purpose, which are tools designed to model the entire sequence of physical processes that occur in a high-energy collision - starting from the initial, parton-level interaction through parton showering, hadronisation, and the modeling of underlying events. In short, the simulations follow from the initial impact to the final particles observed by detectors.
The simulation process unfolds in several of the above stated key stages, each taking into account a different energy scale. It begins with the hard scattering, where two fundamental particles from the colliding beams interact at a very high energy, for example, proton-proton for LHC collisions. This initial interaction then leads to parton showering, where the outgoing high-energy particles (partons) radiate further a cascade of partons. As these partons travel further, they cool down and lose energy and enter the phenomenon of hadronization, a QCD process where they bind together to form observable particles like protons, neutrons, pions, kaons etc. Finally, the simulation accounts for the underlying event, which includes the residual interactions from the colliding particles not directly involved in the hard scattering process, and the subsequent decays of any unstable particles.

Given the probabilistic nature of the underlying quantum mechanical phenomena, each collision results in a different set of final-state particles with varying kinematic properties. Event generators use Monte Carlo (MC) techniques to randomly sample from theoretically calculated probability distributions, thereby producing ensembles of simulated events that can be compared directly to real data collected by the detectors such as ATLAS. Event generators such as Pythia or Herwig provide a realistic and detailed description of the complex environment within a particle collider like the LHC by organizing the physical processes according to their energy scales, as mentioned above. These simulations are essential for interpreting the experimental results, validate various theoretical models, and optimize how future experiments are designed.

This chapter will first discuss the different, energy-dependent stages of simulation. Then the production of simulation samples used in the analysis are described in Section 4.6. The method to

remove double-counted events in the simulations, owing to the generation of same final state particles from different simulation levels, is discussed in Section 4.6.3. Finally, Section 4.7 discusses the categoriation of the simulated events on the basis of origin of the photons in the events, an essential step for the analysis presented in this thesis.

4.1 Hard scattering

The first and most crucial step in any general-purpose event generator is the simulation of the hard scattering process. This refers to the primary, short-distance interaction between the fundamental constituents, or partons, within the colliding hadrons, characterized usually by a large momentum transfer (Q^2). The high momentum transfer ensures that the interaction occurs at very short distances, where the strong coupling constant, $\alpha_S(Q^2)$, is sufficiently small, and the asymptotic freedom of QCD allows for the reliable application of perturbative QCD (pQCD) calculations. Consequently, the cross section and kinematics of this fundamental parton-level process can be calculated with good precision at specific orders of pQCD: leading order (LO), next-to-leading order (NLO), etc.. The calculated cross section essentially quantifies the probability of a particular hard interaction occurring [48].
Event generator programs like Pythia and Herwig manage this step in various ways. They either include built-in leading-order matrix-element (ME) calculations or interface it with external, more specialized, ME generators like MadGraph and Powheg to handle higher-multiplicity final states or to incorporate higher-order corrections. The direct output of the hard scattering simulation is a set of outgoing high-p_T partons. Their kinematics are determined by the calculated partonic cross section and are weighted by the parton distribution functions (PDFs) of the incoming particles (protons) to account for the fact that a proton's momentum is shared among its constituent partons.

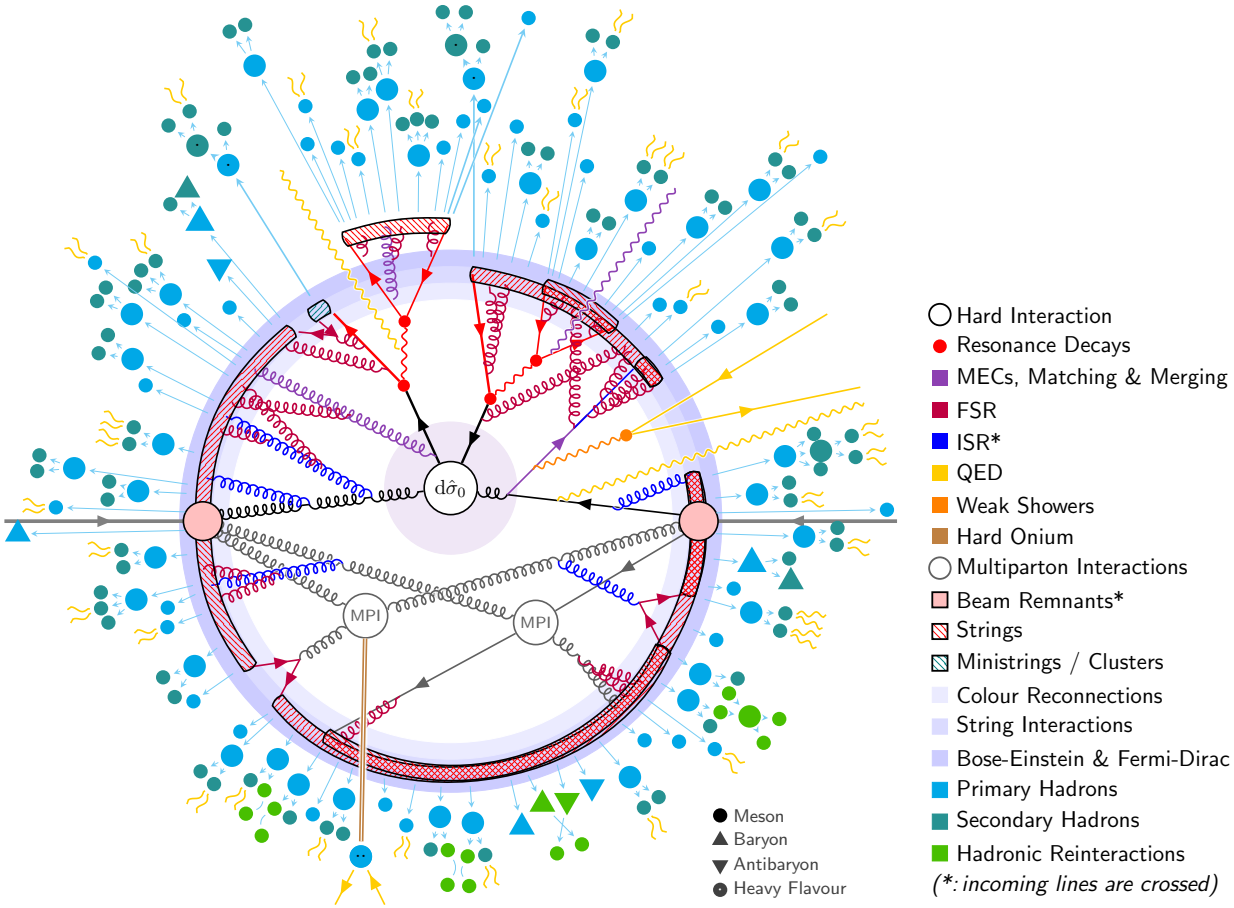

Figure 4.1: Schematic of the structure of a $pp \to t\bar{t}$ event modeled by the event generator PYTHIA [49]. The event is simulated in order of energy scale. The hard interaction is the central high-energy parton collision. Initial and Final State Radiation (ISR/FSR) are partons radiating before and after this interaction. Resonance decays are intermediate unstable particle decays from the hard interaction. The weak shower involves W/Z boson-mediated emissions and decays. Multiple Parton Interactions (MPI) are additional parton scatterings within one collision. Beam remnants are uncollided proton parts. Strings (colour fields) fragment into primary hadrons. colour reconnection rearranges parton colour connections before hadronization; hadronic reconnection is further hadron rearrangement.

4.2 Parton showering

The simulation of hard process is relatively simpler and straightforward, thanks to the pQCD aspect of the calculations involved. A more complex stage of event simulation comes from asking what happens to the incoming and outgoing partons involved in the hard collision. This is described by the parton shower phase of event generators, which encompasses the initial state radiation (ISR) and the final state radiation (FSR):

- **ISR:** Before the hard collision, incoming partons can radiate gluons. These emissions reduce the energy of the colliding partons, effectively altering their momentum fractions and potentially their transverse momentum as they enter the hard interaction.
- **FSR:** After the hard collision, the outgoing partons radiate gluons, and these gluons can further split into additional partons (i.e. more gluons or quark-antiquark pairs). This cascade of emissions constitutes the development of particle "jets" in the detectors.

Incoming and outgoing colour charges radiate gluons which, due to the non-Abelian nature of QCD, can self-interact and trigger further new radiation. This leads to an extended shower that fills up more regions of the phase space determined by the event generators. The parton shower evolution starts from the hard process and works downwards to lower momentum scales to a point where perturbative theory breaks down i.e. the hadronization scale. The evolution of these parton showers is governed by the DGLAP (Dokshitzer-Gribov-Lipatov-Altarelli-Parisi) evolution equations. These equations describe how parton distributions evolve with changing momentum scale, specifically accounting for successive, approximately collinear (emissions nearly parallel to the parent parton) and soft (low-energy) emissions.

Since the hard process is typically calculated with fixed-order pQCD accuracy, higher-order corrections arising from the numerous soft and collinear emissions cannot be neglected. Parton shower algorithms address this by employing resummation, a technique that sums the dominant logarithmic contributions from these additional emissions to all orders in perturbation theory. This approach, instead of calculating a fixed number of emissions, effectively determines the probability of emitting any number of soft or collinear particles. Event generators then approximate this all-orders resummation within their shower algorithms.

As stated earlier, the parton shower evolution starts from the high momentum scale of the hard process and works downwards through successive branchings (e.g., q→qg, g→gg, or g→$(q\bar{q})$) to progressively lower momentum scales. This process continues until a non-perturbative scale (typically around O(1 GeV)) is reached, at which point perturbative QCD calculations are no longer reliable. Different event generators implement this evolution using various ordering variables; for example, Pythia employs a p_T-ordered shower, while Herwig utilizes an angular-ordered algorithm. Thus, the result is a tree-like structure of lower-energy partons whose colour connections then serve as the input for the subsequent hadronization stage.

4.3 Hadronization

The stages of evolution of the physics process in the hard scatter are based on pQCD calculations. However, the resulting partons are not the final state particles as we see them in the detector. Below the perturbative cutoff, QCD confinement takes over and partons must be transformed into colour-singlet

hadrons by a non-perturbative model. This stage, where partons produced at hard interaction form colour neutral hadrons, is aptly called the hadronization stage. Various phenomenological models are used to simulate the final hadrons from initial partons. PYTHIA uses the Lund string fragmentation where the colour-connected partons are tied by a string which "breaks" into $(q\bar{q})$ pairs, producing mesons and baryons. HERWIG instead groups colour-connected partons into clusters according to the cluster model, which then decay into hadrons. Both approaches are tuned to reproduce measured hadron spectra, jet shapes and underlying-event observables.

4.4 Underlying events

While the hard process, parton shower, and hadronization describe the direct products of the primary hard interaction well, they do not account for all activity within a hadron-hadron collision. Hadrons are complex bound states, and when a parton is extracted for the hard scatter, the remaining partons, known as beam remnants, evolve and can also interact. The underlying event (UE) encompasses all activity in a hadronic collision that is not directly attributable to the hard scattering itself or its subsequent parton showers. This primarily includes the MPI between the additional partons from the colliding hadrons, as well as the evolution and hadronization of the beam remnants. Event generators simulate the underlying event using phenomenological models, which are extensively tuned to data.

4.5 Matching and merging

Since the events at the LHC span a wide range of energy scales, it is impractical to perform fixed-order perturbative calculations for every stage of the process. In practice, the initial hard scattering is described using fixed-order matrix element calculations, which provide accurate predictions in the high-energy and low-multiplicity regime. The subsequent evolution of partons, including multiple emissions, is instead modelled using parton shower algorithms, which are valid in the soft and collinear limits and capture the bulk of QCD radiation.

However, these two approaches cover overlapping regions of phase space, which can lead to double counting of emissions if combined naively. Matching and merging techniques provide a consistent framework to integrate fixed-order matrix elements with parton showers. In this way, one obtains both the accurate description of hard, well-separated jets from matrix elements and a detailed modelling of softer, collinear emissions from the shower.

4.6 Simulation of signal and background processes

This section describes the simulation of the signal ($t\bar{t}\gamma\gamma$) and background processes used for the measurements in the analysis. As stated, MC simulations are used to estimate the contributions from the signal and the various background processes by generating corresponding samples. These 'samples' are simulated using various event generators and are centrally produced within the ATLAS simulation infrastructure [50]. The ATLAS detector response is simulated for the generated events using the GEANT4 tool [51]. A full simulation of the detector response for all the simulated samples is computationally expensive. Therefore, for some samples, such as those used to estimate the modelling

uncertainties in the analysis, the fast-simulation package AtlFast-II [52] is used, which parametrises hadronic showers in the calorimeters of the detector to speed up the simulation process.

To account for additional pp interactions from the same bunch crossing (pileup), minimum-bias interactions generated with Pythia8 [53, 54] using the set of tuned parameters called A3 [55] and the NNPDF2.3LO PDF set [56] are superimposed on the hard-scattering events. MC events are then reweighted to match the pile-up conditions observed in data. Three different MC subcampaigns, *mc16a*, *mc16d* and *mc16e*, are defined to reflect the Run 2 data-taking conditions in 2015+16, 2017 and 2018, respectively.

The analysis uses both, *dedicated* samples, where at least one photon is included in the ME-level generation step, and *inclusive* samples, in which processes were generated at ME-level without explicitly including photons in the final state. Dedicated samples with two photons at matrix element are generated for the $t\bar{t}\gamma\gamma$ final state and for $V\gamma\gamma$ processes. They are described in more detail in Section 4.6.1. The inclusive samples used in the analysis, as listed in Section 4.6.2, might still contain photons in the simulation as additional photon emission (irrespective of the generated process at ME) originating from the showering algorithms. To avoid possible double-counting of events, an overlap-removal procedure is applied between dedicated and inclusive samples, as detailed in Section 4.6.3.

The goal of the analysis is to measure processes where a photon is emitted from the hard scattering part of the event. These photons are called 'prompt' photons. However, non-prompt photons can be emitted at different stages of the process - such as during hadronization, decay of hadrons or other charged particles. To distinguish *prompt* photons from the hard scattering and non-prompt photons and other objects faking photon signatures in the detector, truth information of the simulated events is used to identify the true source of all reconstructed photons. The categorisation of reconstructed photons based on their truth information is described in Section 4.7.

4.6.1 Samples with at least one photon at ME

These are the dedicated samples where at least one of the prompt photon is generated at ME level. The candidate processes considered are $t\bar{t}\gamma\gamma$, $t\bar{t}\gamma$, $V\gamma\gamma$, $t\bar{t}H$ and $tW\gamma$.

***$t\bar{t}\gamma\gamma$* sample:**
The $t\bar{t}\gamma\gamma$ events were simulated with MadGraph5_aMC@NLO 2.9.9 [57] as a $2 \rightarrow 8$ process (including one lepton, two photons, two $b-$ quarks, $q\bar{q}$ pair and one neutrino in the $t\bar{t}$ single lepton channel) at leading order (LO) QCD precision. The ME calculation employed the NNPDF3.0nlo set of PDFs [58]. The event generation is interfaced to Pythia 8.306 [59] using the *A14* set of tune parameters [60] and the NNPDF2.3LO PDF set to model parton shower, hadronisation, fragmentation and underlying event.

The decays of bottom and charm hadrons were simulated using the EvtGen 1.7.0 program [61]. The renormalisation and factorisation scales are dynamic and correspond to half of H_T, the sum over all transverse masses of all final-state particles:

$$\mu_R = \mu_F = \frac{H_T}{2}, \quad H_T = \sum_f \sqrt{m_f^2 + p_{T,f}^2}, \tag{4.1}$$

where f runs over all final-state particles, and m_f and $p_{T,f}$ are the rest mass and the transverse momentum of particle f, respectively. To avoid infrared and collinear singularities due to the photon radiation, kinematic cuts are applied on ME level. Leptons and quarks at the ME level are required to have a minimum transverse momentum of 4 GeV and 1 GeV respectively. Photons are required to have a minimum transverse momentum of 15 GeV and isolated according to a smooth-cone isolation (Frixione Isolation [62]) criterion with $\delta_0 = 0.1$, $\epsilon_\gamma = 0.1$ and $n = 2$. This sample is used as the signal sample in the analysis.

Normalisation of the signal sample

Since the $2 \to 8$ $t\bar{t}\gamma\gamma$ sample used in the analysis is produced at LO accuracy, two different $2 \to 4$ $t\bar{t}\gamma\gamma$ production samples were produced, one at NLO and one at LO, and the ratio of their cross sections was used to estimate a K-factor of 1.7 to normalise the $2 \to 8$ $t\bar{t}\gamma\gamma$ sample. The $2 \to 4$ sample, in which photons are emitted from either off-shell top quarks or initial-state particles, can be simulated at NLO, unlike the $2 \to 8$ sample, which is limited by the event generators themselves in handling decay states.

(MadGraph can handle the $2 \to 4$ production process at NLO. However, to get the final state with decayed top quarks, it hands the event over to MadSpin, which decays the top-quarks at LO. The result is a hybrid event where the production part has NLO precision, but the decay part does not.)

The NLO-to-LO K-factor is also estimated in the same fiducial phase space as used in this analysis. It serves as a prior normalisation to the sample, helping improve the data-to-MC agreement, and doesn't affect the final fitted values of the measurement.

***$t\bar{t}\gamma$* production and *$t\bar{t}\gamma$* decay:**

One of the major backgrounds to the $t\bar{t}\gamma\gamma$ process is the $t\bar{t}\gamma$ process, with similar topology as the former albeit with the exception of a single photon. The $t\bar{t}\gamma$ process is generated as two samples - one for production process, where the photon is radiated from ISR and off-shell top quark, and one for decay, where the photon is radiated by either the on-shell top quark or one of its decay products.

The $t\bar{t}\gamma$ production sample was simulated with MadGraph5_aMC@NLO 2.7.3 [57] as a $2 \to 3$ process at NLO QCD precision. Top quarks were decayed at LO using MadSpin [63, 64] to preserve spin correlations. The $t\bar{t}$ with γ from decay events were simulated with MadGraph5_aMC@NLO 2.7.3 [57] as $2 \to 2$ LO $t\bar{t}$ production followed by the decay of the top quarks at LO. In both samples, the ME calculation employed the NNPDF3.0nlo set of PDFs [58]. The event generation is interfaced to Pythia 8.240 [59] using the *A14* set of tune parameters [60] and the NNPDF2.3LO PDF set to model parton shower, hadronisation, fragmentation and underlying event. The decays of bottom and charm hadrons were simulated using the EvtGen 1.6.0 program [61]. The renormalisation and factorisation scales are dynamic and correspond to half of H_T (same as in Eq. (4.1)). Leptons and quarks at the ME level are required to have a minimum transverse momentum of 20 GeV and 1 GeV respectively. Photons are required to have a minimum transverse momentum of 15 GeV and isolated according to the Frixione Isolation with $\delta_0 = 0.1$, $\epsilon_\gamma = 0.1$ and $n = 2$ for both the samples.

The $t\bar{t}\gamma$ production sample is normalised to the NLO cross section given by the MC simulation, while the $t\bar{t}\gamma$ decay sample is rescaled to NLO using an inclusive K-factor (σ_{NLO}/σ_{LO}). The K-factor of 1.5 was derived in Ref. [23] ($t\bar{t}\gamma$ charge asymmetry) by comparing the normalisation of the sum of the NLO $t\bar{t}\gamma$ production sample and the LO $t\bar{t}\gamma$ decay sample with the normalisation of a LO inclusive $2 \to 7$ $t\bar{t}\gamma$ sample corrected with the inclusive K-factor of 1.3. The factor of 1.3 was obtained in

Ref. [65] (the first $t\bar{t}\gamma$ measurement at 13 TeV) using the calculation described in Ref. [66].

***tWγ*:**
Two $tW\gamma$ samples with different photon sources, i.e, production and decay, are considered for the $tW\gamma$ process using MadGraph5_aMC@NLO 2.7.3 [57] at LO. The event generation is interfaced to Pythia 8.240 [59] using the *A14* set of tune parameters [60] and the NNPDF2.3LO PDF set to model parton shower, hadronisation, fragmentation and underlying event. The decays of bottom and charm hadrons were simulated using the EvtGen 1.6.0 program [61]. The renormalisation and factorisation scales are set at $H_T/2$ (Eq. (4.1)).

***Wγγ/Zγγ* and *Wγ/Zγ*:**
Events with $W\gamma\gamma$ and $Z\gamma\gamma$ final states were simulated with Sherpa 2.2.10 [67, 68] at NLO in QCD using the NNPDF3.0NNLO PDF set. The samples are normalised to the cross sections given by the corresponding MC simulations. The simulation includes all steps of the event generation, from the hard process to the observable particles.

Events with $W\gamma$ and $Z\gamma$ final states with one photon simulated at matrix element were generated with Sherpa 2.2.8 [67, 68] at NLO in QCD using the NNPDF3.0NNLO PDF set. The samples are normalised to the cross-sections given by the corresponding MC simulations. The simulation using Sherpa includes all steps of the event generation, from the hard process to the observable particles.

All these samples are matched and merged to the Sherpa-internal parton showering based on Catani-Seymour dipoles [69, 70] using the MEPS@NLO prescription [71–73]. Virtual corrections for the next-to-leading order accuracy in QCD in the matrix element are provided by the OpenLoops library [74, 75].

***tt̄H*:**
Events with $t\bar{t}H$, with the Higgs boson further decaying to two photons, are simulated at NLO in QCD on ME level with MadGraph5_aMC@NLO using the NNPDF3.0NLO PDF set. The ME generator is interfaced to Pythia8 (v8.230), for which the *A14* tune is used in conjunction with the NNPDF2.3LO PDF set. The sample is normalised to the total $t\bar{t}H$ NLO cross-section times the branching fraction of Higgs $\to \gamma\gamma$ ($\sim 0.23\%$).

4.6.2 Inclusive samples (photons from parton shower)

The simulation of these processes involve no photon at the ME-level generation, but additional photons can still come from parton shower. The samples produced are:

***tt̄* production:**
Inclusive $t\bar{t}$ production processes are simulated on ME level at next-to-leading order in QCD using Powheg-Box-v2 [76–78]. The ME generator is interfaced to Pythia88 (v8.230) to simulate parton shower, hadronisation, fragmentation and the underlying event. Heavy-flavour decays are modelled with EvtGen. The ME calculation uses the NNPDF3.0NLO PDF set [58], with the top-quark mass fixed to 172.5 GeV . The internal parameter h_{damp} to control the hardest real emission in Powheg is set to 1.5 times the top-quark mass following Atlas standards. The showering in Pythia8 uses the *A14* tune in conjunction with the NNPDF2.3LO PDF set. By applying a K-factor, the events are normalised to a cross-section value calculated with the Top++2.0 programme at next-to-next-to-leading order in perturbative QCD, including soft-gluon resummation to next-to-next-to-leading-log [79], again assuming a top-quark mass of 172.5 GeV .

Single-top-quark processes:
Single-top-quark processes are modelled separately for the two s- and t-channel production mode,

each of which are generated separately for top-quark and anti-top-quark production. No events from the inclusive tW sample pass the overlap removal described below. Thus, the sample has not been considered as such. The other two production modes are simulated on ME level at next-to-leading order in QCD with Powheg-Box and the NNPDF2.3LO PDF set. The ME generator is interfaced to Pythia88 (v8.230) with the *A14* tune as before. Again, heavy-flavour decays are modelled with EvtGen. The sample cross-sections are normalised to next-to-next-to-leading-order precision or approximate NNLO using K-factors [80–82].

W/Z+jets:
Events with W and Z bosons in association with additional jets are simulated with Sherpa 2.2.1 at next-to-leading order in QCD. The simulation includes the hard-scattering event as well as hadronisation. The NNPDF3.0NLO PDF set is used in conjunction with a dedicated tune provided by the Sherpa authors. The samples are normalised to the next-to-next-to-leading-order cross-section in QCD [83].

Diboson:
Events with two vector bosons, that is WW, WZ and ZZ, are generated with Sherpa versions 2.2.2 (purely leptonic decays) and 2.2.1 (all others) at NLO in QCD. The NNPDF3.0NNLO PDF set is used in conjunction with a dedicated tune provided by the Sherpa authors. The samples are normalised to next-to-leading order cross-sections in QCD [84].

***$t\bar{t}$* +W/Z:**
Events with a $t\bar{t}$ pair and an associated W or Z boson ($t\bar{t}V$) are simulated at next-to-leading order in QCD on ME level with MadGraph5_aMC@NLO using the NNPDF3.0NLO PDF set. The ME generator is interfaced to Pythia88 (v8.210), for which the *A14* tune is used in conjunction with the NNPDF2.3LO PDF set. The samples are normalised to next-to-leading order in both QCD and electroweak theory [85].

4.6.3 Sample-overlap removal procedure

For some processes, two types of MC samples are simulated where photon emission is handled in two different ways: either directly at the ME level (referred to as the dedicated samples previously) or through parton shower algorithms (referred to as the inclusive samples). Once we have dedicated samples, where at least one photon is included in the ME-level generation step, and inclusive samples, in which processes are generated on ME level without explicitly including photons in the final state, employing both types of samples blindly poses a major risk. The samples can also have photons from the showering algorithms and there is a risk of double counting of these events between dedicated and inclusive samples. To mitigate this, a sample-overlap removal procedure needs to be employed. The basic idea is to define an overlap region in the generated phase space using some kinematic cuts in which such events exist. Once the events are grouped together in this overlap region, the events are kept in the more precisely calculated dedicated samples and removed from the less-precise inclusive samples. The overlap region is defined by requiring photons with $p_T > 15$ GeV and $\Delta R(\ell, \gamma) > 0.2$ between the photon and lepton, corresponding to kinematics of the $t\bar{t}\gamma\gamma$ signal sample.

The implementation of this overlap removal procedure involves a careful examination of particles generated at the ME level (truth information). All generated photons and leptons are listed and identified by their PDG IDs. Crucially, these candidates must originate from the primary vertex and not from detector interactions or hadronic activity (verified using their barcode and truth origin), and they must be stable (or considered before their decay, such as muons and τ-leptons). For instance, if a τ-lepton decays leptonically, its decay products are excluded from the candidate list, and the

τ-lepton itself is considered. After the lists are compiled, all photon candidates are checked against the above $p_T(\gamma) > 15\,\text{GeV}$ criterion. For the remaining photon candidates, $\Delta R(\ell, \gamma) > 0.2$ is tested with all lepton candidates, and the photon candidate is discarded as soon as it overlaps with one lepton candidate. If any of the photon candidates of the event pass both p_T and ΔR requirement, the event is considered to fall into the overlap region. Events from inclusive X samples, that is, $t\bar{t}$, single top (t-channel), W+jets and Z+jets, are *vetoed* if there's only one candidate photon because of which the event falls into the overlap region. This is to preserve the other events from such samples where the second non-candidate photon can result in a fake event. Events from $X\gamma$ samples, that is, $t\bar{t}\gamma$ and $W\gamma$, $Z\gamma$ are vetoed if both the photons are candidate photons and the event thus falls into the overlap region.

4.7 Categorisation of photons

As stated before, the main focus of this analysis are $t\bar{t}$ events where two additional photons are generated in the hard-scattering event. These are also called *prompt* photons. However, photons can occur at many other stages of what is being recorded as an "event" with the ATLAS detector. In addition, other particles and activities in the detector may fake photon signatures and be identified as such. Among the photon candidates detected and reconstructed with the ATLAS detector, three classes of photons are considered based on their origin:

1. **Prompt photons:** The photons originating from the hard-scattering event itself.

2. **Electron-fake (e-fake) photons:** Electron-fake photons, denoted as *e-fake photons*, which are electrons mis-reconstructed as photons in the EM calorimeter.

3. **Hadron-fake (h-fake) photons:** Non-prompt photons originating from hadrons, for example $\pi^0 \to \gamma\gamma$ decays, and photon signatures faked by hadronic energy depositions in the calorimeter are considered in one category, referred to as hadron-fake photons, denoted as *h-fake photons*.

To assess and estimate contributions to these three classes in simulation, the MC truth information is used to identify the origin of a reconstructed photon candidate. The MC-truth matching procdure acts as such: First, the truth object $\gamma^{\text{cand}}_{\text{truth}}$ associated to the photon candidate is retrieved. Then, according to the origin and truth values of that truth object, the photon candidate is classified into one of the three categories above.

A photon candidate is classified as an e-fake photon if any of the following conditions are satisfied:

- PDG ID of ± 11 indicates an electron,

- $\Delta R(\gamma^{\text{cand}}_{\text{truth}}, e_{\text{truth}}) < 0.1$, where e denotes a truth electron.

To avoid any possible double-classification, all photon candidates that match either of the two above e-fake photon criteria, are categorised as such and not examined further.

Likewise, a photon candidate is classified as an h-fake photon if any of the following conditions are satisfied:

- The origin of the object is a hadron (baryon or a meson).

- The $\gamma^{\text{cand}}_{\text{truth}}$ originating from $\pi^0 \to \gamma\gamma$ decays.

- The hadronic calorimeter energy deposit does not align with any truth-matched photon.

If the photon candidate classifies as neither e-fake photon nor h-fake photon, it is treated as prompt. One should note that such a truth-level information is absent in the data events collected by the detector. Therefore, the fake-events are modeled and correction factors are applied for them, which is discussed in section 5.3.

The signal and background processes are finally grouped as shown in the Table 4.1. Events from the $t\bar{t}\gamma$ and $t\bar{t}$ samples in the non-overlapped regions of $t\bar{t}\gamma\gamma$ are not added to the signal template because by construction they do not fulfill the requirements at particle level defined to measure the cross section measurement.

Table 4.1: The table summarises grouping of processes as used later in the analysis and in the figures. The categories $t\bar{t}\gamma\gamma$, $t\bar{t}\gamma$ (prompt γ), Other $\gamma\gamma$ correspond to events with two prompt photons, while the fake categories correspond to events with at least one fake photon.

Groups	Processes
$t\bar{t}\gamma\gamma$	$t\bar{t}\gamma\gamma$ events with two prompt photons regardless of the origin of the photon
$t\bar{t}\gamma$ (prompt γ)	$t\bar{t}\gamma$ production and decay events in the non-overlapped region with two prompt photons
Other $\gamma\gamma$	Events with two prompt photons from diboson($+VV\gamma\gamma$) $t\bar{t}$ (non-overlapped region) $t\bar{t}H$ ($H \to \gamma\gamma$) tWγ $t\bar{t}W$, $t\bar{t}Z$ $Z\gamma\gamma$, $Z\gamma$, Z+jets (non-overlap region) $W\gamma\gamma$, $W\gamma$, W+jets (non-overlap region) single top [$s-$, $t-$ channels]
e-fake γ	Events with at least one electron fake γ from any of the processes
h-fake γ	Events with at least a hadron fake γ and no e-fakes from any of the processes

CHAPTER 5

Event selection

"The map is not the territory."

— Alfred Korzybski

This chapter discusses the events selected for the analysis. First, the data set collected by ATLAS for purpose of the analysis is described, followed by the normalisations and weight corrections applied to the MC simulated samples in Section 5.2. Section 5.3 discusses briefly the data driven scale factors derived in the $t\bar{t}\gamma$ analysis [1] to correct for fake-photon events and used directly in the analysis presented in this thesis as well. Section 5.4 discusses the selection requirements for the events considered for further measurements in the analysis. Finally, some kinematic distributions are shown to demonstrate the good description of data by the MC simulations within the selected events.

5.1 Data set

The data used in the analysis was recorded during Run 2 of the LHC with the ATLAS detector between 2015 and 2018 at a $\sqrt{s}$ of 13 TeV. The dataset corresponds to an integrated luminosity of 140.1 fb^{-1} for the full Run 2 period, with an uncertainty of ±0.83 %, obtained using the LUCID-2 detector for the primary luminosity measurements [86]. Only data-taking periods, where the ATLAS detector was fully operational and the recorded data satisfies quality criteria, were considered.

Both, the observed data and MC simulation samples, are processed with the same analysis tools and software versions to prepare them for further analysis.

5.2 MC normalisation

MC simulated events are assigned weights to ensure they accurately represent the physical processes which are being studied. These weights are essential for converting a finite sample of generated events into a robust prediction for the expected events in the analysis.

MC generators calculate the cross section by integrating the generated phase space more accurately using sophisticated integration techniques. This is known as the MC-predicted cross section (σ^{MC}), which is more precise than the cross-section obtained directly from the generated event weights.

The generated events are then normalized by dividing each weight by the sum of all weights. This normalization gives the relative probability of each event within the sample [10]. To determine the

expected number of events for the process, these normalized weights are scaled by the more precise MC-predicted cross-section as well. Thus, the weight of each event after normalization and scaling becomes:

$$w_i = \left(\frac{\text{weight_mc}^i}{\sum_i^N \text{weight_mc}^i} \times \sigma^{\text{MC}} \right), \tag{5.1}$$

where w_i is the weight of the i-th event and N is the total number of events generated. σ^{MC} is the MC predicted cross-section and weight_mc^i is the MC generator weight of the i-th event.

To obtain the expected number of events in the data, the events are further scaled to the luminosity of the data by the following formula. Additionally, the reconstruction level events are corrected by scale factors (SFs) related to object identification efficiency, isolation efficiencies, trigger efficiencies, JVT efficiency, and b-tagging efficiency. These SFs are calculated as the ratio of the efficiencies in data and in MC and are applied to MC events to correct the discrepancies in the simulated events [10]. Including all these corrections, the event weight for a reconstruction level event becomes:

$$w_i = \frac{\sigma^{\text{MC}} \times \text{weight_mc}^i \times \text{Luminosity} \times \text{weight_pileup} \times \text{SF_photon} \times \text{SF_lepton} \times \text{SF_JVT} \times \text{SF_bTag}}{\sum_i^N \text{weight_mc}^i}. \tag{5.2}$$

5.3 Data-driven estimates of fake-photon background processes

As discussed in Section 4.7, events can have fake (mis-reconstructed) photons due to detector effects and photon reconstruction algorithms. Although the detector simulation models these fake photon events, there are often some disagreement between the data and the MC simulation. The mis-modeling of e-fake photon and h-fake photon events in MC is corrected using data-driven methods. These were estimated for each photon in an event in the $t\bar{t}\gamma$ analysis [1] [10]. Since the photons in this analysis are treated uncorrelated in terms of their kinematics, the correction factors have been borrowed for the $t\bar{t}\gamma\gamma$ measuements in this analysis as such. They are implemented in the analysis as scale-factors to correct the MC simulated events. Below is a short description of the methods used to estimate these events.

5.3.1 Electron-fake background (e-fake)

The contribution from electrons that are misidentified as photons, known as e-fake, is estimated directly from experimental data [10]. This estimation leverages processes where the true composition of events is well-understood. For instance, events containing electron-positron pairs from $Z \to e^+e^-$ decays are used as a control sample. The method involves defining two distinct control regions: one rich in pure electron-positron pairs, and another, specifically designed to be enriched in e-fake events, which selects events with an electron and a reconstructed photon that satisfy the analysis's selection criteria. By comparing the observed invariant mass spectra around the known Z-boson mass peak in these two regions, the e-fake rate can be determined. Before this comparison, any known background contributions in these control regions are subtracted, mostly by analyzing the sidebands of the Z-boson peak. This e-fake rate is measured as a function of the photon's η and p_T, and is determined separately for converted and unconverted photon candidates. The systematic uncertainty in this background

estimate largely stems from the chosen functional forms used to model the Z-boson mass peak and the underlying background in the control regions, as well as the specific mass range considered for the Z-boson peak. These data-derived e-fake rates are then used to correct the e-fake background predicted by simulation in the signal region, ensuring that the background estimate reflects actual detector performance. One notable source of e-fake background often arises from $t\bar{t}$ events where an electron from the top quark decay chain is misidentified as a photon, mimicking the signature of a signal process.

5.3.2 Hadron-fake background (h-fake)

The background contribution from events where hadronic energy depositions in the EM calorimeter, or hadron decays, are misidentified as photons (referred to as h-fake) is also estimated using a data-driven approach, typically the 'ABCD' method. This method relies on defining multiple statistically independent control regions that are enriched in h-fake photon events but are orthogonal to the signal region. These regions are constructed by inverting photon isolation criteria or by loosening specific photon identification requirements. By counting the number of selected data events in these h-fake-enriched regions, and subsequently subtracting contributions from prompt photons and any e-fake background, the number of h-fake events in the signal region can be reliably evaluated. This allows for the determination of correction factors relative to the MC simulation's prediction. These correction factors are obtained as a function of the photon's p_T and η, and are applied separately for converted and unconverted photon candidates to determine the final h-fake background contribution. The dominant source of systematic uncertainty for the h-fake background often arises from the modeling uncertainties of the processes that are the primary origin of these fake photons, such as $t\bar{t}$ production. Additional uncertainties also come from the normalization of other background contributions (like prompt photons) and the uncertainties associated with the data-driven e-fake background estimation in the h-fake-enriched regions.

5.4 Event selection in $t\bar{t}$ single lepton channel

The measurements presented in the analysis are performed on a subset of events which follow some specific selection criteria. The selection criteria used in this analysis are used to define the signal region (SR) at reconstruction level, and closely follows the $t\bar{t}\gamma$ analysis [1] to faciliate the further measurements. Using the reconstructed physics objects described in 3.3, events are selected in single-lepton $t\bar{t}$ channel. Selected events require exactly two tight and isolated photons and exactly one electron or muon, which must be matched to an online reconstructed electron or muon, respectively. The p_T thresholds for the leptons are 25 GeV in 2015 data, 27 GeV in 2016 data, and 28 GeV in 2017 and 2018 data. The different thresholds are done to avoid differences due to the calibration of the objects used in the trigger logic, and objects used in the physics analysis. Events with an additional lepton with $p_T > 7$ GeV and/or fulfilling |m(e,γ)-91.19 GeV |<5 GeV (events around the Z-boson mass) are vetoed. Additionally, the events must contain at least four jets and at least one b-tagged jet. A $\Delta R > 0.4$ cut is implemented between the two photons as well. These selections essentially define the signal-enriched region in which the measurements are performed. The kinematic and other requirements are listed in Table 5.1.

The observed event yields from data and the expected yields from the MC simulations are shown in

Table 5.1: Event selection for the single lepton channel.

Selection	Channel	
	e+jets	μ+jets
1 Lepton	$\|\eta\| < 1.37$ or $1.52 < \|\eta\| < 2.47$	$\|\eta\| < 2.5$
	p_T > 25/27/28 GeV (15/16 & 17/18 data)	
2 Photons	p_T > 20 GeV and $\Delta R(\gamma, \gamma) > 0.4$ $\|\eta\| < 1.37$ or $1.52 < \|\eta\| < 2.37$	
Anti-k_t R=0.4 jets	$N_{\text{jets}} \geq 4$ p_T > 25 GeV, $\|\eta\| < 2.5$	
b-tagging	$\geq$ 1 jets with DL1r tagging algorithm at 70%	
m(e,γ) veto	|m(e,γ)-91.19 GeV |>5 GeV	–

Table 5.2: Expected event yields in the signal and background categories. The h-fake category corresponds to events with at least one h-fake photon but not e-fakes. The e-fake category includes events with at least one e-fake photon.

Category	Yields
$t\bar{t}\gamma\gamma$	69.1
h-fakes	13.3
e-fakes	24.6
Other $\gamma\gamma$	17.7
Total	124.7
Data	122.0

Table 5.2. Out of the total of 24.3 e-fake events, 1.2 events correspond to cases where both photons are fake, one being an e-fake and one and h-fake. The MC simulated samples slightly overestimate the number of events expected, a major reason being the $t\bar{t}\gamma\gamma$ events normalised with K-factor. Still, they are in good agreement with the data. The e-fake events constitute about 20% of the total expected events, while h-fake and two prompt photons events contribute ~11% and ~14%, respectively. The contribution of the individual MC processes to the e-fakes is shown in Table 5.3 and for h-fakes is shown in 5.4. Table 5.5 shows the breakdown of number of events with two prompt photons from different processes. The expected number of signal events after event selection is ~55% of the total number of expected events. The $W/Z\gamma\gamma$ process contributes largely to the Other $\gamma\gamma$ category as well. The $t\bar{t}\gamma$ process mostly contributes through fake photons, which indicates that the sample-overlap removal procedure (Section 4.6.3) is able to reject the events from $t\bar{t}\gamma$ process where both photons (one from ME and another from PS) are prompt. The $t\bar{t}$ events also mostly contribute to the fakes category, while the yields from the other background processes is low. All the events from the $t\bar{t}H$ (H$\rightarrow \gamma\gamma$) process, whose final state is exactly similar to the $t\bar{t}\gamma\gamma$ process, contribute to the Other $\gamma\gamma$ category only.

Table 5.3: Breakdown of e-fakes yields from the different processes. Table includes only e-fake events where one or both photons are e-fakes, not the combined-fake cases where one photon is e-fake and another photon is h-fake.

Source of e-fake events	Yields
$t\bar{t}\gamma\gamma$	0.5
$t\bar{t}\gamma$ production	10
$t\bar{t}\gamma$ decay	9.4
$W\gamma$	0.0
$Z\gamma$	1.8
W + jets	0.0
Z + jets	0.1
$Wt\gamma$	0.8
$t\bar{t}$	0.5
$t\bar{t}H$	0.0
single t, s-channel	0.0
single t, t-channel	0.0
$t\bar{t}V$	0.5
VV	0.1
$W\gamma\gamma$	0.0
$Z\gamma\gamma$	0.2

Table 5.4: Breakdown of h-fake yields from different processes. The largest contribution of $t\bar{t}$ h-fake events corresponds to events with two h-fakes (1.4 events).

Source of h-fake events	Yields
$t\bar{t}\gamma\gamma$	0.2
$t\bar{t}\gamma$ production	4.8
$t\bar{t}\gamma$ decay	5.6
$W\gamma$	0.0
$Z\gamma$	0.0
W + jets	0.2
Z + jets	0.0
$Wt\gamma$	0.6
$t\bar{t}$	1.6
$t\bar{t}H$	0.0
single t, s-channel	0.0
single t, t-channel	0.2
$t\bar{t}V$	0.2
VV	0.0
$W\gamma\gamma$	0.0
$Z\gamma\gamma$	0.0

Table 5.5: Breakdown of events with prompt photons from different processes.

Groups	Processes	Yields
$t\bar{t}\gamma\gamma$	$t\bar{t}\gamma\gamma$ events with two prompt photons regardless of the origin of the photon	69.1
$t\bar{t}\gamma$ (prompt γ)	$t\bar{t}\gamma$ production	1.2
	$t\bar{t}\gamma$ decay	1.2
Other $\gamma\gamma$	$t\bar{t}$	0.4
	$t\bar{t}H$ ($H \to \gamma\gamma$)	3.9
	tWγ	2.9
	$t\bar{t}W$, $t\bar{t}Z$	0.6
	$W\gamma\gamma$	4.8
	$Z\gamma\gamma$	1.3
	$W/Z\gamma$	0.1
	W+jets	0.0
	Z+jets	0.0
	Diboson (VV)	0.0
	single top [s-channel]	0.1
	single top [t-channel]	1.2

The figures 5.1 to 5.5 show some of the variable distributions with the total expected and observed (data) events, after applying all the event selections and before performing any fit with data. An overall good agreement can be seen between the data and MC simulated events in the SR, all within 1-2σ deviation, as reflected in the corresponding χ^2 value. The photons are referred to as leading and subleading based on their p_T-ordering.

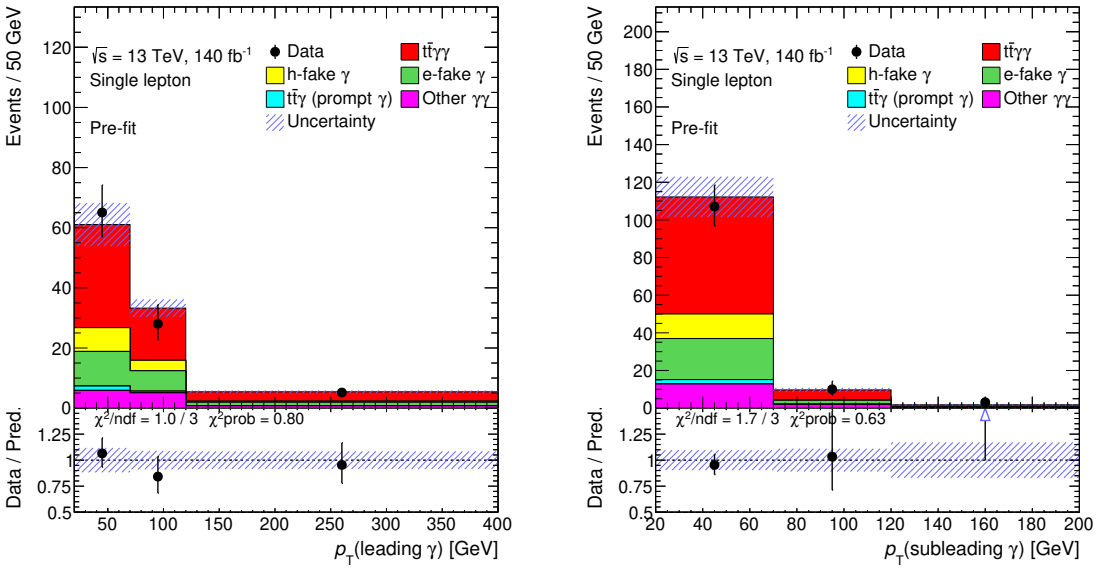

(a) (b)

Figure 5.1: The p_T distributions of the (a) leading and (b) subleading photons. The uncertainty band represents the total uncertainty before the fit to the data.

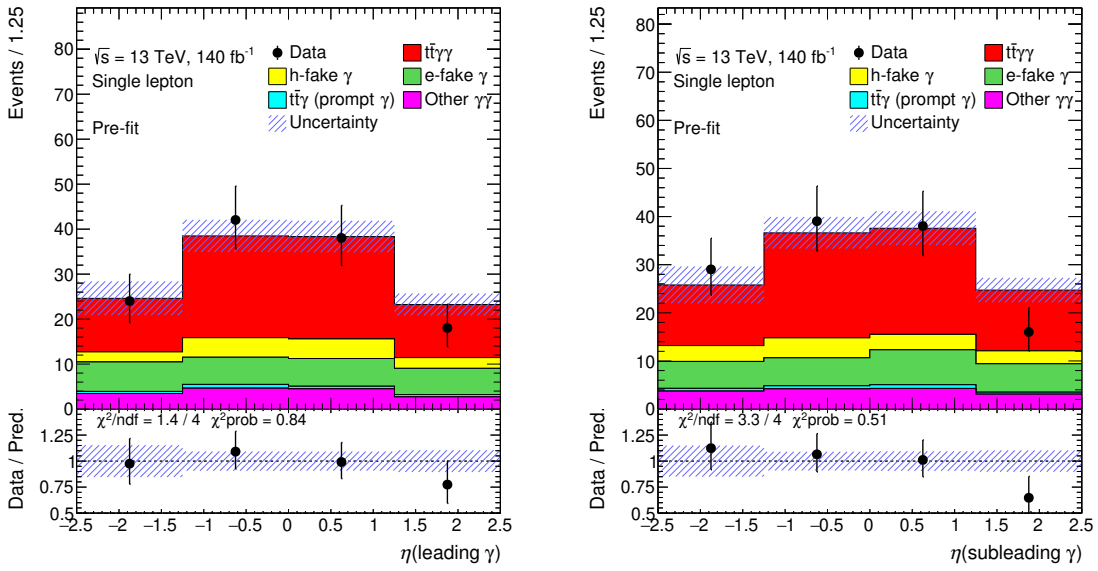

(a) (b)

Figure 5.2: The η distributions of the (a) leading and (b) subleading photons. The uncertainty band represents the total uncertainty before the fit to the data.

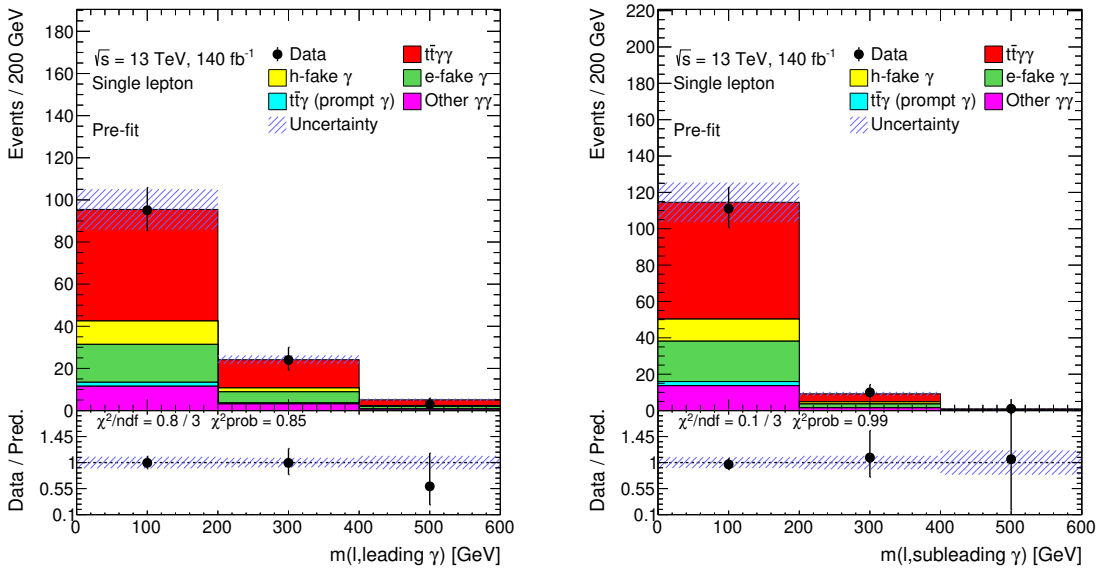

(a) (b)

Figure 5.3: The invariant mass distributions of the lepton and the (a) leading or (b) subleading photon. The uncertainty band represents the total uncertainty before the fit to the data.

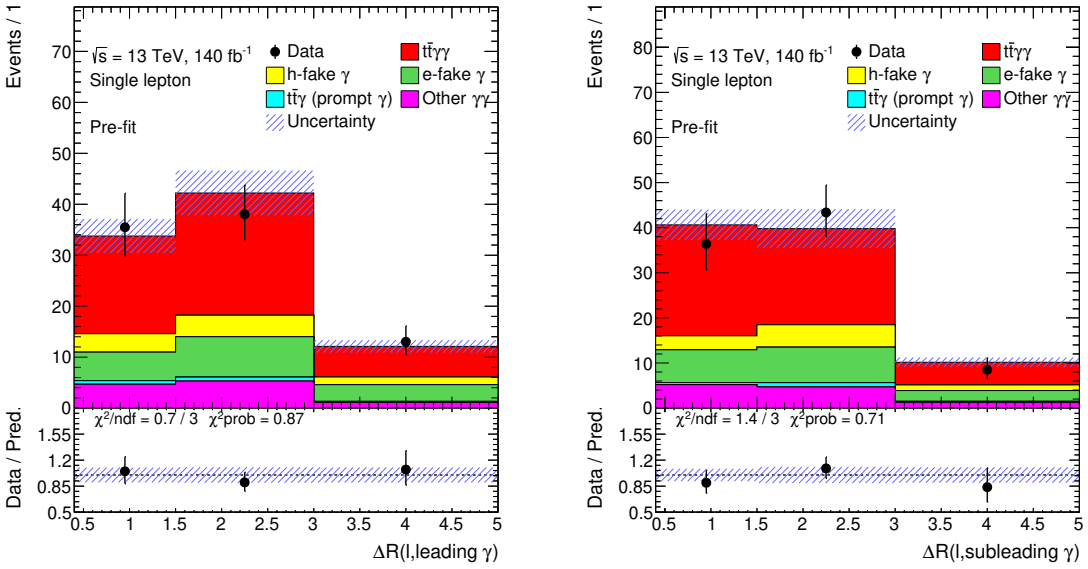

(a) (b)

Figure 5.4: The ΔR distributions between the lepton and the (a) leading and (b) subleading photon. The uncertainty band represents the total uncertainty before the fit to the data.

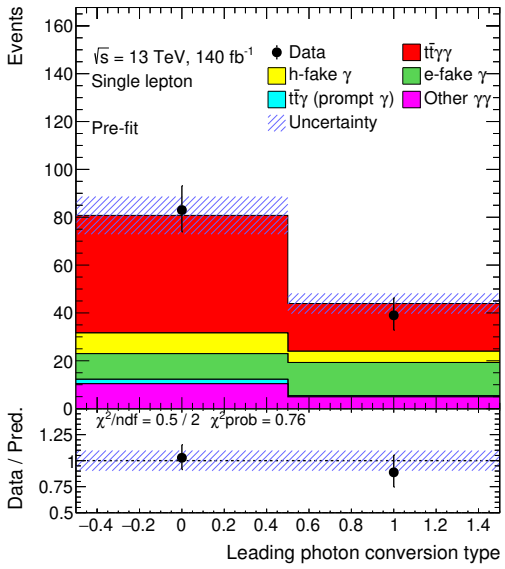

(a)

Figure 5.5: The photon conversion type of the leading photon by p_T. The first bin of the distribution corresponds to the unconverted photons, while the second bin corresponds to the sum of all converted photon types. The uncertainty band represents the total uncertainty before the fit to the data.

CHAPTER 6

Signal and background discrimination

"Two roads diverged in a yellow wood,
And sorry I could not travel both. . . "

— Robert Frost, *The Road Not Taken* (1916)

Effective discrimination between signal and background is essential to maximise the sensitivity of the measurement. Traditional cut-based selections may fail to fully exploit the discriminating power of correlated observables. Therefore, multivariate techniques are often employed to capture these correlations and achieve improved signal–background separation. In this analysis as well, a Boosted Decision Tree (BDT) is employed to exploit correlations between multiple input observables, providing better separation power than sequential, cut-based selections. BDTs have been increasingly useful in HEP analyses in the past as well.

The results of the current analysis are extracted from fit to the BDT output of this model. This chapter lays out the groundwork for the results obtained in the analysis presented in this thesis. It begins with a general overview of decision trees in Section 6.1, then discusses the method of collective ensemble learning in Section 6.2, building up to BDTs in Section 6.3.1. The various algorithms and hyperparameters of BDT are also discussed in this section. Section 6.4 discusses the training of the BDT model using XGBoost algorithm, which is used in the analysis. The training setup of the BDT and the performance metrics are further discussed and shown in Section 6.4.3. Finally, Section 6.4.5 shows the results of the BDT output, which is used for the final measurements in Chapter 8.

6.1 Decision Tree

A decision tree can be thought of as a flowchart-like model used for classification or regression tasks. It operates by splitting the data into subsets based on the value of the input features, following a hierarchy of specific rules. Each decision tree is composed of:

- **Nodes:** Represent decisions based on the input feature values. At each internal node, the algorithm chooses a feature and a threshold to split the data in a way that best separates the target classes for classification problems or minimizes prediction error for regression problems.
- **Branches:** Represent the outcomes of the decision rules. For example, "is energy > 50 GeV?" would have two branches - yes or no.

- **Leaves:** Terminal nodes that assign a final prediction — a class label in classification or a numerical value in regression problems, respectively.

To construct a tree, an algorithm selects the best feature and threshold at each node by optimizing a criterion such as Gini impurity, entropy, or mean squared error. It continues splitting the data recursively until a stopping condition is reached, such as maximum depth of the tree or a minimum number of samples per leaf. This splitting is demonstrated in Figure 6.2 with the help of the iris flower data set [87] as an illustrative example for pedagogical purpose only, where the dataset is split according to input features like petal length and petal width.

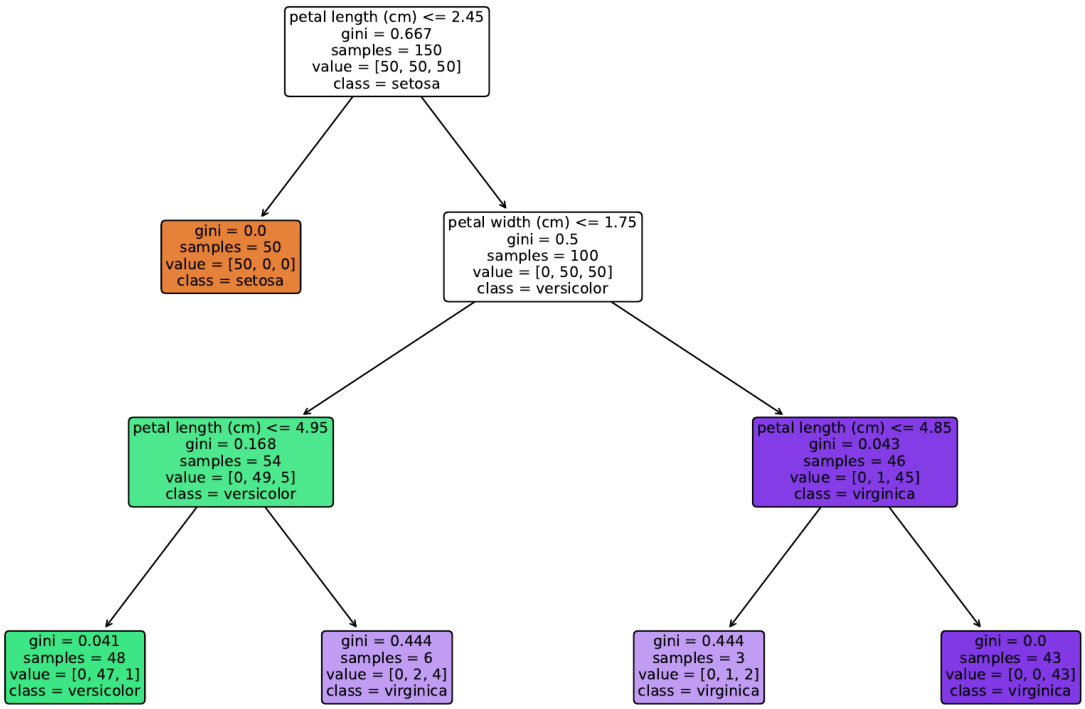

Figure 6.1: Illustrative example of node branching in a decision tree using the Iris dataset. The split criteria are chosen for demonstration purposes.

Decision trees are interpretable and flexible, but when grown deep, they can overfit the training data. Conversely, when made shallow (e.g., just a few levels deep), they tend to generalize poorly and are referred to as 'weak learners'. Since a decision tree is deterministic in nature, it is therefore possible to interpret a tree in terms of physics objects and selection criteria.

6.1.1 Decision tree algorithm

Decision trees are rooted binary trees i.e. they consider only 2 classes - signal and background. A decision tree starts from an initial node of set of variables which gets split into daughter branches until

some stopping condition is reached. The basic algorithm is described below:
One begins with a dataset consisting of signal events s_i and background events b_j, each described by a set of input variables $\vec{x}_i$, and associated weights w_i^s and w_j^b. This dataset defines the "root node" of the decision tree. The tree is then constructed recursively using the following steps:

- **Check for stopping criteria.**
  If the current node satisfies any predefined stopping condition (such as minimum number of events, maximum tree depth, or node purity), label it as a *leaf node* and terminate the splitting process for this branch.
- **Sort events by each variable.**
  For each input variable $x_k \in \vec{x}$, sort the events according to their values of x_k.
- **Evaluate possible splits.**
  For each variable, examine all possible threshold values to split the node into two subsets. For each split, compute a separation metric (e.g., Gini impurity, entropy, or another figure of merit). If no split results in improved separation, declare the current node a leaf and stop.
- **Select the best split.**
  Choose the variable x_k and corresponding threshold θ that maximize the separation between signal and background. Split the node into two children:
  - One child node with events satisfying $x_k < \theta$,
  - One child node with events satisfying $x_k \geq \theta$.
- Apply steps (1) through (4) recursively to each child node.

6.2 Ensemble Learning

A weak learner is a model that performs just slightly better than random guessing. For instance, a shallow decision tree may only capture a basic trend or a rough boundary between classes based on the input features, but fails to model complex, non-linear relationships. In isolation, such a tree would be insufficient for high-precision tasks of, say classification. However, weak learners have an important advantage: they are fast to train, simple, and unlikely to overfit on their own which makes them ideal candidates for use in ensemble methods. Ensemble learning is an approach where multiple weak learner models are combined to form a more powerful predictor. The underlying assumption is that the collective decision of many models can outperform any individual model, especially when their errors are uncorrelated. There are two primary ensemble strategies:

- Bagging (Bootstrap Aggregating): Multiple models are trained in parallel on random subsets of the data, and their predictions are averaged or voted on. Random Forests are a prominent example [88].
- Boosting: Models are trained sequentially, and each new model tries to correct the mistakes made by the previous ones. The final output is a weighted sum of all learners.

Boosting is highly effective for signal-background classification as it iteratively focuses on events that are difficult to distinguish, progressively refining the separation between signal and background [89].

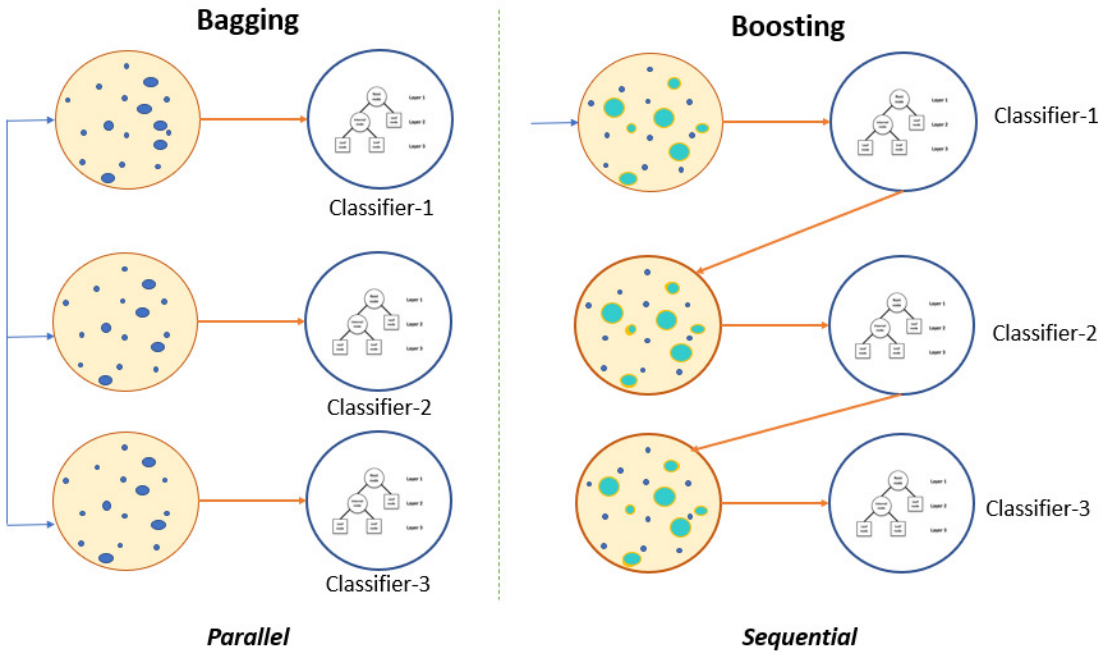

Figure 6.2: Bagging versus Booting [90].

6.3 Boosted Decision Trees

6.3.1 Introduction

As mentioned before, a Boosted Decision Tree (BDT) is an ensemble learning algorithm. It constructs a strong predictive model by combining the predictions of many simpler, individual decision trees (weak learners). This way, rather than relying on a single, deep, and potentially overfitted tree, BDTs leverage a multitude of shallow trees, with each successive tree specifically trained to correct the residual errors or mis-classifications made by the ensemble of trees preceding it.

The general process of training a BDT involves an iterative sequence:

1. **Initial Model and Weighting:** A first decision tree is trained on the data. In subsequent iterations, a new decision tree is trained, where individual data points are re-weighted. Data points that were misclassified or had large prediction errors by the previous trees in the ensemble are assigned higher weights, forcing the new tree to focus more on these "difficult" cases.

2. **Sequential Learning:** Each new tree in the sequence attempts to model the residual errors of the combined ensemble from the previous steps. This means the new tree is trained to improve the overall prediction where the current ensemble performs poorly.

3. **Ensemble Combination:** The predictions of all individual trees are then combined to form the final output. For classification tasks (like distinguishing signal from background), this combination often involves a weighted sum or vote, where the weight of each tree's contribution can depend on its performance during training. For regression tasks (like estimating a continuous value), the outputs are typically summed up.

6.3.2 Key BDT Algorithms

Building upon the concept of boosting, there are many algorithms available, each with distinct mechanisms for refining the ensemble. Some of them are briefly mentioned below:

1. **AdaBoost (Adaptive Boosting):** An early boosting mechanism which iteratively adjusts the weights of training examples based on whether they were correctly classified in the previous step and then combines the weak learners' outputs using weights proportional to their accuracy.
2. **Gradient Boosting:** A more generalized boosting framework in which each new tree learns to correct previous errors by fitting to the negative gradient of the loss function, iteratively minimizing the overall prediction error.
3. **Advanced Gradient Boosting Implementations:**
   - **XGBoost (eXtreme Gradient Boosting):** A highly optimized variant of gradient boosting, incorporating multiple novel techniques to be more efficient than the traditional gradient boosting algorithms [91], discussed in more detail in Section 6.4.3.
   - **LightGBM (Light Gradient Boosting Machine):** Developed for high efficiency and speed, LightGBM uses a novel tree growth algorithm that significantly reduces training time on large datasets while maintaining accuracy.

6.3.3 Hyperparameters of BDTs

The performance of BDTs heavily depends on their hyperparameters, which are predefined, non-learnable configuration settings that govern the training process. Some of the key hyperparameters are:

- **Number of Estimators (Trees)**: Determines how many trees should be built in the sequence. More trees can increase accuracy but also the risk of overfitting and computational cost.
- **Depth of Trees**: Controls the maximum depth of each tree. Deeper trees can model more complex patterns but might lead to overfitting.
- **Learning Rate**: A smaller learning rate requires more trees but can lead to better generalization.
- **Maximum Features**: Number of features to consider when looking for the best split in a BDT.
- **Minimum Samples Split**: Minimum number of samples required to split an internal node.
- **Minimum Samples Leaf**: Minimum number of samples required to be at a leaf node.

It should be noted that of the above hyperparameters, the first 3 can be referred to as hyperparameters of the model, and bottom 3 are essentially hyperparameters of the training process rather than the model itself.

Some of the key experiments that use or have used BDTs include ATLAS and CMS for Higgs and BSM physics, LHCb for CP violation, IceCube for neutrino classification, and MiniBooNE/MicroBooNE for sterile neutrino searches [92][93][94][95].

The training of the BDT model used for the analysis are described in the subsequent sections.

6.4 BDT framework used for signal-background discrimination

Given the subtle differences between signal and background distributions in the current analysis as well, traditional analysis methods or single-variable cuts are not expected to yield optimal results. Figures 6.3 to 6.6 highlight this issue by showing some of the kinematic variable distributions with the $t\bar{t}\gamma\gamma$ signal laid over the background, where the shape of the distributions overlap.

Preliminary Asimov fits were performed to some of these variables with moderate signal-background separation power. Some of the variables, such as the photon conversion type for the leading photon and the ΔR between subleading photon and lepton, showed good potential yielding expected significances approaching 5σ. These studies are presented in Appendix A. However, to maximise the sensitivity of measuring the $t\bar{t}\gamma\gamma$ signal process and properly exploit the available information better, a better multivariate discriminator is required. For this purpose, an approach employing a BDT is selected over more complex approaches, such as deep neural networks, to provide better performance without overfitting.

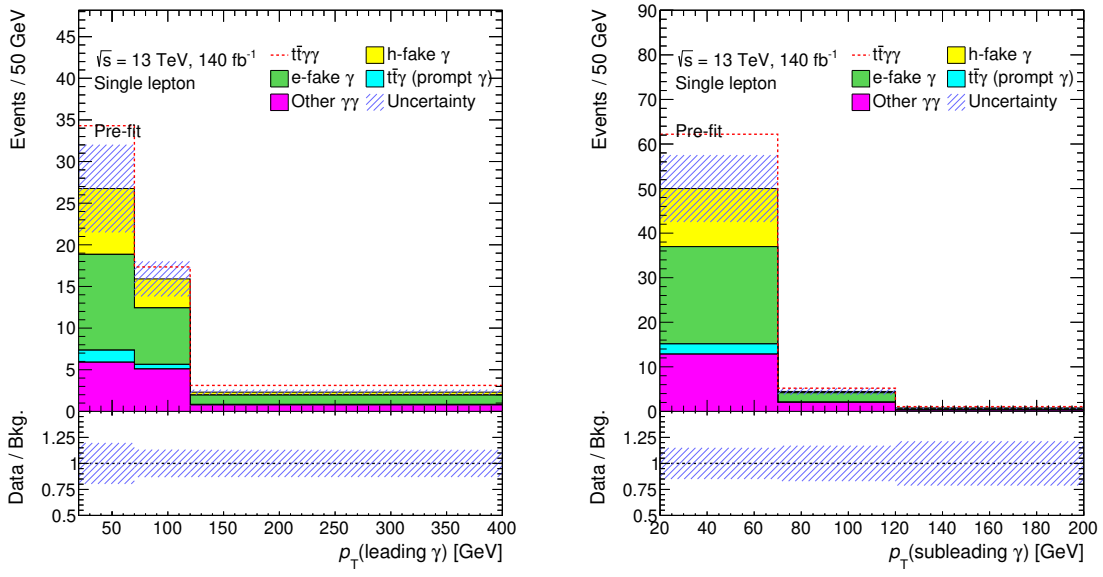

(a) (b)

Figure 6.3: The p_T distributions of the (a) leading and (b) subleading photons. The uncertainty band corresponds to the pre-fit uncertainties of the background samples. The $t\bar{t}\gamma\gamma$ signal is scaled to the total number of background events.

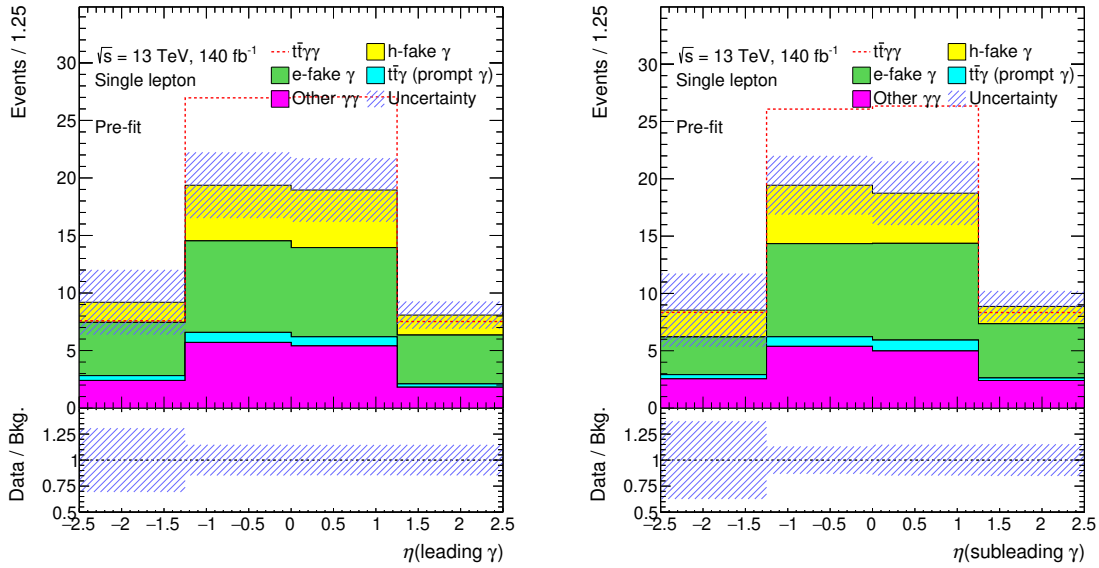

(a) (b)

Figure 6.4: The η distributions of the (a) leading and (b) subleading photons. The uncertainty band corresponds to the pre-fit uncertainties of the background samples. The $t\bar{t}\gamma\gamma$ signal is scaled to the total number of background events.

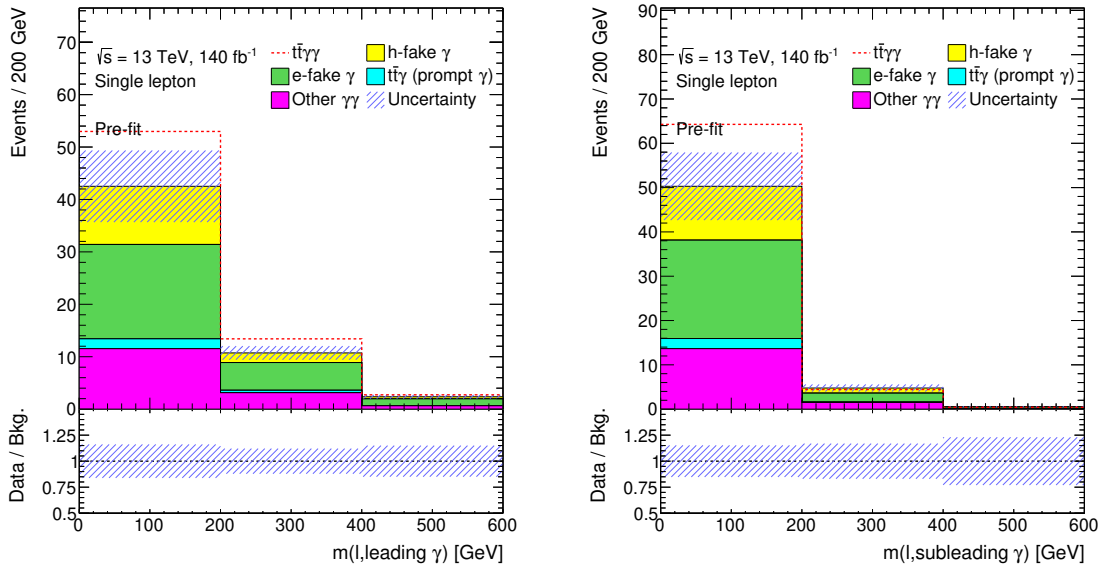

(a) (b)

Figure 6.5: The invariant mass distributions of the lepton and the (a) leading or (b) subleading photon. The uncertainty band corresponds to the pre-fit uncertainties of the background samples. The $t\bar{t}\gamma\gamma$ signal is scaled to the total number of background events.

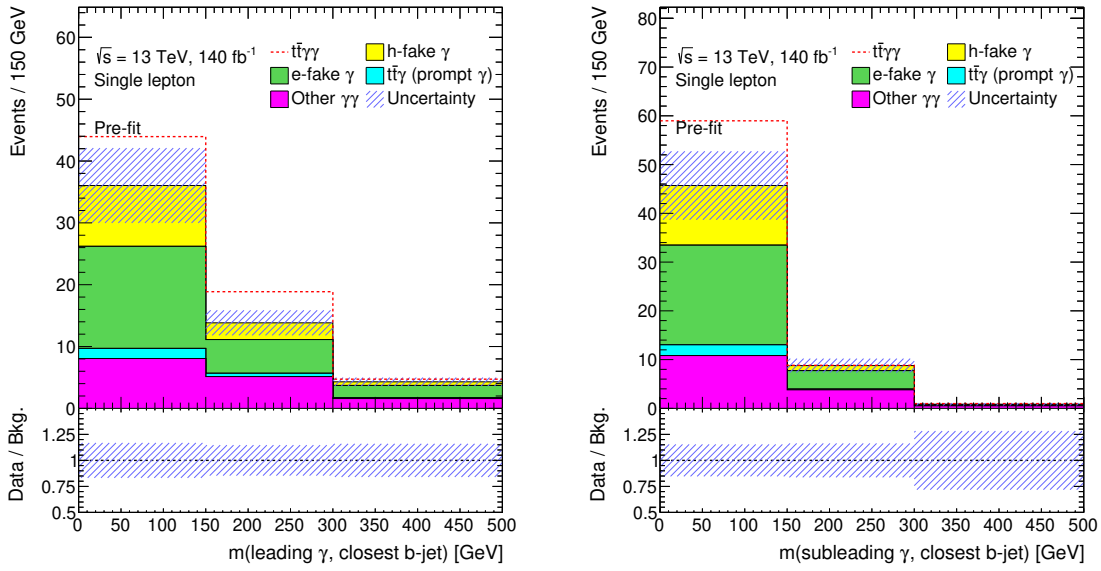

(a) (b)

Figure 6.6: The invariant mass distributions of the (a) leading or (b) subleading photon and the closest b-jet. The uncertainty band corresponds to the pre-fit uncertainties of the background samples. The $t\bar{t}\gamma\gamma$ signal is scaled to the total number of background events.

6.4.1 Training dataset

As discussed in section 4, there are multiple background processes considered within the analysis. But the overall statistics in the signal region, defined in Section 5.4, are dominated by two major sources of background - $t\bar{t}\gamma$ (production and decay) and $V\gamma\gamma$, accounting for ~70% of the total background contribution. To that end, a binary classification model is employed where the BDT model learns to classify the $t\bar{t}\gamma\gamma$ events as signal and $t\bar{t}\gamma$ and $V\gamma\gamma$ as background. The simulation events are weighted according to their individual event weights while training, only taking absolute MC event weights while training.

6.4.2 Variable selection for BDT training

At the beginning of employing any multivariate analysis (MVA) technique, it is necessary to identify a suite of suitable variables to serve as inputs for the training model. This requires that the distributions of the variables exhibit distinct shapes for the different categories that the MVA method is intended to classify. The measure of this distinction in shape, essential for effective classification, is also referred to as separation. It is quantified as:

$$S = \frac{1}{2} \sum_{i \in \text{bins}} \frac{(s-b)^2}{s+b}, \tag{6.1}$$

where s is the number of signal events in bin i and b the number of background events.

For the purpose of the analysis, a large set of variables (pertaining to kinematics of the physics objects, event yields etc.) were chosen. After studying the separation power of multiple such variables, the following 19 variables, listed below, were selected to train the BDT model for the analysis:

- Photon conversion type (converted or unconverted) of the leading photon in p_T
- ΔR between the leading and subleading photons
- η of the subleading photon
- Invariant mass of the subleading photon and lepton
- Diphoton invariant mass
- p_T of the leading jet
- ΔR between the subleading photon and lepton
- η of the leading photon
- p_T of the subleading jet
- ΔR between the leading photon and lepton
- Pseudo-continuous b-tagging distribution of the jet with the highest score
- Invariant mass of all jets, the lepton and the photons

- $E_{\mathrm{T}}^{\mathrm{miss}}$
- Invariant mass of the leading photon and closest b-jet
- Invariant mass of the leading photon and lepton
- p_T of the leading photon
- Invariant mass of the subleading photon and closest b-jet
- p_T of the subleading photon
- Number of b-tagged jets (70% working point)

Note: The PCBT (Pseudo-continuous b-Tagging) score is a calibrated, integer-binned representation of the DL1r tagger's continuous output discriminant (see section 3.3.5). It assigns a discrete score (1 to 5) to a jet based on the tightest b-tagging efficiency working point (e.g., 85%, 77%, 70%, 60% b-jet efficiency) that the jet's discriminant value satisfies.

6.4.3 Training and optimization of the BDT

The training of the BDT was performed with XGBoost classifier from the XGBoost library [91]. The section below discusses how XGBoost is more efficient than traditional gradient boosting classifiers from other machine learning libraries such as scikit-learn [96].

XGBoost versus traditional boosting methods

XGBoost offers several key enhancements over traditional gradient boosting methods.

The primary advantage of XGBoost is its regularized objective function, which penalizes model complexity to prevent overfitting. It is defined as;

$$\mathrm{Obj}^{(t)} = \sum_{i=1}^{n} l\left(y_i, \hat{y}_i^{(t-1)} + f_t(x_i)\right) + \Omega(f_t), \tag{6.2}$$

where n is the number of training samples, y_i is the true label of the i-th sample, $\hat{y}_i^{(t-1)}$ is the prediction after $(t-1)$ boosting rounds, $f_t(x_i)$ is the new function (a regression tree) added at step t, $l(y_i, \hat{y}_i)$ is the loss function measuring the difference between prediction and target, and $\Omega(f_t)$ is a regularization term penalizing the complexity of f_t.

The regularization term is typically defined as

$$\Omega(f_t) = \gamma T + \frac{1}{2}\lambda \sum_{j=1}^{T} w_j^2, \tag{6.3}$$

where T is the number of leaves in the tree, w_j is the weight assigned to leaf j, and γ and λ are regularization parameters controlling the penalty on the number of leaves and the magnitude of the leaf weights, respectively.

Other than the regularized objective function, XGBoost also employs optimized algorithms which make it more efficient than traditional gradient boosting methods, such as employing parallel processing

for faster computation. XGBoost also includes sparsity-awareness algorithm that takes into account sparsity (or density) of the data in different splits in the boosting process.

For the purpose of the analysis, the nascent XGBoost classifier with its default parameter values (i.e. number of estimators (trees)=100, learning rate=0.1, max_depth=3) was used. It was observed that changing these default parameter values of the model did not affect the separation values significantly, so they are taken as such without further need for tuning.

The training statistics includes the raw MC simulated events from the $t\bar{t}\gamma\gamma$ sample (tagged as signal) and from the $t\bar{t}\gamma$ and $V\gamma\gamma$ samples (tagged as background). The training is performed using a k-fold approach with 4 folds. The simulated events are therefore split into four sets, approximately equal sized parts. This means that in each iteration of fitting the model, approximately 75% of the data is used for training, while 25% is for testing. This strategy ensures that all the training data is used both for training and testing over the four folds. As is typical in a k-fold cross-validation, each test set effectively acts as a validation set during its respective iteration during the training process.

Treatment of negative weights during training:

Negative weights in simulated events are common. Usually at higher-orders such as NLO, the new diagrams that get added can have a phase that causes them to interfere destructively with the lower-order amplitudes. This destructive interference leads to a reduction in the overall probability of certain outcomes. In MC simulations, this reduction is represented by assigning negative weights to some of the events. Samples with negatively weighted events can have reduced statistical power [97].

Negatively weighted events contribute little to the overall statistics of the training dataset. In particular they only contribute visibly to the background samples (by ~15% in total), particularly to the $t\bar{t}\gamma$ production sample which is produced with NLO accuracy. Machine learning models, such as XGBoost, are designed to minimize the loss function. A negative weight would mean that a training example's mis-classification would improve the total loss rather than increase it. This is counterintuitive and would make the optimization process unstable because the model could "learn" to mis-classify negatively weighted events to artificially lower the loss. Thus, to preserve the convexity of the loss function, negative weights of such events are treated as absolute values in the training of the 4-fold models. It was checked that the shape of the input variables is not significantly affected by such this pragmatic treatment. These studies are added in Appendix B.

Furthermore, since the ratio of the weighted signal to background events used for training is disproportionate, the signal ($t\bar{t}\gamma\gamma$) and the total background were scaled by applying appropriate sample weights such they are equally represented in the training.

Figure 6.17 shows the signal-background separation for 4 of the 19 variables which are used in the BDT, from the training dataset - photon conversion type of the leading photon, ΔR between lepton and leading and subleading photons and the invariant mass of lepton and the subleading photon. The plots show the separation power of these input variables of the BDT model, and the model is expected to have an aggregate separation better than all its input variables.

Choice of binning

The choice of binning used for an observable (BDT output in case of this analysis) can significantly impact the results. More bins provide higher resolution which allow for a finer distinction between

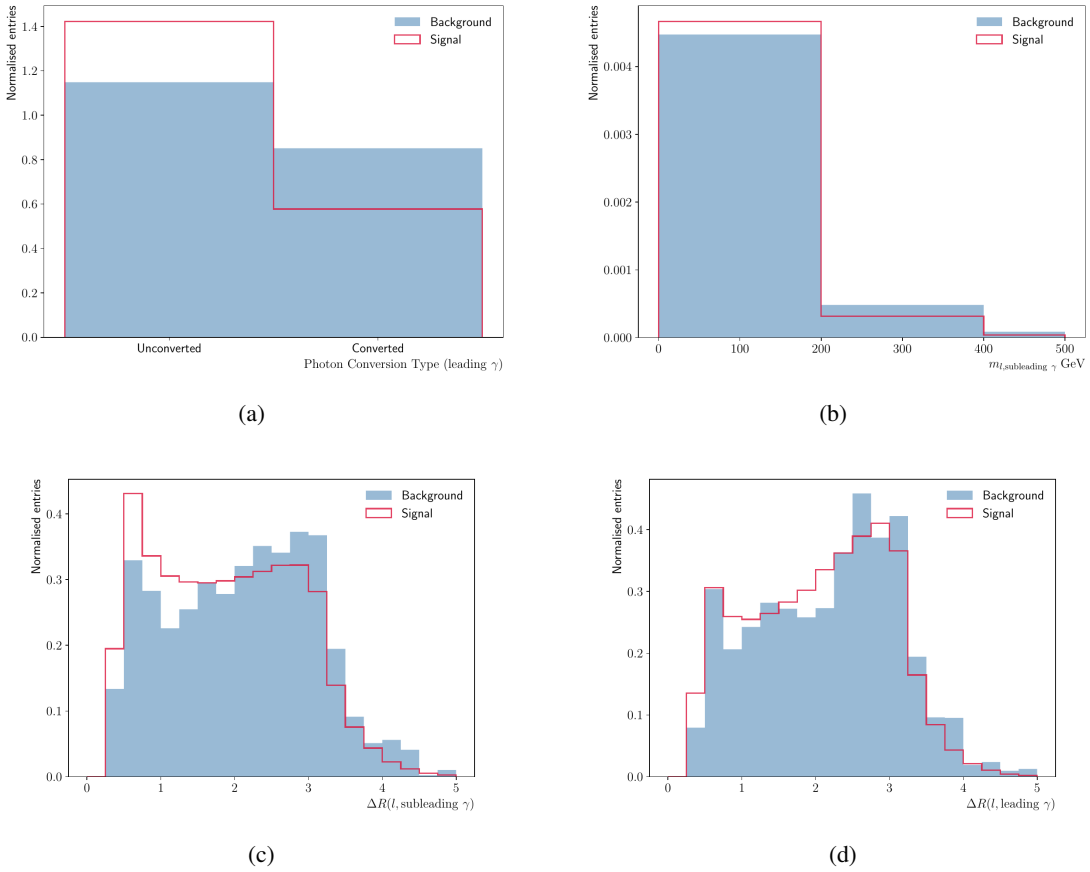

Figure 6.7: Signal-Background separation in 4 variables from the training dataset, as example.

signal and background distributions. However, they can also introduce greater statistical noise due to fewer entries per bin. Conversely, fewer bins may reduce resolution but improve stability and are often more characteristic of the data. Thus, optimised bin widths were obtained with an ALTAS-internal autobinning algorithm which enhances signal-to-background separation while ensuring smooth templates for even the small background contributions. The automatic binning algorithm scans the original distribution, starting from the bin with largest BDT output, and merges bins until a certain fraction of signal and background events is obtained [98]. This binning algorithm results in bins [0,0.4,0.6,1] for the BDT output. This same binning is used in the final fits performed on the BDT in Chapter 8.

6.4.4 Performance metrics of the BDT

This section shows the performance plots for the BDT model trained for signal-background separation. Figure 6.8(a) shows the separation of 6.07% between the signal and background with the 4 folds combined, and with the optimised binning as discussed in Section 6.4.3. A slightly larger separation of about 7.8% between signal and background is observed when using a finer binning of the BDT output, as shown in Figure 6.8(b). In this case, the distribution is divided into 10 bins instead of

fewer, which enhances the visual discrimination between the signal and background. It is crucial to note that this apparent increase in separation is artifact of the binning choice rather than an intrinsic improvement in BDT performance. The finer binning provides a higher-resolution view of the BDT's output, thereby highlighting more subtle differences in the distribution shapes. However, the true discrimination power of the BDT classifier is an integral property of the full distribution. Since binning inherently quantizes this continuous output, it can create a misleading impression of improved separation. This finer binning is therefore adopted for illustrative purposes only, to better visualize the classifier's ability to separate the two classes.

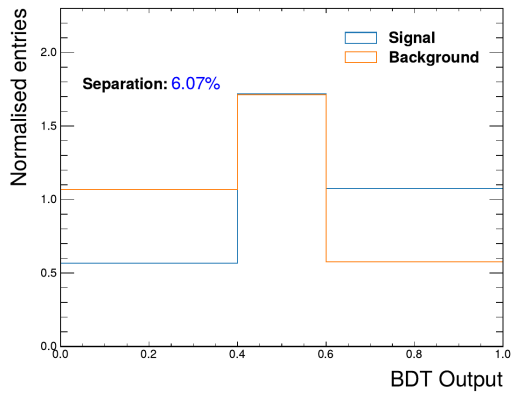

(a) BDT output from the training process, using binning as used in the fit.

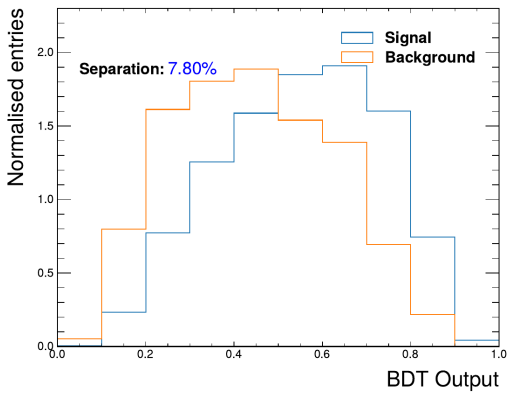

(b) BDT output from the training process, using uniform 10-bin binning.

Figure 6.8: BDT output distributions for the signal and background processes, combined over 4 folds.

The loss curves, as shown in Figure 6.9 per-fold, converge for both test and train sets, although there's some visible separation between them. This separation is expected as the model learns more of the larger set of signal events during the training than background events. Thus, the loss values converge better at lower values for the train sets. However, the overall convergence for both the training and testing sets are consistent across all the folds.

The Area Under the Receiver Operating Characteristic (ROC) curve (AUC) quantifies the BDT's overall performance by measuring the area beneath its curve. Figure 6.10 shows that AUC values for train and test sets are off by about 7-8%. The performance is still consistent for train and test sets individually over the 4 folds.

As mentioned earlier, XGBoost treats each cross-validation fold as a separate model fit problem, and thus, the importance of the input variables (features in the model) vary within folds. The feature importance can be evaluated based on how often and how effectively a feature is used in decision tree splits (based on metrics such as gini score, frequency of splits, etc.). The impact of the input variables used in the BDT can be seen in the feature importance ranking plot in Figure 6.11. The red line at 2% signifies that even though the least important features, such as the invariant mass of the two photons ($m_{\text{leading } \gamma \text{ subleading } \gamma}$), the p_T of the photons etc., contribute to only ~10% of the separation power compared to the most important feature such as the leading photon's conversion type, their combined effect is however significant.

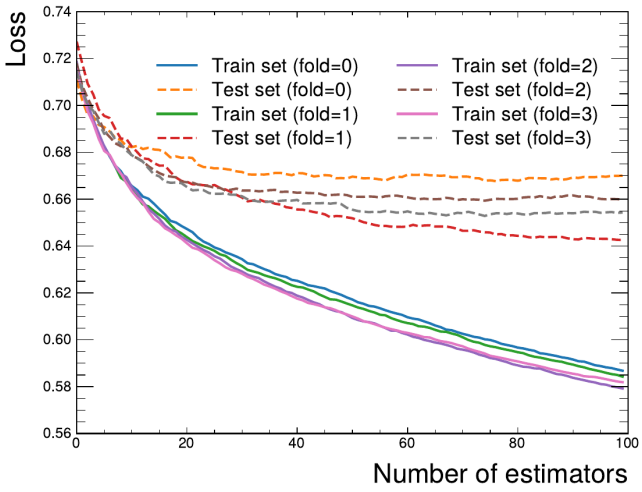

Figure 6.9: Loss curve per fold for the training and the testing sets over the 100 estimators used in the BDT.

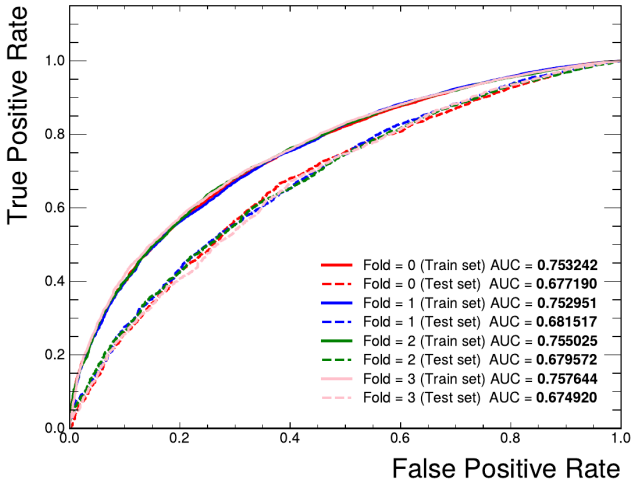

Figure 6.10: AUC score per fold for the training and the testing sets used in the BDT.

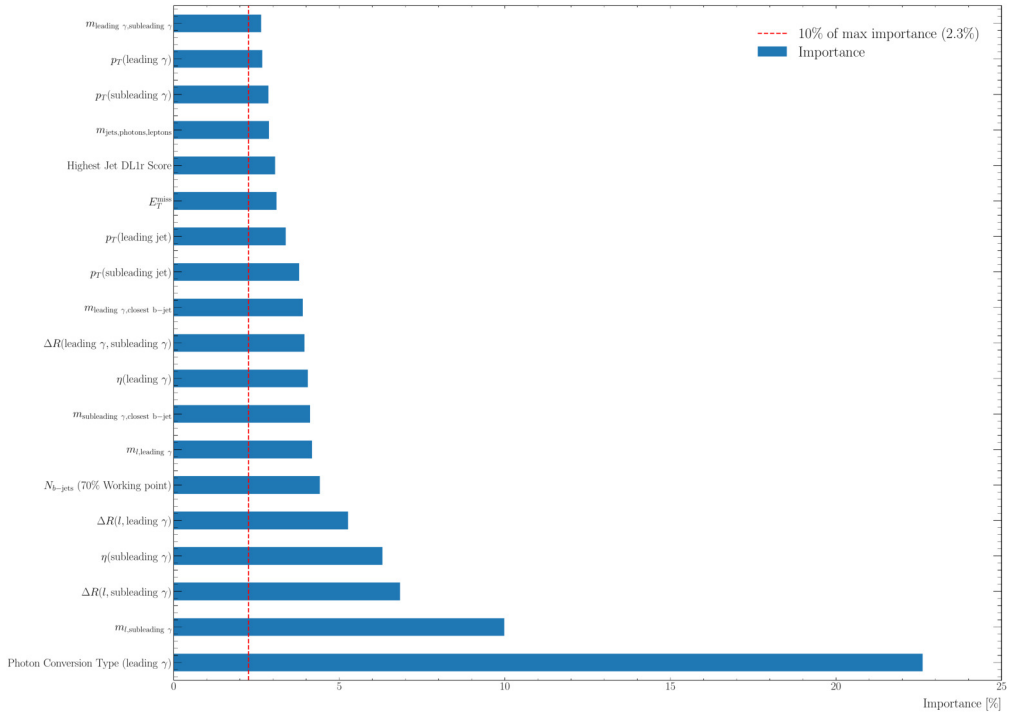

Figure 6.11: Importance ranking of input features used in the BDT (averaged over all 4 folds).

SHAP visualizations (illustrative only)

SHAP (SHapley Additive exPlanations) values are a way to explain individual predictions of any machine learning model [99]. They represent how much each feature contributes to pushing the model's output from an average prediction (baseline raw value) to the actual prediction for a specific instance. Basically, SHAP value of a feature demonstrates its magnitude (importance) and direction (whether that feature's value pushes the prediction higher or lower).

For illustrative purposes only, a subset of the total training dataset (1,000 events) are used to evaluate the inner workings of the BDT training and are discussed below. Firstly, figure 6.12 shows the beeswarm plots for the four folds of the BDT. A beeswarm plot for SHAP values generally shows how much each feature contributes to the model's prediction across many different data points. Each dot represents a single event, positioned horizontally by its SHAP value (its impact on the prediction from -1 to 1) and coloured by its original feature value - red for higher values of the variable, blue for the lower values (not to be confused with signal and background colour-coding). A feature's dots clustered around 0 means it usually has little impact, while a spread-out "swarm" indicates it has a strong and varied influence on predictions. From e.g., one can say that the lower values of $\Delta R(l, \text{leading } \gamma)$ tend to be more signal like. This is true when one sees the histogram in 6.7. If the value of $\Delta R(l, \text{leading } \gamma)$ is more, however, it means that event is more likely to be a background than signal. For the most important feature in the BDT, the leading photon's conversion type, this distinction is clear.

A SHAP decision plot helps visualize how individual model predictions are constructed for the trained events. These are shown for the initial 10 variables that the BDT encounters, and then all the 19 variables, in Figure 6.13. Each line on the plot represents a single event's prediction, beginning at the model's average prediction (the model's raw base value) and then cumulatively showing the positive or negative contribution of each feature's SHAP value, tracing the path to that event's final predicted output. One can see that 10 variables can only split events in range -1.5 to 1 of the raw model value. But most of the separation happens beyond these variables, which further spread the events over a range of -3 to 3. The leading photon conversion type (as shown in the bottom row in 6.13(b)) contributes the most to signal-background separation, as is also reflected in 6.11.

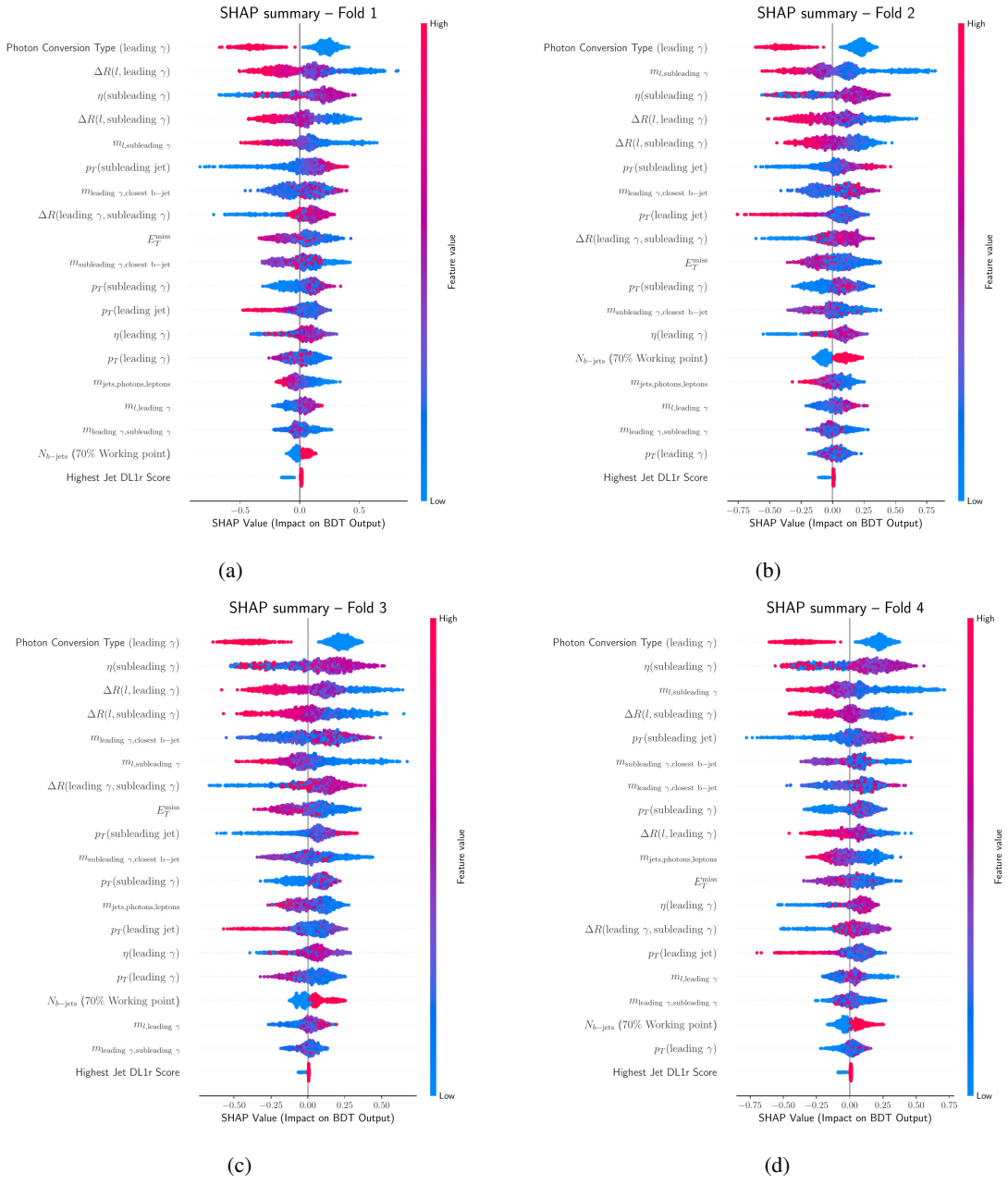

Figure 6.12: SHAP beeswarm plots illustrating the impact of features on the BDT output for each of the four model folds. The BDTs were trained on a subset of 1,000 events.



(a) 10 variables

(b) 19 variables

Figure 6.13: SHAP decision plot with (a) 10 and (b) 19 variables for a single fold (0) of the BDT.

χ^2 tests

To evaluate how well the final BDT scores of the training and testing data match with each other, the χ^2 tests were performed over the four folds. They essentially show how likely the training and testing dataset are drawn from the same underlying distribution. A χ^2 probability of 1 and around indicates a good agreement between train and test datasets, as can be seen in figure 6.14.

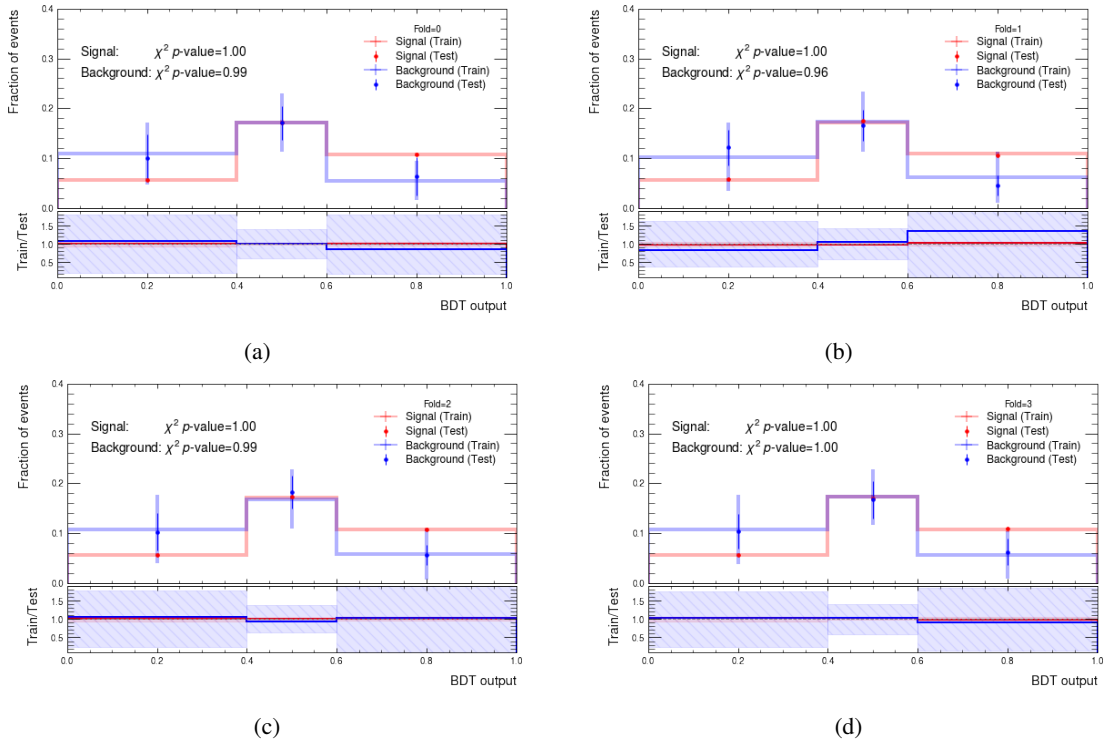

Figure 6.14: The results of the χ^2 test are given for signal and background simulations for the training and testing sets in bins used for fitting for the folds (a) 0, (b) 1, (c) 2, and (d) 3 of the BDT output.

6.4.5 Correlation matrices

To assess the modelling of the input features used in the BDT training, correlation matrices of the variables are studied for the signal, background, and for the data events. These plots provide a compact overview of how strongly pairs of variables are correlated, and allow one to visually compare whether the correlation patterns observed in simulation are consistent with those seen in data. In this analysis, the signal and background MC samples are combined to form the 'signal+background' prediction, which is then compared to the data distributions.

It should be noted that small differences between simulation and data are expected, partly due to the modified treatment of negative event weights in the NLO samples when constructing the correlation matrices. Since correlation coefficients require non-negative effective weights, absolute event weights are used for this purpose. The correlation plots are therefore not used for direct quantitative conclusions, but instead to illustrate the overall agreement in the structure of the input features. In general, the

signal and background show similar correlation patterns, and the differences with respect to the data are typically at the $O(10\%)$ level, consistent with statistical uncertainties. This indicates that the BDT output is not dominated by any single variable, but rather exploits the combined information from multiple inputs to achieve discrimination.

The correlation coefficients between the various input variables and the BDT score itself for the signal and background processes are shown in Figures 6.15 and 6.16. The correlation matrices are calculated such as to avoid divergences occurring from negative weights in the NLO samples.

Figure 6.17 highlights the difference in the correlation patterns between the signal and background distributions. From the figure, one can conclude that, with very few exceptions, the correlation values for signal and background distributions are pretty similar and the differences are mostly ∼10%. This suggests that discrimination between signal and background is distributed across multiple features rather than driven by a single strongly decorrelated variable. Given that the statistical uncertainties on the correlation values of data events are ∼10%, the differences between the correlation values for signal+background and data, shown in Figure 6.18, are in general below ∼10%, with few exceptions where the differences are up to 30% (e.g., the correlation among the invariant mass of subleading photon and closest b-jet and the p_T of leading jet.). This indicates that, in general, the overall correlations between the variables in the signal and background closely mirror the data. This is true in particular for the most discriminant variables.

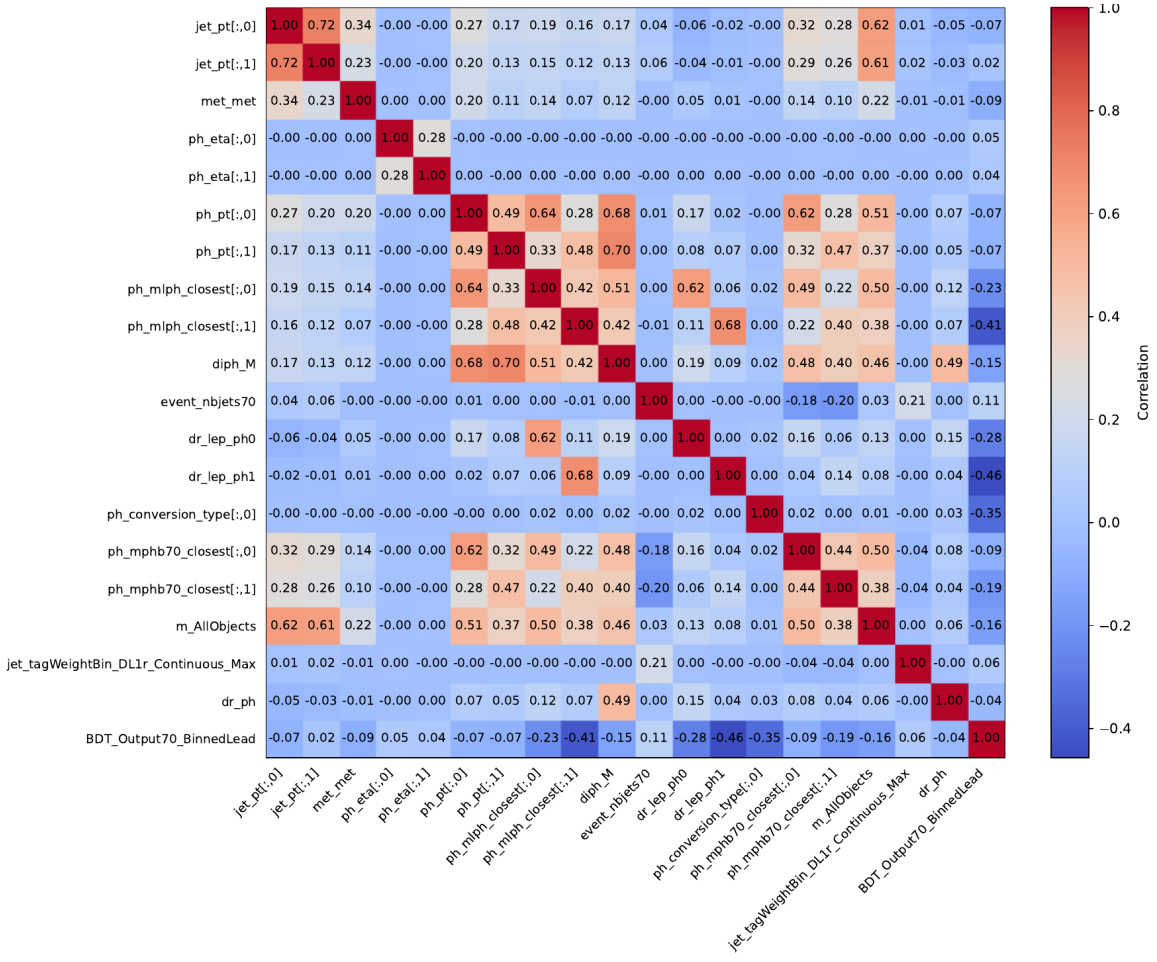

Figure 6.15: Correlation coefficients among the input variables and with the BDT score for the trained signal sample in the BDT.

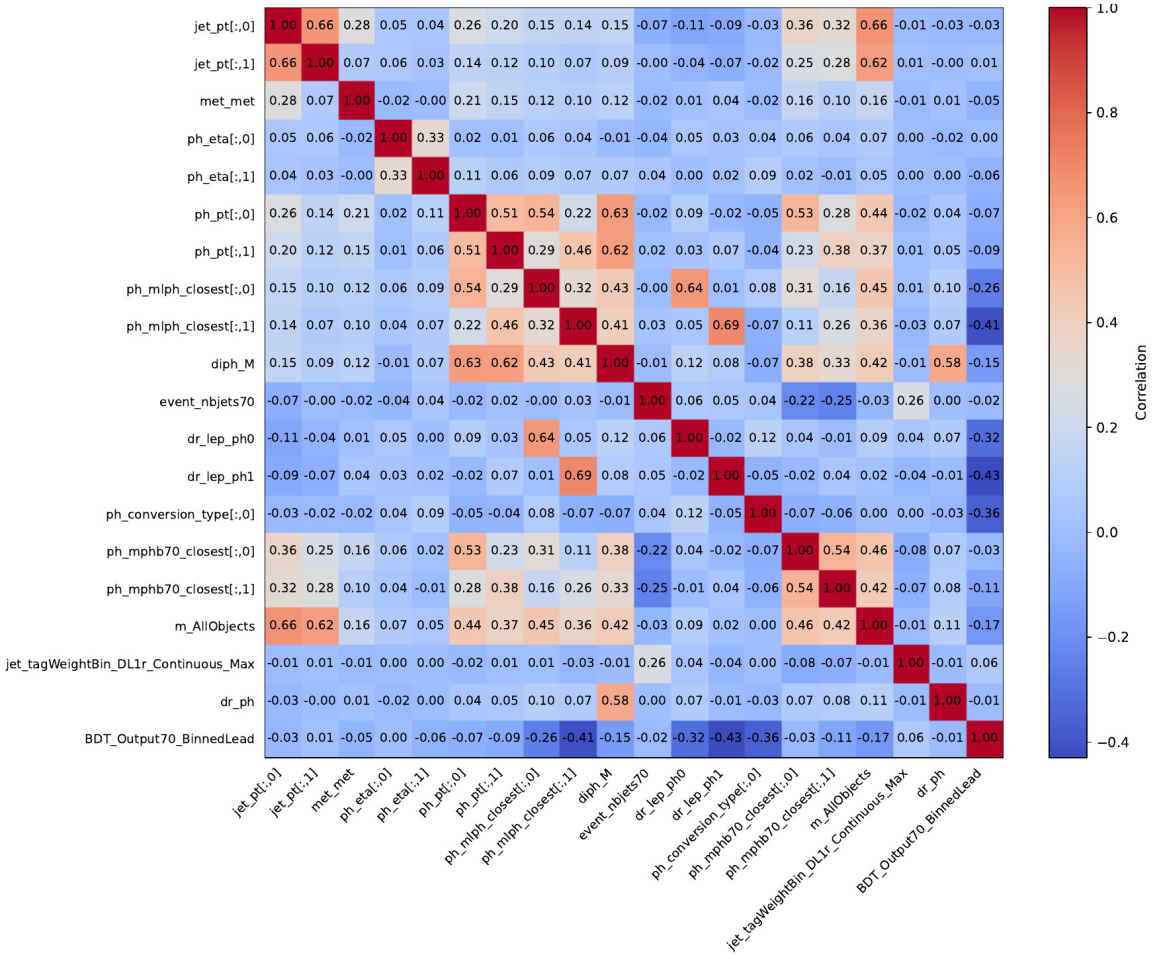

Figure 6.16: Correlation coefficients among the input variables and with the BDT score for the trained background samples in the BDT.

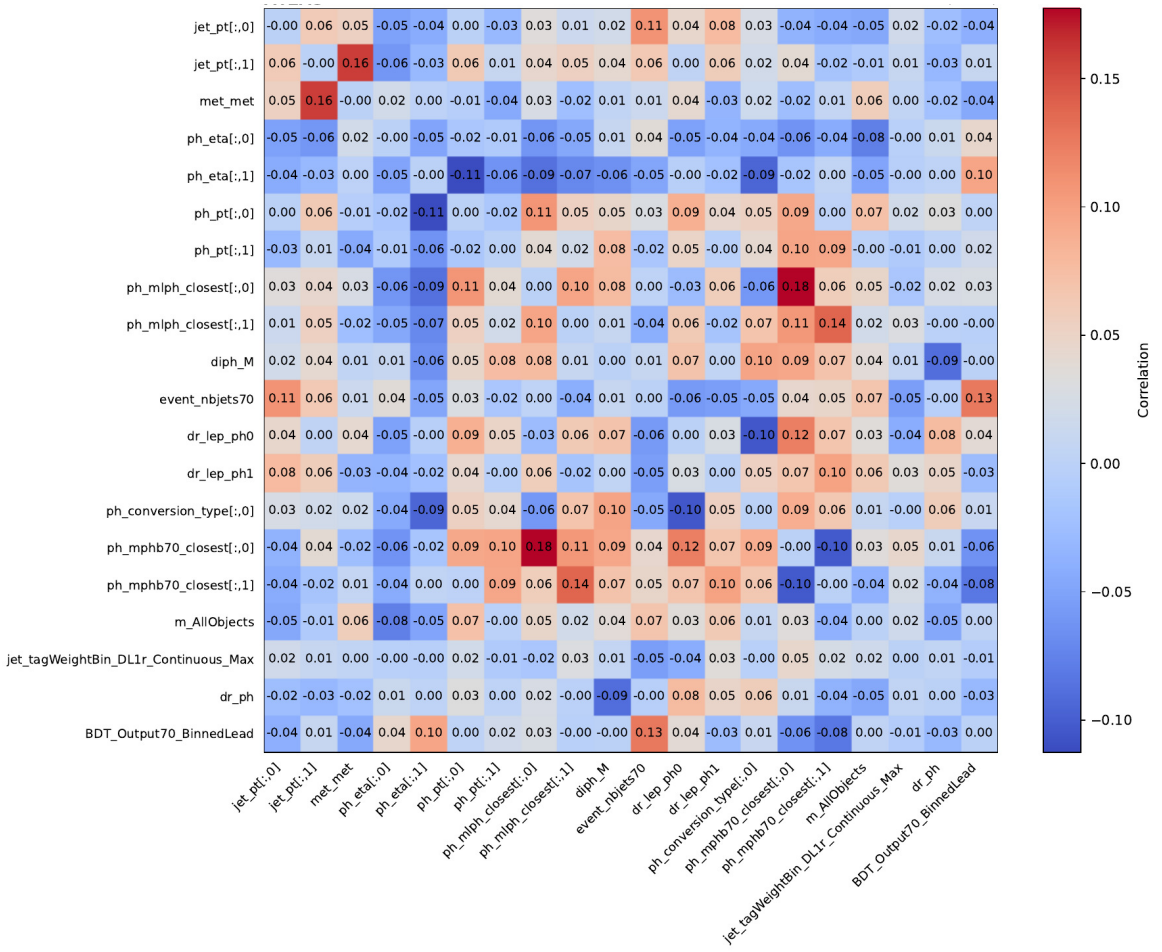

Figure 6.17: Correlation difference among the input variables and BDT scores between the trained signal and background samples in the BDT.

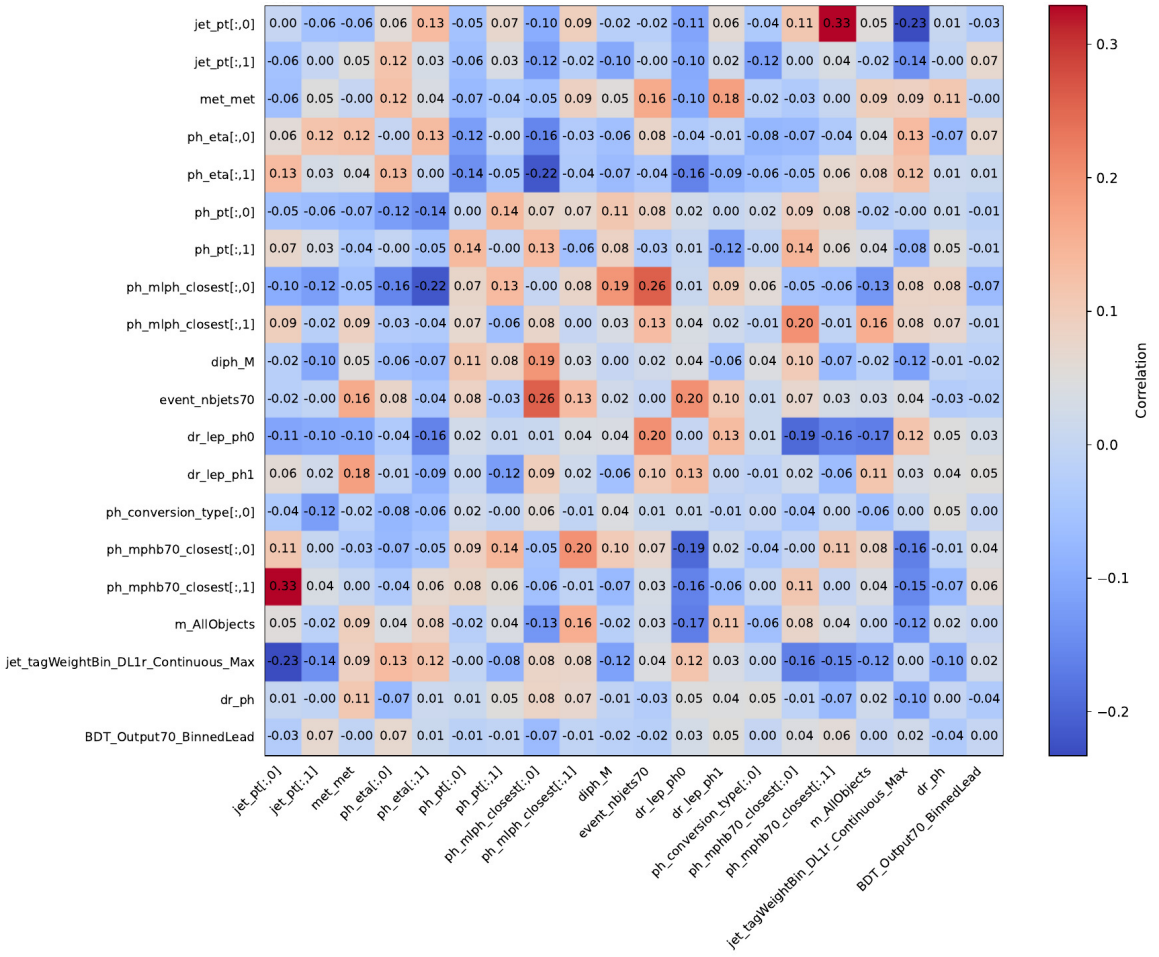

Figure 6.18: Correlation difference among the input variables and BDT scores between the trained signal-background samples and data.

Results of the BDT training

The BDT model described in the previous sections is also used to evaluate other background processes that are not included in the training. As the BDT is agnostic to these untrained processes, its output is derived solely from the learned classifications. For each event in these processes, a BDT score is evaluated using the *predict_proba* function [100] to get the final prediction of all the processes.

The full BDT output distribution, containing all the processes, included as categories, can thus be seen in Figure 6.19 (a). Once signal is laid over the background, the separation between signal and background becomes more evident, as seen in Figure 6.19 (b).

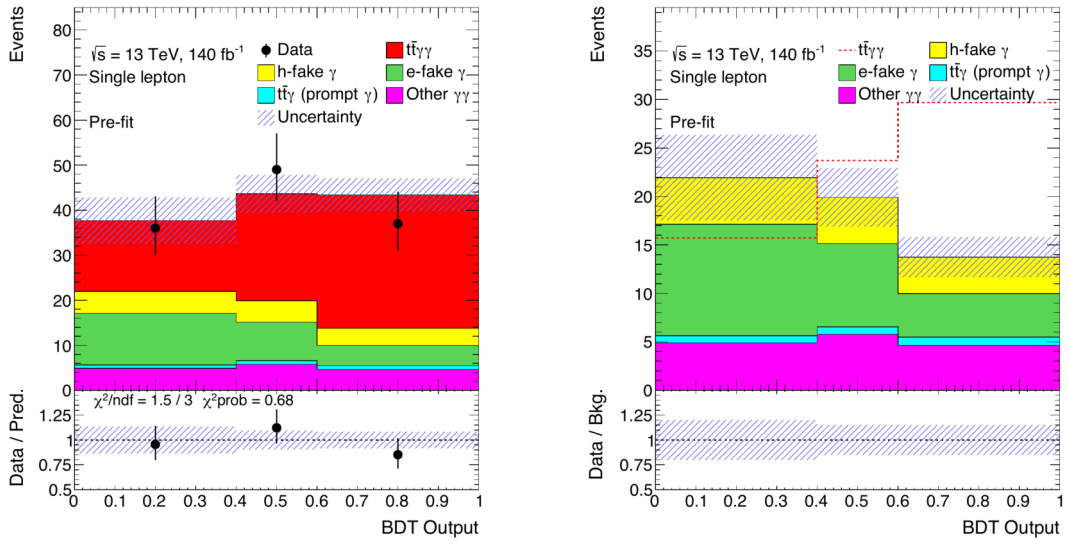

(a) (b)

Figure 6.19: BDT output distribution in simulation: (a) $t\bar{t}\gamma\gamma$ and all backgrounds are stacked, (b) the signal is normalised to the total number of background events and shown overlaid. The uncertainty band corresponds to the total pre-fit uncertainty in (a) and to the pre-fit uncertainties of the background samples in (b).

CHAPTER 7

Systematic uncertainties

"If a man will begin with certainties, he shall end in doubts;
but if he will be content to begin with doubts, he shall end in certainties."

— Francis Bacon, *Novum Organum* (1620)

Uncertainties are an inherent and unavoidable aspect of any measurement in experimental physics. For the results to be accurate, interpretative and reproducible, their proper quantification and propagation in the measurement performed in the analysis is essential. To that end, this chapter first gives a brief overview of the uncertainties in Section 7.1. Then the modelling uncertainties which arise from limitations of theoretical models used to simulate the MC events are described in Section 7.2. Section 7.3 describes the uncertainties arising from the experimental limitations of the ATLAS detector itself. The uncertainties which arise from the inaccuracy of the cross section measurements of the background processes in the analysis are included as normalisation uncertainties and discussed in Section 7.4. Section 7.5 talks about how the uncertainties arising from the estimation of fake photon backgrounds using data-driven methods are applied.

7.1 Overview of uncertainties

In collider-based analyses such as the one presented in this thesis, uncertainties generally fall into two broad categories: statistical uncertainties and systematic uncertainties.

Statistical uncertainties stem from the finite size of both data and simulated samples. As events in HEP occur stochastically, the observed count of events, N, in any given bin or selection region naturally fluctuates. For uncorrelated events, for instance, this count follows a Poisson distribution, for which the fundamental statistical uncertainty is directly proportional to the square root of the observed number:

$$\sigma_N = \sqrt{N}$$

This uncertainty reflects the sampling variability and its reduction is intrinsically tied to increasing the sample size, which experimentally means acquiring more integrated luminosity or simulating larger Monte Carlo events.

Systematic uncertainties, in contrast, are associated with imperfect knowledge or modelling of the detector, the reconstruction techniques used, and the theoretical predictions.

Broadly, systematic uncertainties in this analysis are categorized into three types: modelling uncertainties, experimental uncertainties, and cross-section (normalisation) uncertainties.

7.2 Modelling uncertainties

As has been mentioned in Chapter 4, MC simulations are used for modelling both signal and background processes in the analysis. However, these simulations rely on some theoretical choices and approximations, which introduce what are known as modelling uncertainties, which must be carefully estimated and propagated through the measurements performed. For the $t\bar{t}\gamma\gamma$ signal and the main contributing background processes to the analysis, namely $t\bar{t}\gamma$ production, $t\bar{t}\gamma$ decay, $t\bar{t}$ and $tW\gamma$, alternative generator scenarios are tested for the simulation. The differences between the nominal signal simulation and the alternative scenarios, normalised to the same fiducial cross section of the nominal simulation, are then used as systematic variations. In this way, the modelling variations impact mostly the shape of the fitted distribution with normalisation effect arising only from detector related acceptance and efficiencies. The modelling systematic uncertainties among processes ($t\bar{t}\gamma\gamma$, $t\bar{t}\gamma$ production and decay, $t\bar{t}$) are treated as uncorrelated. This follows the same treatment as in the $t\bar{t}\gamma$ measurement [1].

7.2.1 Renormalisation, factorisation and FSR scale uncertainties (μ_R, μ_F, and α_s)

These theoretical scales such as the renormalization (μ_R) and factorization scale (μ_F) determine the precision of the perturbative calculations within the MC generator. Uncertainties related to their choice are estimated by varying μ_R and μ_F independently by a factor of 2 and 0.5 relative to their nominal values. These variations are implemented by reweighting events within the $t\bar{t}\gamma\gamma$, $t\bar{t}\gamma$, $t\bar{t}$ and $tW\gamma$ MC samples.

Additionally, the strength of the strong force, governed by the strong coupling constant (α_s), is related to the renormalization scale. Variations in α_s, particularly affecting the emission of gluons in the final state (FSR), are assessed by variations in the μ_R scale, and similarly applied through event weights for the $t\bar{t}\gamma\gamma$ simulation.

7.2.2 Parton shower and hadronization model uncertainties

After the initial hard interaction, quarks and gluons evolve through the complex process of parton showering and hadronization, where they form observable hadrons. The models describing these phenomena (the parton shower and hadronization models) are phenomenological and introduce uncertainties. These uncertainties are generally estimated by comparing the predictions from the nominal MC samples (e.g., those using the Pythia8 parton shower) with alternative samples generated using a different parton shower and hadronization model (e.g., Herwig7). This comparison, thereby, includes the differences arising from the fundamental approach to simulating these non-perturbative effects. The PS are applied to $t\bar{t}\gamma\gamma$, $t\bar{t}\gamma$, $t\bar{t}$ and $tW\gamma$ simulations.

7.2.3 ISR uncertainties

The modelling of Initial-State Radiation (ISR) can vary between different generator tunes. Uncertainties associated with ISR are typically assessed by comparing the nominal MC samples with alternative

samples or by using specific event weights that represent scenarios with higher or lower amounts of initial-state radiation. These alternative scenarios often come from different tunes or configurations of the parton shower model. For the $t\bar{t}\gamma\gamma$, $t\bar{t}\gamma$ production, $t\bar{t}\gamma$ decay and $t\bar{t}$ simulations, this uncertainty is estimated by comparing the nominal samples with the *A14 var3c* eigentune of PYTHIA88 for low and high radiation scenarios.

7.2.4 Parton Distribution Function uncertainties

Parton Distribution Functions (PDFs) describe the probability of finding a specific type of parton carrying a certain fraction of the colliding proton's momentum at a given energy scale. Since PDFs are determined from global fits to experimental data and have intrinsic uncertainties, these uncertainties must be propagated to MC simulations as well.

This is done for the $t\bar{t}\gamma\gamma$, $t\bar{t}\gamma$ production and decay samples using the standardized PDF4LHC15 prescription [101]. This involves evaluating the nominal prediction alongside a set of 30 alternative PDF variations ("eigenvectors"). The uncertainty is quantified by comparing the results obtained with these PDF variations to the baseline prediction, using alternative MC generator weights for each PDF variation.

7.2.5 Hard gluon emission uncertainties

For some specific processes, such as $t\bar{t}$ production, the modelling of hard gluon emission can significantly impact the kinematics of the event. This is governed by parameters within the matrix-element generator itself (e.g., the 'hdamp' parameter in POWHEG). The uncertainty associated with this modelling choice is estimated by generating alternative sets of events where this parameter is varied (e.g., set to twice its nominal value). The results from these alternative samples are then compared to the nominal prediction.

7.3 Experimental uncertainties

In rare process searches, such as that of $t\bar{t}\gamma\gamma$, it's easy to realise that the measurements depend highly on reconstruction of the final state particles (leptons, photons, jets and $E_{\mathrm{T}}^{\mathrm{miss}}$). Therefore, it's important to take into account these experimental uncertainties that arise directly from the detector measurement itself. These arise from limitations in the reconstruction and identification of objects, uncertainties on the energy and momentum scales and resolutions, flavor tagging of the jets, measuremnt of integrated luminosity, and modelling of the pile-up events. Such uncertainties affect both the signal and background simulations by altering the event kinematics. The following subsections detail these uncertainty sources based on the reconstructed objects that serve as inputs to the analysis.

Lepton uncertainties

Electrons are reconstructed from ID tracks and energy deposits in EM calorimeter while muons are reconstructed using ID tracks and MS information. The MC simulations are corrected to describe the efficiency in data. Lepton *efficiency* refers to the reconstruction and identification efficiencies, isolation efficiency as well as the trigger efficiency. For MC samples, these efficiencies are corrected by applying scale factors, calculated as the ratio between the efficiencies measured in data and those in

simulation using the tag-and-probe method in $Z \to ee$ decays for electrons, as well as $Z \to \mu\mu$ decays for muons. These scale factors, which vary with $E_T^{\text{miss}}$and η, are varied up and down by one standard deviation to study the impact of lepton efficiency uncertainties on the analysis result [39, 102].

The measured lepton energy/momentum is calibrated using Monte-Carlo-based techniques. Correction factors, derived from the study of dileptonic decays of the Z boson, are applied to correct possible detector mis-modelling in the calibration. These correction factors, are varied up and down by one standard deviation to study the lepton energy (momentum) scale uncertainty. For electrons, the energy scale and resolution are calculated in conjunction with those of photons and are called e/γ scale and resolution.

Uncertainties on these corrections are propagated to the analysis by creating varied templates.

Photon uncertainties

Photons are reconstructed from the energy deposits in the EM calorimeter. The identification of prompt photons in the dense hadronic environment such as that in LHC is challenging because of the presence of the overwhelming amount of non-prompt photons from hadron decays. Photons are identified with certain selection criteria on the shape and properties of the electromagnetic showers and also by requiring them to be isolated from other particles. These techniques come with some efficiencies as well, which are corrected in the MC simulatiosn to better describe the data. The scale factor for the photon ID efficiency is derived from three measurements: the radiative Z boson method using a sample enriched in events with radiative Z boson decays, the electron extrapolation technique using a sample enriched in $Z \to ee$ events where the similarity between electrons and photons in the detector is exploited, and the matrix method using a sample enriched with isolated, high-p_{T} photons and exploiting that the narrow-strip variables are only weakly correlated to the isolation. The scale factor is computed as the ratio of the efficiency measured in data and that determined in simulation. The sets of scale factors of all measurements are combined into one single set that is applied to simulation to correct for deviations between efficiencies measured in data and found in simulation. The scale factors for photon isolation were measured in Ref. [103]. These scale factors are varied up and down by one standard deviation to study their impact on the analysis. The photon energy calibration and the study of its scale and resolution uncertainties are calculated together with the electrons as e/γ scale and resolution.

Uncertainties on these corrections are also propagated to the analysis by creating varied templates.

Jet uncertainties

The uncertainties come mainly from the jet energy scale, resolution and jet vertex tagging.

The jet energy calibration, called jet energy scale (JES), used in this analysis has a total of 30 nuisance parameter components [43, 104]. The calibration of this uncertainty is done in several steps, combining MC simulation and *in situ* measurements, to correct for pile-up, jet flavour composition, single-particle response, and effects of jets not contained within the calorimeter. Its uncertainty is split into several independent categories: modelling and statistical uncertainties on the extrapolation of the jet calibration from the central region, jet flavour composition, high-p_{T} jet behaviour, b-jet energy scale uncertainties, uncertainties due to pile-up, uncertainties on *in situ* jet energy corrections, etc. In one category, there are usually more than one physical source of the uncertainty. To study the JES uncertainty, each source is varied up and down independently by its corresponding uncertainty.

The jet energy resolution (JER) is measured using the balance between jets and well measured objects like photons or Z bosons. There are a total of seven effective nuisance parameters associated to JER in the category reduction scheme, and a single source of uncertainty for the agreement between data and Monte Carlo, all of which are varied by one sigma to study their impact on the analysis.

The systematic uncertainty associated with the JVT discriminant for pile-up jet rejection is obtained by varying the efficiency correction factors [44].

b-tagging uncertainties

The uncertainties in the b-tagging calibration are determined separately for b-jets, c-jets, and light-flavor jets. These uncertainties account for the challenge of distinguishing b-quarks from other jet types, and are quantified by varying calibration scale factors. For each jet category, the uncertainties are decomposed into several uncorrelated components using the eigenvector method, resulting in a number of nuisance parameters (e.g., 45 for b-jets and 20 for c-jets and light-flavor jets each) [45]. Additionally, a 50% normalization uncertainty is applied to events containing high-p_T jets that exceed the calibration limits for b-tagging.

Missing Transverse Momentum uncertainties

The uncertainty in missing transverse momentum ($E_{\mathrm{T}}^{\mathrm{miss}}$) primarily arises from the propagation of uncertainties in the energy and momentum scales and resolutions of all reconstructed objects (electrons, muons, photons, and jets). An additional contribution to the $E_{\mathrm{T}}^{\mathrm{miss}}$ systematic uncertainty comes from the modeling of its soft terms, which account for unclustered energy deposits. The scale and resolution of these soft terms are assessed by comparing data and simulation, and these uncertainties are propagated to the analysis.

Pile-up uncertainties

The uncertainty arising from the modeling of pile-up (additional proton-proton interactions) is determined by varying the pile-up reweighting applied to correct the MC simulation to better describe the data [105]. This uncertainty is based on the disagreement between the instantaneous luminosity in data and simulation.

Luminosity uncertainties

As quoted in Section 5, the total integrated luminosity has an uncertainty of ±0.83 %, which impacts the normalisation of all simulated templates [86].

7.4 Background uncertainties

Theoretical predictions of cross sections often have inherent limitations or incomplete higher-order calculations, meaning their absolute magnitudes are not known perfectly, even if their kinematic distributions are well-modeled. These uncertainties are considered for all the processes except for the signal, for which the normalization is measured from the data. A normalisation uncertainty of 7% is considered for the $t\bar{t}\gamma$ decay, which is based on the measured uncertainty of the $t\bar{t}\gamma$ decay

process from the latest $t\bar{t}\gamma$ cross-section analysis [1]. Similarly, for the $t\bar{t}\gamma$ production process, a normalisation uncertainty of 7% is considered based on the measured uncertainty of the cross section of that process. A 6% normalisation uncertainty is assigned for $t\bar{t}$ [79], which corresponds to the uncertainty of the NNLO in perturbative QCD,and a 10% uncertainty is assigned to the $t\bar{t}H$ process based on the calculations from Ref. [106], corresponding to an NLO QCD+EWK calculation. For $W/Z\gamma\gamma$ and $W/Z\gamma$ events, a 50% normalisation uncertainty is assigned based on certain conservative estimates [107] [23]. For the minor background processes (single top quark (t- and s- channel), $t\bar{t}V$, $W/Z+$jets, $Wt\gamma$ and diboson processes), a conservative 50% uncertainty is assigned as well, matching the uncertainties assigned in the $t\bar{t}\gamma$ measurement [1].

7.5 Data-driven fake estimate uncertainties

For the backgrounds estimated with data driven methods, i.e., electron fakes and hadron fakes, apart from all the experimental uncertainties, the corresponding uncertainties of the SFs are considered separately in the measurements presented in this analysis. A detailed description of the extraction of these SF uncertainties can be found in Ref. [107].

CHAPTER 8

Measurement of the $t\bar{t}\gamma\gamma$ cross section

"With four parameters I can fit an elephant, and with five I can make him wiggle his trunk."

— John von Neumann, *Los Alamos Report* (1955)

The measurement of the $t\bar{t}\gamma\gamma$ cross section is presented in this chaper. First, the fiducial phase space at particle level in which the measurements are performed is defined in Section 8.1. The definitions of likelihood and profile likehood fit used to extract the strength of the signal $t\bar{t}\gamma\gamma$ process are presented in Section 8.2. The cross section of the $t\bar{t}\gamma\gamma$ process is defined in the context of the analysis in Section 8.3, along with the treatment of systematic uncertainties in the fit. Next, the fits performed with pseudodata to extract the signal strength of the $t\bar{t}\gamma\gamma$ process in the single-lepton decay channel are presented in Section 8.4. Finally, the results with fit to the actual data, along with the final measurements of the cross section are presented in Section 8.5. The fit results with data yield a significance of 5.2 σ which constitutes the first observation of the $t\bar{t}\gamma\gamma$ process.

8.1 Fiducial phase space at particle level

The measurements are performed at the particle level in a fiducial (*Latin: fiducia*, which means reliable) phase space. Particle level refers to the state where final state, stable particles have undergone respective decays, parton showering and hadronization but haven't interacted with the detector yet. This, essentially, means that the true, underlying properties of the stable particles are preserved before their interaction with detector material at detector (or reconstruction) level. The fiducial region is defined such that it closely follows the kinematic requirements at the reconstruction level (as described in Section 5.4). The region is defined with the particle level objects as follows:

- **Photons:** The photons should not originate from the hadron decay and must fulfill $p_T > 20\,\text{GeV}$ and $|\eta| < 2.37$. Additionally, they must be isolated such that the sum of transverse momenta of all charged particles surrounding the photon within $\Delta R \leq 0.2$ must be smaller than 5% of their own p_{T}.
- **Leptons:** Electrons and muons are selected "dressed" with nearby photons within a $\Delta R < 0.1$ cone around the lepton (excluding photons originating from hadron decays). Leptons are required to have $p_{\text{T}} > 25$ GeV and $|\eta| < 2.5$, and should not originate from hadron decays.

- **Jets:** Jets are clustered using the anti-kt algorithm with a radius of R=0.4, with $p_{\mathrm{T}} > 25$ GeV and $|\eta| < 2.5$. Non-interacting particles and muons are not considered in this clustering.
- ***b*-jets:** A jet is identified as a b-jet if it is associated with a hadron (with $p_T > 5$ GeV) containing a b-quark. The association is done using the ghost-matching [108] procedure, where simulated b-hadrons are added to the jet clustering as "ghost" particles with infinitesimal momentum to uniquely associate a reconstructed jet with its true b-quark origin.
- An overlap removal procedure among the objects is further performed:
  - If a muon or an electron is within $\Delta R(\mu, j) \leq 0.4$ of a jet, the muon or the electron is removed.
  - If there is a photon within $\Delta R(j, \gamma) \leq 0.4$ of a jet, the jet is removed.
  - Events are additionally required to satisfy $\Delta R(\gamma, \ell) > 0.4$ and $\Delta R(\gamma, \gamma) > 0.4$, where ℓ is the electron or muon.

The fiducial phase space is defined by requiring exactly two photons, exactly one electron or muon, at least four jets, among which at least one is a b-jet. Events are rejected if there are additional leptons with $p_{\mathrm{T}} > 7$ GeV.

8.2 Likelihood Function

A likelihood function quantifies how well a statistical model, given some specific parameter values, explains the observed data. It is essentially the probability of observing the data, given those parameters, viewed as a function of the parameters themselves. This makes the likelihood function an essential cornerstone of any statistical inferences drived from the measurements. It quantifies the probability of observing the data under a given model, as in the analysis presented, and is used extensively in parameter estimation, hypothesis testing, and setting confidence intervals.

8.2.1 The Likelihood function

Given a dataset $\mathcal{D} = \{x_1, x_2, \ldots, x_n\}$ consisting of n observed events and a statistical model characterized by a set of parameters $\boldsymbol{\theta}$, the likelihood function $\mathcal{L}(\boldsymbol{\theta})$ is defined as:

$$\mathcal{L}(\boldsymbol{\theta}) = P(\mathcal{D} \mid \boldsymbol{\theta}) = \prod_{i=1}^{n} f(x_i \mid \boldsymbol{\theta}), \tag{8.1}$$

where $f(x_i \mid \boldsymbol{\theta})$ is the probability density function (PDF) of the discrete data. In practice, for binned analyses, the likelihood is often modelled as a product of Poisson probabilities for each bin i:

$$\mathcal{L}(\boldsymbol{\mu}, \boldsymbol{\theta}) = \prod_{i=1}^{N_{\text{bins}}} \frac{(\nu_i(\boldsymbol{\mu}, \boldsymbol{\theta}))^{n_i}}{n_i!} e^{-\nu_i(\boldsymbol{\mu}, \boldsymbol{\theta})}, \tag{8.2}$$

where:

- n_i is the observed number of events in bin i,

- $\nu_i(\boldsymbol{\mu}, \boldsymbol{\theta})$ is the predicted number of events in bin i,
- $\boldsymbol{\mu}$ is the parameter of interest (e.g. signal strength),
- $\boldsymbol{\theta}$ represents nuisance parameters (NPs) encoding systematic uncertainties.

8.2.2 Profile Likelihood Function

The *Profile Likelihood Fit* (PLF) is a method used to estimate the value of a parameter of interest (POI), μ, while simultaneously accounting for the effect of nuisance parameters (NPs), $\boldsymbol{\theta}$. This is achieved by constructing the profile likelihood function:

$$\mathcal{L}_{\text{profile}}(\mu) = \mathcal{L}(\mu, \hat{\hat{\boldsymbol{\theta}}}(\mu)), \tag{8.3}$$

where $\hat{\hat{\boldsymbol{\theta}}}(\mu)$ are the values of the nuisance parameters that maximize the likelihood for a fixed value of μ:

$$\hat{\hat{\boldsymbol{\theta}}}(\mu) = \arg\max_{\boldsymbol{\theta}} \mathcal{L}(\mu, \boldsymbol{\theta}). \tag{8.4}$$

The role of profiling is crucial in this analysis. By adjusting the $\boldsymbol{\theta}$ for each hypothesized value of μ, one effectively "absorbs" the impact of systematic uncertainties, thus reducing their influence on the parameter estimate. This leads to a more robust and interpretable inference of the measurement. The maximization over NPs effectively profiles them out, leaving a function of the POI(s) only.

In practical implementations such as `HistFactory` [109], each NP can be constrained by auxiliary measurements or modelled with Gaussian priors, resulting in a composite likelihood that includes both signal and control regions. Maximization is then performed over the full parameter space, with profiling applied to extract the POI, which is the signal strength of the $t\bar{t}\gamma\gamma$ process in this analysis.

8.3 Cross section definition and profile likelihood fit

The fiducial $t\bar{t}\gamma\gamma$ cross section is extracted using a profile likelihood fit to the observable of the BDT (BDT output) in the analysis, as briefly discussed below. As mentioned before, the cross section is measured at particle level, which ensures that the measurement is not affected by the detector and can be compared with future theoretical calculations and data from future experiments. One essentially needs to bridge this gap from reconstruction level to the true, underlying physics at the particle level. This is achieved by first extracting a signal strength, μ, from the fit to observed data at the reconstruction level, and then translating this into a particle level cross section using well-defined correction factors.

Briefly put, the steps involved are:

1. A fiducial phase space is defined in which the measurement is performed, which is discussed in Section 8.1.

2. Expected signal and background events are fitted via PLF to observed data at reconstruction level. This fit yields μ, essentially defined as the ratio of observed and expected number of signal

events and scales the nominal signal prediction:

$$\mu = \frac{\sigma^{\text{observed}}}{\sigma^{\text{expected}}}. \tag{8.5}$$

3. Proper correction factors are calculated from the number of events in both, reconstruction and particle levels, and the cross section is evaluated at particle level as $\sigma^{\text{LO,fiducial}}$ from the number of events in the defined fiducial phase space.

4. The observed cross section is then measured using the particle level cross section scaled with μ and the K-factor$^{\text{NLO/LO}}$ (to account for proper scaling of the $t\bar{t}\gamma\gamma$ LO cross section prediction to NLO accuracy) as:
$\sigma_{\text{observed}} = \mu \times \text{K-factor}^{\text{NLO/LO}} \times \sigma^{\text{LO,fiducial}}$.

The above steps in context of the analysis are discussed in more detail below.

The likelihood function is defined from the product over all bins of the BDT distribution in the signal region of the fiducial phase space as:

$$\mathcal{L} = \prod_i P(N_i^{\text{obs}} \mid N_i^s(\vec{\theta}) + \textstyle\sum_b N_i^b(\vec{\theta})) \times \displaystyle\prod_t G(0 \mid \theta_t, 1)\,,$$

where N_i^{obs}, N_i^s, and N_i^b are the observed number of events in data, the predicted number of signal events, and the estimated number of background events in bin i of the corresponding distributions, respectively. They combine to form a Poisson term P in a bin. The NP θ_t is used to parameterise a systematic uncertainty t, which is constrained by a Gaussian $G(0|\theta_t, 1)$ in such a way, that when it changes from 0 to ± 1, the quantities affected by this variation in the likelihood change by $\pm 1\sigma$. The collection of all systematic uncertainties is denoted as $\vec{\theta}$. For systematic uncertainties related to the finite number of MC events, the Gaussian terms in the likelihood are replaced by Poisson terms. Each systematic uncertainty affects N_i^s and N_i^b in each bin of the fitted BDT distribution.

The MC-predicted cross section, $\sigma^{\text{LO}}_{t\bar{t}\gamma\gamma}$, is evaluated at particle level in the fiducial phase space as:

$$\sigma^{\text{LO}}_{t\bar{t}\gamma\gamma} = \frac{N_i^s}{L},$$

where N_i^s are the number of $t\bar{t}\gamma\gamma$ particle level events in the fiducial phase space and L is the total integrated luminosity, 140.1 fb^{-1}.

The cross section in the fiducial phase space at particle level, $\sigma_{t\bar{t}\gamma\gamma}$, can then be evaluated as:

$$\sigma_{t\bar{t}\gamma\gamma} = \mu \times \text{K-factor}^{\text{NLO/LO}} \times \sigma^{\text{LO}}_{t\bar{t}\gamma\gamma} \tag{8.6}$$

where the K-factor$_{\text{NLO/LO}}$ is defined as $\sigma^{\text{NLO, fid}}_{t\bar{t}\gamma\gamma}/\sigma^{\text{LO, fid}}_{t\bar{t}\gamma\gamma}$, with a value of 1.7, as discussed in Section 4.6.1.

The fits in the analysis are performed using the TRExFitter framework [110], which is internally available for ATLAS members only. It is a framework for binned template profile likelihood fits. The choice of binning used in the fit is mentioned in Section 6.4.3.

TrexFitter utilizes the HistFactory formalism [109] to define binned likelihood models. The inherent

HistFactory framework constructs the statistical models from histograms of signal, background, and systematic uncertainties. The model specifications are then translated into a RooFit `RooWorkspace`, containing the full PDF and its parameters. Subsequently, RooStats [111] is used to perform statistical procedures, which include maximizing the likelihood for best-fit parameter values and their uncertainties, performed by scanning over the likelihood values as a function of μ.

Likelihood scan for μ

The signal strength, μ, and its uncertainty are estimated by maximizing the likelihood, or more precisely, by minimizing the negative log-likelihood (NLL), defined as

$$\mathrm{NLL}(\mu, \boldsymbol{\theta}) = -\ln L(\mu, \boldsymbol{\theta}),$$

where $\boldsymbol{\theta}$ are the NPs. This minimization is performed using the `Minuit2` framework [112], using the `MIGRAD` and `MINOS` algorithms.

The likelihood is profiled over all NPs to obtain the profiled NLL,

$$\mathrm{NLL}_{\mathrm{profiled}}(\mu) = -\ln L(\mu, \hat{\hat{\boldsymbol{\theta}}}(\mu)),$$

with $\hat{\hat{\boldsymbol{\theta}}}(\mu)$ being the conditional minimum. The 1σ uncertainty on μ is given by the interval where $\Delta\mathrm{NLL}(\mu) = 0.5$, with $\Delta\mathrm{NLL}(\mu) = \mathrm{NLL}_{\mathrm{profiled}}(\mu) - \mathrm{NLL}_{\mathrm{min}}$. The statistical and systematic uncertainties can be added in quadrature to derive the total uncertainty:

$$\Delta_{\mathrm{tot}} = \sqrt{(\Delta_{\mathrm{stat}})^2 + (\Delta_{\mathrm{syst}})^2} \tag{8.7}$$

where:

- Δ_{tot} is the total uncertainty on the POI,
- Δ_{stat} is the statistical uncertainty, and
- Δ_{syst} is the systematic uncertainty.

However, the breakdown of uncertainties presented in the subsequent sections are evaluated using a covariance matrix breakdown approach, where the total systematic uncertainty is evaluated first, and then subtracted (in quadrature) from the total uncertainty to get the statistical uncertainty.

Finally, the significance of the POI (μ) is extracted from the test statistic $q_0 = -2\Delta\mathrm{NLL}(\mu = 0)$ and converted to a p-value and a corresponding standard deviation Z using the asymptotic approximation [113].

8.3.1 Treatment of systematic uncertainties in the fit

Various sources of systematic uncertainties, which impact the measurement, require careful treatment before being included in the statistical analysis. The impact of the systematic uncertainties on the measurement are implemented as varied templates with respect to the nominal predictions from the MC simulations. In general, each systematic source is encoded as an NP in the fit, with corresponding 'up' and 'down' variations derived from the simulations, allowing the fit to account for its impact on the measurement. Some key procedures applied to these uncertainties to make the fit more robust are smoothing, symmetrisation and pruning, described below.

Smoothing

Some systematic uncertainties can be affected by the statistical fluctuations where bin-to-bin migration of some events can happen or where the variation leads to a difference in the selected events due to changes in the object kinematics. This can lead to fit convergence issues during the fit or strange pulls or constraints on the NPs. The smoothing technique is used for such uncertainties to reduce the impact of statistical fluctuations in the template to be fit.

Symmetrisation

Systematic uncertainties often come with "up" and "down" variations from the nominal prediction of the expected number of events, which may not be symmetrical. Symmetrisation, effectively, adjusts these variations to be symmetric around the nominal value, simplifying their use in statistical fit. The variations of the systematic uncertainties in the analysis are symmetrised by taking half the difference between the upward and downward variations as the uncertainty. If both variations have the same sign, the average of the difference between each variation and the nominal value is chosen as a "two-sided" uncertainty. If only one variation is available (e.g. the PDF uncertainties), the difference between the nominal and varied prediction is taken as the size of the uncertainty.

Pruning

Pruning is a procedure to remove systematic uncertainties with a negligible impact on the analysis. This improves the stability and speed of the statistical fit by reducing the number of parameters. The decision to prune is made independently for an uncertainty's impact on the normalization (overall event count) and its effect on the shape of distributions. For example, if an uncertainty's effect on normalization is below a set threshold (e.g., 0.1%), that component can be pruned. Similarly, if its effect on the shape of any distribution bin is below the threshold, that shape component can be pruned. This ensures that only uncertainties with a meaningful impact are included in the final fit. For the measurements performed, a pruning threshold of 0.1%, both for normalisation and shape, was chosen, same as in the $t\bar{t}\gamma$ analysis [1]. The fit setup was, however, checked with other pruning thresholds of 0.05% and 0.2% as well with no overall impact on the signal strength of the measurements by such choices.

8.3.2 Treatment for modelling uncertainties

For the modelling uncertainties of the $t\bar{t}\gamma\gamma$ signal sample, which includes the $t\bar{t}\gamma\gamma$ PS (Herwig7), μ_R, μ_F, FSR (α_s) scales and *A14 var3c* eigentune of Pythia8 variation, the varied samples need to be normalised to the same fiducial cross section as with the nominal Pythia8 sample. This defines these modelling variations as shape-only uncertainties in the statistical model, such that only distortions in the distributions of the observables are propagated. The overall signal normalisation is parametrised separately (via the signal strength parameter μ), and therefore any rate change from the generator variations is removed to avoid double-counting between modelling effects and the normalisation component.

As a result, the resulting uncertainty templates differ from the nominal prediction only in their differential behaviour within the same fiducial phase space, ensuring a consistent comparison. Technically, this is done by reweighting the templates by the ratio of the number of events in the fiducial

phase space at particle level $N_{fid}^{nominal}/N_{fid}^{varied}$ to absorb the effects of normalisation. Both values are obtained using the same total cross section (i.e. the same event normalisation) and the corresponding (nominal or varied) MC event weights, so that the ratio used for correcting these variations de facto account for the differences in acceptance from full phase space of generator level to fiducial phase space. The correction factors used to scale the $t\bar{t}\gamma\gamma$ modelling templates are shown in table 8.1.

Table 8.1: Factor used to scale the varied templates, $N_{fid}^{nominal}/N_{fid}^{varied}$, for the different modelling uncertainties.

Systematic uncertainty	Acceptance correction
Alternative sample	
HERWIG7	1.078
Nominal sample with varied weights	
$t\bar{t}\gamma\gamma$ FSR up	0.985
$t\bar{t}\gamma\gamma$ FSR down	1.027
$t\bar{t}\gamma\gamma$ var3c up	0.975
$t\bar{t}\gamma\gamma$ var3c down	1.025
μ_F up	1.008
μ_F down	0.990
μ_R up	0.996
μ_R down	1.005

8.4 Test of fit setup with Asimov data

To test the expected sensitivity and the stability of the fit model, the measurement is first performed using Asimov (pseudo) data. The Asimov data is a synthetic dataset where each bin's event count is set to the exact expected number of events from the MC simulations, used to determine the sensitivity of the search for the $t\bar{t}\gamma\gamma$ process.

The Asimov fit is performed on the BDT output considering one parameter of interest (POI) corresponding to the signal $t\bar{t}\gamma\gamma$ contribution, defined as μ. All the sources of systematic uncertainties are included as nuisance parameters (NPs) in the fit.

The fit determines the $t\bar{t}\gamma\gamma$ signal strength as 1, as it should be in the case of an Asimov fit, given the fit is performed to the same number of events. The number of events, thus, remain the same before and after the fit. The total expected uncertainty on the $t\bar{t}\gamma\gamma$ signal strength is found to be $^{+23\%}_{-21\%}$ from the Asimov fit. This total uncertainty is dominated by the statistical part of $^{+18\%}_{-15\%}$. Figure 8.1 shows the BDT distribution before and after the fit is performed.

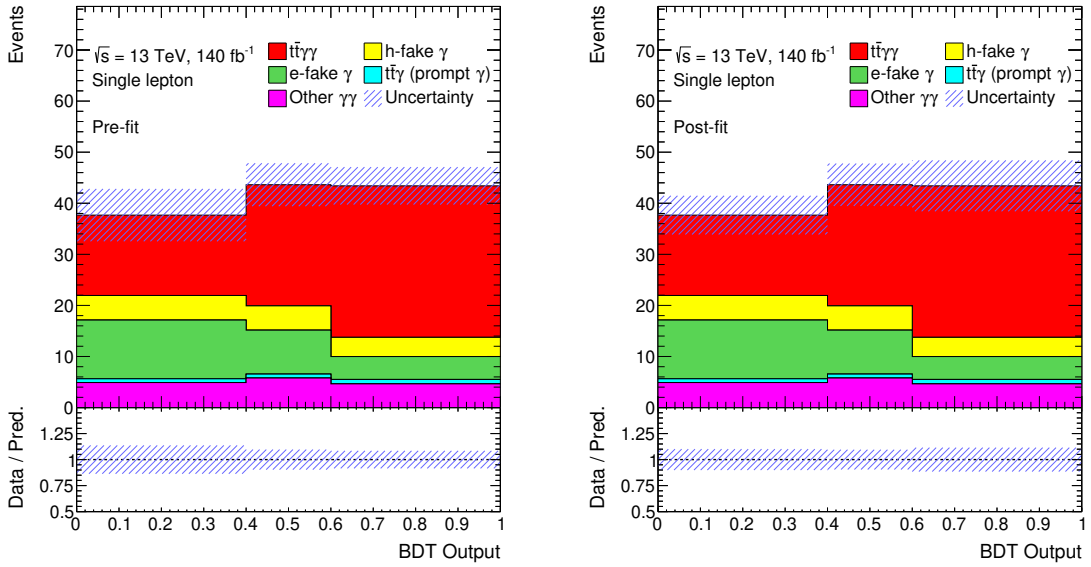

(a) (b)

Figure 8.1: BDT output distribution (a) before and (b) after fit to Asimov data. The uncertainty band corresponds to the total pre-fit uncertainty in (a) and to the total post-fit uncertainty in (b).

The expected significance from the above fit setup, computed using asymptotic method described before, is 5.6σ, indicating a strong expected sensitivity to the presence of the $t\bar{t}\gamma\gamma$ signal process over the background-only hypothesis. The corresponding likelihood scan at the (best-fit) value of μ of 1 is shown in Figure 8.2. The likelihood procedure repeats the fit multiple times for the POI by fixing the parameter to a predefined value and then running the minimisation procedure. In this procedure, the μ parameter is scanned and the corresponding profile negative log-likelihood (NLL) values are computed. The test statistic q_0, defined as the difference in NLL between the background-only hypothesis ($\mu = 0$) and the best-fit point, quantifies the level of agreement of the data with the background-only hypothesis. This test statistic is then converted into a Gaussian-equivalent significance using the asymptotic

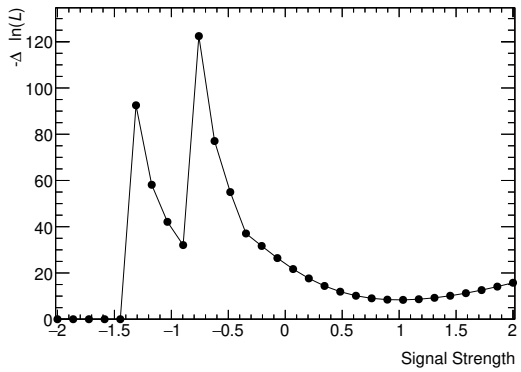

Figure 8.2: The likelihood scan performed over signal strength of $t\bar{t}\gamma\gamma$ process, with its best-fit value determined at 1.

formula described before in Section 8.3.

In this case, the expected test statistic corresponds to an expected sensitivity of 5.6σ with respect to the background-only hypothesis. The kinks in the Figure 8.2 usually come from the μ being taken as negative, which is unphysical. Also, the local minima for negative μ are far from the minimum reached by the fit. These kinks usually represent the real non-smooth properties of the likelihood function.

The test statistic, following $q_0 = -2\Delta\text{NLL}(\mu = 0)$, is evaluated at $\hat{\mu} = 1$ and at $\mu = 0$, which results in a value of 31.4. Therefore, the expected significance, $\sqrt{q_0}$, yields 5.6σ.

Figure 8.3 shows the ranking of the systematic uncertainties with the largest impact on the signal strength, as obtained from the fit using a covariance matrix breakdown method. Some of the most important NPs are: jet pile-up rho topology, jet flavor composition, h-fakes scale factor, photon isolation, photon identification, e-fakes scale factor and $W\gamma\gamma$ normalisation.

In the ranking plots, each NP is characterised both by its post-fit impact on the POI and by its pull. For a given NP θ_i, the pull is defined as

$$\text{Pull}(\theta_i) = \frac{\hat{\theta}_i - \theta_i^0}{\Delta\theta_i},$$

where $\hat{\theta}_i$ denotes the fitted value, θ_i^0 the nominal (pre-fit) value, and $\Delta\theta_i$ the corresponding pre-fit uncertainty. A pull consistent with zero indicates agreement with the prior expectation, while large pulls may signal tension between the data and prior constraints.

The NPs, which represent the various sources of systematic uncertainties in the analysis, show no significant pulls and it can be concluded that the fit performs well on the Asimov dataset.

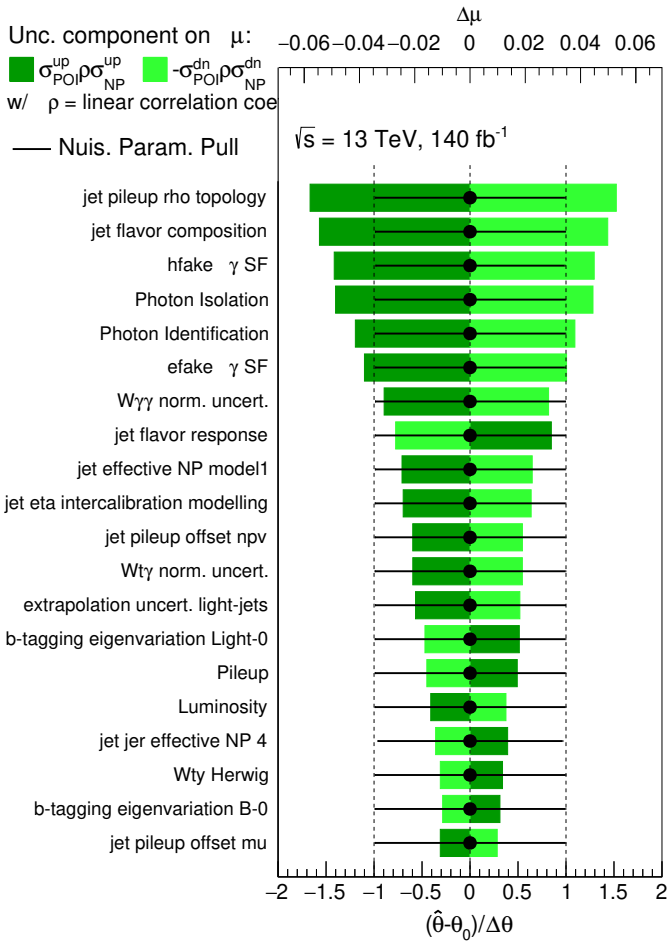

Figure 8.3: The ranking plot of the 20 most important NPs for the signal strength in the Asimov fit with the POI corresponding to the $t\bar{t}\gamma\gamma$ signal process.

Figure 8.4 shows the correlations of NPs with the signal strength for $t\bar{t}\gamma\gamma$ process. The correlation threshold is set at 10%. The matrix essentially quantifies the linear relationships between pairs of NPs and the signal strength. The correlation values in the matrix show that, except for the jet flavor reponse, all the major uncertainties are anti-correlated with the signal strength within ~25%.

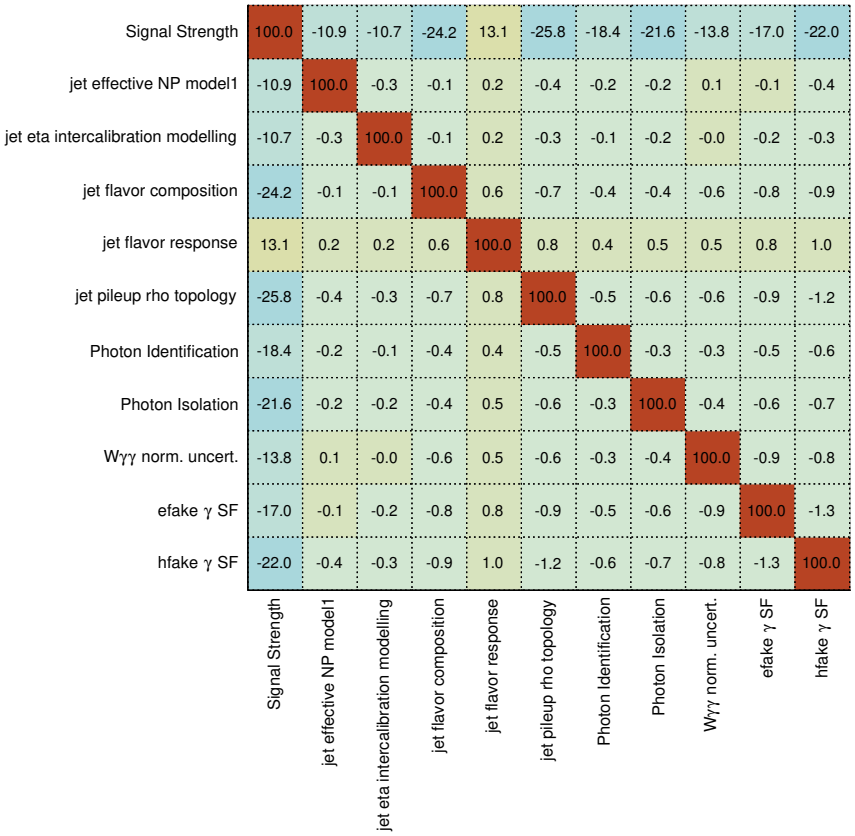

Figure 8.4: Correlations of NPs (with threshold of 10%) with the signal strength for $t\bar{t}\gamma\gamma$ signal process in the Asimov fit.

8.5 Measurement of the $t\bar{t}\gamma\gamma$ cross section

Once the fit setup is validated using the Asimov pseudodataset as described in Section 8.4, the fit is then performed with the observed data. The subsequent sections discuss the results of this fit.

8.5.1 Results for the $t\bar{t}\gamma\gamma$ cross section

The fit to data is performed on the BDT output with the POI corresponding to the $t\bar{t}\gamma\gamma$ contribution, μ, yielding a best-fit value of $\mu = 0.927$. The total observed uncertainty on the μ is $^{+22\%}_{-20\%}$, dominated by the statistical part of $^{+18\%}_{-15\%}$.

The value of μ is slightly lower than 1, which means that the MC predictions slightly overestimate the expected events in the fiducial phase space of the measurement by ~10%. Figure 8.5 (b), shows the BDT output distribution after fitting to data. As reflected in the value of μ, the total expected number of events after the fit is 120.9, in good agreement with data. The number of events before and after the fit are shown in Table 8.2.

Table 8.2: Number of events per category before and after the fit

Category	Pre-fit	Post-fit
$t\bar{t}\gamma\gamma$	69.1	64.4
h-fakes	13.3	13.7
e-fakes	24.6	24.8
$t\bar{t}\gamma$(prompt γ)	2.4	2.4
Other $\gamma\gamma$	15.3	15.7
Total	124.7	120.9
Data	122.0	122.0

As discussed in Section 8.3, the measurement is performed in a fiducial phase space defined at particle level.

The nominal $t\bar{t}\gamma\gamma$ signal expectation is derived from the $t\bar{t}\gamma\gamma$ MadGraph5_aMC@NLO + Pythia8 simulation at leading order. The predicted fiducial cross section is $\sigma^{\text{LO}}_{t\bar{t}\gamma\gamma}$(expected) = $1.53^{+0.40}_{-0.52}$(scale)$^{+0.05}_{-0.03}$(PDF) fb, including the scale and PDF uncertainties of the simulated sample, corresponding to an acceptance of ~19% between the particle level phase space and the defined fiducial region.

The $t\bar{t}\gamma\gamma$ fiducial cross section at particle level in the defined fiducal phase space, extracted using the PL fit to the BDT output, results in:

$$\begin{aligned}\sigma^{\text{fid}}_{t\bar{t}\gamma\gamma}\ \text{(observed)} &= \mu \times \sigma^{\text{NLO}}_{t\bar{t}\gamma\gamma}\ \text{(expected)} \\ &= 2.42^{+0.58}_{-0.53}\ \text{fb} \\ &= 2.42^{+0.46}_{-0.38}\ \text{(stat)}\ ^{+0.35}_{-0.38}\ \text{(syst)}\ \text{fb}.\end{aligned}$$

Here $\sigma^{\text{NLO}}_{t\bar{t}\gamma\gamma}$ (expected) = K-factor$^{\text{NLO/LO}} \times \sigma^{\text{LO}}_{t\bar{t}\gamma\gamma}$ represents the expected number of events shown in the plots at NLO accuracy.

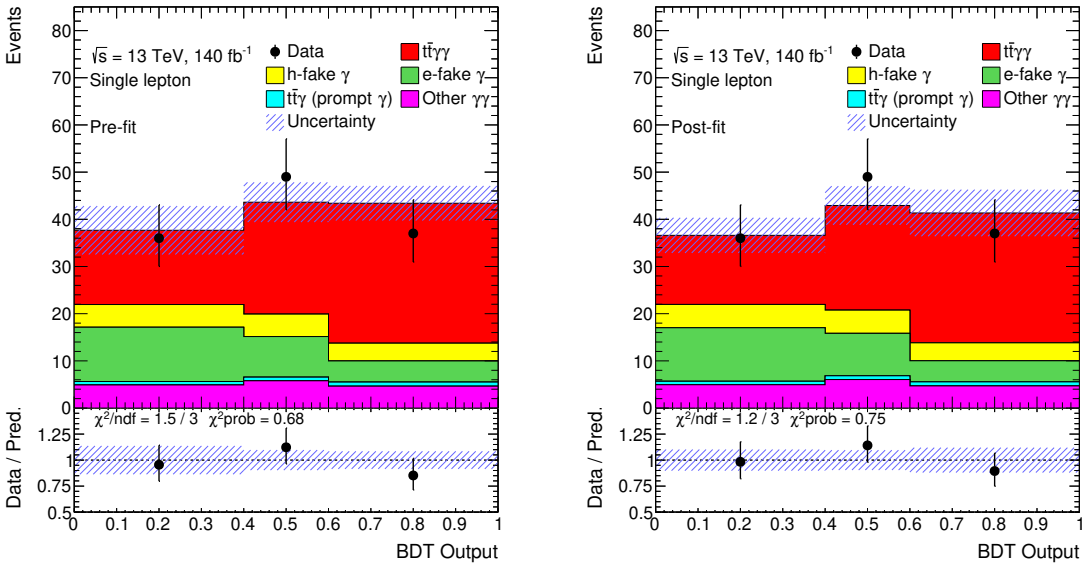

(a) (b)

Figure 8.5: BDT output distribution (a) before and (b) after fitting to data. The uncertainty band corresponds to the total pre-fit uncertainty in (a) and to the total post-fit uncertainty in (b).

The uncertainties are calculated from the statistical and systematic uncertainties of μ using the relation:

$$\Delta\sigma^{\text{fid}}_{t\bar{t}\gamma\gamma} = \Delta\mu \times \sigma^{\text{NLO}}_{t\bar{t}\gamma\gamma}. \tag{8.8}$$

Here,

- $\Delta\sigma^{\text{fid}}_{t\bar{t}\gamma\gamma}$ denotes the uncertainty on the measured fiducial cross section at particle level;
- $\Delta\mu$ represents the corresponding uncertainty on the fitted μ;
- $\sigma^{\text{NLO}}_{t\bar{t}\gamma\gamma}$ is the predicted (expected) fiducial cross section at NLO accuracy.

The pulls on the nuisance parameters, as determined by the fit, are presented in the pull plots in Figures 8.6 and 8.7. The plots provide a visual summary of how the NPs shift during the fit.

As shown in Figure 8.6, a small pull is observed for the $W\gamma\gamma$ normalisation uncertainty. This is expected given that the $W\gamma\gamma$ process contributes to ~31% of the expected events in the Other $\gamma\gamma$ category. The comparison of this uncertainty between the nominal and the varied templates on the events in the Other $\gamma\gamma$ category can be seen in Figure 8.8, where the black line shows the nominal expectation value, while the red and blue lines show the up and down variations of ~16%. The modelling of $t\bar{t}$ p_T-hard and $t\bar{t}\gamma\gamma$ PS (Herwig7) are also slightly shifted with respect to the nominal values, as shown in Figure 8.6. The impact on $t\bar{t}\gamma\gamma$ PS modelling uncertainty is shown in Section 8.9. The varied $t\bar{t}\gamma\gamma$ Herwig7 sample is normalised to the fiducial cross section calculated with the nominal Pythia8 sample, as described in Section 8.3.2. Therefore, the impact of 0.2% on this template is mostly on the shape of the distribution.

The data-driven e-fake and h-fake photon backgrounds also show small pulls in one direction. The e-fake uncertainties impact all the templates in the fit by about 10%-13% while the impact of h-fake uncertainties is about ~30%, as can be seen in Figures 8.16 and 8.17, respectively.

Some of the experimental uncertainties, such as photon identification and isolation and a few jet related uncertainties (JER, flavor response, flavor compostiton), are also shifted, as well as the extrapolation uncertainty for uncalibrated light jets, which can be seen in Figure 8.7. Their impact on the different categories of the processes can be seen in Figure 8.10 for the $t\bar{t}\gamma$ prompt γ and Other $\gamma\gamma$ category, and Figures 8.11 and 8.12 for the e-fake and h-fake categories respectively. As mentioned before, the fit setup in the analysis consists of multiple templates corresponding to the groupings of different MC samples based on photon origin, described in Section 4.7 [1]. The plots are, therefore, split corresponding to these templates affected by the systematic in the fit.

The impact of photon isolation are shown in Figure 8.13, impacting the $t\bar{t}\gamma$ prompt γ and Other $\gamma\gamma$, and Figures 8.14 and 8.15, impacting the e-fake and h-fake categories respectively.

None of the NPs are significantly constrained by the fit though. Their best-fit values are well within 1σ deviation of their pre-fit estimates from the MC simulations.

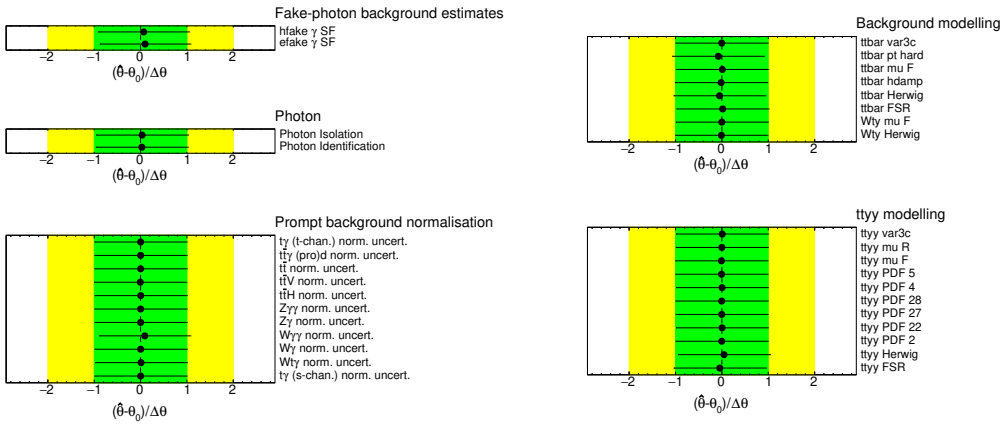

Figure 8.6: Post-fit nuisance parameters for uncertainties related to fake photons, photon reconstruction, prompt background normalisation, background modelling and $t\bar{t}\gamma\gamma$ modelling used in the fit to data.

[1] The $t\bar{t}\gamma$ decay contribution is shown separately in these plots just for a small technicality when producing the plots because it is normalised with an NLO/LO K-factor, while other background samples are not. However, the contribution is included in the corresponding template in the fit.

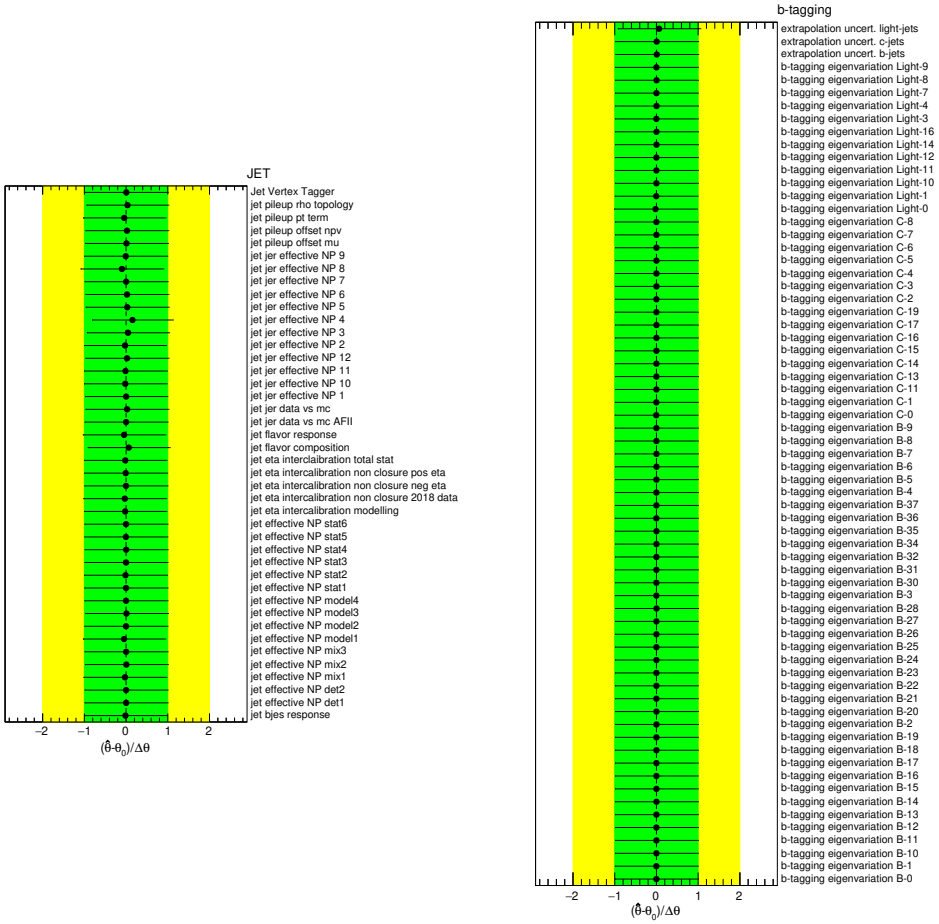

Figure 8.7: The NPs for uncertainties related to jets, and b-tagging for the fit to data.

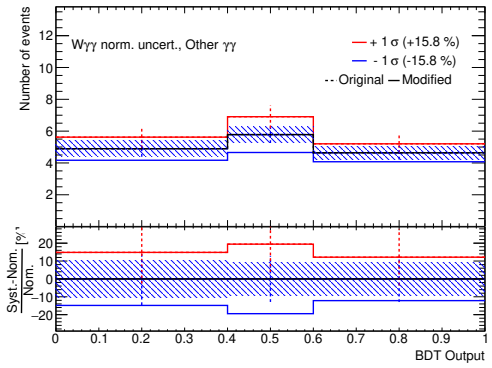

(a)

Figure 8.8: Nominal (black) and varied (red/blue) templates corresponding to the $W\gamma\gamma$ normalisation uncertainty. (The dashed lines show the shape of the systematic before the smoothing procedure is applied.)

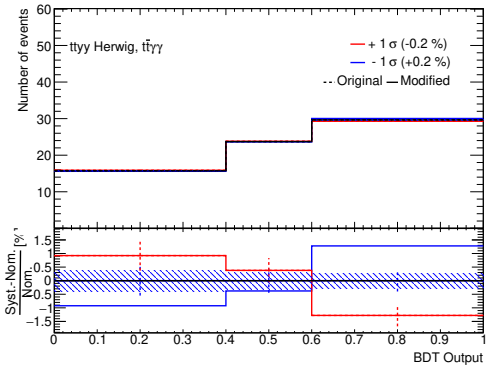

(a)

Figure 8.9: Nominal (black) and varied (red/blue) templates corresponding to the $t\bar{t}\gamma\gamma$ shower variation of HERWIG7. (The dashed lines show the shape of the systematic before the smoothing procedure is applied.)

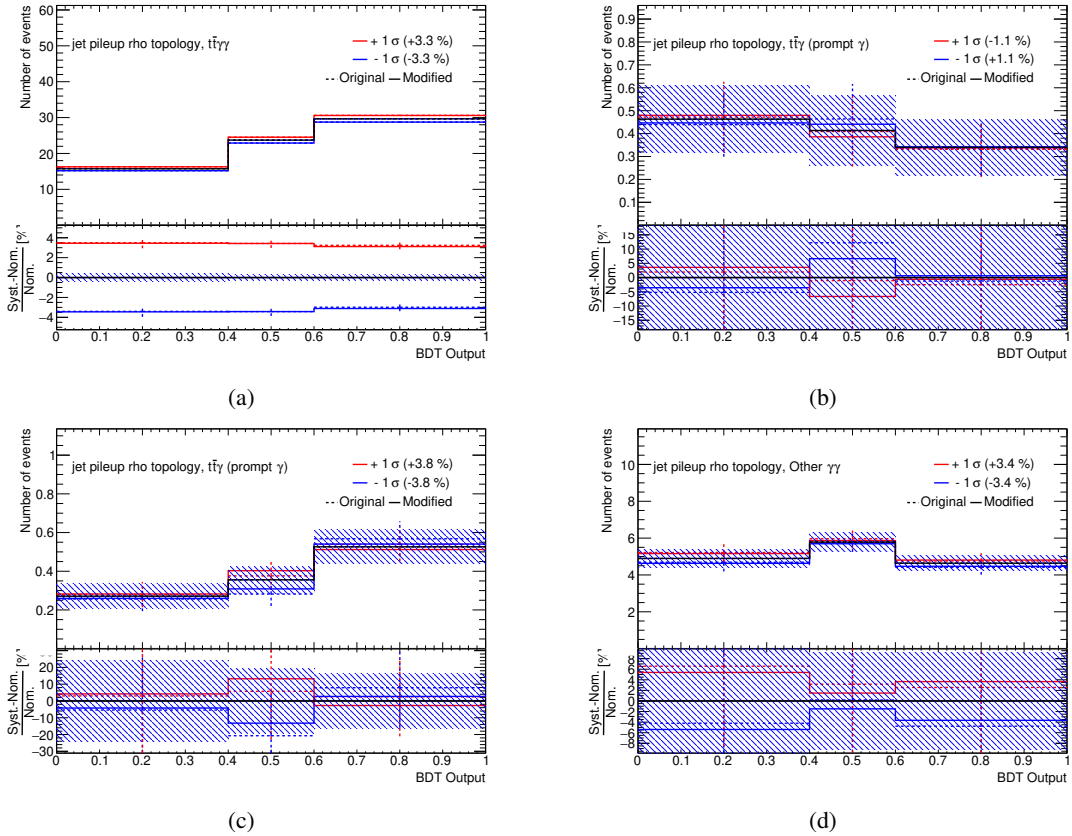

(a) (b)

(c) (d)

Figure 8.10: Nominal (black) and varied (red/blue) templates corresponding to the Jet pileup rho topology uncertainty for $t\bar{t}\gamma\gamma$ (a), $t\bar{t}\gamma$ production (b) and $t\bar{t}\gamma$ decay (c), treated as one template ($t\bar{t}\gamma$ (Prompt γ)) in the fit, and Other $\gamma\gamma$ (d). (The dashed lines show the shape of the systematic before the smoothing procedure is applied.)

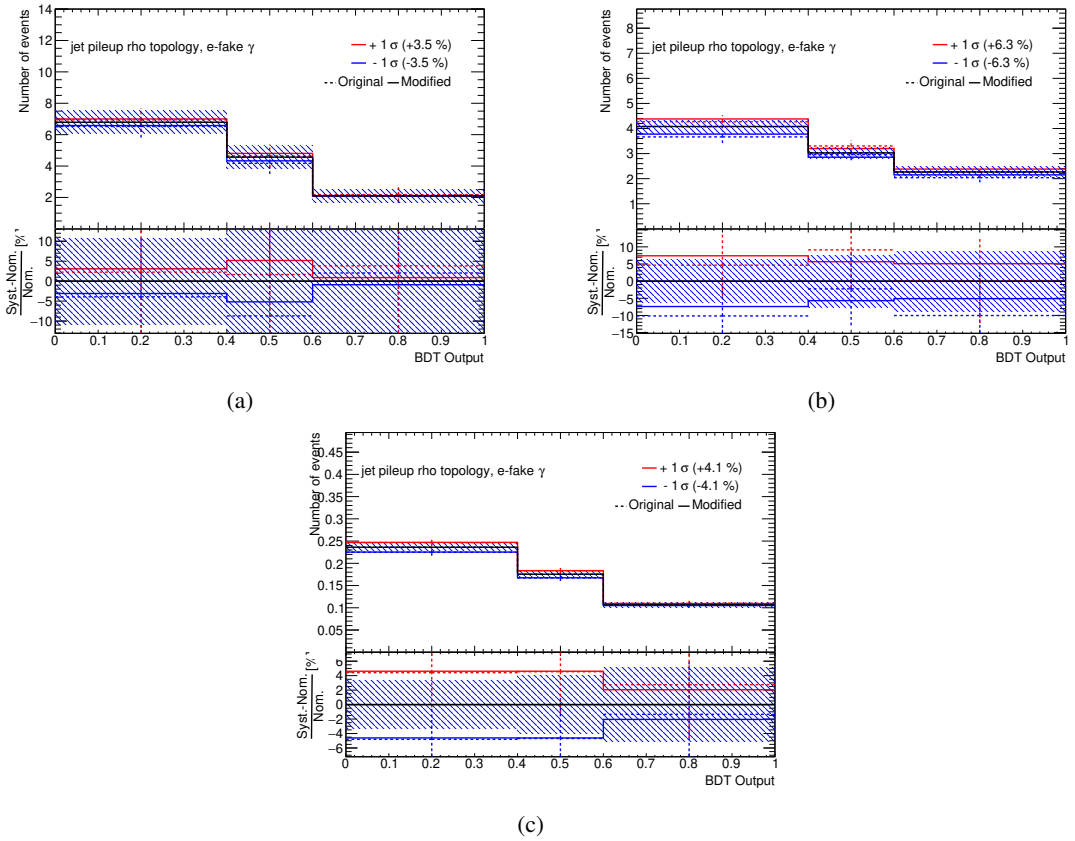

Figure 8.11: Nominal (black) and varied (red/blue) templates corresponding to the Jet pileup rho topology uncertainty for the e-fake category with one e-fake photon and one prompt photon for all processes except for $t\bar{t}\gamma$ decay and $t\bar{t}\gamma\gamma$ (a), $t\bar{t}\gamma$ decay (b) and $t\bar{t}\gamma\gamma$ processes (c). These categories are added up and treated as one template in the fit. (The dashed lines show the shape of the systematic before the smoothing procedure is applied.)

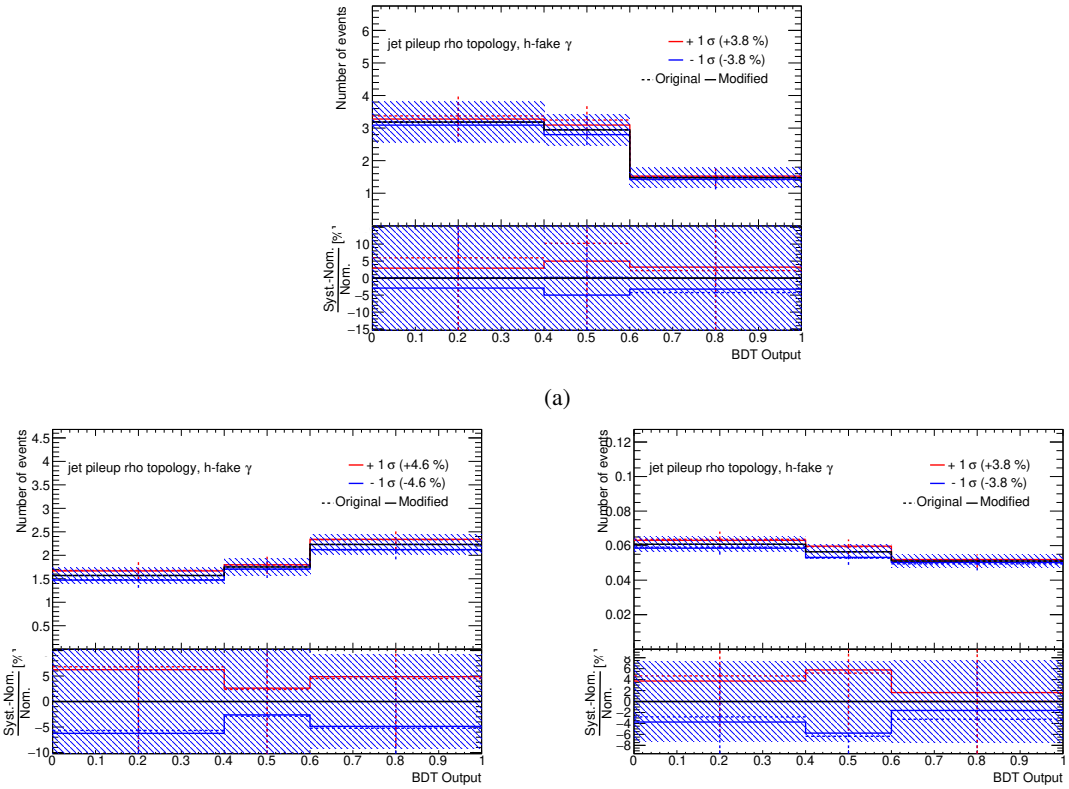

Figure 8.12: Nominal (black) and varied (red/blue) templates corresponding to the Jet pileup rho topology uncertainty for the h-fake category for all processes except for $t\bar{t}\gamma$ decay and $t\bar{t}\gamma\gamma$ (a), $t\bar{t}\gamma$ decay (b) and $t\bar{t}\gamma\gamma$ (c). These categories are added up and treated as one template in the fit. (The dashed lines show the shape of the systematic before the smoothing procedure is applied.)

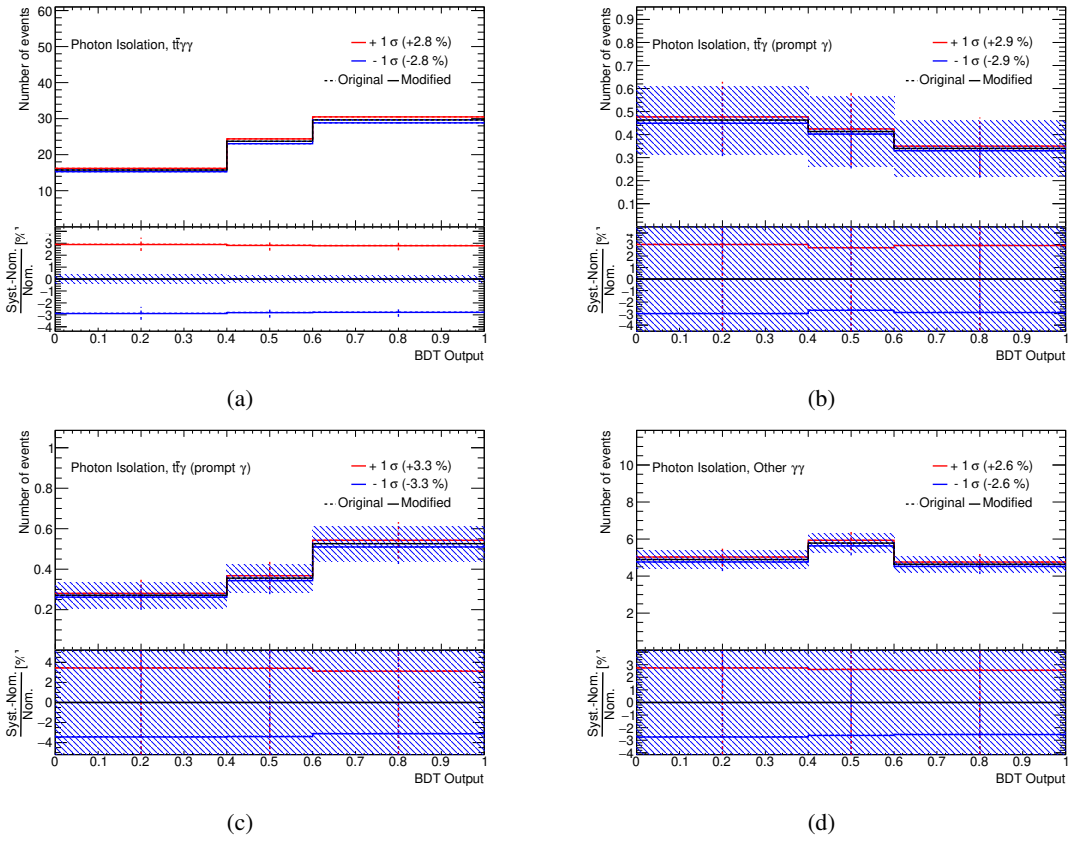

Figure 8.13: Nominal (black) and varied (red/blue) templates corresponding to the photon isolation uncertainty for $t\bar{t}\gamma\gamma$ (a), $t\bar{t}\gamma$ production (b) and $t\bar{t}\gamma$ decay (c), treated as one template ($t\bar{t}\gamma$ (Prompt γ)) in the fit, and Other $\gamma\gamma$ (d). (The dashed lines show the shape of the systematic before the smoothing procedure is applied.)

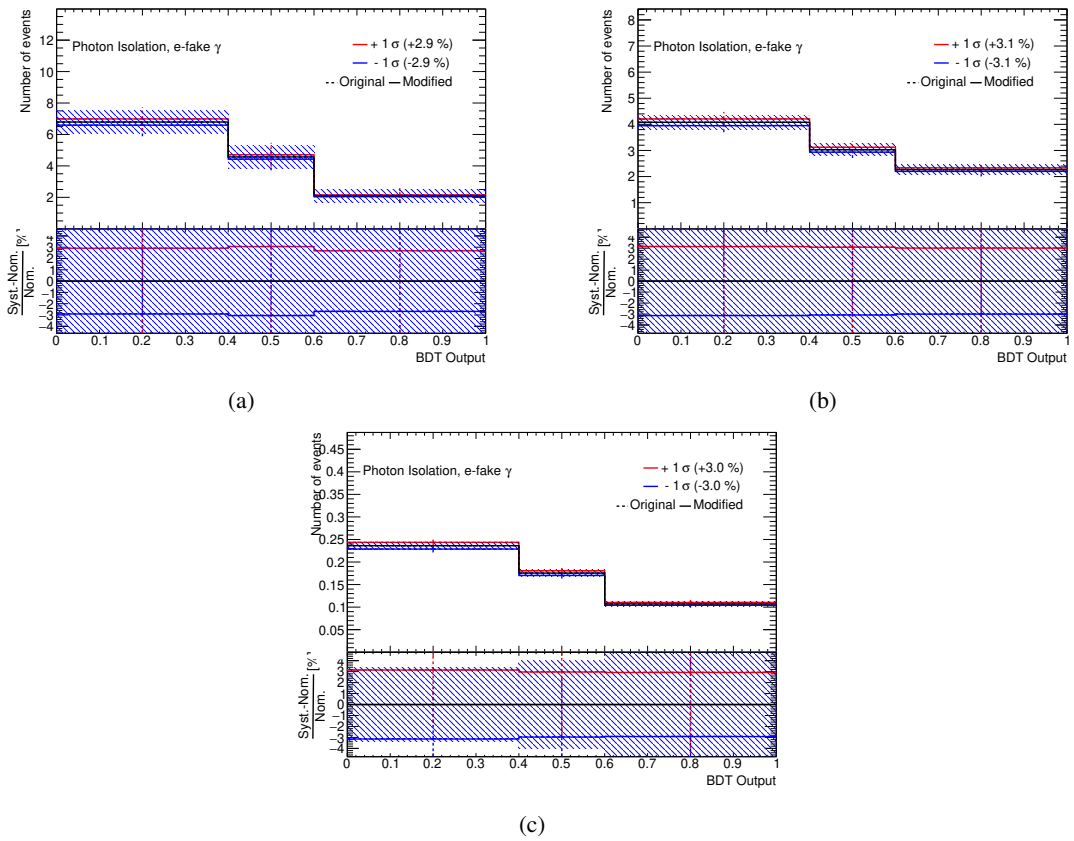

Figure 8.14: Nominal (black) and varied (red/blue) templates corresponding to the photon isolation uncertainty for the e-fake category with one e-fake photon and one prompt photon for all processes except for $t\bar{t}\gamma$ decay and $t\bar{t}\gamma\gamma$ (a), $t\bar{t}\gamma$ decay (b) and $t\bar{t}\gamma\gamma$ processes (c). These categories are added up and treated as one template in the fit. (The dashed lines show the shape of the systematic before the smoothing procedure is applied.)

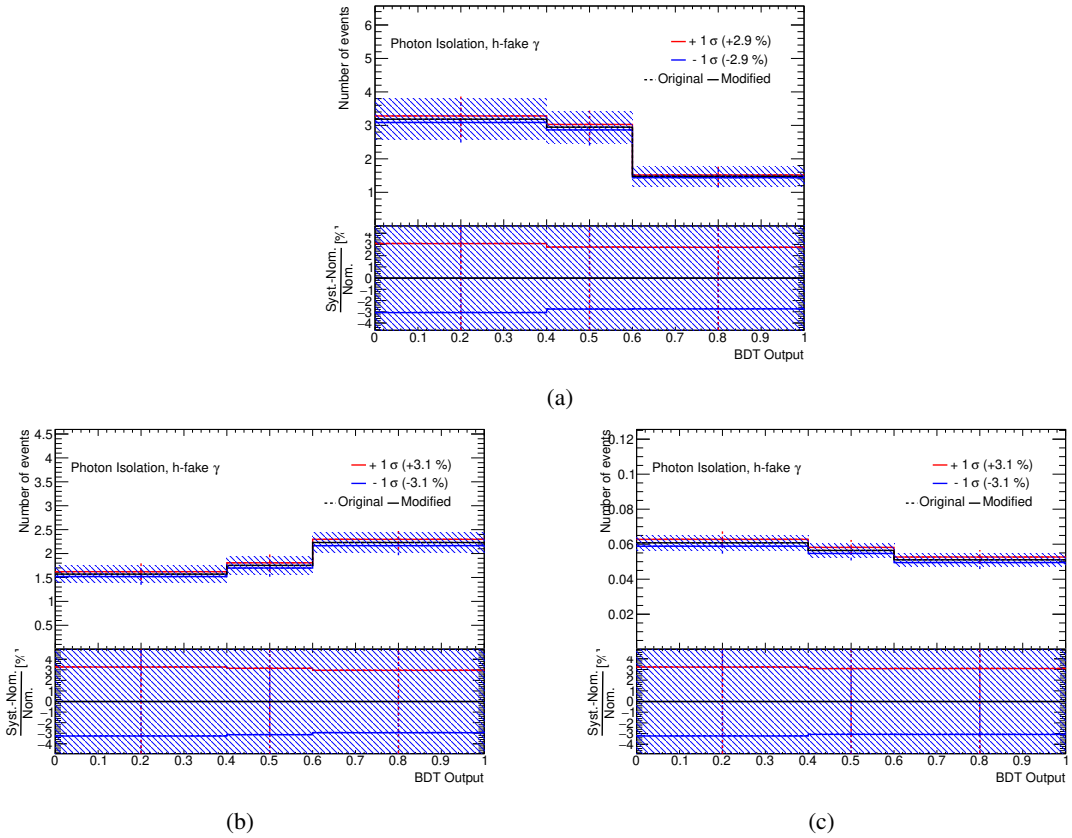

Figure 8.15: Nominal (black) and varied (red/blue) templates corresponding to the photon isolation uncertainty for the h-fake category for all processes except for $t\bar{t}\gamma$ decay and $t\bar{t}\gamma\gamma$ (a), $t\bar{t}\gamma$ decay (b) and $t\bar{t}\gamma\gamma$ (c). These categories are added up and treated as one template in the fit. (The dashed lines show the shape of the systematic before the smoothing procedure is applied.)

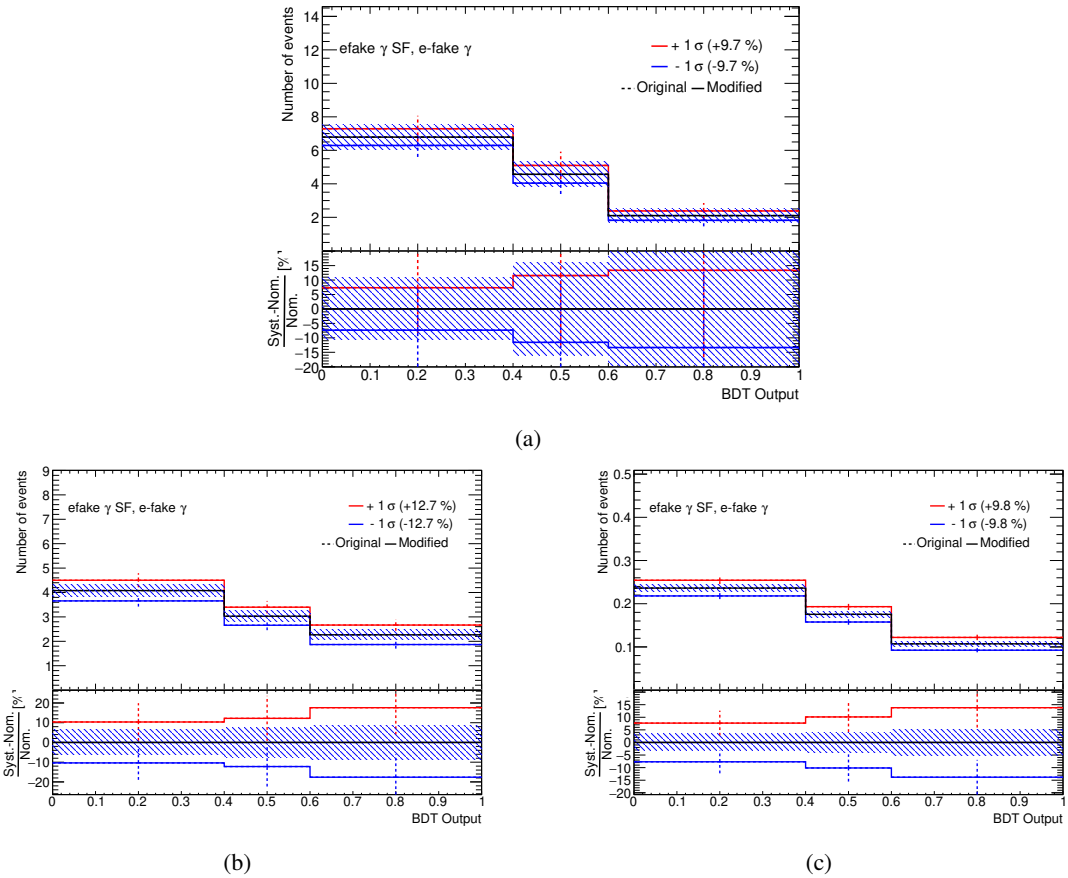

Figure 8.16: Nominal (black) and varied (red/blue) templates corresponding to the e-fake uncertainty for the e-fake category with one e-fake photon and one prompt photon for all processes except for $t\bar{t}\gamma$ decay and $t\bar{t}\gamma\gamma$ (a), $t\bar{t}\gamma$ decay (b) and $t\bar{t}\gamma\gamma$ processes (c). These categories are added up and treated as one template in the fit These uncertainties affect only to the corresponding categories with fakes photons. (The dashed lines show the shape of the systematic before the smoothing procedure is applied.)

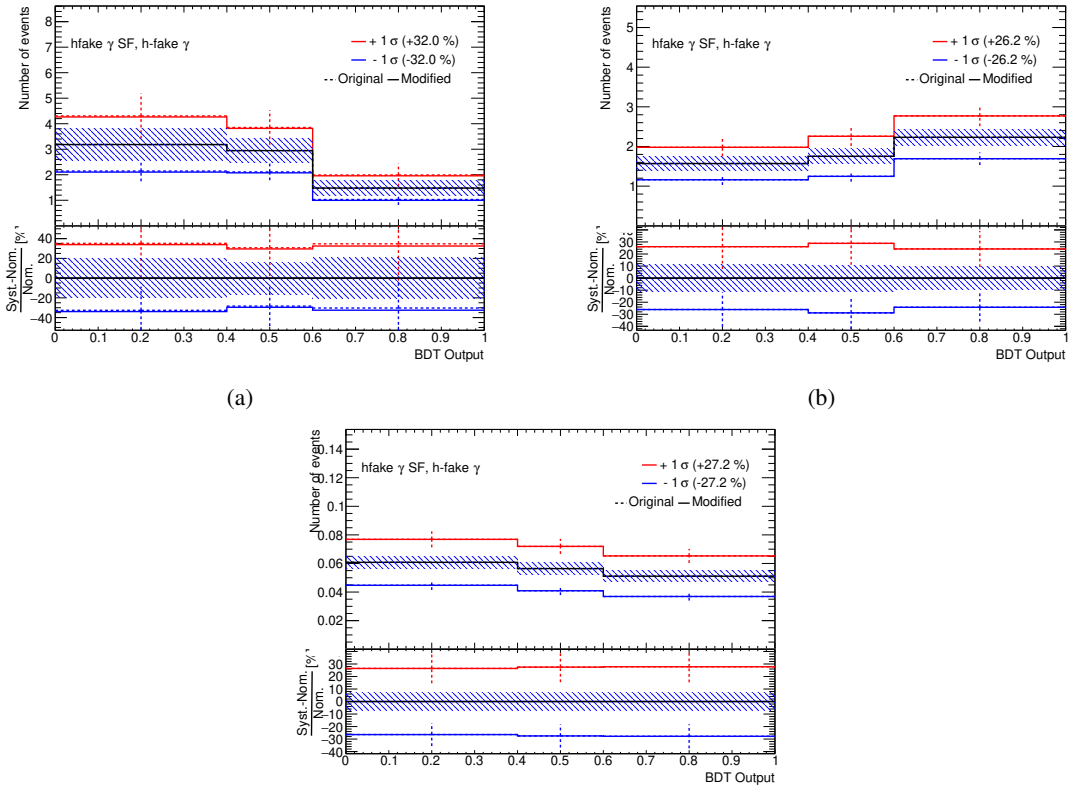

Figure 8.17: Nominal (black) and varied (red/blue) templates corresponding to the h-fake SF uncertainty for all processes except for $t\bar{t}\gamma$ decay and $t\bar{t}\gamma\gamma$ (a), $t\bar{t}\gamma$ decay (b) and $t\bar{t}\gamma\gamma$ (c). These categories are added up and treated as one template in the fit. These uncertainties affect only to the corresponding categories with fakes photons. (The dashed lines show the shape of the systematic before the smoothing procedure is applied.)

In Figure 8.18, the correlation matrix between μ and the NPs is shown, with a threshold of 10%. Except for JET flavour response, most of the NPs are negatively correlated with the signal strength, which means that during fitting with data, higher values of these NPs contribute to lower best-fit value of μ, and vice versa. This is in agreement with the Asimov fit results.

The breakdown of individual groups of uncertainties within the total uncertainty is obtained by using the covariance matrix obtained from the fit setup, as described in [114]. In this approach, the impact of a given NP on a given POI is estimated by reading the right element of the covariance matrix. The contribution of individual uncertainty sources to the total uncertainty on the POI is quantified using the covariance matrix obtained from the fit. Specifically, the impact of an NP, n, on a POI a is calculated as:

$$I = \sigma^a_{\text{total}} \times C_{a,n} \times \sigma^n$$

where σ^a_{total} is the total uncertainty of POI a, $C_{a,n}$ is the correlation coefficient between POI a and NP n, and σ^n is the uncertainty of NP n. This method allows for a clear breakdown of how each NP contributes to the overall uncertainty of the POI. As mentioned before, adding together the impact of all NPs gives the total systematic uncertainty which can then be subtracted (in quadrature) from the total uncertainty to get statistical uncertainty.

Table 8.3 shows this breakdown of the impact of the uncertainties, grouped together according to their source, on the $t\bar{t}\gamma\gamma$ measurement after fit to data. The uncertainties quoted for μ in the table are absolute. The up and down uncertainties on the μ are also shown for all the groups.

Table 8.3: Summary of the impact of the systematic uncertainties on the signal strength of the $t\bar{t}\gamma\gamma$ cross section in the unblinded single-lepton channel, grouped into different categories. The category 'JET' corresponds to the combined effect of JES, jet resolution and JVT uncertainties, while the categories 'Photon' and 'Leptons' correspond to all experimental uncertainties related to photons and leptons, respectively. The category '$t\bar{t}\gamma\gamma$ modelling' includes the PDF and theoretical modelling uncertainties on $t\bar{t}\gamma\gamma$.

Source	$\Delta\mu_{t\bar{t}\gamma\gamma}$	Up/Down Uncertainty
Background modelling	0.012	(+0.013, –0.012)
Fake-photon background estimates	0.060	(+0.063, –0.058)
JET	0.090	(+0.094, –0.086)
Leptons	0.014	(+0.015, –0.013)
Luminosity	0.013	(+0.014, –0.013)
MET	0.004	(+0.004, –0.003)
Photon	0.060	(+0.063, –0.057)
Pileup	0.015	(+0.016, –0.014)
Prompt background normalisation	0.039	(+0.040, –0.037)
b-tagging	0.031	(+0.033, –0.030)
$t\bar{t}\gamma$ decay normalisation	0.001	(+0.001, –0.001)
$t\bar{t}\gamma$ decay modelling	0.003	(+0.003, –0.003)
$t\bar{t}\gamma$ production Herwig7	0.002	(+0.002, –0.002)
$t\bar{t}\gamma$ production modelling	0.003	(+0.003, –0.003)
$t\bar{t}\gamma\gamma$ modelling	0.013	(+0.014, –0.012)
MC statistical uncertainty	0.023	(+0.022, –0.024)
Total systematic uncertainty	0.139	(+0.145, –0.133)

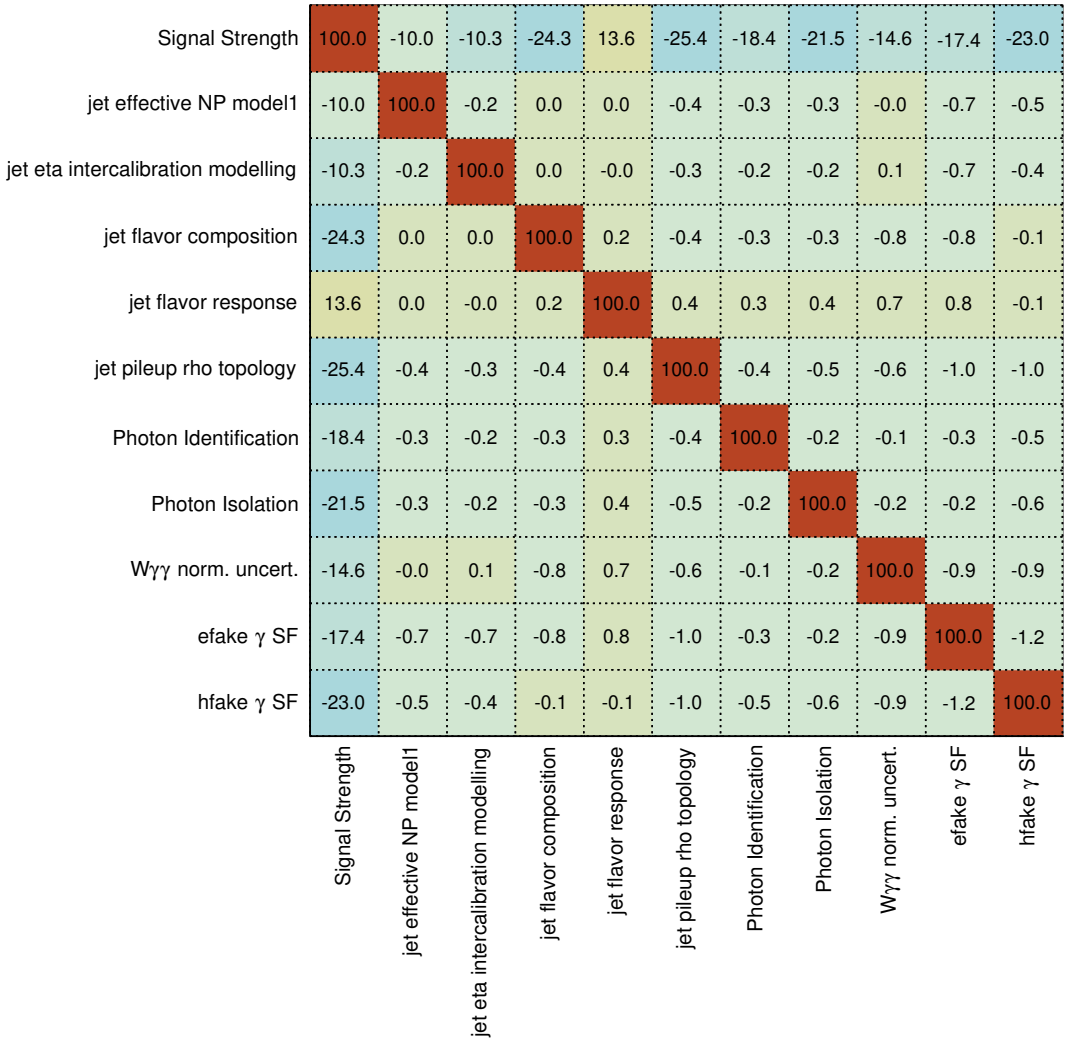

Figure 8.18: Correlations of NPs (with threshold of 10%) with the signal strength for the $t\bar{t}\gamma\gamma$ signal process in the fit to data.

Ranking of nuisance parameters

Based on the impact of an NP on the signal strength, evaluated from the covariance matrix approach described before, the ranking of various uncertainties is determined, as shown in Figure 8.19. The major systematic uncertainties are: jet pile-up rho topology, jet flavor composition, h-fakes scale factor, photon isolation, photon identification, e-fakes scale factor, $W\gamma\gamma$ normalisation, which are also reflected in the pull plots and the red-blue plots shown before. The ranking of these systematic uncertainties is in agreement with the results from the Asimov fit (Figure 8.3).

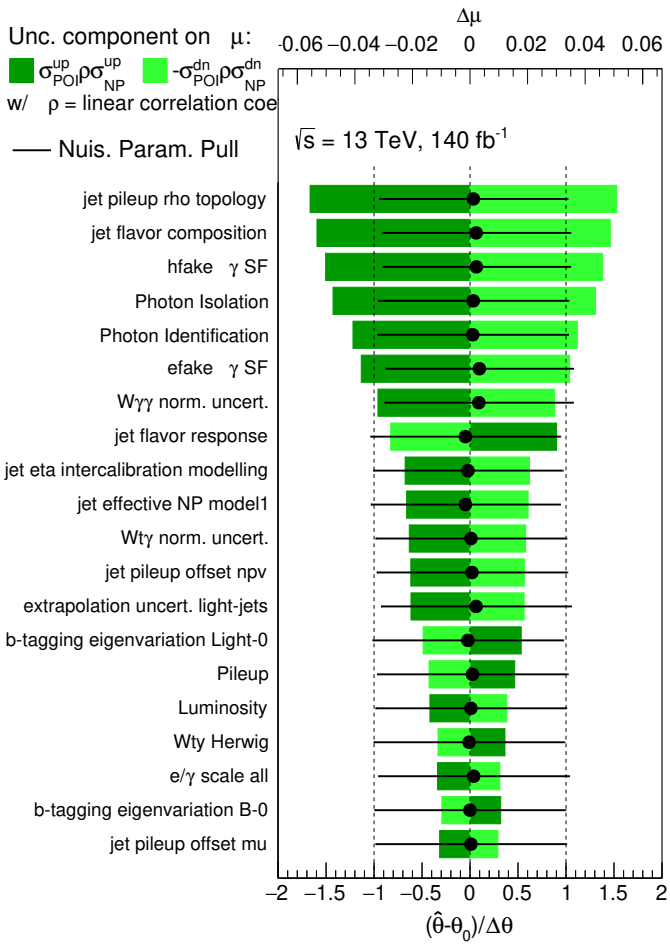

Figure 8.19: The ranking plot of the 20 most important NPs for the signal strength in the fit to data in the single-lepton channel with one POI corresponding to the $t\bar{t}\gamma\gamma$ signal process.

8.5.2 BDT input distributions after fit to data

After the fit to data has been performed, the best-fit values of the fitted likelihood parameters from the fit to BDT output are then used the plot other kinematic distributions to evaluate the resulting distributions. Figures 8.20 to 8.29 show the post-fit input variable distributions of the BDT, after fit to data. A good agreement between data and MC events is observed in these cases. This means that the fit with data not only performs good for the BDT output, but is also able to better describe the input variable distributions of the BDT itself.

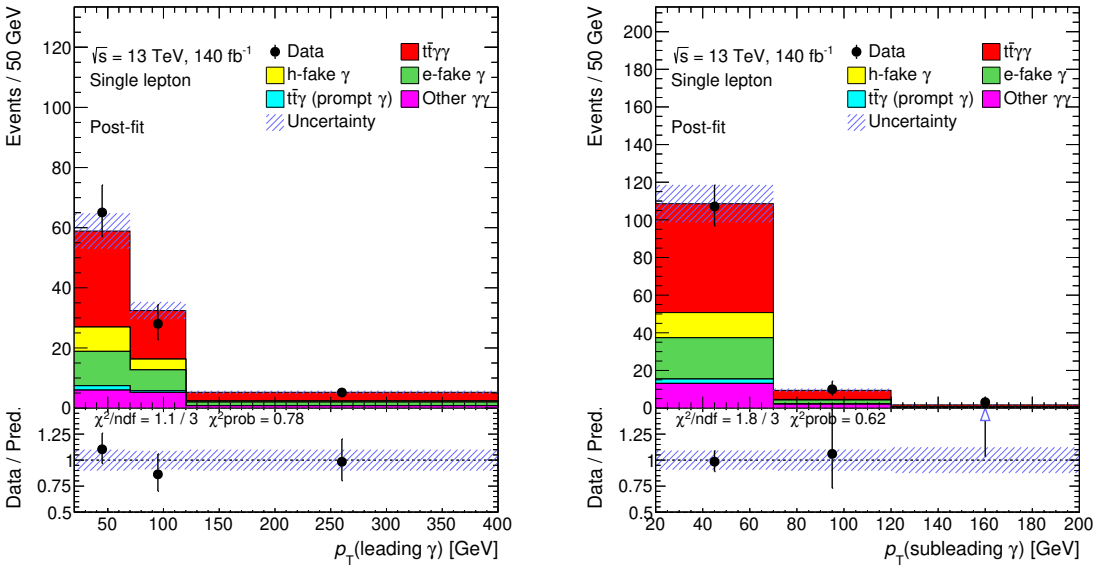

(a) (b)

Figure 8.20: The p_{T} distributions of the (a) leading and (b) subleading photons. The uncertainty band represents the total uncertainty after the fit to the data.

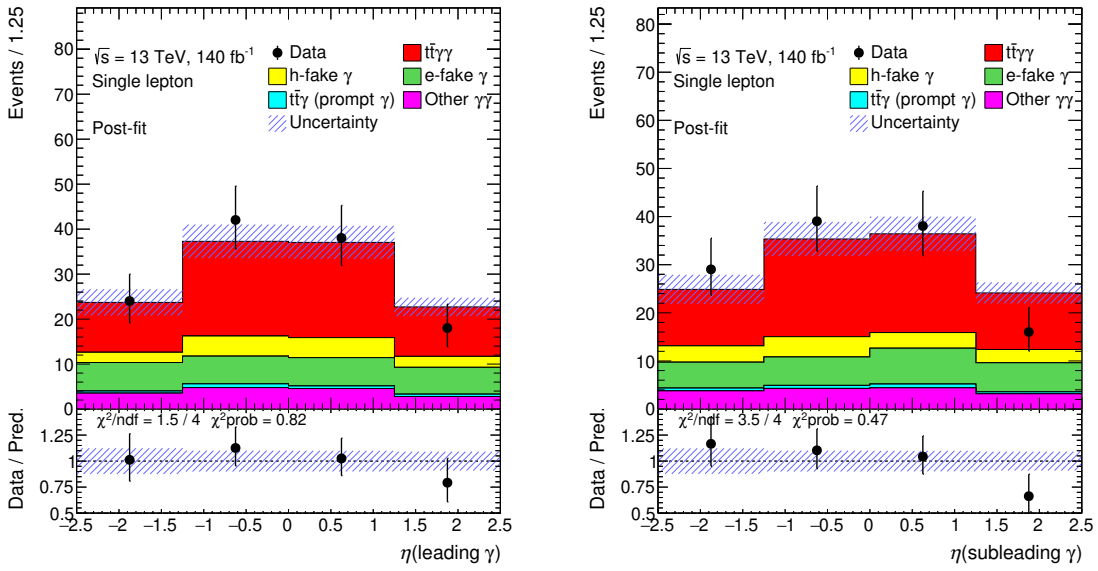

(a) (b)

Figure 8.21: The η distributions of the (a) leading and (b) subleading photons. The uncertainty band represents the total uncertainty after the fit to the data.

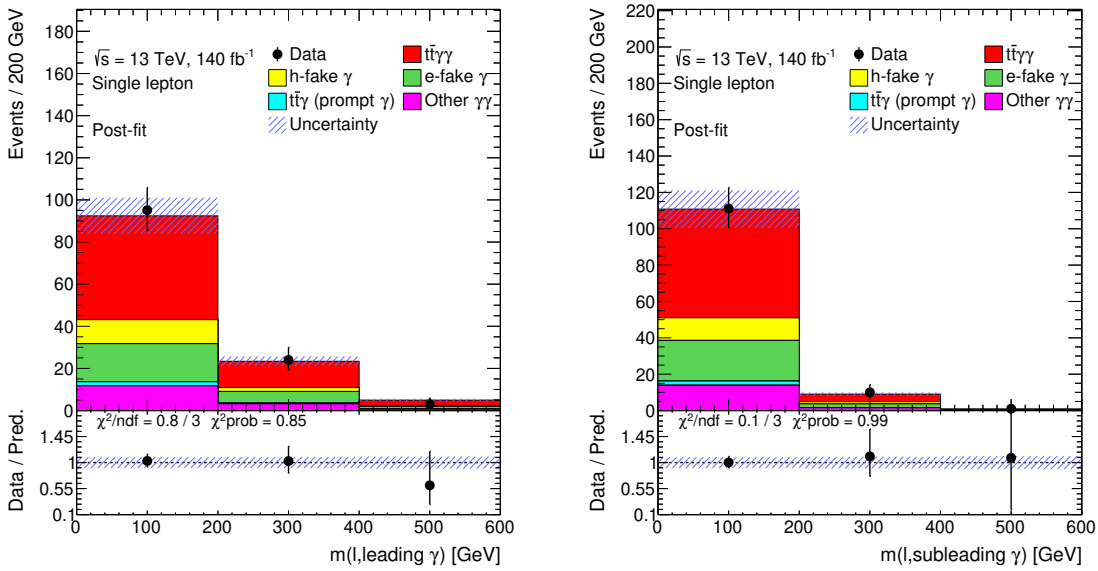

(a) (b)

Figure 8.22: The invariant mass distributions of the lepton and the (a) leading or (b) subleading photon. The uncertainty band represents the total uncertainty after the fit to the data.

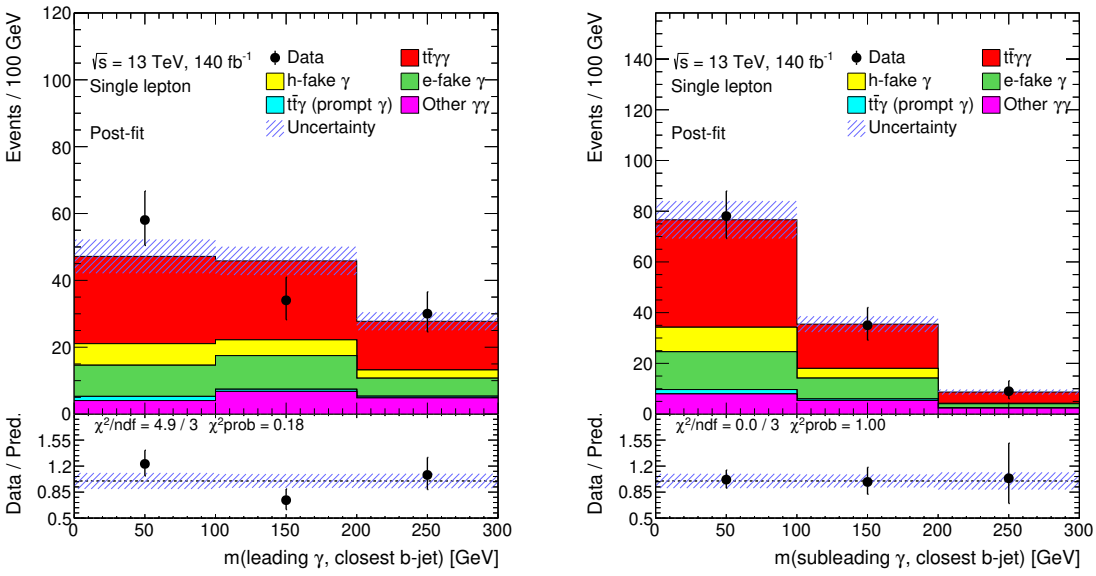

(a) (b)

Figure 8.23: The invariant mass distributions of the (a) leading or (b) subleading photon and the closest b-jet. The uncertainty band represents the total uncertainty after the fit to the data.

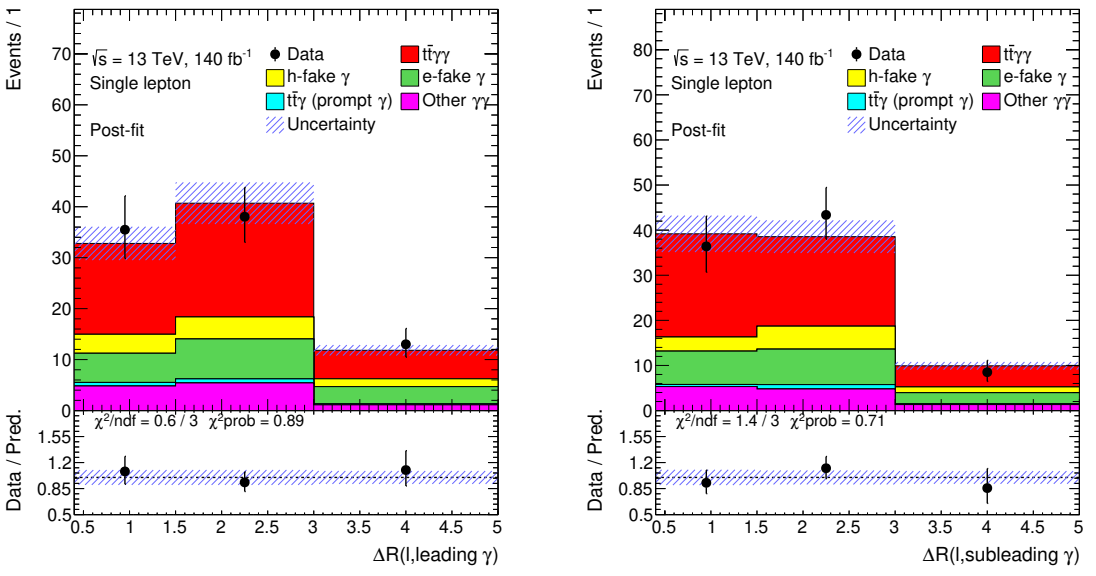

(a) (b)

Figure 8.24: The ΔR distributions between the lepton and the (a) leading and (b) subleading photon. The uncertainty band represents the total uncertainty after the fit to the data.

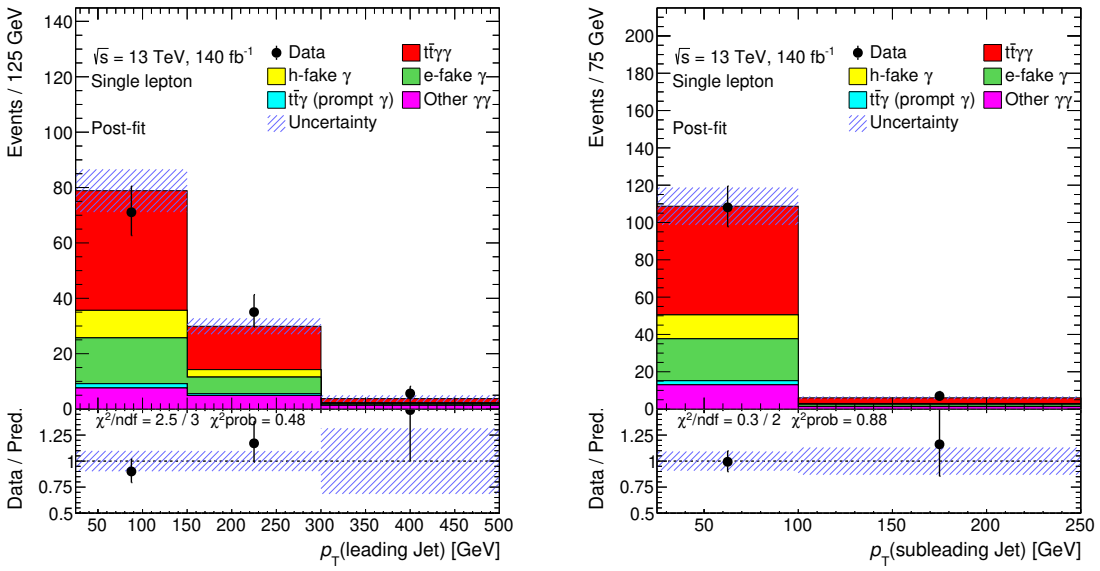

(a) (b)

Figure 8.25: The p_{T} distributions of the (a) leading and (b) subleading jets. The uncertainty band represents the total uncertainty after the fit to the data.

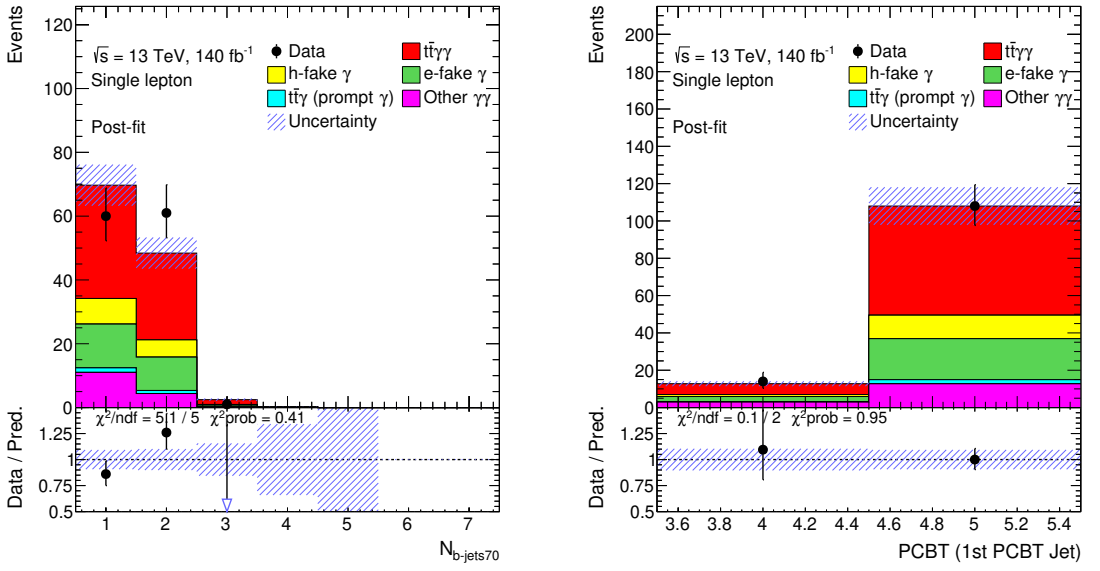

(a) (b)

Figure 8.26: The distributions of (a) the number of b-jets at 70% WP and (b) the highest DL1r score for the jet with PCBT binning. The uncertainty band represents the total uncertainty after the fit to the data.

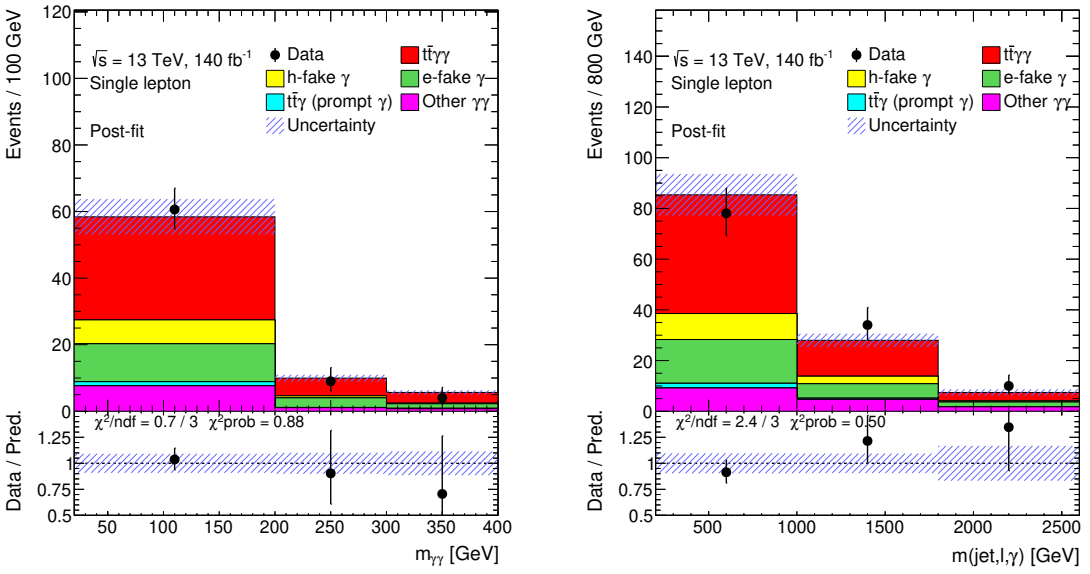

(a) (b)

Figure 8.27: (a) Diphoton invariant mass and (b) invariant mass of all jets, the lepton, and both photons. The uncertainty band represents the total uncertainty after the fit to the data.

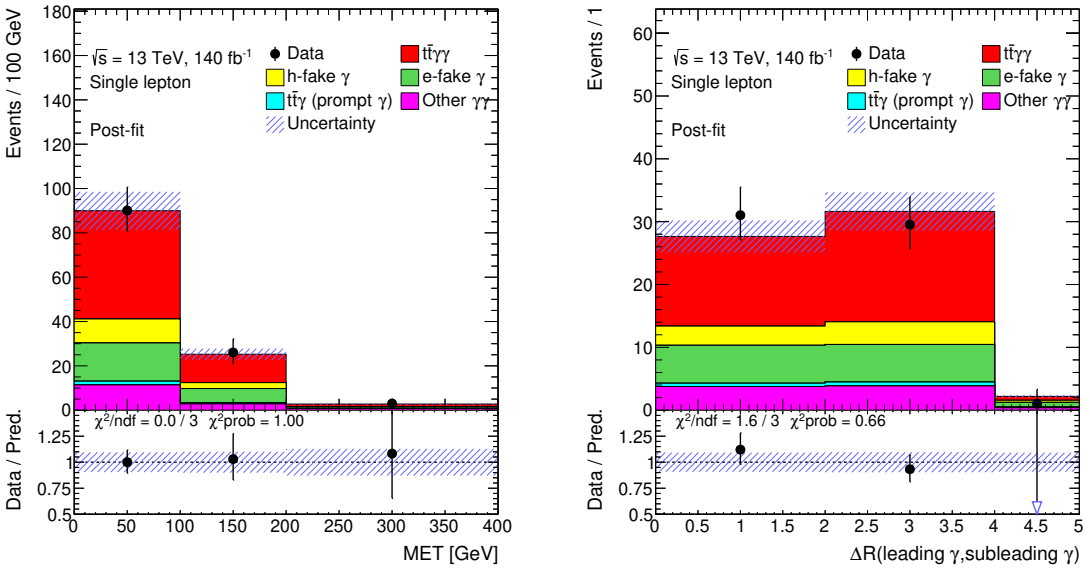

(a) (b)

Figure 8.28: (a) $E_{\mathrm{T}}^{\mathrm{miss}}$ distribution and (b) ΔR distributions between leading and subleading photons. The uncertainty band represents the total uncertainty after the fit to the data.

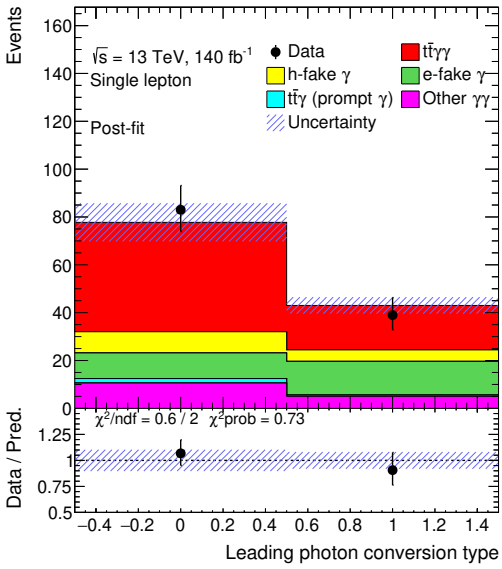

(a)

Figure 8.29: The photon conversion type of the leading photon. The first bin of the distribution corresponds to the unconverted photons, while the second bin corresponds to the sum of all converted photon types. The uncertainty band represents the total uncertainty after the fit to the data.

CHAPTER 9

Measurement results for $t\bar{t}\gamma\gamma/t\bar{t}\gamma$ ratio

"Perfection is achieved, not when there is nothing more to add, but when there is nothing left to take away."

— Antoine de Saint-Exupéry, *Wind, Sand and Stars*

As mentioned in the Chapter 2, one of the goals of the analysis presented in this thesis is to measure the ratio of the cross sections of $t\bar{t}\gamma\gamma$ and $t\bar{t}\gamma$ processes. The results of this ratio measurement are discussed in this chapter. The measurement of $t\bar{t}\gamma$ cross section was also performed in the same fiducial phase space as the $t\bar{t}\gamma\gamma$ cross section, as described in Section 8.1. First, the extraction method of the ratio by employing a multi-fit approach between the $t\bar{t}\gamma\gamma$ and $t\bar{t}\gamma$ process, along with the corresponding signal and control regions of the fit processes, are described in Section 9.1. The correlation of systematic uncertainties between the two processes is also discussed in this section. The measurement of the ratio, performed with pseudodata, is discussed in Section 9.2. The results with fit to the observed data, along with the final measurements of the analysis are presented in Section 9.3.

9.1 Definition and extraction of ratio

In this section, the ratio, R, of the cross sections of the $t\bar{t}\gamma\gamma$ process and the total $t\bar{t}\gamma$ process (including $t\bar{t}\gamma$ production and $t\bar{t}\gamma$ decay) in the single-lepton channel at particle level along with its extraction is described.

The R is defined as the ratio of cross sections of $t\bar{t}\gamma\gamma$ and $t\bar{t}\gamma$ process in the same fiducial phase space at particle level. The strength of the POI from the fit with data, μ_{ratio}, is used to measure the ratio, R as:

$$R = \frac{\sigma_{t\bar{t}\gamma\gamma}}{\sigma_{t\bar{t}\gamma}} \tag{9.1}$$

$$= \mu_{\text{ratio}} \times \frac{\text{K-factor}^{\text{NLO/LO}}_{t\bar{t}\gamma\gamma} \times \sigma^{\text{LO}}_{t\bar{t}\gamma\gamma}}{\sigma^{\text{NLO}}_{t\bar{t}\gamma,\,\text{production}} + \text{K-factor}^{\text{NLO/LO}}_{t\bar{t}\gamma} \times \sigma^{\text{LO}}_{t\bar{t}\gamma,\,\text{decay}}}, \tag{9.2}$$

where the total $t\bar{t}\gamma$ process includes both, photon from production as well as photon from decay, of the $t\bar{t}$ single-lepton decay channel. The $\text{K-factor}^{\text{NLO/LO}}_{t\bar{t}\gamma}$ is the ratio of the NLO to LO cross section of

the $t\bar{t}\gamma$ decay process. The $\sigma_{t\bar{t}\gamma\gamma}$ is what is measured in Chapter 8.

The $t\bar{t}\gamma$ measurement: In the $t\bar{t}\gamma$ measurement [1], a 4-class neural network was used to separate $t\bar{t}\gamma$ production (signal region, SR) from the $t\bar{t}\gamma$ decay, fake photon and other prompt photon backgrounds (control regions, CRs). The classifiers of this multi-class NN are listed below:

1. $t\bar{t}\gamma$ production classifier in the SR
2. $t\bar{t}\gamma$ decay classifier in the $t\bar{t}\gamma$ decay CR
3. second largest pseudo-continuous b-tagging score in the fake photon CR
4. second largest pseudo-continuous b-tagging score in the other prompt photon CR.

These classified distribution regions are shown in Figure 9.1. The inclusive $t\bar{t}\gamma$ total (including $t\bar{t}\gamma$ production and decay) cross section was then obtained via a profile likelihood fit to the discriminating variables in the SR and CRs. In the single-lepton channel, the fit is performed in the four regions. In the $t\bar{t}\gamma$ production and the $t\bar{t}\gamma$ decay regions, the output of the corresponding NN classifiers are used as fitted distributions, while in the photon fakes CR and in the other prompt photon CR, the distributions of the second largest pseudo-continuous $b-$tagging score are used. The choice of the fitted variable in the photon fakes CR and in the other prompt photon CR is motivated by a requirement to have bins that are sufficiently well populated by the targeted processes that are statistically limited. Additionally, since most of the other prompt photon backgrounds have fewer b-jets than the signal, the second largest $b-$tagging score distribution provides a reasonably good discrimination. The total uncertainties on the measuements were found to be in agreement with the MC predictions, though the cross sections were found to be slightly underestimated.

Correlation of systematic uncertainties in the ratio

As mentioned before, the $t\bar{t}\gamma\gamma$ measurement is harmonised so as to use the same object selection and the same sources of systematic uncertainties as in the $t\bar{t}\gamma$ measurement. The uncertainties related to the object reconstruction, luminosity and pile-up modelling are kept fully correlated between the two measurements. The uncertainties related to the modelling and the normalisation of the common processes which are estimated with the exact same MC samples ($t\bar{t}\gamma$ production, $t\bar{t}\gamma$ decay, $t\bar{t}$, $tW\gamma$, t-channel and s-channel single top quark, $t\bar{t}V$, $V\gamma$, V+jets, inclusive diboson samples) are also correlated among the two measurements. Background normalisation uncertainties and the uncertainties on the data-driven e-fake and h-fake photons are also correlated. Modelling uncertainties between different processes (e.g. parton shower uncertainties between $t\bar{t}\gamma$ and $t\bar{t}\gamma\gamma$) are considered uncorrelated as in the individual analysis.

Measurement

The ratio of $t\bar{t}\gamma\gamma$ to $t\bar{t}\gamma$ cross section is obtained by simultaneously fitting the $t\bar{t}\gamma\gamma$ BDT output and the corresponding variables used in the signal and background regions of the $t\bar{t}\gamma$ measurement described above. The BDT input to the combined fit are taken as documented in the $t\bar{t}\gamma\gamma$ measurement in this thesis, while the inputs of the $t\bar{t}\gamma$ measurement are taken from the $t\bar{t}\gamma$ measurement [1], as described before.

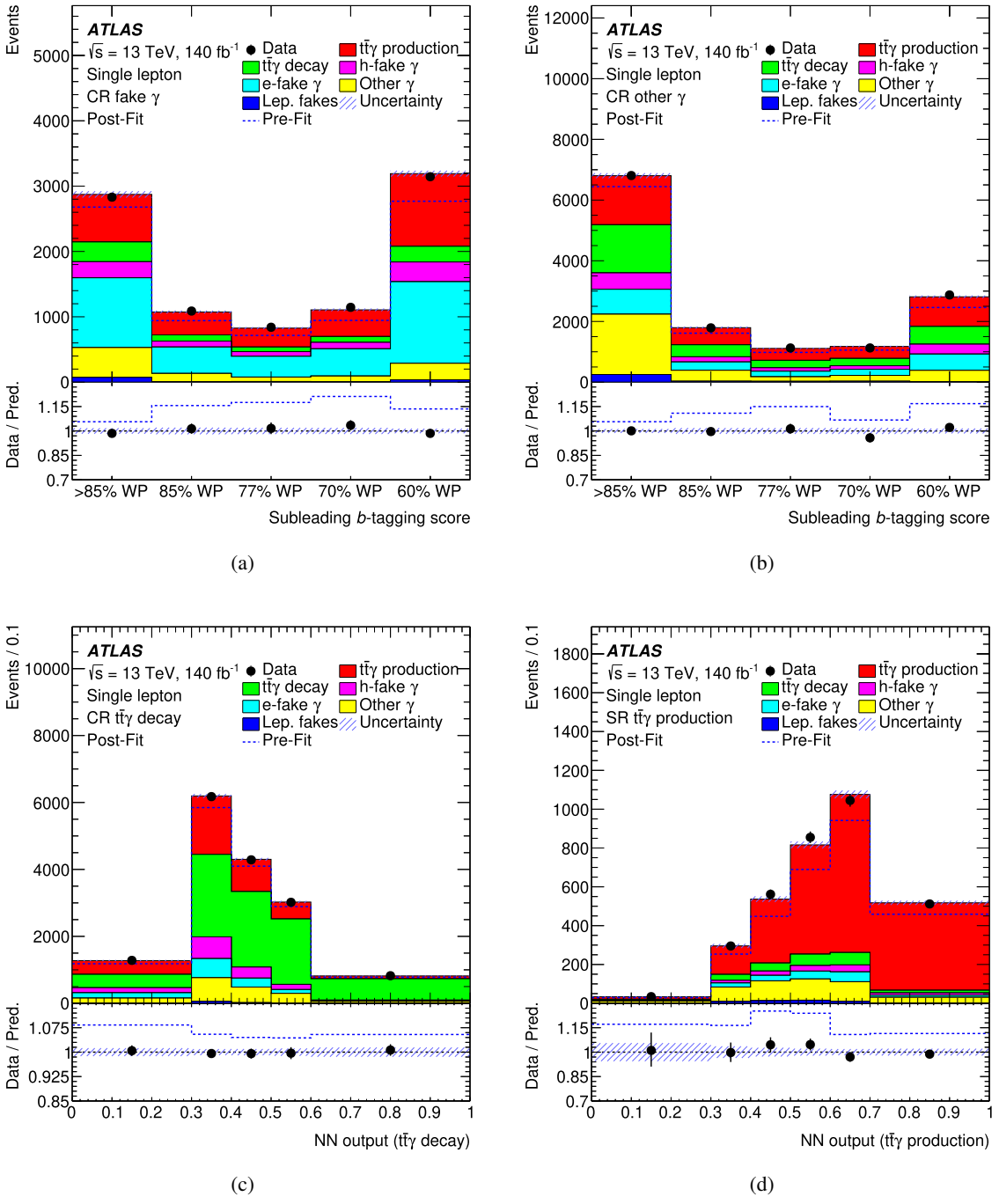

Figure 9.1: Distributions of (a) the $t\bar{t}\gamma$ production classifier in the SR, (b) the $t\bar{t}\gamma$ decay classifier in the $t\bar{t}\gamma$ decay CR and the second largest pseudo-continuous b-tagging score in (c) the photon fakes CR and (d) the other prompt photon CR after the fit to data for the measurement of the $t\bar{t}\gamma$ production cross section in the single-lepton channel. The uncertainty band represents the total post-fit uncertainty in the prediction [Plots taken from [1]].

In the fit setup for the ratio, a common normalisation factor is added to the likelihood for $t\bar{t}\gamma\gamma$ and $t\bar{t}\gamma$ processes using the same parameter, allowing for a simultaneous scaling of both. Another normalisation factor is associated only to the $t\bar{t}\gamma\gamma$ events. This results in $t\bar{t}\gamma\gamma$ events scaled by two normalisation factors, with one of the normalisation factors shared with the $t\bar{t}\gamma$ events. This means that the normalisation factor attached only to the $t\bar{t}\gamma\gamma$ events acts as a relative normalisation factor on top of the $t\bar{t}\gamma$ events, which is effectively the ratio parameter of both the cross sections that is to be measured. This allows to extract the ratio directly from the fit, along with its proper uncertainties which can be used to assess the impact of cancelation of the correlated systematic uncertainties in the ratio.

Since the normalisation of the total $t\bar{t}\gamma$ process is freely-floating in the fit, no normalisation uncertainty is considered for the $t\bar{t}\gamma$ production and decay templates. A 20% normalisation uncertainty is, however, considered for the $t\bar{t}\gamma$ decay template, which is the pre-fit uncertainty associated to the normalisation of the $t\bar{t}\gamma$ decay in the total $t\bar{t}\gamma$ measurement. This gives the fit freedom to adjust the fraction of $t\bar{t}\gamma$ production and $t\bar{t}\gamma$ decay events [1].

9.2 Test of fit setup with Asimov data

As was done for the $t\bar{t}\gamma\gamma$ cross section measurement (see Section 8.4), the combined $t\bar{t}\gamma\gamma$ and $t\bar{t}\gamma$ ratio fit is also performed with Asimov datasets for the inputs and setup described in Section 9.1. The expected strength of the ratio from the Asimov fit is 1, with a total uncertainty of $^{+20\%}_{-18\%}$, with a large statistical component of $^{+17\%}_{-15\%}$.

Since the measurement of the standalone $t\bar{t}\gamma\gamma$ process in the Asimov fit has a total uncertainty of $^{+23\%}_{-21\%}$, it can be concluded that there is a cancelation of systematic uncertainties between the two measurements in the ratio.

The plots for the NPs for the ratio measurement can be seen in Figures 9.2. Some of the NPs which are particular to the $t\bar{t}\gamma$ measurement, including the $W\gamma$, $Z\gamma$ and fake lepton uncertainties, are found to be constrained. Also, the pre-fit uncertainty of 20% on the K-factor of the $t\bar{t}\gamma$ decay template is also significantly constrained. Additionally, the $t\bar{t}\gamma$ production and $t\bar{t}\gamma$ decay modelling uncertainties, and the data-driven fake estimation uncertainties are also constrained. These constraints stem from the inclusion of the $t\bar{t}\gamma$ events in the combined fit setup. As mentioned earlier, the definitions of all these physics objects, photons, leptons, jets, b-quark jets and missing transverse momentum, are the same as in the $t\bar{t}\gamma$ analysis [1] to facilitate the measurement of the ratio of their cross-sections. While evaluating the impact of systematic uncertainties on the ratio, several experimental uncertainties, such as luminosity, jet, $b-$tagging, lepton uncertainties, are found to be reduced with respect to the individual measurement of $t\bar{t}\gamma\gamma$. This is expected since these uncertainties are fully correlated among the $t\bar{t}\gamma\gamma$ and $t\bar{t}\gamma$ processes and their effect cancels out in the ratio. Additionally, $t\bar{t}\gamma$ production and decay modelling uncertainties play a larger role, as is expected by the inclusion of the total $t\bar{t}\gamma$ process in the fit. This is further highlighted in the ranking plot of the major uncertainties as shown in Figure 9.3, where the $t\bar{t}\gamma$ modelling uncertainties ($t\bar{t}\gamma$ decay PS (Herwig7) and $t\bar{t}\gamma$ decay ISR) show up.

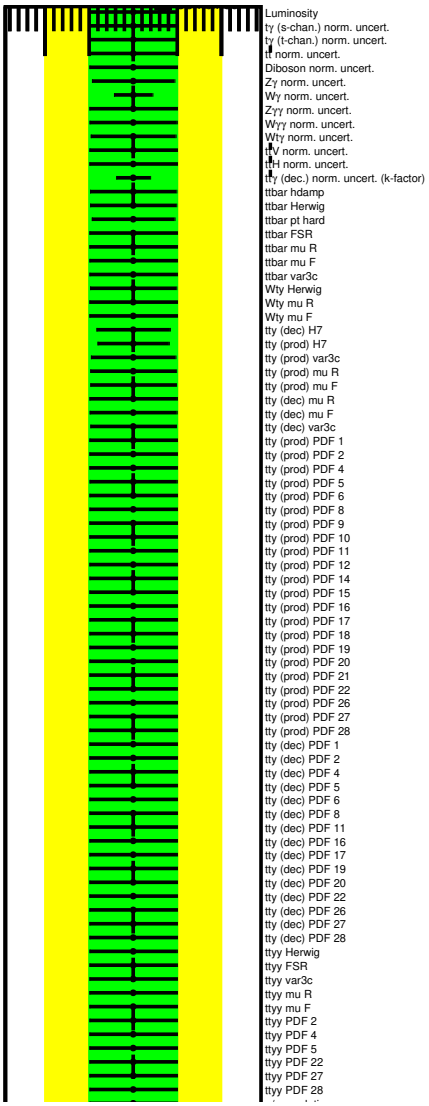
Luminosity
tγ (s-chan.) norm. uncert.
tγ (t-chan.) norm. uncert.
tt norm. uncert.
Diboson norm. uncert.
Zγ norm. uncert.
Wγ norm. uncert.
Zγγ norm. uncert.
Wγγ norm. uncert.
Wtγ norm. uncert.
ttV norm. uncert.
ttH norm. uncert.
ttγ (dec.) norm. uncert. (k-factor)
ttbar hdamp
ttbar Herwig
ttbar pt hard
ttbar FSR
ttbar mu R
ttbar mu F
ttbar var3c
Wty Herwig
Wty mu R
Wty mu F
tty (dec) H7
tty (prod) H7
tty (prod) var3c
tty (prod) mu R
tty (prod) mu F
tty (dec) mu R
tty (dec) mu F
tty (dec) var3c
tty (prod) PDF 1
tty (prod) PDF 2
tty (prod) PDF 4
tty (prod) PDF 5
tty (prod) PDF 6
tty (prod) PDF 8
tty (prod) PDF 9
tty (prod) PDF 10
tty (prod) PDF 11
tty (prod) PDF 12
tty (prod) PDF 14
tty (prod) PDF 15
tty (prod) PDF 16
tty (prod) PDF 17
tty (prod) PDF 18
tty (prod) PDF 19
tty (prod) PDF 20
tty (prod) PDF 21
tty (prod) PDF 22
tty (prod) PDF 26
tty (prod) PDF 27
tty (prod) PDF 28
tty (dec) PDF 1
tty (dec) PDF 2
tty (dec) PDF 4
tty (dec) PDF 5
tty (dec) PDF 6
tty (dec) PDF 8
tty (dec) PDF 11
tty (dec) PDF 16
tty (dec) PDF 17
tty (dec) PDF 19
tty (dec) PDF 20
tty (dec) PDF 22
tty (dec) PDF 26
tty (dec) PDF 27
tty (dec) PDF 28
ttyy Herwig
ttyy FSR
ttyy var3c
ttyy mu R
ttyy mu F
ttyy PDF 2
ttyy PDF 4
ttyy PDF 5
ttyy PDF 22
ttyy PDF 27
ttyy PDF 28

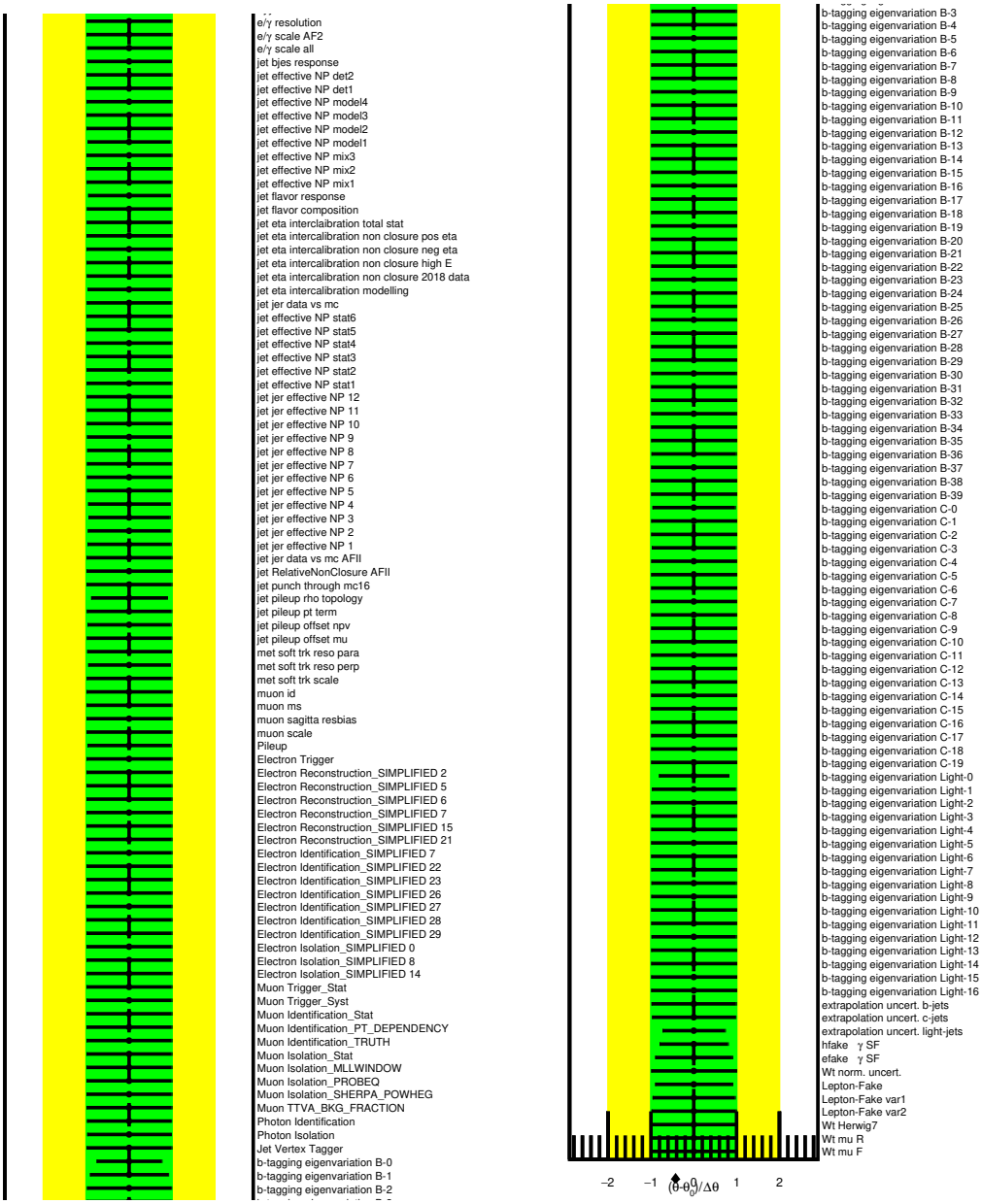

Figure 9.2: Plot showing the pulls and constraints of nuisance parameters for the ratio of $t\bar{t}\gamma\gamma$ to $t\bar{t}\gamma$ in fit to Asimov dataset.

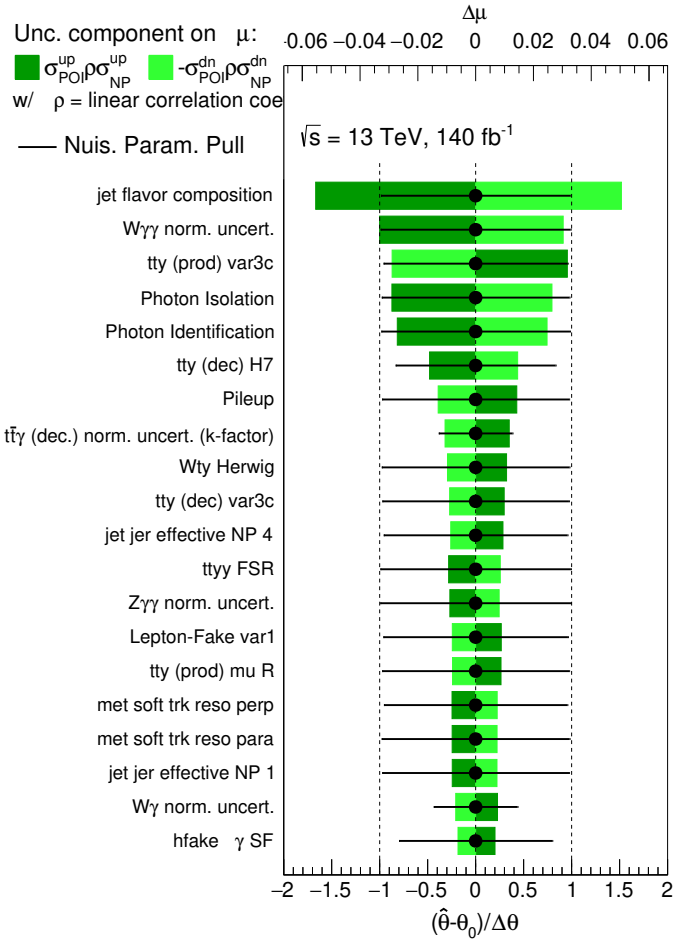

Figure 9.3: The ranking plot of the 20 most important nuisance parameters for the ratio of $t\bar{t}\gamma\gamma$ to $t\bar{t}\gamma$ in fit to Asimov dataset.

9.3 Results for the ratio of $t\bar{t}\gamma\gamma$ to total $t\bar{t}\gamma$ processes

The combined fit with Asimov dataset works well, with the impact on systematic uncertainties as expected from the inclusion of the $t\bar{t}\gamma$ events from the corresponding measurement. As a check for the validity of the combined fit setup, the signal strength of the $t\bar{t}\gamma$ process was also extracted as an independent POI. The uncertainties on the $t\bar{t}\gamma$ signal strength were found to be $^{+7.2\%}_{-6.6\%}$, which is in agreement with the $t\bar{t}\gamma$ measurement[1]. The fit setup is then used to fit with the observed data, akin to what was done in Section 8.5 for both the $t\bar{t}\gamma\gamma$ and $t\bar{t}\gamma$ processes.

The signal strength, μ_{ratio}, corresponding to the ratio in the combined fit of $t\bar{t}\gamma$ and $t\bar{t}\gamma\gamma$ processes is observed to be 0.79. The total expected uncertainty of the strength of the ratio is $^{+17\%}_{-16\%}$ and is dominated by the statistical uncertainty of $^{+15\%}_{-13\%}$, with a systematic component of ~8%. The ratio, R, is calculated from Equation 9.2 as:

$$R(\text{observed}) = \frac{\sigma_{t\bar{t}\gamma\gamma}}{\sigma_{t\bar{t}\gamma}} \tag{9.3}$$

$$= \mu_{\text{ratio}} \times R(\text{expected}) \tag{9.4}$$

$$= \mu_{\text{ratio}} \times \frac{\sigma^{\text{NLO}}_{t\bar{t}\gamma\gamma}(\text{expected})}{\sigma_{t\bar{t}\gamma,\text{total}}(\text{expected})} \tag{9.5}$$

$$\tag{9.6}$$

where $\sigma_{t\bar{t}\gamma\gamma} = 2.62\,\text{fb}$.

The $\sigma_{t\bar{t}\gamma}$ at the particle level has been evaluated to be:
$624.49^{+88.79}_{-0.109.25}(\text{scale})^{+13.11}_{-8.94}(\text{PDF})\,\text{fb}$.

The value of the ratio from fit to data is, thus, calculated by employing the μ_{ratio} in Equation 9.6 as:

$$R = (3.30^{+0.70}_{-0.65}) \times 10^{-3} = (3.30^{+0.63}_{-0.55}(\text{stat})^{+0.32}_{-0.34}(\text{syst})) \times 10^{-3} \tag{9.7}$$

In the above calculations, the uncertainties are calculated using the uncertainties on μ_{ratio}:

$$\Delta R = \Delta\mu_{\text{ratio}} R(\text{expected}) \tag{9.8}$$

With a total uncertainty of $^{+22\%}_{-20\%}$ on the signal strength of the $t\bar{t}\gamma\gamma$ cross section (see Section 8.5), it can again be concluded that there is a small cancelation of systematic uncertainties between the two measurements in the ratio.

The pull plots for the NPs in the ratio measurement can be seen in Figure 9.4. The larger shifts on the $t\bar{t}\gamma$ modelling uncertainties are expected from the $t\bar{t}\gamma$ fit, and are in agreement with observations of the $t\bar{t}\gamma$ analysis. The Herwig7 PS uncertainty of $t\bar{t}\gamma$ production is largely constrained, by more than 1σ. This means that Herwig7 seems to better describes the data than the nominal Pythia8 sample used for $t\bar{t}\gamma$ production. The $W\gamma$ normalisation uncertainty and the pre-fit uncertainty of the $t\bar{t}\gamma$ decay template are significantly constrained by the fit to the $t\bar{t}\gamma$ regions. In addition, several experimental uncertainties related to the jets, b-tagging, $e\gamma$ scale and $E_{\text{T}}^{\text{miss}}$ are pulled in the fit with data. These pulls were not observed for the $t\bar{t}\gamma\gamma$ cross section measurement, but they are in agreement

with the $t\bar{t}\gamma$ measurement [1].

Figure 9.5 shows the correlation of the NPs and the ratio POI in the measurement after fit to data. Apart from the jet flavor compositon, which has an anti-correlation of ~29% with the ratio, all the correlation values between the ratio and the NPs are found to be less than 20%.

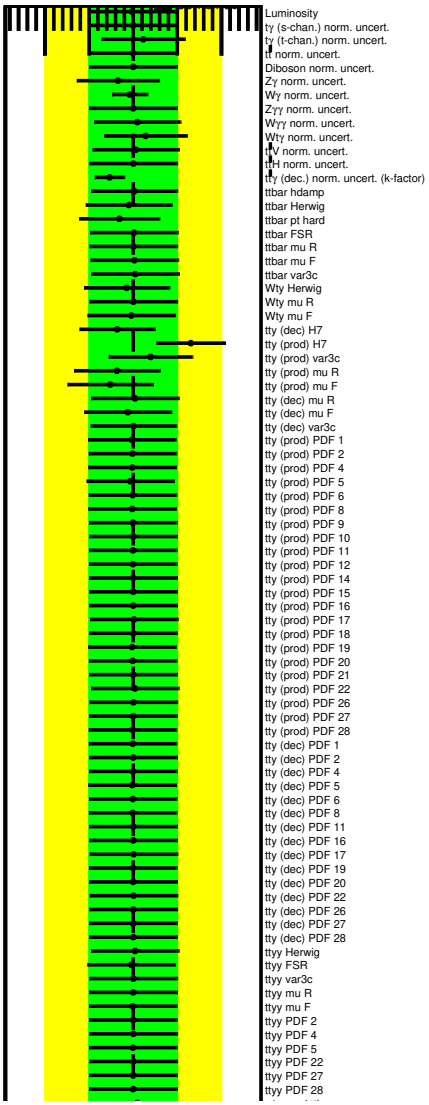

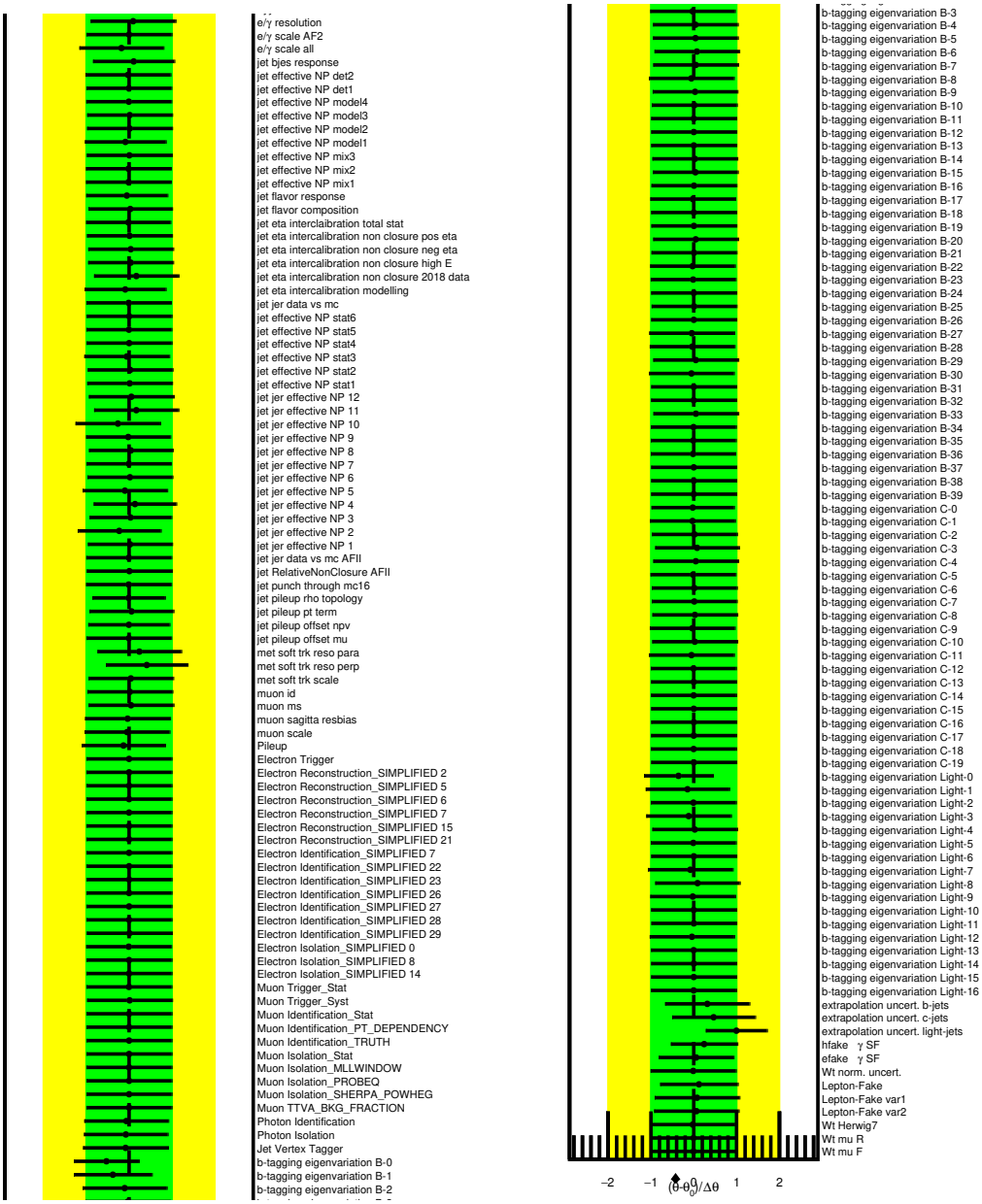

Figure 9.4: Plot showing the pulls and constraints of nuisance parameters on the ratio with fit to data in single-lepton channel

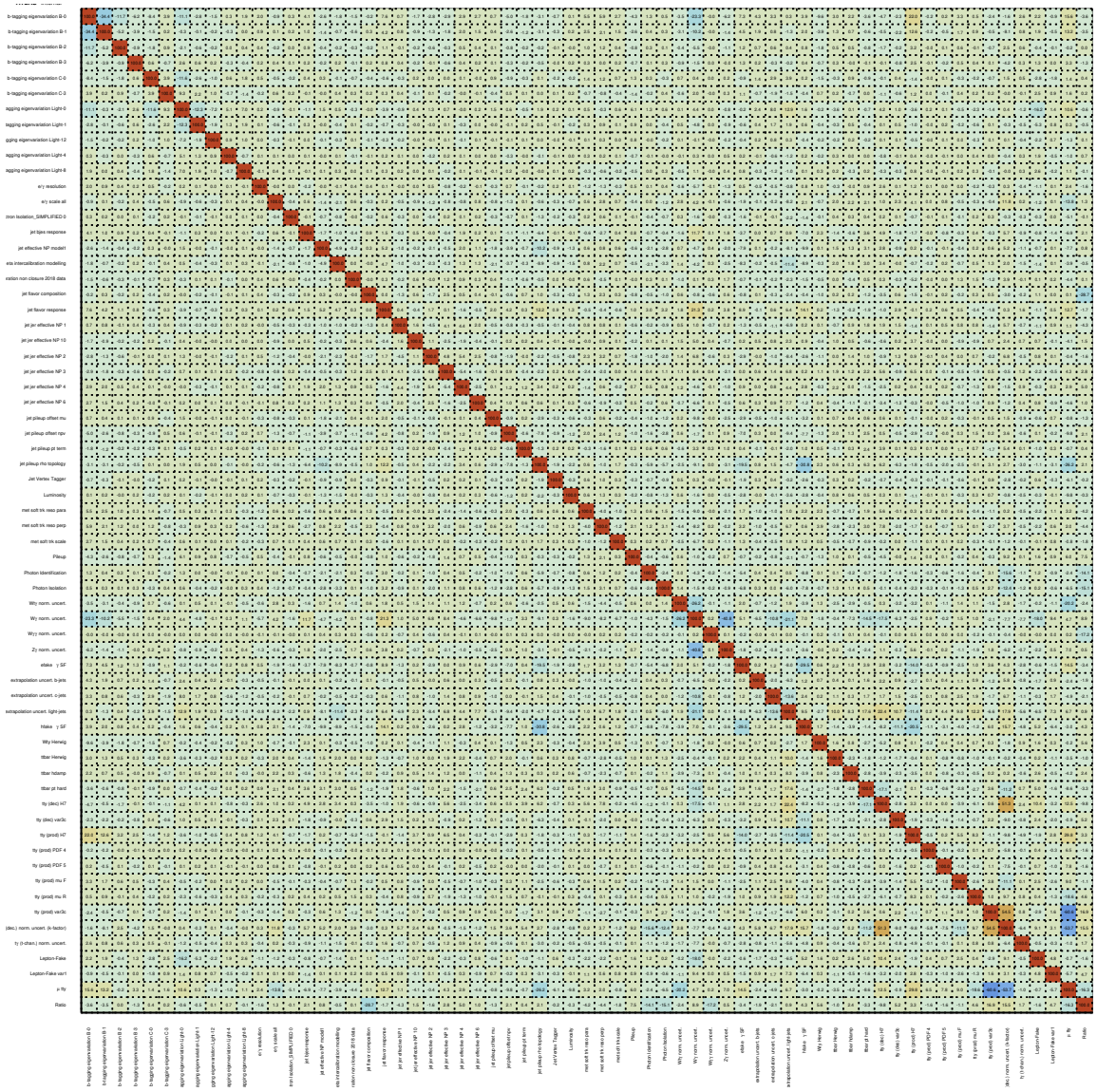

Figure 9.5: Correlations of NPs (with threshold of 10%) with the ratio measurement of $t\bar{t}\gamma\gamma$ to $t\bar{t}\gamma$ in the fit to data. $\mu_{t\bar{t}\gamma}$, which scales the $t\bar{t}\gamma$ process, is the second POI in the combined fit.

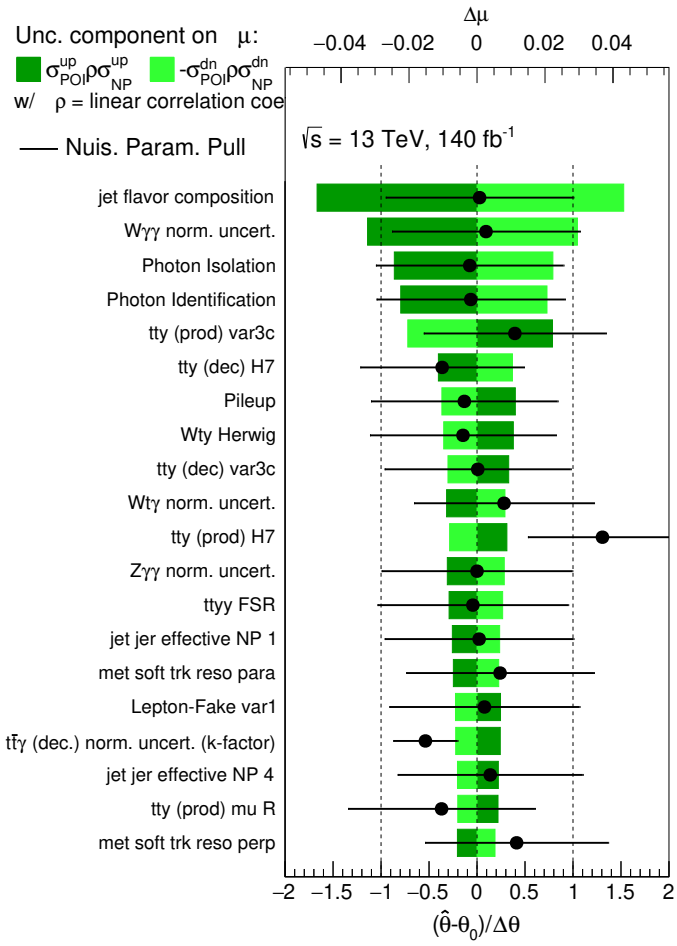

Figure 9.6: The ranking plot of the 20 most important nuisance parameters for the ratio measurement of $t\bar{t}\gamma\gamma$ to $t\bar{t}\gamma$ in fit to data.

Ranking of nuisance parameters

The impact of the most dominant systematic uncertainties are shown in Figure 9.6. The significant pull on the HERWIG7 PS uncertainty of $t\bar{t}\gamma$ production already reflects the pulls shown before. The impact of the $t\bar{t}\gamma$ modelling uncertainties, mostly owing to the inclusion of $t\bar{t}\gamma$ events, increases in the fit with data, compared to the Asimov fit results.

Table 9.1 shows the grouped impact of the systematic uncertainties on the ratio for various sources of uncertainties grouped together. Compared to the impact of the systematic uncertainties in the $t\bar{t}\gamma\gamma$ cross section measurement (Table 8.3), the impact reduces in the ratio. The total absolute uncertainty of ∼14% in the $t\bar{t}\gamma\gamma$ cross section reduces to ∼8% in the ratio. Several uncertainties get reduced with respect to the individual measurement of $t\bar{t}\gamma\gamma$. In particular, the largest cancellation is related to experimental uncertainties such as luminosity, jet, b-tagging, lepton uncertainties (expected since they are fully correlated among processes). Some background related uncertainties such as photon fake uncertainties have a smaller impact as well, owing to the constraints arising from the inclusion of the $t\bar{t}\gamma$ regions. Additionally, the $t\bar{t}\gamma$ production and decay modelling uncertainties increase, as expected

from including the $t\bar{t}\gamma$ measurement regions in the fit. One can, therefore, conclude that the ratio of $t\bar{t}\gamma\gamma$ to $t\bar{t}\gamma$ effectively constrains many systematic uncertainties through cancellation, compared to the standalone $t\bar{t}\gamma\gamma$ cross-section measurement. This is facilitated by the harmonisation of object definitions and phase space selections between the two processes. This cancelation of uncertainties is better illustrated in the comparison table of relative uncertainties of both the $t\bar{t}\gamma\gamma$ cross section and the ratio measuement in Section 9.4.

Table 9.1: Summary of the absolute impact of the systematic uncertainties on the signal strength of the ratio of $t\bar{t}\gamma\gamma$ to $t\bar{t}\gamma$ in the single-lepton channel, grouped into different categories. The category 'JET' corresponds to the combined effect of JES, jet resolution and JVT uncertainties, while 'Photon' and 'Leptons' correspond to all experimental uncertainties related to photons and leptons, respectively. The category '$t\bar{t}\gamma\gamma$ modelling' includes the PDF and theoretical modelling uncertainties on $t\bar{t}\gamma\gamma$.

Source	$\Delta\mu_{t\bar{t}\gamma\gamma/t\bar{t}\gamma}$	Up/Down Uncertainty
Background modelling	0.012	(+0.012, –0.011)
Fake-lepton background estimate	0.007	(+0.007, –0.007)
Fake-photon background estimates	0.004	(+0.004, –0.004)
JET	0.047	(+0.049, –0.045)
Leptons	0.003	(+0.003, –0.003)
Luminosity	0.001	(+0.001, –0.001)
MET	0.009	(+0.009, –0.009)
Photon	0.032	(+0.033, –0.030)
Pileup	0.011	(+0.011, –0.010)
Prompt background normalisation	0.034	(+0.036, –0.033)
b-tagging	0.008	(+0.008, –0.008)
$t\bar{t}\gamma$ decay normalisation	0.007	(+0.007, –0.006)
$t\bar{t}\gamma$ decay modelling	0.014	(+0.015, –0.014)
$t\bar{t}\gamma$ production Herwig7	0.008	(+0.009, –0.008)
$t\bar{t}\gamma$ production modelling	0.022	(+0.023, –0.021)
$t\bar{t}\gamma\gamma$ modelling	0.010	(+0.010, –0.009)
MC statistical uncertainties	0.022	(+0.021, –0.023)
Total systematic uncertainty	0.079	(+0.082, –0.076)

9.4 Relative uncertainties in the measurements

Table 9.2 shows the relative uncertainties of the measurement on both, the measured cross section of $t\bar{t}\gamma\gamma$ process as well as the ratio of $t\bar{t}\gamma\gamma$ to $t\bar{t}\gamma$, illustrating the impact of the cancelation of systematic uncertainties in the ratio. As is expected with the inclusion of $t\bar{t}\gamma$ process in the fit, the relative impact of $t\bar{t}\gamma$ production and decay modelling uncertainties increases compared with the measurement of the $t\bar{t}\gamma\gamma$ cross section. A lot of experimental uncertainties, such as the ones related to jets (including $b-$tagged), photons, leptons and $E_{\mathrm{T}}^{\mathrm{miss}}$ are reduced. The uncertainty related to luminosity almost cancels out, given that both the measurements make use of the data collected at the same luminosity. Since the $t\bar{t}\gamma$ measurement is able to better constrain the fake-photon background, these uncertainties also largely reduce. The relative impact of the total systematic uncertainty reduces from 15% in $t\bar{t}\gamma\gamma$ measurement to 10% in the ratio measurement.

Table 9.2: Summary of the relative impact of the systematic uncertainties, in percentage, on the $t\bar{t}\gamma\gamma$ fiducial inclusive cross section and $R_{t\bar{t}\gamma\gamma/t\bar{t}\gamma}$ grouped into different categories. The category 'Jet' corresponds to the effect of JES, jet resolution and JVT uncertainties, 'Photon' and 'Leptons' include all experimental uncertainties related to photons and leptons, respectively.

Source	$\Delta\sigma_{t\bar{t}\gamma\gamma}/\sigma_{t\bar{t}\gamma\gamma}$ [%]	$\Delta R_{t\bar{t}\gamma\gamma/t\bar{t}\gamma}/R_{t\bar{t}\gamma\gamma/t\bar{t}\gamma}$ [%]
$t\bar{t}\gamma\gamma$ modelling	1.4	1.3
Prompt-photon background norm. & modelling	4.4	5.8
Fake-photon background estimates	6.5	0.5
Fake-lepton background estimate	–	0.9
Jet	9.7	5.9
Photon	6.5	4.0
b-tagging	3.4	1.0
Leptons	1.5	0.3
Luminosity	1.4	0.1
$E_{\mathrm{T}}^{\mathrm{miss}}$	0.4	1.1
Pile-up	1.6	1.4
MC statistical uncertainties	2.5	2.8
Total systematic uncertainty	15.0	10.0

CHAPTER 10

Summary and Conclusion

The measurements performed in the analysis and presented in the thesis are summarized here, along with the subsequent results obtained. These include the measurement of the $t\bar{t}\gamma\gamma$ cross section and its ratio with the $t\bar{t}\gamma$ cross section. The measurments are performed in $t\bar{t}$ single-lepton channel using the Run 2 dataset (2015-2018) corresponding to a total luminosity of 140.1 fb^{-1} collected by ATLAS at $\sqrt{s}$ of 13 TeV.

For the $t\bar{t}\gamma\gamma$ cross section, a BDT is employed to discriminate the $t\bar{t}\gamma\gamma$ signal from the background processes, and the cross section is obtained by performing a profile likelihood fit to the BDT output. Various systematic uncertainties, stemming from modelling, experiment and background normalisations, are considered in the fit. Data-driven fake photon estimates, which were evaluated for the $t\bar{t}\gamma$ analysis [1], were also used in this analysis and help to better describe the observed data.

The $t\bar{t}\gamma\gamma$ cross section is measured at particle level in a fiducial phase space. The cross section is found to be $\sigma_{t\bar{t}\gamma\gamma} = 2.42^{+0.58}_{-0.53}$ fb $= 2.42^{+0.46}_{-0.38}$ (stat) $^{+0.35}_{-0.38}$(syst) fb. The significance of the signal process is evaluted at 5.2σ, which serves as the first experimental observation of the $t\bar{t}\gamma\gamma$ process.

Furthermore, the ratio of $t\bar{t}\gamma\gamma$ to $t\bar{t}\gamma$ is evaluated using input regions from the $t\bar{t}\gamma$ measurement in single-lepton channel [1] and the BDT output correspoding to the $t\bar{t}\gamma\gamma$ measurement. The $t\bar{t}\gamma\gamma$ measurement is kept in close agreement with the $t\bar{t}\gamma$ measurement in terms of kinematic cuts on physics objects as well as the treatment of systematic uncertainties. The ratio, $R_{t\bar{t}\gamma\gamma/t\bar{t}\gamma}$, is obtained from a combined fit of the $t\bar{t}\gamma\gamma$ and $t\bar{t}\gamma$ signal and control regions, the former of which is presented in this thesis. The value of the ratio is found to be $(3.30^{+0.70}_{-0.65}) \times 10^{-3} = (3.30^{+0.63}_{-0.55}\ (\text{stat})^{+0.32}_{-0.34}\ (\text{syst})) \times 10^{-3}$.

Though both, the $t\bar{t}\gamma\gamma$ cross section and the ratio measurements, are dominated by statistical uncertainty, the latter shows an appreciable cancellation of several systematic uncertainties. In general, a lot of experimental uncertainties, such as jets (including $b-$tagged), photons, leptons and $E_{\text{T}}^{\text{miss}}$ related uncertainties, partially cancel out. The relative impact of the total systematic uncertainty reduces from 15% in $t\bar{t}\gamma\gamma$ measurement to 10% in the ratio measurement.

Due to the lack of available theoretical calculations of the ratio that would allow for a direct comparison with the measured value, a reference ratio is calculated using the nominal MadGraph5_aMC@NLO +Pythia 8 samples. The reference ratio of the fiducial $t\bar{t}\gamma\gamma$ LO cross section to the $t\bar{t}\gamma$ cross section (estimated as the sum of the NLO $t\bar{t}\gamma$ production and $t\bar{t}\gamma$ decay contributions, including the NLO/LO K-factor), yields a value of $(2.46^{+0.73}_{-0.94}\ (\text{scale})^{+0.10}_{-0.06}\ (\text{PDF})) \times 10^{-3}$. However, the uncertainties on the reference ratio are based on a combination of LO and NLO predictions, and no uncertainty is assigned to the K-factor applied to the $t\bar{t}\gamma$ decay contribution. Also, since the scale

and PDF uncertainties are evaluated assuming uncorrelated uncertainties between the individual cross sections of both the processes, the reference value and its uncertainty are meant to be treated as illustrative only, and not viable for direct comparison with the measured value.

The measurements presented in this thesis are limited by the data statistics. Therefore, it is expected that more data in future collider experiment runs will help refine the measurements even further. In this regard, if there is enough data, a combined measurement of the $t\bar{t}\gamma\gamma$ cross section, including single-lepton and dilepton channels, can also be performed, as is already done in the $t\bar{t}\gamma$ analysis. The ratio calculated from such a combined fit will help constrain the systematic uncertainties even more, while leveraging the reduced statistical uncertainty. Probing new physics effects such as anomalous couplings can become more feasible as well.

Also, since the $t\bar{t}\gamma\gamma$ process is an irreducible background to the $t\bar{t}H$ (H$\rightarrow \gamma\gamma$) process, the results presented in this thesis can help refine the $t\bar{t}H$ studies with a better background modelling.

This work presented in this analysis is summarized in a public arXiv preprint [29] and has been submitted to Physics Letter B for publication. Overall, though the measurements lack proper theoretical validation, they set a stage for future analyses performed with larger datasets which can probe new physics phenomena more effectively.

APPENDIX A

Preliminary studies with other variables

In the preliminary stages of the analysis for the $t\bar{t}\gamma\gamma$ process, various discriminating variables were evaluated for their sensitivity. Key variables, such as the photon conversion type (converted or unconverted) for the leading photon, the ΔR between subleading photon and lepton, and the invariant mass of subleading photon and lepton were initially employed to distinguish between signal and background components. To quantify their effectiveness, template fits to pseudodata were performed using each variable independently. These studies demonstrated that the individual variables provided non-negligible discriminating power. However, to achieve sensitivity approaching the discovery threshold, a more sophisticated multivariate approach based on BDT was adopted. Below are the results for some of the tested variables and the corresponding significance achieved:

The expected significances for the mentioned variables were found to be as follows from the Asimov fit:

1. ΔR between subleading photon and lepton - 5.0σ
2. Invariant mass of subleading photon and lepton - 4.9σ
3. Leading photon conversion type - 4.8σ

The post-fit plots of the variables are shown in Figure A.1. The above variables already hint at evidence of the $t\bar{t}\gamma\gamma$ process with greater than 4.0σ expected significance. The BDT score used in the analysis further enhances the expected significance to 5.6σ, thus validating its usefulness.

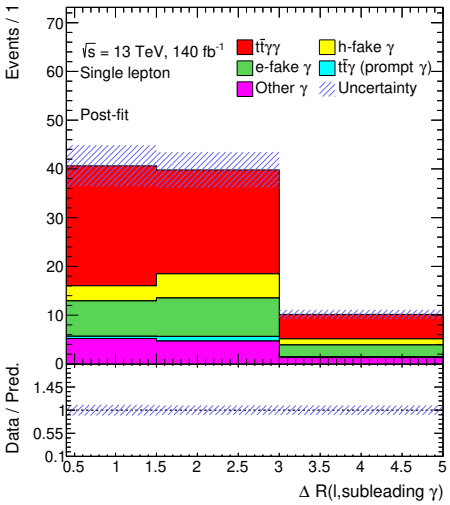

(a) ΔR between subleading photon and lepton

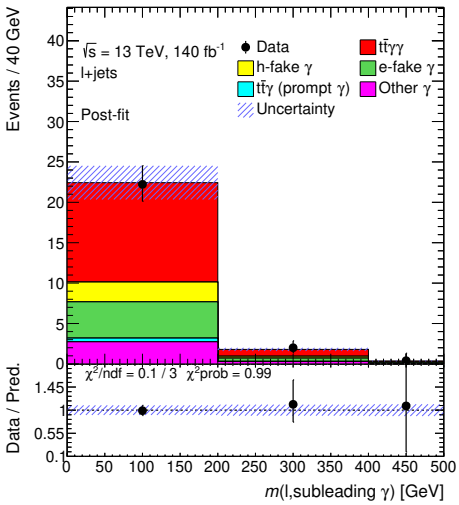

(b) Invariant mass of subleading photon and lepton

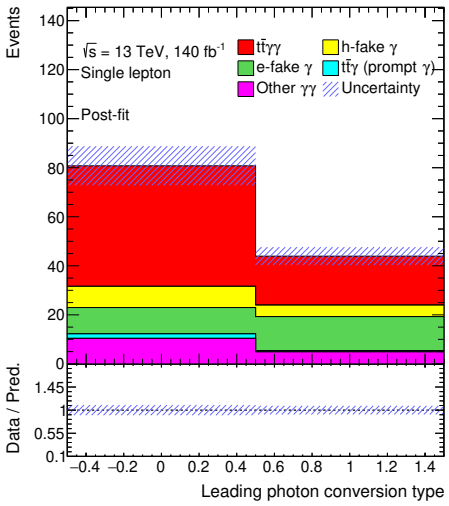

(c) Leading photon conversion type

Figure A.1: Distributions of variables after fitting to Asimov data. The uncertainty band represents the total post-fit uncertainty.

APPENDIX B

Treatment of negative weights in BDT training

In this section, plots are presented that show the impact of using absolute weights on the shapes of the input distributions of signal and background samples used in the BDT training. Each plot contains two histograms, one for the signal simulation and one for the background processes included in the training. One histogram shows the nominal variable distribution including all events with their corresponding negative or positive weights (solid line). The second histogram shows the corresponding distribution using only absolute weights and rescaled to the nominal distribution (dashed line). In the ratio plot the ratio of the corrected distribution with respect to the nominal distribution is shown, which are mostly flat. The shapes of the distributions are not largely impacted by such a normalisation, and the variables retain their discriminating power, thus validating their use in the BDT.

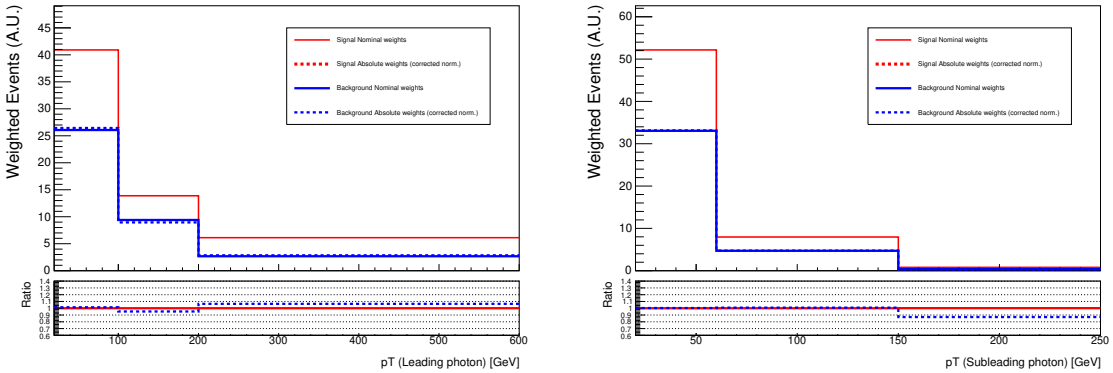

(a) (b)

Figure B.1: The impact of using absolute weights on the p_{T} distributions of the (a) leading and (b) subleading photons.

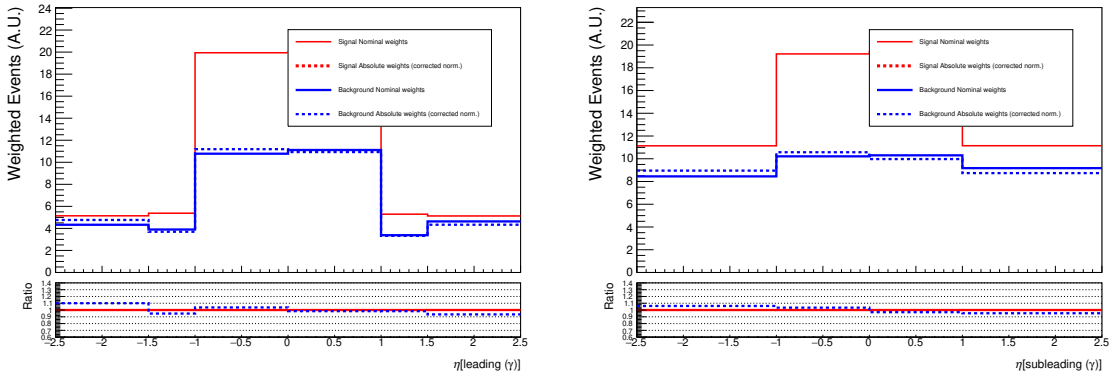

(a) (b)

Figure B.2: The impact of using absolute weights on the η distributions of the (a) leading and (b) subleading photons.

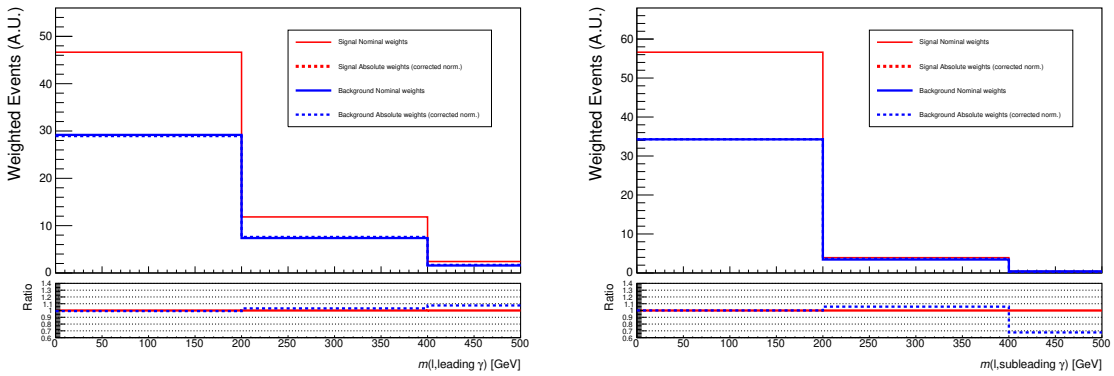

(a) (b)

Figure B.3: The impact of using absolute weights on the invariant mass distributions of the lepton and the (a) leading or (b) subleading photon.

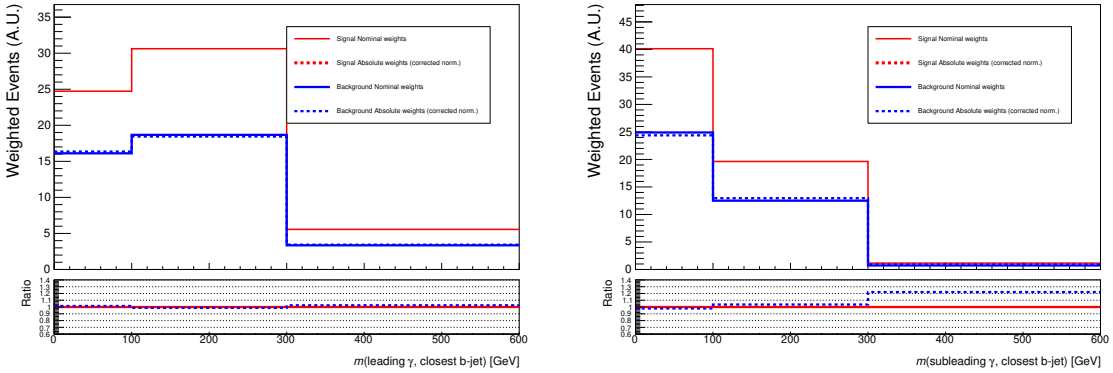

(a) (b)

Figure B.4: The impact of using absolute weights on the invariant mass distributions of the (a) leading or (b) subleading photon and the closest b-jet.

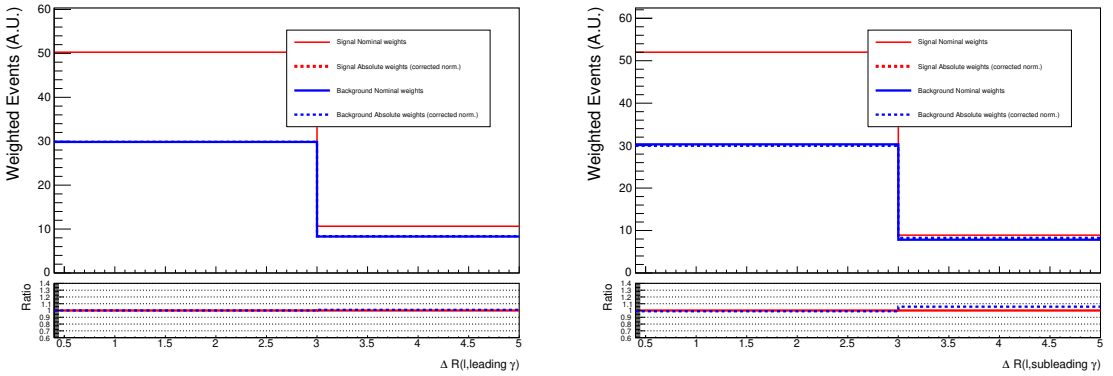

(a) (b)

Figure B.5: The impact of using absolute weights on the ΔR distributions between the lepton and the (a) leading and (b) subleading photon.

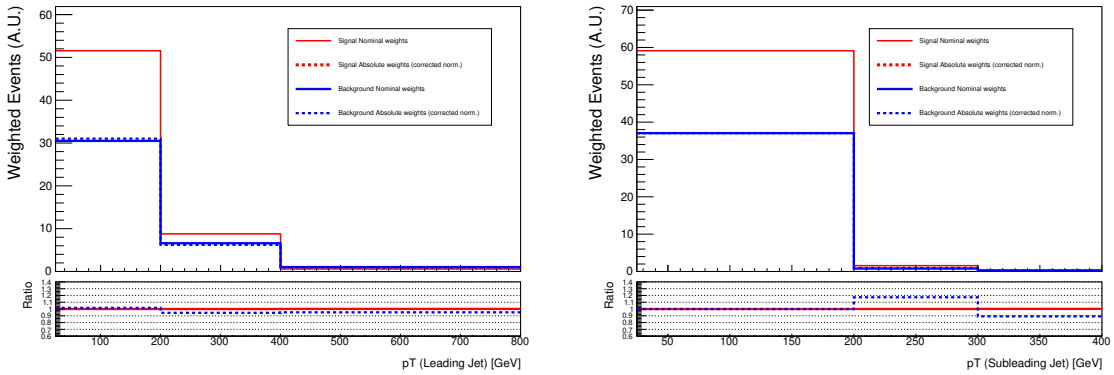

(a) (b)

Figure B.6: The impact of using absolute weights on the p_{T} distributions of the (a) leading and (b) subleading jets.

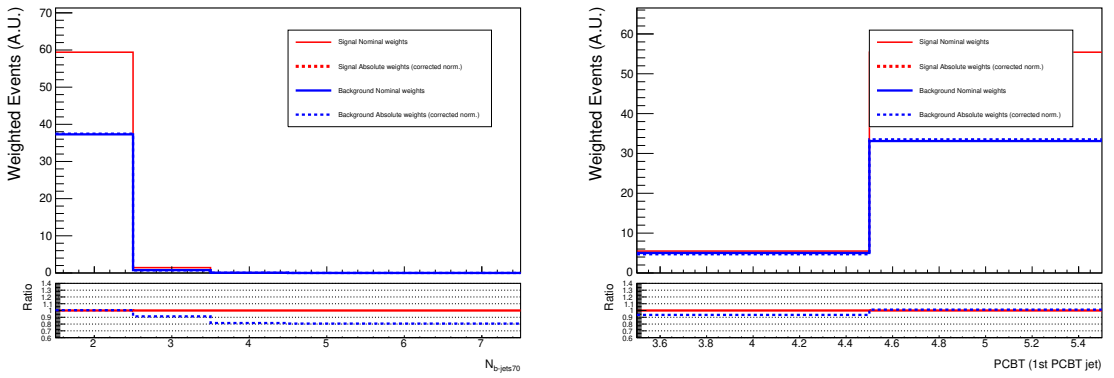

(a) (b)

Figure B.7: The impact of using absolute weights on the distributions of (a) the number of b-jets at 70% WP and (b) the highest DL1r score for the jet with PCBT binning.

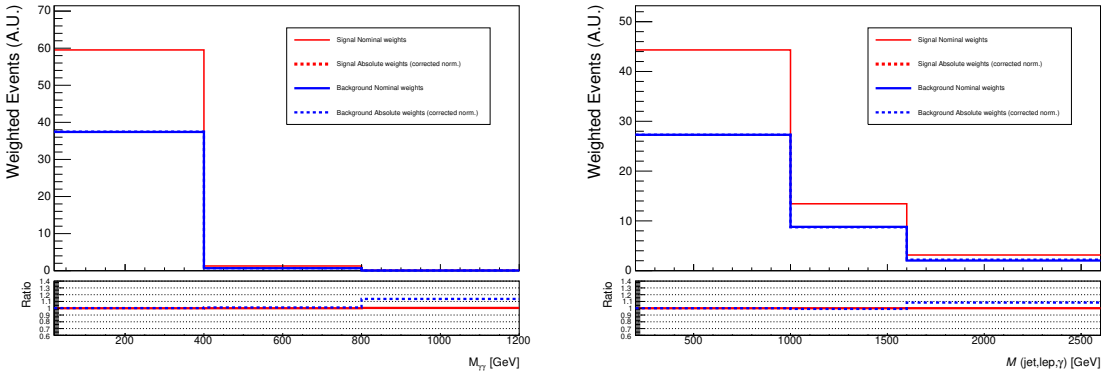

(a) (b)

Figure B.8: The impact of using absolute weights on the (a) Diphoton invariant mass and (b) invariant mass of all jets, the lepton, and both photons.

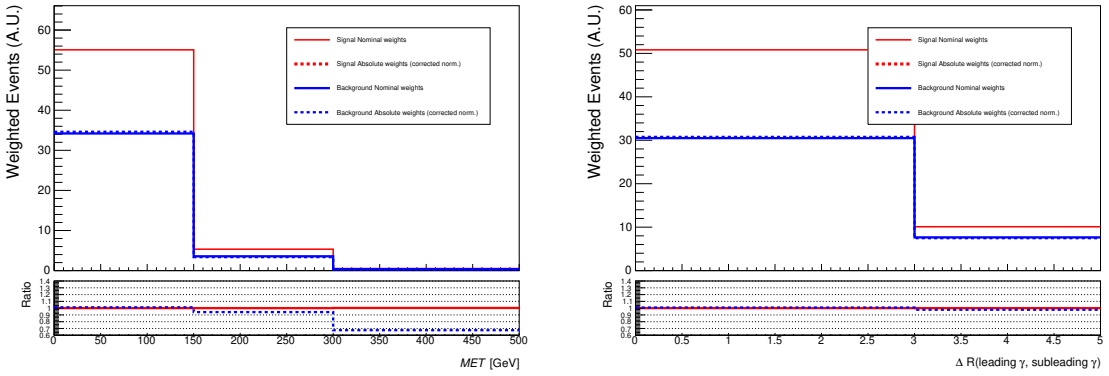

(a) (b)

Figure B.9: The impact of using absolute weights on the (a) $E_{\mathrm{T}}^{\mathrm{miss}}$ distribution and (b) ΔR distributions between leading and subleading photons.

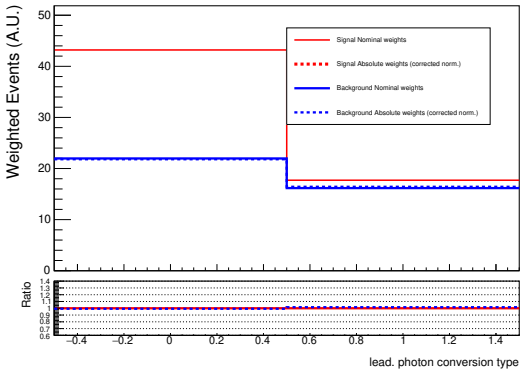

(a)

Figure B.10: The impact of using absolute weights on the photon conversion types (converted or unconverted) for the leading photon.

APPENDIX C

BDT study with 3-class classification

As a further study to check the impact of loosening the selection to increase the statistics of the background samples in the training, a three-class classification approach for the BDT was also trained using the b-tagging WP of 85% to leverage the increased statistics of the processes. The background processes were properly reweighted per process in such a way that the background is composed the same way as in the main event selection. Technically, the background processes at WP85 were scaled by the ratio of number of events selected with the WP70 and WP85, as shown in Table C.1. The total background was divided into two categories: background events with prompt photons and background events with fake photons. This was done for each of the background processes per category (prompt photons and fake photons backgrounds) included in the training. The scaling factors used to scale the samples can be seen in Table C.1. The input variables for this BDT are the same as used in the analysis (see Section 6) but only switching the variables involving the WP *viz.* number of b-jets and invariant mass of photon (both leading and subleading) and closest b-jet.

Process	**Photon type**	**85% WP Cut**	**70% WP Cut**	**Scaling Factor (70/80)**
$t\bar{t}\gamma$ production (NLO)	Prompts	222	203	0.914
$t\bar{t}\gamma$ production (NLO)	Fakes	1928	1748	0.907
$t\bar{t}\gamma$ decay (LO)	Prompts	141	126	0.894
$t\bar{t}\gamma$ decay (LO)	Fakes	1036	942	0.909
$W\gamma\gamma$	Prompts	368	130	0.353
$W\gamma\gamma$	Fakes	0	0	NA
$Z\gamma\gamma$	Prompts	2073	774	0.373
$Z\gamma\gamma$	Fakes	87	36	0.414
Total:		**5855**	**3959**	

Table C.1: Raw MC event counts for different processes and types for WP85 and WP70, including scaling factors.

The initial choice of the BDT parameters for the 3-class classifier was essentially to be comparable to the parameters of the 2-class classifiers, if not fully similar. Unfortunately, the set of parameters between the two classifiers don't fully translate for XGBoost, given the different algorithms for the two types of classifiers used. In the 2-class classifier, the signal and background are essentially being separated over 100 boosted trees (estimators). In the case of 3-class classification, the signal is

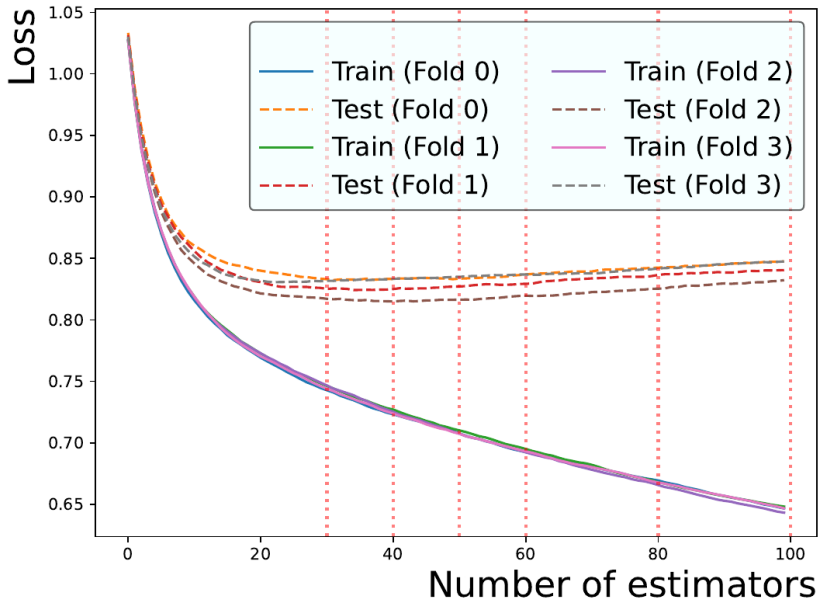

Figure C.1: Loss curve per fold for the training and the test samples for 100 estimators. The vertical lines mark the estimator numbers (33, 40, 50, 60, 80 and 100) chosen for testing the performance of the 3-class BDT model.

separated from "both" the background categories, which means that the number of estimators being used would be used for the signal and both the categories of background to separate each event into one of the 3 classes. A scan was done over multiple estimators, as shown in Fig. C.1. At around 40 estimators, the loss curves become stable and start to increase then on. Therefore, 40 estimators were chosen for further evaluating the sensitivity of the 3-class BDT.

C.1 Training and optimization

The BDT was trained to classify signal separately against both background categories of prompt and fake photons. The motivation behind this approach was to test if the further division of background events could help the BDT to better discriminate the signal from the prompt background as well. A caveat of this approach is the smaller number of MC events used in each training with respect to having one category, so background fluctuations would have a larger impact. A similar discrimination is observed between signal and fake background events and the separation of signal and prompt background events, as shown in Figure C.2. The separation of the three-class classifier between signal and the combination of the background categories with the same binning criteria as used in the analysis is ~9.8%, as shown in Figure C.2. The performance is slightly better than with the current BDT approach (~6.1%) though.

The loss curves per-fold converge for both test and train sets, as can be seen in Figure C.3. The curves show a definitive initial decrease and gradual flattening in the loss values with the increasing number of estimators. This indicates that the 3-class classifier seems to be slightly less overtrained

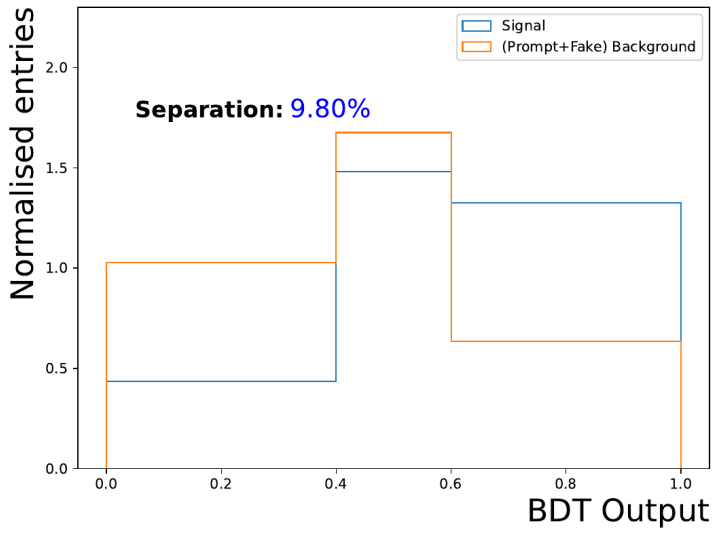

Figure C.2: BDT output for the signal and the total background (both prompt and fake), in bins used for fitting over all folds.

than the 2-class classifier used in the analysis.

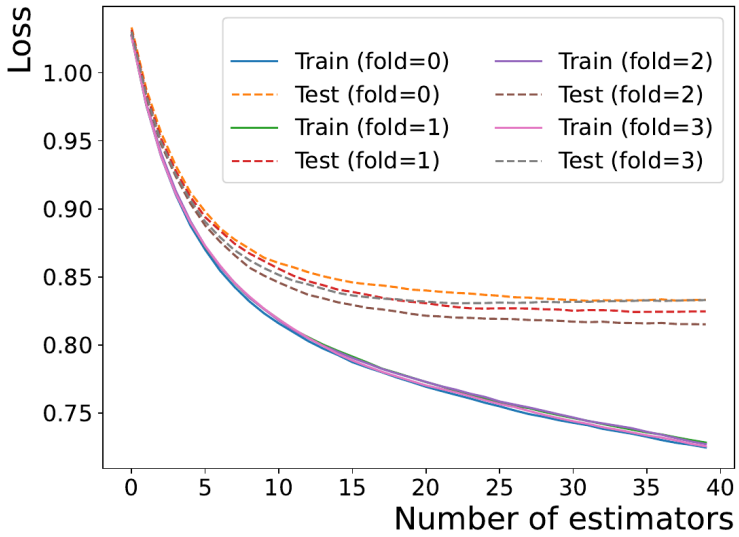

Figure C.3: Loss curve per fold for the training and the test samples for 40 estimators.

C.2 Measurement of $t\bar{t}\gamma\gamma$ cross-section

The total expected uncertainty from the Asimov fit performed on the $t\bar{t}\gamma\gamma$ signal strength (μ), when quoted in 3 significant digits, is $^{+23\%}_{-22\%}$. The total uncertainty is dominated by the statistical part of $^{+16\%}_{-15\%}$. Figure C.4 shows the BDT output distribution before and after the fit with Asimov data.

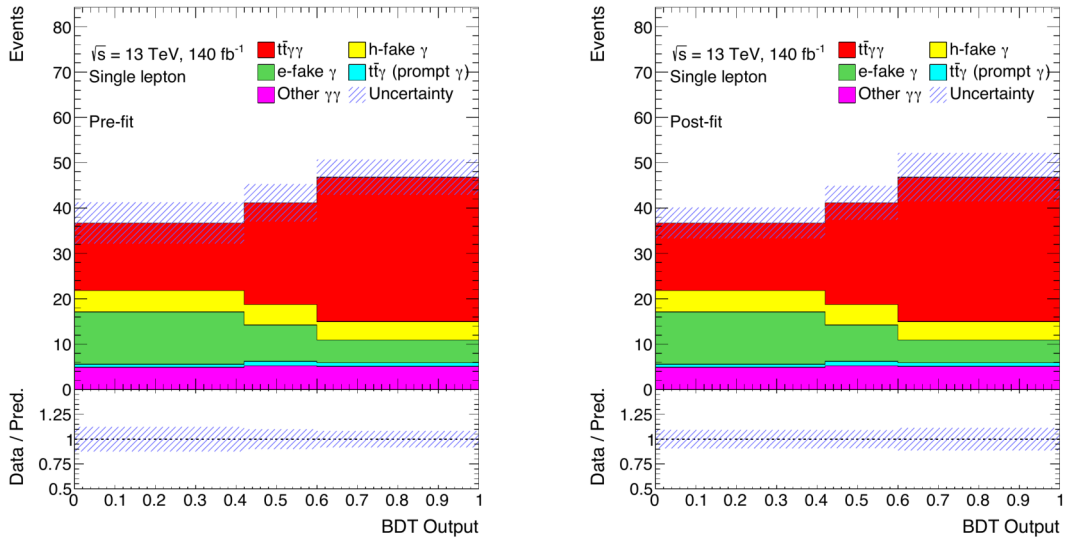

(a) (b)

Figure C.4: (a) Pre-fit BDT output distribution and (b) BDT distribution after fitting to Asimov data. The uncertainty band corresponds to the total pre-fit uncertainty in (a) and to the total post-fit uncertainty in (b).

The most dominant NPs, as shown in Figure C.5, remain the same as they are in the $t\bar{t}\gamma\gamma$ cross section measurement, only with slight shuffling among themselves.

The expected significance from the above fit setup was found to be 5.6σ, which is similar to the performance of the BDT used within the analysis with minimum gain in expected sensitivity. The model training also comes with a trade-off of increased statistical fluctuations and complexity. Therefore, the idea to approach the measurements with 3-class classifiers was abandoned.

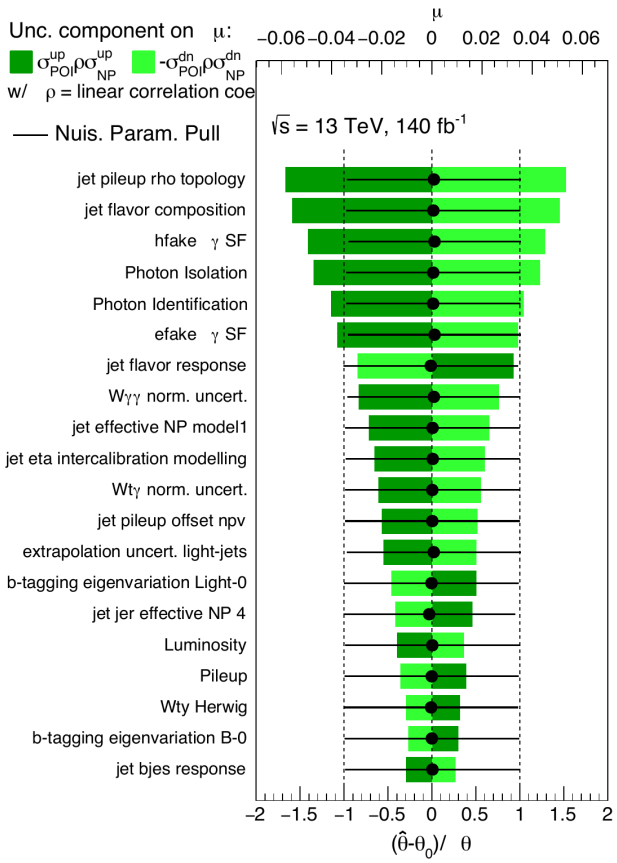

Figure C.5: The ranking plot of the 20 most important NPs for the signal strength in the fit in the single lepton channel with one POI corresponding to the $t\bar{t}\gamma\gamma$ signal process.

APPENDIX D

Pseudo-Experiments for Significance Estimation

In addition to the asymptotic fit used for the measurements in Chapters 8 and 9, a complementary study was carried out using toy Monte Carlo simulations. In this approach, the nuisance parameters representing the systematic uncertainties are randomly varied within their expected ranges, and the full analysis is repeated many times to build up an ensemble of pseudo-experiments. The spread of results from these toys provides a direct way to assess the impact of systematic effects, while the distribution of the test-statistic from toys indicates how likely the observed signal is under different assumptions.

Pseudo-experiments were performed using `PyHF` [115][116] with the full serialized statistical model for the $t\bar{t}\gamma\gamma$ process, containing the observed data, signal and background expectations, systematic uncertainties, and their associated nuisance parameter constraints, under the background-only hypothesis. A total of 4.5 billion toy datasets were generated to evaluate the test-statistic distribution depending on the signal strength parameter, μ. The test-statistic used is the profile likelihood ratio, q_0, which measures the compatibility of the observed data with the background-only hypothesis and is defined as:

$$q_0 = -2 \ln \frac{\mathcal{L}(\mu = 0, \hat{\theta}_0)}{\mathcal{L}(\hat{\mu}, \hat{\theta})}, \tag{D.1}$$

where $\mathcal{L}$ represents the likelihood function, $\hat{\mu}$ is the best-fit signal strength, and θ are the nuisance parameters. The likelihood function at $\mu = 0$ corresponds to the background-only null hypothesis. Larger values of q_0 indicate stronger evidence for the presence of signal.

A p-value is computed as the fraction of background-only pseudo-experiments where the test-statistic exceeds the observed (Asimov) test-statistic:

$$p = \frac{N(q_0 \geq q_0^{\text{obs}})}{N_{\text{toys}}}, \tag{D.2}$$

where N_{toys} is the total number of generated pseudo-experiments. The significance, in terms of standard deviations (σ), is obtained from the one-tailed normal quantile function:

$$Z = \Phi^{-1}(1 - p) \tag{D.3}$$

where Φ^{-1} is the inverse cumulative distribution function of the standard normal distribution.

The result from these pseudo-experiment studies yield the expected significance for the $t\bar{t}\gamma\gamma$ cross section as 5.7σ, corresponding to a p-value of 6.9×10^{-9}. This is consistent with the expected significance of 5.6σ from the asymptotic method used in Section 8.4. The test-statistics were also evaluated at different expected signal strength values of $\mu = 0.5, 0.8, 1.0$, with results close to the asymptotic predictions. Thus, the pseudo-experiments confirm the validity of the asymptotic approach being used in the analysis to quote the significance, highlighting if only a slight underestimation of significance computed with the asymptotic method.

Figure D.1 shows the test-statistic for various values of signal strength, including the observed signal strength, against the number of background-only pseudo-experiments. Out of the 4.5 billion toys, only a few background-only pseudo-experiments cross the test-statistic values of observed data (in $\mathcal{O}(100)$) and the expected signal strength of $\mu = 1.0$ (in $\mathcal{O}(10)$).

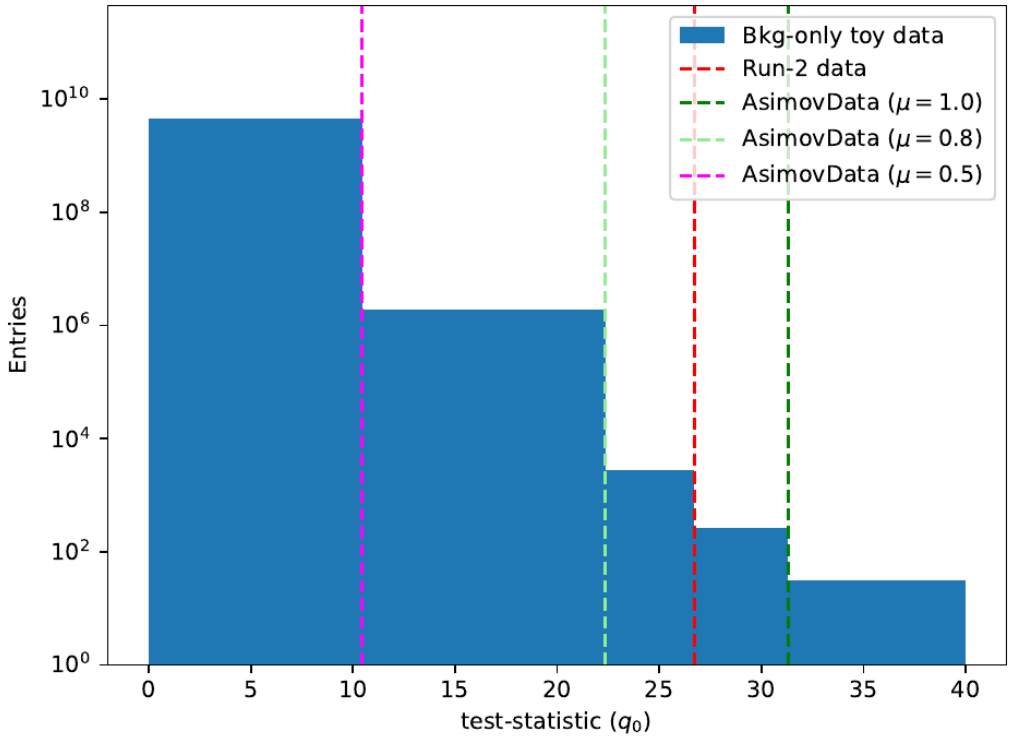

Figure D.1: The profile likelihood ratio test-statistic for background-only pseudo-experiments for different signal strengths (μ) of the $t\bar{t}\gamma\gamma$ process. The red line marks the test-statistic for the observed data.

Bibliography

[1] ATLAS Collaboration, *Measurements of inclusive and differential cross-sections of $t\bar{t}\gamma$ production in pp collisions at $\sqrt{s} = 13$ TeV with the ATLAS detector*, JHEP **10** (2024) 191, arXiv: 2403.09452 [hep-ex] (cit. on pp. 1, 12, 13, 39–41, 76, 80, 86, 114–116, 120, 121, 127).

[2] M. K. Gaillard, P. D. Grannis and F. J. Sciulli, *The standard model of particle physics*, Reviews of Modern Physics **71** (1999) S96, ISSN: 1539-0756, URL: http://dx.doi.org/10.1103/RevModPhys.71.S96 (cit. on p. 3).

[3] ATLAS Collaboration, *Observation of a new particle in the search for the Standard Model Higgs boson with the ATLAS detector at the LHC*, Phys. Lett. B **716** (2012) 1, arXiv: 1207.7214 [hep-ex] (cit. on p. 4).

[4] CMS Collaboration, *Observation of a new boson at a mass of 125 GeV with the CMS experiment at the LHC*, Phys. Lett. B **716** (2012) 30, arXiv: 1207.7235 [hep-ex] (cit. on p. 4).

[5] Wikimedia Foundation, *Satellite Image of Earth*, https://upload.wikimedia.org/wikipedia/commons/0/00/Standard_Model_of_Elementary_Particles.svg, Accessed: 4 May 2024, 2021 (cit. on p. 4).

[6] F. Abe et al., *Observation of Top Quark Production in $\bar{p}p$ Collisions with the Collider Detector at Fermilab*, Phys. Rev. Lett. **74** (14 1995) 2626, URL: https://link.aps.org/doi/10.1103/PhysRevLett.74.2626 (cit. on p. 9).

[7] S. Abachi et al., *Observation of the Top Quark*, Phys. Rev. Lett. **74** (14 1995) 2632, URL: https://link.aps.org/doi/10.1103/PhysRevLett.74.2632 (cit. on p. 9).

[8] T. Aaltonen et al., *Observation of Electroweak Single Top-Quark Production*, Phys. Rev. Lett. **103** (9 2009) 092002, URL: https://link.aps.org/doi/10.1103/PhysRevLett.103.092002 (cit. on p. 9).

[9] V. M. Abazov et al., *Observation of Single Top-Quark Production*, Phys. Rev. Lett. **103** (9 2009) 092001, URL: https://link.aps.org/doi/10.1103/PhysRevLett.103.092001 (cit. on p. 9).

[10] B. Mondal, *Measurement of differential cross-sections of the process with the ATLAS detector*, PhD thesis: Universität Siegen, 2024, URL: https://doi.org/10.25819/ubsi/10622 (cit. on pp. 11, 39, 40).

[11] J. L. Hewett and T. G. Rizzo, *Using b —> s gamma to probe top quark couplings*, Phys. Rev. D **49** (1994) 319, arXiv: hep-ph/9305223 (cit. on p. 11).

[12] J. A. Aguilar-Saavedra, *A Minimal set of top anomalous couplings*, Nucl. Phys. B **812** (2009) 181, arXiv: 0811.3842 [hep-ph] (cit. on p. 11).

[13] F. Maltoni, D. Pagani and I. Tsinikos, *Associated production of a top-quark pair with vector bosons at NLO in QCD: impact on* $\mathrm{t\bar{t}H}$ *searches at the LHC*, Journal of High Energy Physics **2016** (2016), ISSN: 1029-8479, URL: http://dx.doi.org/10.1007/JHEP02(2016)113 (cit. on p. 11).

[14] A. I. Hernández-Juárez, G. Tavares-Velasco and A. Moyotl, *Chromomagnetic and chromoelectric dipole moments of the top quark in the fourth-generation THDM*, Phys. Rev. D **98** (3 2018) 035040, URL: https://link.aps.org/doi/10.1103/PhysRevD.98.035040 (cit. on p. 11).

[15] A. I. Hernández-Juárez, G. Tavares-Velasco and A. Moyotl, *Chromomagnetic and chromoelectric dipole moments of quarks in the reduced 331 model*, Chinese Physics C **45** (2021) 113101, URL: https://dx.doi.org/10.1088/1674-1137/ac1b9a (cit. on p. 11).

[16] S. M. Etesami and E. Darvish Roknabadi, *Probing the nonstandard top-gluon couplings through* $t\bar{t}\gamma\gamma$ *production at the LHC*, Phys. Rev. D **100** (1 2019) 015023, URL: https://link.aps.org/doi/10.1103/PhysRevD.100.015023 (cit. on p. 11).

[17] ATLAS Collaboration, *Measurement of the* $t\bar{t}\gamma$ *production cross section in proton-proton collisions at* $\sqrt{s} = 8$ *TeV with the ATLAS detector*, JHEP **11** (2017) 086, arXiv: 1706.03046 [hep-ex] (cit. on p. 12).

[18] CMS Collaboration, *Measurement of the semileptonic* $\mathrm{t\bar{t}} + \gamma$ *production cross section in pp collisions at* $\sqrt{s} = 8$ *TeV*, JHEP **10** (2017) 006, arXiv: 1706.08128 [hep-ex] (cit. on p. 12).

[19] ATLAS Collaboration, *Measurements of inclusive and differential fiducial cross-sections of* $t\bar{t}\gamma$ *production in leptonic final states at* $\sqrt{s} = 13$ *TeV in ATLAS*, Eur. Phys. J. C **79** (2019) 382, arXiv: 1812.01697 [hep-ex] (cit. on p. 12).

[20] ATLAS Collaboration, *Measurements of inclusive and differential cross-sections of combined* $t\bar{t}\gamma$ *and* $tW\gamma$ *production in the* $e\mu$ *channel at 13 TeV with the ATLAS detector*, JHEP **09** (2020) 049, arXiv: 2007.06946 [hep-ex] (cit. on p. 12).

[21] CMS Collaboration, *Measurement of the inclusive and differential* $t\bar{t}\gamma$ *cross sections in the single-lepton channel and EFT interpretation at* $\sqrt{s} = 13$ *TeV*, JHEP **12** (2021) 180, arXiv: 2107.01508 [hep-ex] (cit. on p. 12).

[22] CMS Collaboration, *Measurement of the inclusive and differential* $\mathrm{t\bar{t}}\gamma$ *cross sections in the dilepton channel and effective field theory interpretation in proton-proton collisions at* $\sqrt{s}$ *=13 TeV*, JHEP **05** (2022) 091, arXiv: 2201.07301 [hep-ex] (cit. on p. 12).

[23] ATLAS Collaboration, *Measurement of the charge asymmetry in top-quark pair production in association with a photon with the ATLAS experiment*, Phys. Lett. B **843** (2023) 137848, arXiv: 2212.10552 [hep-ex] (cit. on pp. 12, 33, 80).

[24] A. Kardos and Z. Trócsányi,
Hadroproduction of t–anti-t pair with two isolated photons with PowHel,
Nuclear Physics B **897** (2015) 717, ISSN: 0550-3213, URL:
https://www.sciencedirect.com/science/article/pii/S0550321315002060
(cit. on p. 12).

[25] H. van Deurzen et al., *Spin polarisation of $t\bar{t}\gamma\gamma$ production at NLO+PS with GoSam interfaced to MadGraph5_aMC@NLO*, Eur. Phys. J. C **76** (2016),
arXiv: 1509.02077 [hep-ph],
URL: https://doi.org/10.1140/epjc/s10052-016-4048-2 (cit. on p. 12).

[26] D. Pagani, H.-S. Shao, I. Tsinikos and M. Zaro,
Automated EW corrections with isolated photons: $t\bar{t}\gamma$, $t\bar{t}\gamma\gamma$ and $t\gamma j$ as case studies,
Eur. Phys. J. **C76** (2016) 466, arXiv: 2106.02059 [hep-ph] (cit. on p. 12).

[27] D. Stremmer and M. Worek, *Associated production of a top-quark pair with two isolated photons at the LHC through NLO in QCD*, JHEP **08** (2023) 179,
arXiv: 2306.16968 [hep-ph] (cit. on p. 12).

[28] D. Stremmer and M. Worek,
Complete NLO corrections to top-quark pair production with isolated photons,
JHEP **07** (2024) 091, arXiv: 2403.03796 [hep-ph] (cit. on p. 12).

[29] ATLAS Collaboration,
Observation of $t\bar{t}\gamma\gamma$ production at $\sqrt{s}$ =13 TeV with the ATLAS detector, 2025,
arXiv: 2506.05018 [hep-ex], URL: https://arxiv.org/abs/2506.05018
(cit. on pp. 13, 128).

[30] L. Evans and P. Bryant, *LHC Machine*, JINST **3** (2008) S08001 (cit. on p. 16).

[31] *LHC layout*, URL: https://cds.cern.ch/record/2800984 (cit. on p. 17).

[32] ATLAS Collaboration, *ATLAS Insertable B-Layer: Technical Design Report*,
ATLAS-TDR-19; CERN-LHCC-2010-013, 2010,
URL: https://cds.cern.ch/record/1291633 (cit. on p. 18),
Addendum: ATLAS-TDR-19-ADD-1; CERN-LHCC-2012-009, 2012, URL:
https://cds.cern.ch/record/1451888.

[33] B. Abbott et al., *Production and integration of the ATLAS Insertable B-Layer*,
JINST **13** (2018) T05008, arXiv: 1803.00844 [physics.ins-det] (cit. on p. 18).

[34] ATLAS Collaboration, *The ATLAS Experiment at the CERN Large Hadron Collider*,
JINST **3** (2008) S08003 (cit. on p. 19).

[35] *ATLAS Detector slice with layerwise particle interactions*,
URL: https://cds.cern.ch/record/2770815 (cit. on p. 21).

[36] ATLAS Collaboration, *Electron reconstruction and identification in the ATLAS experiment using the 2015 and 2016 LHC proton–proton collision data at $\sqrt{s}$ = 13 TeV*,
Eur. Phys. J. C **79** (2019) 639, arXiv: 1902.04655 [hep-ex] (cit. on p. 23).

[37] ATLAS Collaboration, *Electron and photon energy calibration with the ATLAS detector using 2015–2016 LHC proton–proton collision data*, JINST **14** (2019) P03017,
arXiv: 1812.03848 [hep-ex] (cit. on pp. 23, 24).

[38] ATLAS Collaboration, *Measurement of the photon identification efficiencies with the ATLAS detector using LHC Run 2 data collected in 2015 and 2016*, Eur. Phys. J. C **79** (2019) 205, arXiv: 1810.05087 [hep-ex] (cit. on p. 24).

[39] ATLAS Collaboration, *Muon reconstruction performance of the ATLAS detector in proton–proton collision data at* $\sqrt{s} = 13$ *TeV*, Eur. Phys. J. C **76** (2016) 292, arXiv: 1603.05598 [hep-ex] (cit. on pp. 24, 78).

[40] M. Cacciari, G. P. Salam and G. Soyez, *The anti-*k_t *jet clustering algorithm*, JHEP **04** (2008) 063, arXiv: 0802.1189 [hep-ph] (cit. on p. 24).

[41] M. Cacciari, G. P. Salam and G. Soyez, *FastJet user manual*, Eur. Phys. J. C **72** (2012) 1896, arXiv: 1111.6097 [hep-ph] (cit. on p. 24).

[42] ATLAS Collaboration, *Jet reconstruction and performance using particle flow with the ATLAS Detector*, Eur. Phys. J. C **77** (2017) 466, arXiv: 1703.10485 [hep-ex] (cit. on p. 24).

[43] ATLAS Collaboration, *Jet energy scale measurements and their systematic uncertainties in proton–proton collisions at* $\sqrt{s} = 13$ *TeV with the ATLAS detector*, Phys. Rev. D **96** (2017) 072002, arXiv: 1703.09665 [hep-ex] (cit. on pp. 25, 78).

[44] ATLAS Collaboration, *Tagging and suppression of pileup jets with the ATLAS detector*, ATLAS-CONF-2014-018, 2014, URL: https://cds.cern.ch/record/1700870 (cit. on pp. 25, 79).

[45] ATLAS Collaboration, *Optimisation and performance studies of the ATLAS b-tagging algorithms for the 2017-18 LHC run*, ATL-PHYS-PUB-2017-013, 2017, URL: https://cds.cern.ch/record/2273281 (cit. on pp. 25, 79).

[46] ATLAS Collaboration, E_T^{miss} *performance in the ATLAS detector using 2015–2016 LHC* pp *collisions*, ATLAS-CONF-2018-023, 2018, URL: https://cds.cern.ch/record/2625233 (cit. on p. 25).

[47] ATLAS Collaboration, *Performance of missing transverse momentum reconstruction with the ATLAS detector using proton–proton collisions at* $\sqrt{s} = 13$ *TeV*, Eur. Phys. J. C **78** (2018) 903, arXiv: 1802.08168 [hep-ex] (cit. on p. 25).

[48] M. H. Seymour and M. Marx, *Monte Carlo Event Generators*, 2013, arXiv: 1304.6677 [hep-ph], URL: https://arxiv.org/abs/1304.6677 (cit. on p. 28).

[49] C. Bierlich et al., *A comprehensive guide to the physics and usage of PYTHIA 8.3*, SciPost Phys. Codeb. **2022** (2022) 8, arXiv: 2203.11601 [hep-ph] (cit. on p. 29).

[50] ATLAS Collaboration, *The ATLAS Simulation Infrastructure*, Eur. Phys. J. C **70** (2010) 823, arXiv: 1005.4568 [physics.ins-det] (cit. on p. 31).

[51] S. Agostinelli et al., *GEANT4–a simulation toolkit*, Nucl. Instrum. Meth. A **506** (2003) 250 (cit. on p. 31).

[52] ATLAS Collaboration, *The ATLAS Simulation Infrastructure*, Eur. Phys. J. C **70** (2010) 823, arXiv: 1005.4568 [physics.ins-det] (cit. on p. 32).

[53] T. Sjöstrand, S. Mrenna and P. Z. Skands, *PYTHIA 6.4 physics and manual*, JHEP **05** (2006) 026, arXiv: hep-ph/0603175 (cit. on p. 32).

[54] T. Sjöstrand et al., *An introduction to PYTHIA 8.2*, Comput. Phys. Commun. **191** (2015) 159, arXiv: 1410.3012 [hep-ph] (cit. on p. 32).

[55] ATLAS Collaboration, *The Pythia 8 A3 tune description of ATLAS minimum bias and inelastic measurements incorporating the Donnachie–Landshoff diffractive model*, ATL-PHYS-PUB-2016-017, 2016, URL: https://cds.cern.ch/record/2206965 (cit. on p. 32).

[56] J. Pumplin et al., *New Generation of Parton Distributions with Uncertainties from Global QCD Analysis*, JHEP **07** (2002) 012, arXiv: hep-ph/0201195 (cit. on p. 32).

[57] J. Alwall et al., *The automated computation of tree-level and next-to-leading order differential cross sections, and their matching to parton shower simulations*, JHEP **07** (2014) 079, arXiv: 1405.0301 [hep-ph] (cit. on pp. 32–34).

[58] The NNPDF Collaboration, R. D. Ball et al., *Parton distributions for the LHC run II*, JHEP **04** (2015) 040, arXiv: 1410.8849 [hep-ph] (cit. on pp. 32–34).

[59] T. Sjöstrand, S. Mrenna and P. Skands, *A brief introduction to PYTHIA 8.1*, Comput. Phys. Commun. **178** (2008) 852, arXiv: 0710.3820 [hep-ph] (cit. on pp. 32–34).

[60] ATLAS Collaboration, *ATLAS Pythia 8 tunes to 7 TeV data*, ATL-PHYS-PUB-2014-021, 2014, URL: https://cds.cern.ch/record/1966419 (cit. on pp. 32–34).

[61] D. J. Lange, *The EvtGen particle decay simulation package*, Nucl. Instrum. Meth. A **462** (2001) 152 (cit. on pp. 32–34).

[62] S. Frixione, *Isolated photons in perturbative QCD*, Phys. Lett. B **429** (1998) 369, arXiv: hep-ph/9801442 (cit. on p. 33).

[63] S. Frixione, E. Laenen, P. Motylinski and B. R. Webber, *Angular correlations of lepton pairs from vector boson and top quark decays in Monte Carlo simulations*, JHEP **04** (2007) 081, arXiv: hep-ph/0702198 (cit. on p. 33).

[64] P. Artoisenet, R. Frederix, O. Mattelaer and R. Rietkerk, *Automatic spin-entangled decays of heavy resonances in Monte Carlo simulations*, JHEP **03** (2013) 015, arXiv: 1212.3460 [hep-ph] (cit. on p. 33).

[65] ATLAS Collaboration, *Measurements of inclusive and differential fiducial cross-sections of $t\bar{t}\gamma$ production in leptonic final states at $\sqrt{s} = 13$ TeV in ATLAS*, Eur. Phys. J. C **79** (2019) 382, arXiv: 1812.01697 [hep-ex] (cit. on p. 34).

[66] K. Melnikov, M. Schulze and A. Scharf, *QCD corrections to top quark pair production in association with a photon at hadron colliders*, Phys. Rev. D **83** (2011) 074013, arXiv: 1102.1967 [hep-ph] (cit. on p. 34).

[67] T. Gleisberg et al., *Event generation with SHERPA 1.1*, JHEP **02** (2009) 007, arXiv: 0811.4622 [hep-ph] (cit. on p. 34).

[68] S. Höche, F. Krauss, S. Schumann and F. Siegert, *QCD matrix elements and truncated showers*, JHEP **05** (2009) 053, arXiv: 0903.1219 [hep-ph] (cit. on p. 34).

[69] T. Gleisberg and S. Höche, *Comix, a new matrix element generator*, JHEP **12** (2008) 039, arXiv: 0808.3674 [hep-ph] (cit. on p. 34).

[70] S. Schumann and F. Krauss,
A parton shower algorithm based on Catani–Seymour dipole factorisation,
JHEP **03** (2008) 038, arXiv: 0709.1027 [hep-ph] (cit. on p. 34).

[71] S. Höche, F. Krauss, M. Schönherr and F. Siegert,
A critical appraisal of NLO+PS matching methods, JHEP **09** (2012) 049,
arXiv: 1111.1220 [hep-ph] (cit. on p. 34).

[72] S. Catani, F. Krauss, B. R. Webber and R. Kuhn, *QCD Matrix Elements + Parton Showers*, JHEP **11** (2001) 063, arXiv: hep-ph/0109231 (cit. on p. 34).

[73] S. Höche, F. Krauss, M. Schönherr and F. Siegert,
QCD matrix elements + parton showers. The NLO case, JHEP **04** (2013) 027,
arXiv: 1207.5030 [hep-ph] (cit. on p. 34).

[74] F. Cascioli, P. Maierhöfer and S. Pozzorini, *Scattering Amplitudes with Open Loops*, Phys. Rev. Lett. **108** (2012) 111601, arXiv: 1111.5206 [hep-ph] (cit. on p. 34).

[75] A. Denner, S. Dittmaier and L. Hofer,
Collier: A fortran-based complex one-loop library in extended regularizations,
Comput. Phys. Commun. **212** (2017) 220, arXiv: 1604.06792 [hep-ph] (cit. on p. 34).

[76] P. Nason, *A new method for combining NLO QCD with shower Monte Carlo algorithms*, JHEP **11** (2004) 040, arXiv: hep-ph/0409146 (cit. on p. 34).

[77] S. Frixione, P. Nason and C. Oleari,
Matching NLO QCD computations with parton shower simulations: the POWHEG method,
JHEP **11** (2007) 070, arXiv: 0709.2092 [hep-ph] (cit. on p. 34).

[78] S. Alioli, P. Nason, C. Oleari and E. Re, *A general framework for implementing NLO calculations in shower Monte Carlo programs: the POWHEG BOX*, JHEP **06** (2010) 043, arXiv: 1002.2581 [hep-ph] (cit. on p. 34).

[79] M. Czakon and A. Mitov,
Top++: A program for the calculation of the top-pair cross-section at hadron colliders,
Comput. Phys. Commun. **185** (2014) 2930, arXiv: 1112.5675 [hep-ph] (cit. on pp. 34, 80).

[80] N. Kidonakis,
Next-to-next-to-leading logarithm resummation for s-channel single top quark production,
Phys. Rev. **D81** (2010) 054028, arXiv: 1001.5034 [hep-ph] (cit. on p. 35).

[81] N. Kidonakis, *Two-loop soft anomalous dimensions for single top quark associated production with a W^- or H^-*, Phys. Rev. D **82** (2010) 054018, arXiv: 1005.4451 [hep-ph] (cit. on p. 35).

[82] N. Kidonakis, *Next-to-next-to-leading-order collinear and soft gluon corrections for t-channel single top quark production*, Phys. Rev. **D83** (2011) 091503, arXiv: 1103.2792 [hep-ph] (cit. on p. 35).

[83] ATLAS Collaboration, *Measurement of $W^\pm$ and Z Boson Production Cross Sections in pp Collisions at $\sqrt{s} = 13$ TeV with the ATLAS Detector*, ATLAS-CONF-2015-039, 2015,
URL: https://cds.cern.ch/record/2045487 (cit. on p. 35).

[84] J. M. Campbell and R. K. Ellis, *Update on vector boson pair production at hadron colliders*, Phys. Rev. D **60** (1999) 113006, arXiv: hep-ph/9905386 (cit. on p. 35).

[85] D. de Florian et al.,
Handbook of LHC Higgs Cross Sections: 4. Deciphering the Nature of the Higgs Sector, (2016), arXiv: 1610.07922 [hep-ph] (cit. on p. 35).

[86] ATLAS Collaboration, *Luminosity determination in pp collisions at $\sqrt{s}$ = 13 TeV using the ATLAS detector at the LHC*, Eur. Phys. J. C **83** (2023) 982, arXiv: 2212.09379 [hep-ex] (cit. on pp. 39, 79).

[87] R. Fisher, *Iris Dataset*, UCI Machine Learning Repository,
Accessed via UCI Machine Learning Repository, 1936,
URL: https://doi.org/10.24432/C56C76 (cit. on p. 50).

[88] L. Breiman, *Random Forests*, Machine Learning **45** (2001) 5 (cit. on p. 51).

[89] Y. Freund and R. E. Schapire,
A Decision-Theoretic Generalization of On-Line Learning and an Application to Boosting, Journal of Computer and System Sciences **55** (1997) 119, ISSN: 0022-0000, URL: https://www.sciencedirect.com/science/article/pii/S002200009791504X (cit. on p. 51).

[90] *Bagging versus Boosting*,
URL: https://www.pluralsight.com/resources/blog/guides/ensemble-methods-bagging-versus-boosting (cit. on p. 52).

[91] T. Chen and C. Guestrin, "XGBoost: A Scalable Tree Boosting System", *Proceedings of the 22nd ACM SIGKDD International Conference on Knowledge Discovery and Data Mining*, KDD '16, ACM, 2016 785, URL: http://dx.doi.org/10.1145/2939672.2939785 (cit. on pp. 53, 58).

[92] R. Aaij et al., *Observation of CP violation in charm decays*,
Phys. Rev. Lett. **122** (2019) 211803, arXiv: 1903.08726 [hep-ex] (cit. on p. 53).

[93] M. G. Aartsen et al.,
Evidence for High-Energy Extraterrestrial Neutrinos at the IceCube Detector,
Science **342** (2013) 1242856, arXiv: 1311.5238 [astro-ph.HE] (cit. on p. 53).

[94] A. A. Aguilar-Arevalo et al., *Unexplained Excess of Electronlike Events From a 0.8-GeV Neutrino Beam in the MiniBooNE Experiment*, Phys. Rev. Lett. **121** (2018) 221801,
arXiv: 1805.08517 [hep-ex] (cit. on p. 53).

[95] P. Abratenko et al., *Search for Sterile Neutrino Oscillations with the MicroBooNE Detector*, Phys. Rev. Lett. **128** (2022) 241802, arXiv: 2207.03746 [hep-ex] (cit. on p. 53).

[96] J. H. Friedman, *Greedy Function Approximation: A Gradient Boosting Machine*,
Annals of Statistics **29** (2001) 1189 (cit. on p. 58).

[97] K. Danziger, S. Höche and F. Siegert,
Reducing negative weights in Monte Carlo event generation with Sherpa, 2021,
arXiv: 2110.15211 [hep-ph], URL: https://arxiv.org/abs/2110.15211
(cit. on p. 59).

[98] ATLAS Collaboration,
Search for the production of a Higgs boson in association with top quarks and decaying into a b-quark pair and b-jet identification with the ATLAS experiment at LHC,
Master's Thesis: Georg-August-Universität Göttingen, 2017,
URL: https://uni-goettingen.de/en/msc+theses/563505.html (cit. on p. 60).

[99] S. M. Lundberg and S.-I. Lee, "A Unified Approach to Interpreting Model Predictions",
Advances in Neural Information Processing Systems, vol. 30, 2017,
URL: https://proceedings.neurips.cc/paper/2017/file/8a20a862197863d76e031c55986fe9bb-Paper.pdf (cit. on p. 63).

[100] F. Pedregosa et al., *Scikit-learn: Machine Learning in Python*,
Journal of Machine Learning Research **12** (2011) 2825 (cit. on p. 73).

[101] J. Butterworth et al., *PDF4LHC recommendations for LHC Run II*,
J. Phys. G **43** (2016) 023001, arXiv: 1510.03865 [hep-ph] (cit. on p. 77).

[102] ATLAS Collaboration, *Electron efficiency measurements with the ATLAS detector using the 2015 LHC proton–proton collision data*, ATLAS-CONF-2016-024, 2016,
URL: https://cds.cern.ch/record/2157687 (cit. on p. 78).

[103] ATLAS Collaboration, *Photon identification in 2015 ATLAS data*,
ATL-PHYS-PUB-2016-014, 2016, URL: https://cds.cern.ch/record/2203125
(cit. on p. 78).

[104] ATLAS Collaboration, *Jet energy measurement and its systematic uncertainty in proton–proton collisions at* $\sqrt{s} = 7$ *TeV with the ATLAS detector*, Eur. Phys. J. C **75** (2015) 17,
arXiv: 1406.0076 [hep-ex] (cit. on p. 78).

[105] ATLAS Collaboration, *Luminosity determination in* pp *collisions at* $\sqrt{s} = 8$ *TeV using the ATLAS detector at the LHC*, Eur. Phys. J. C **76** (2016) 653, arXiv: 1608.03953 [hep-ex]
(cit. on p. 79).

[106] D. de Florian et al.,
Handbook of LHC Higgs Cross Sections: 4. Deciphering the Nature of the Higgs Sector,
2/2017 (2016), arXiv: 1610.07922 [hep-ph] (cit. on p. 80).

[107] B. Batool et al., *Measurements of inclusive and differential cross-sections of* $t\bar{t}\gamma$ *production at 13 TeV with the ATLAS detector*, tech. rep., CERN, 2019,
URL: https://cds.cern.ch/record/2712912 (cit. on p. 80).

[108] M. Cacciari, G. P. Salam and G. Soyez, *The catchment area of jets*, JHEP **04** (2008) 005,
arXiv: 0802.1188 [hep-ph] (cit. on p. 82).

[109] K. Cranmer, A. Lewis, L. Moneta, S. Schmitt and W. Wagner,
HistFactory: A tool for creating statistical models for use with RooFit and RooStats,
Eur. Phys. J. C **72** (2012) 2164, arXiv: 1206.4834 [hep-ex] (cit. on pp. 83, 84).

[110] ATLAS Collaboration, *TrexFitter: A framework for statistical analysis in ATLAS*,
See relevant ATLAS internal notes or public documentation, e.g.,
https://gitlab.cern.ch/trexfitter/trexfitter, 202X,
URL: https://gitlab.cern.ch/trexfitter/trexfitter (cit. on p. 84).

[111] L. Moneta et al., *RooStats: A tool for statistical data analysis*, PoS ACAT2010 **047** (2010), URL: https://pos.sissa.it/114/047/pdf (cit. on p. 85).

[112] F. James and M. Winkler, *MINUIT User's Guide*, (2004) (cit. on p. 85).

[113] G. Cowan, K. Cranmer, E. Gross and O. Vitells, *Asymptotic formulae for likelihood-based tests of new physics*, **C 71** (2011) 1554, Erratum: **C 73** (2013) 2501, arXiv: 1007.1727 (cit. on p. 85).

[114] A. Pinto et al., *Uncertainty components in profile likelihood fits*, Eur. Phys. J. C **84** (2024) 593, arXiv: 2307.04007 [physics.data-an] (cit. on p. 104).

[115] L. Heinrich, M. Feickert and G. Stark, *pyhf: v0.7.6*, version 0.7.6, https://github.com/scikit-hep/pyhf/releases/tag/v0.7.6, URL: https://doi.org/10.5281/zenodo.1169739 (cit. on p. 143).

[116] L. Heinrich, M. Feickert, G. Stark and K. Cranmer, *pyhf: pure-Python implementation of HistFactory statistical models*, Journal of Open Source Software **6** (2021) 2823, URL: https://doi.org/10.21105/joss.02823 (cit. on p. 143).

List of Figures

2.1 The Standard Model of particle physics, including all the known elementary fermions and bosons [5] . . . 4
2.2 Examples of LO Feynman diagrams for top quark pair production via gluon-gluon fusion, quark-antiquark annihilation, and t-channel production. . . . 10
2.3 Examples of LO Feynman diagrams for single top quark production via s-channel, t-channel, and tW-channel, respectively. . . . 10
2.4 Feynman diagrams for leading-order $t\bar{t}\gamma\gamma$ production in the single-lepton $t\bar{t}$ final state, with photons radiated by (a) an off-shell top quark and the charged lepton and (b) an initial-state quark and the charged lepton, respectively. [Diagrams taken from [29]] . 13

3.1 The CERN accelerator complex including the preaccelerators to the LHC, the Proton Synchrotron (PS) and the Super Proton Synchrotron (SPS). [31] . . . 17
3.2 The ATLAS detector with all its sub-detector systems showing (1) Muon spectrometer in forward and barrel region (2) Toroid magnet in froward and barrel region (3) Solenoid magnet (4) Transition radion tracker (5) Semi-conductor tracker (6) Pixel detector (7) Liquid Argon calorimeter (8) Tile calorimeter. . . . 18
3.3 A cross sectional slice of the ATLAS detector including visualisations of how different particles interact with its different sub-detectors. [35] . . . 21

4.1 Schematic of the structure of a $pp \rightarrow t\bar{t}$ event modeled by the event generator Pythia [49]. The event is simulated in order of energy scale. The hard interaction is the central high-energy parton collision. Initial and Final State Radiation (ISR/FSR) are partons radiating before and after this interaction. Resonance decays are intermediate unstable particle decays from the hard interaction. The weak shower involves W/Z boson-mediated emissions and decays. Multiple Parton Interactions (MPI) are additional parton scatterings within one collision. Beam remnants are uncollided proton parts. Strings (colour fields) fragment into primary hadrons. colour reconnection rearranges parton colour connections before hadronization; hadronic reconnection is further hadron rearrangement. . . . 29

5.1 The p_T distributions of the (a) leading and (b) subleading photons. The uncertainty band represents the total uncertainty before the fit to the data. . . . 45
5.2 The η distributions of the (a) leading and (b) subleading photons. The uncertainty band represents the total uncertainty before the fit to the data. . . . 46

5.3 The invariant mass distributions of the lepton and the (a) leading or (b) subleading photon. The uncertainty band represents the total uncertainty before the fit to the data. 46
5.4 The ΔR distributions between the lepton and the (a) leading and (b) subleading photon. The uncertainty band represents the total uncertainty before the fit to the data. 47
5.5 The photon conversion type of the leading photon by p_T. The first bin of the distribution corresponds to the unconverted photons, while the second bin corresponds to the sum of all converted photon types. The uncertainty band represents the total uncertainty before the fit to the data. 47

6.1 Illustrative example of node branching in a decision tree using the Iris dataset. The split criteria are chosen for demonstration purposes. 50
6.2 Bagging versus Booting [90]. 52
6.3 The p_T distributions of the (a) leading and (b) subleading photons. The uncertainty band corresponds to the pre-fit uncertainties of the background samples. The $t\bar{t}\gamma\gamma$ signal is scaled to the total number of background events. 54
6.4 The η distributions of the (a) leading and (b) subleading photons. The uncertainty band corresponds to the pre-fit uncertainties of the background samples. The $t\bar{t}\gamma\gamma$ signal is scaled to the total number of background events. 55
6.5 The invariant mass distributions of the lepton and the (a) leading or (b) subleading photon. The uncertainty band corresponds to the pre-fit uncertainties of the background samples. The $t\bar{t}\gamma\gamma$ signal is scaled to the total number of background events. 55
6.6 The invariant mass distributions of the (a) leading or (b) subleading photon and the closest b-jet. The uncertainty band corresponds to the pre-fit uncertainties of the background samples. The $t\bar{t}\gamma\gamma$ signal is scaled to the total number of background events. 56
6.7 Signal-Background separation in 4 variables from the training dataset, as example. . 60
6.8 BDT output distributions for the signal and background processes, combined over 4 folds. 61
6.9 Loss curve per fold for the training and the testing sets over the 100 estimators used in the BDT. 62
6.10 AUC score per fold for the training and the testing sets used in the BDT. 62
6.11 Importance ranking of input features used in the BDT (averaged over all 4 folds). . . 63
6.12 SHAP beeswarm plots illustrating the impact of features on the BDT output for each of the four model folds. The BDTs were trained on a subset of 1,000 events. 65
6.13 SHAP decision plot with (a) 10 and (b) 19 variables for a single fold (0) of the BDT. 66
6.14 The results of the χ^2 test are given for signal and background simulations for the training and testing sets in bins used for fitting for the folds (a) 0, (b) 1, (c) 2, and (d) 3 of the BDT output. 67
6.15 Correlation coefficients among the input variables and with the BDT score for the trained signal sample in the BDT. 69
6.16 Correlation coefficients among the input variables and with the BDT score for the trained background samples in the BDT. 70
6.17 Correlation difference among the input variables and BDT scores between the trained signal and background samples in the BDT. 71
6.18 Correlation difference among the input variables and BDT scores between the trained signal-background samples and data. 72

6.19 BDT output distribution in simulation: (a) $t\bar{t}\gamma\gamma$ and all backgrounds are stacked, (b) the signal is normalised to the total number of background events and shown overlaid. The uncertainty band corresponds to the total pre-fit uncertainty in (a) and to the pre-fit uncertainties of the background samples in (b). 73

8.1 BDT output distribution (a) before and (b) after fit to Asimov data. The uncertainty band corresponds to the total pre-fit uncertainty in (a) and to the total post-fit uncertainty in (b). 88

8.2 The likelihood scan performed over signal strength of $t\bar{t}\gamma\gamma$ process, with its best-fit value determined at 1. 89

8.3 The ranking plot of the 20 most important NPs for the signal strength in the Asimov fit with the POI corresponding to the $t\bar{t}\gamma\gamma$ signal process. 90

8.4 Correlations of NPs (with threshold of 10%) with the signal strength for $t\bar{t}\gamma\gamma$ signal process in the Asimov fit. 91

8.5 BDT output distribution (a) before and (b) after fitting to data. The uncertainty band corresponds to the total pre-fit uncertainty in (a) and to the total post-fit uncertainty in (b). 93

8.6 Post-fit nuisance parameters for uncertainties related to fake photons, photon reconstruction, prompt background normalisation, background modelling and $t\bar{t}\gamma\gamma$ modelling used in the fit to data. 94

8.7 The NPs for uncertainties related to jets, and b-tagging for the fit to data. 95

8.8 Nominal (black) and varied (red/blue) templates corresponding to the $W\gamma\gamma$ normalisation uncertainty. (The dashed lines show the shape of the systematic before the smoothing procedure is applied.) 95

8.9 Nominal (black) and varied (red/blue) templates corresponding to the $t\bar{t}\gamma\gamma$ shower variation of Herwig7. (The dashed lines show the shape of the systematic before the smoothing procedure is applied.) 96

8.10 Nominal (black) and varied (red/blue) templates corresponding to the Jet pileup rho topology uncertainty for $t\bar{t}\gamma\gamma$ (a), $t\bar{t}\gamma$ production (b) and $t\bar{t}\gamma$ decay (c), treated as one template ($t\bar{t}\gamma$ (Prompt γ)) in the fit, and Other $\gamma\gamma$ (d). (The dashed lines show the shape of the systematic before the smoothing procedure is applied.) 96

8.11 Nominal (black) and varied (red/blue) templates corresponding to the Jet pileup rho topology uncertainty for the e-fake category with one e-fake photon and one prompt photon for all processes except for $t\bar{t}\gamma$ decay and $t\bar{t}\gamma\gamma$ (a), $t\bar{t}\gamma$ decay (b) and $t\bar{t}\gamma\gamma$ processes (c). These categories are added up and treated as one template in the fit. (The dashed lines show the shape of the systematic before the smoothing procedure is applied.) 97

8.12 Nominal (black) and varied (red/blue) templates corresponding to the Jet pileup rho topology uncertainty for the h-fake category for all processes except for $t\bar{t}\gamma$ decay and $t\bar{t}\gamma\gamma$ (a), $t\bar{t}\gamma$ decay (b) and $t\bar{t}\gamma\gamma$ (c). These categories are added up and treated as one template in the fit. (The dashed lines show the shape of the systematic before the smoothing procedure is applied.) 98

8.13 Nominal (black) and varied (red/blue) templates corresponding to the photon isolation uncertainty for $t\bar{t}\gamma\gamma$ (a), $t\bar{t}\gamma$ production (b) and $t\bar{t}\gamma$ decay (c), treated as one template ($t\bar{t}\gamma$ (Prompt γ)) in the fit, and Other $\gamma\gamma$ (d). (The dashed lines show the shape of the systematic before the smoothing procedure is applied.) 99
8.14 Nominal (black) and varied (red/blue) templates corresponding to the photon isolation uncertainty for the e-fake category with one e-fake photon and one prompt photon for all processes except for $t\bar{t}\gamma$ decay and $t\bar{t}\gamma\gamma$ (a), $t\bar{t}\gamma$ decay (b) and $t\bar{t}\gamma\gamma$ processes (c). These categories are added up and treated as one template in the fit. (The dashed lines show the shape of the systematic before the smoothing procedure is applied.) 100
8.15 Nominal (black) and varied (red/blue) templates corresponding to the photon isolation uncertainty for the h-fake category for all processes except for $t\bar{t}\gamma$ decay and $t\bar{t}\gamma\gamma$ (a), $t\bar{t}\gamma$ decay (b) and $t\bar{t}\gamma\gamma$ (c). These categories are added up and treated as one template in the fit. (The dashed lines show the shape of the systematic before the smoothing procedure is applied.) 101
8.16 Nominal (black) and varied (red/blue) templates corresponding to the e-fake uncertainty for the e-fake category with one e-fake photon and one prompt photon for all processes except for $t\bar{t}\gamma$ decay and $t\bar{t}\gamma\gamma$ (a), $t\bar{t}\gamma$ decay (b) and $t\bar{t}\gamma\gamma$ processes (c). These categories are added up and treated as one template in the fit These uncertainties affect only to the corresponding categories with fakes photons. (The dashed lines show the shape of the systematic before the smoothing procedure is applied.) 102
8.17 Nominal (black) and varied (red/blue) templates corresponding to the h-fake SF uncertainty for all processes except for $t\bar{t}\gamma$ decay and $t\bar{t}\gamma\gamma$ (a), $t\bar{t}\gamma$ decay (b) and $t\bar{t}\gamma\gamma$ (c). These categories are added up and treated as one template in the fit. These uncertainties affect only to the corresponding categories with fakes photons. (The dashed lines show the shape of the systematic before the smoothing procedure is applied.) 103
8.18 Correlations of NPs (with threshold of 10%) with the signal strength for the $t\bar{t}\gamma\gamma$ signal process in the fit to data. 105
8.19 The ranking plot of the 20 most important NPs for the signal strength in the fit to data in the single-lepton channel with one POI corresponding to the $t\bar{t}\gamma\gamma$ signal process. . 106
8.20 The p_{T} distributions of the (a) leading and (b) subleading photons. The uncertainty band represents the total uncertainty after the fit to the data. 107
8.21 The η distributions of the (a) leading and (b) subleading photons. The uncertainty band represents the total uncertainty after the fit to the data. 108
8.22 The invariant mass distributions of the lepton and the (a) leading or (b) subleading photon. The uncertainty band represents the total uncertainty after the fit to the data. 108
8.23 The invariant mass distributions of the (a) leading or (b) subleading photon and the closest b-jet. The uncertainty band represents the total uncertainty after the fit to the data. 109
8.24 The ΔR distributions between the lepton and the (a) leading and (b) subleading photon. The uncertainty band represents the total uncertainty after the fit to the data. 109
8.25 The p_{T} distributions of the (a) leading and (b) subleading jets. The uncertainty band represents the total uncertainty after the fit to the data. 110

8.26 The distributions of (a) the number of b-jets at 70% WP and (b) the highest DL1r score for the jet with PCBT binning. The uncertainty band represents the total uncertainty after the fit to the data. . . . 110
8.27 (a) Diphoton invariant mass and (b) invariant mass of all jets, the lepton, and both photons. The uncertainty band represents the total uncertainty after the fit to the data. 111
8.28 (a) $E_{\mathrm{T}}^{\mathrm{miss}}$ distribution and (b) ΔR distributions between leading and subleading photons. The uncertainty band represents the total uncertainty after the fit to the data. . . . 111
8.29 The photon conversion type of the leading photon. The first bin of the distribution corresponds to the unconverted photons, while the second bin corresponds to the sum of all converted photon types. The uncertainty band represents the total uncertainty after the fit to the data. . . . 112

9.1 Distributions of (a) the $t\bar{t}\gamma$ production classifier in the SR, (b) the $t\bar{t}\gamma$ decay classifier in the $t\bar{t}\gamma$ decay CR and the second largest pseudo-continuous b-tagging score in (c) the photon fakes CR and (d) the other prompt photon CR after the fit to data for the measurement of the $t\bar{t}\gamma$ production cross section in the single-lepton channel. The uncertainty band represents the total post-fit uncertainty in the prediction [Plots taken from [1]]. . . . 115
9.2 Plot showing the pulls and constraints of nuisance parameters for the ratio of $t\bar{t}\gamma\gamma$ to $t\bar{t}\gamma$ in fit to Asimov dataset. . . . 118
9.3 The ranking plot of the 20 most important nuisance parameters for the ratio of $t\bar{t}\gamma\gamma$ to $t\bar{t}\gamma$ in fit to Asimov dataset. . . . 119
9.4 Plot showing the pulls and constraints of nuisance parameters on the ratio with fit to data in single-lepton channel . . . 122
9.5 Correlations of NPs (with threshold of 10%) with the ratio measurement of $t\bar{t}\gamma\gamma$ to $t\bar{t}\gamma$ in the fit to data. $\mu_{t\bar{t}\gamma}$, which scales the $t\bar{t}\gamma$ process, is the second POI in the combined fit. . . . 123
9.6 The ranking plot of the 20 most important nuisance parameters for the ratio measurement of $t\bar{t}\gamma\gamma$ to $t\bar{t}\gamma$ in fit to data. . . . 124

A.1 Distributions of variables after fitting to Asimov data. The uncertainty band represents the total post-fit uncertainty. . . . 130

B.1 The impact of using absolute weights on the p_{T} distributions of the (a) leading and (b) subleading photons. . . . 131
B.2 The impact of using absolute weights on the η distributions of the (a) leading and (b) subleading photons. . . . 132
B.3 The impact of using absolute weights on the invariant mass distributions of the lepton and the (a) leading or (b) subleading photon. . . . 132
B.4 The impact of using absolute weights on the invariant mass distributions of the (a) leading or (b) subleading photon and the closest b-jet. . . . 133
B.5 The impact of using absolute weights on the ΔR distributions between the lepton and the (a) leading and (b) subleading photon. . . . 133
B.6 The impact of using absolute weights on the p_{T} distributions of the (a) leading and (b) subleading jets. . . . 134

B.7 The impact of using absolute weights on the distributions of (a) the number of b-jets at 70% WP and (b) the highest DL1r score for the jet with PCBT binning. 134
B.8 The impact of using absolute weights on the (a) Diphoton invariant mass and (b) invariant mass of all jets, the lepton, and both photons. 135
B.9 The impact of using absolute weights on the (a) $E_{\mathrm{T}}^{\mathrm{miss}}$ distribution and (b) ΔR distributions between leading and subleading photons. 135
B.10 The impact of using absolute weights on the photon conversion types (converted or unconverted) for the leading photon. 136

C.1 Loss curve per fold for the training and the test samples for 100 estimators. The vertical lines mark the estimator numbers (33, 40, 50, 60, 80 and 100) chosen for testing the performance of the 3-class BDT model. 138
C.2 BDT output for the signal and the total background (both prompt and fake), in bins used for fitting over all folds. 139
C.3 Loss curve per fold for the training and the test samples for 40 estimators. 139
C.4 (a) Pre-fit BDT output distribution and (b) BDT distribution after fitting to Asimov data. The uncertainty band corresponds to the total pre-fit uncertainty in (a) and to the total post-fit uncertainty in (b). 140
C.5 The ranking plot of the 20 most important NPs for the signal strength in the fit in the single lepton channel with one POI corresponding to the $t\bar{t}\gamma\gamma$ signal process. 141

D.1 The profile likelihood ratio test-statistic for background-only pseudo-experiments for different signal strengths (μ) of the $t\bar{t}\gamma\gamma$ process. The red line marks the test-statistic for the observed data. 144

List of Tables

4.1 The table summarises grouping of processes as used later in the analysis and in the figures. The categories $t\bar{t}\gamma\gamma$, $t\bar{t}\gamma$ (prompt γ), Other $\gamma\gamma$ correspond to events with two prompt photons, while the fake categories correspond to events with at least one fake photon. 37

5.1 Event selection for the single lepton channel. 42
5.2 Expected event yields in the signal and background categories. The h-fake category corresponds to events with at least one h-fake photon but not e-fakes. The e-fake category includes events with at least one e-fake photon. 42
5.3 Breakdown of e-fakes yields from the different processes. Table includes only e-fake events where one or both photons are e-fakes, not the combined-fake cases where one photon is e-fake and another photon is h-fake. 43
5.4 Breakdown of h-fake yields from different processes. The largest contribution of $t\bar{t}$ h-fake events corresponds to events with two h-fakes (1.4 events). 43
5.5 Breakdown of events with prompt photons from different processes. 44

8.1 Factor used to scale the varied templates, $N_{fid}^{nominal}/N_{fid}^{varied}$, for the different modelling uncertainties. 87
8.2 Number of events per category before and after the fit 92
8.3 Summary of the impact of the systematic uncertainties on the signal strength of the $t\bar{t}\gamma\gamma$ cross section in the unblinded single-lepton channel, grouped into different categories. The category 'JET' corresponds to the combined effect of JES, jet resolution and JVT uncertainties, while the categories 'Photon' and 'Leptons' correspond to all experimental uncertainties related to photons and leptons, respectively. The category '$t\bar{t}\gamma\gamma$ modelling' includes the PDF and theoretical modelling uncertainties on $t\bar{t}\gamma\gamma$. . 104

9.1 Summary of the absolute impact of the systematic uncertainties on the signal strength of the ratio of $t\bar{t}\gamma\gamma$ to $t\bar{t}\gamma$ in the single-lepton channel, grouped into different categories. The category 'JET' corresponds to the combined effect of JES, jet resolution and JVT uncertainties, while 'Photon' and 'Leptons' correspond to all experimental uncertainties related to photons and leptons, respectively. The category '$t\bar{t}\gamma\gamma$ modelling' includes the PDF and theoretical modelling uncertainties on $t\bar{t}\gamma\gamma$. . 125

9.2 Summary of the relative impact of the systematic uncertainties, in percentage, on the $t\bar{t}\gamma\gamma$ fiducial inclusive cross section and $R_{t\bar{t}\gamma\gamma/t\bar{t}\gamma}$ grouped into different categories. The category 'Jet' corresponds to the effect of JES, jet resolution and JVT uncertainties, 'Photon' and 'Leptons' include all experimental uncertainties related to photons and leptons, respectively. 126

C.1 Raw MC event counts for different processes and types for WP85 and WP70, including scaling factors. 137

.

Acknowledgements

With this modest piece of paper, I would like to thank all those whose guidance, encouragement, trust, and support have motivated me and earned my sincerest respect. I am deeply grateful to my friends, family, colleagues, and supervisors, whose invaluable help has carried me through this thesis.

I owe special thanks to Prof. Dr. Ivor Fleck, whose guidance, patience, and appreciation have shaped me not only as a young researcher but also as a person. His trust and encouragement have been a constant source of strength throughout my PhD journey. I have always been able to bring my questions to him candidly, and I deeply value his thoughtful insights.

I am also profoundly thankful to Dr. Carmen Diez Pardos, whose patience and mentoring have been instrumental in my PhD journey. Her exceptional guidance has helped me recognize and work on my own shortcomings, while her insights have repeatedly reminded me of the significance of my work. I especially appreciate her promptness to defend my research and place her trust in me, often going beyond what is required of a mentor.

Often, the most valuable lessons come from the simplest interactions. I am grateful to my colleagues and friends—Buddhadeb, Jan, Amartya, Binish, and Diptaparna—for the countless discussions we have shared over coffee or at the whiteboard. Each exchange has been a learning moment for me, not only in physics but also in many other topics. Their trust and companionship have carried me through both challenges and lighter moments. I also thank my dear friend Chainika, whose cheerful nature and sharp intelligence continue to inspire me, even after more than a decade of friendship.

I extend my sincerest appreciation to all the ATLAS collaborators, many of whom have helped me in subtle yet significant ways—whether by solving pesky technical issues or helping me gain a better understanding of physics. Their enthusiasm and keen observations have helped me sharpen my thinking and made me a better researcher. I am equally thankful to my colleagues in the Experimental Particle Physics Department at Universität Siegen, with whom I have shared countless memorable moments. I hope I have picked up some of the good qualities I found in each of them.